

It's not that I'm so smart, it's just that I stay with problems longer.

Albert Einstein

University of Alberta

**Polymer/Nanoparticle Nanocomposite Thin Films for Optoelectronics:
Experiment and Theory**

by

Sean Aaron McClure

A thesis submitted to the Faculty of Graduate Studies and Research
in partial fulfillment of the requirements for the degree of

Doctor of Philosophy

Department of Chemistry

©Sean Aaron McClure
Spring 2011
Edmonton, Alberta

Permission is hereby granted to the University of Alberta Libraries to reproduce single copies of this thesis and to lend or sell such copies for private, scholarly or scientific research purposes only. Where the thesis is converted to, or otherwise made available in digital form, the University of Alberta will advise potential users of the thesis of these terms.

The author reserves all other publication and other rights in association with the copyright in the thesis and, except as herein before provided, neither the thesis nor any substantial portion thereof may be printed or otherwise reproduced in any material form whatsoever without the author's prior written permission.

To my parents Douglas and Lesley McClure

Abstract

Third-generation optoelectronics, which utilize nanoscale materials, have received a considerable amount of attention in the chemical sciences and are poised to make a large impact in both fundamental research and real-world application. In order to make a contribution to the field, this thesis describes a route towards highly stable, water-soluble semiconductor nanorods and their incorporation into nanoparticle/polymer composite thin films. To characterize the photoelectrical properties of these multilayers, and to provide a proof-of-concept for a functional optoelectronic device, the films were integrated into an excitonic solar cell. To gain further insight into the physical properties of the thin films, computational modeling of the carrier transport in thiophenes was conducted, and the limits to device performance were described in the context of their charge transport characteristics.

Electrostatic layer-by-layer (ELBL) assembly was used for the synthesis of multilayer nanorod/polymer composite films. CdSe nanorods (NRs) were synthesized and made cationic and water-soluble using ligand exchange chemistry. The NRs were partnered with anionic polymers including poly(sodium 4-styrenesulfonate) (PSS) and the two polythiophene-based photoactive polymers, sodium poly[2-(3-thienyl)-ethoxy-4-butylsulfonate] (PTEBS) and poly[3-(potassium-6-hexanoate)thiophene-2,5-diyl] (P3KHT).

Multilayer growth, with nanoscale control, is shown through UV-vis spectroscopy, cross-sectional scanning electron microscopy (SEM) and surface analytical techniques including atomic force microscopy (AFM). The formation

of an intimate nanorod/conducting polymer bulk heterojunction is confirmed through cross-sectional SEM, transmission electron microscopy (TEM), and scanning Auger analysis. A series of photovoltaic devices was fabricated on ITO electrodes using CdSe NRs in combination with PTEBS or P3KHT. A thorough device analysis showed that performance was limited by carrier transport throughout the films.

Computational modeling of the thiophene component in polymer-based third-generation devices was done using density functional theory (DFT) with core potentials added to account for long range dispersion interactions inherent to optoelectronic thin films. Binding energies and orbital splittings in dimers composed of monomers up to six rings were investigated. The combination of experimental and computational studies elucidates some of the underlying mechanisms behind the production of third-generation solar energy.

Acknowledgements

I am extremely grateful to the following people who have guided me through my graduate studies at the University of Alberta. Their advice has been invaluable, and without their assistance this thesis would not be possible.

Firstly, I would like to express my gratitude for my supervisor, Professor Jillian Buriak. Her passion for science is an inspiration and her energy contagious. She has given me the freedom to carve out my own research path and instilled in me a sense of independence as a scientific researcher.

I would also like to thank Dr. Gino DiLabio. His willingness to guide me in the field of computational chemistry has made possible my progress in this area and has allowed me to investigate my project at the fundamental level.

Special thanks go to my committee members Professor Jonathan Veinot, Professor Steven H. Bergens, Professor Richard McCreery, Professor Alexander Brown, Professor Andriy Kovalenko, and Professor Anastasia Elias for their insightful questions and comments throughout my progress reports and candidacy.

I would like to thank my friends and colleagues of the Buriak research group. Past and present members which I have had the pleasure of working with include Professor David Rider, Brian Worfolk, Jeffrey Murphey, Jennifer Bruce, Dr. Kenneth Harris, Nicole Dehm, Sayed Nagy, Anne Cooper, Nathaniel Wu, David Grewer, Torsten Doerschel, Lawrence Huck, Tate Hauger, and Albert Xiaojiang. I would especially like to thank Professor David Rider and Brian Worfolk for all their hard work in helping make the hybrid solar cell project a reality.

I would like to thank my partner, Melissa Dooley, for her support throughout the final years of my degree. Her confidence in my abilities and her support of my career will always be remembered.

Finally, I would like to thank my family members who have provided support throughout my entire academic career. My parents Douglas and Lesley McClure for their undying support and my grandparents Ted and Edna Towsley and my gramma Margaret McClure for all their assistance. Also my brother Micah and my sister Cari and her husband Jason and the newest addition to the family, Jazlyn.

Table of Contents

Abstract

Acknowledgements

Table of Contents

List of Figures

List of Tables

List of Equations

List of Abbreviations

Chapter 1	General Introduction.....	1
1.1	Background.....	2
1.2	Optoelectronic Processes between Conducting Polymers and Semiconductor Nanoparticles	6
1.3	Electrical Characterization of Photoactive Films.....	13
1.4	Molecular Origins of Device Parameters.....	15
1.5	Semiconductor Nanoparticles.....	19
	Physical Chemistry of Semiconductor Nanoparticles	20
	Nanoparticle Synthesis.....	24
1.6	Design Principles for Polymer Based Third-Generation Photovoltaics	36
1.7	Semiconductor Nanoparticles in Hybrid Solar Cells.....	41
	Particle Size and Shape.....	44
	Film Morphology.....	53
	Particle Surface Chemistry.....	62
	Future Applications.....	66
1.8	Computational Studies of Charge Transport in Thiophenes.....	72
	Density Functional Theory – An Introduction	74
	Charge Transport in Organic Semiconductors.....	82
	Modeling Charge Transport: The Energy Splitting in Dimer Method.....	86
1.9	Organization of Thesis.....	89
1.10	References.....	91

Chapter 2	Electrostatic Layer-by-Layer Assembly of CdSe Nanorod/Polymer Films.....	104
2.1	Introduction.....	104
	Water-Soluble Semiconductor Nanoparticles.....	105
	Electrostatic Layer-by-Layer (ELBL) Assembly of Thin Films.....	107
2.2	Results and Discussion.....	113
	Water-Soluble CdSe Nanorods.....	113
	Electrostatic Layer-by-Layer Assembly of CdSe / Conducting Polymer Nanocomposite Thin Films.....	121
2.3	Conclusion.....	131
2.4	Experimental Section.....	132
2.5	References.....	138
Chapter 3	Hybrid Solar Cells from Nanocomposite Thin Films.....	147
3.1	Introduction.....	147
3.2	Results and Discussion.....	155
	Photovoltaic Devices Fabricated using ELBL with CdSe Nanorods and Conducting Polymer.....	155
3.3	Conclusion.....	168
3.4	Experimental Section.....	170
3.5	References.....	172
Chapter 4	Transport Properties of Thiophenes.....	176
4.1	Introduction.....	176
4.2	Computational Details.....	181
4.3	Results and Discussion.....	186
	Orbital Splittings in a T1 Dimer Model.....	186
	Binding Energies and Orbital Splittings in Mono- and Oligothiophene Dimers.....	199
	Dimers of T4, T5 and T6.....	214
	Changes in Splittings as a Consequence of Molecular Vibration.....	216
4.4	Conclusion.....	220
4.5	References.....	222

Chapter 5	Conclusion.....	227
5.1	Chapter Summaries.....	228
5.2	Proposed Research Directions.....	231
	Layer-by-Layer Film Deposition onto High	
	Surface Area Electrodes.....	231
	Electric Field Alignment of Nanorods.....	234
	Modeling Charge Transfer between CdSe and Thiophenes.....	237
5.3	References.....	244

List of Figures

- Figure 1.1** The five steps involved in solar energy conversion include **1)** the initial absorption of the incident radiation and generation of the exciton, **2)** diffusion of the exciton throughout the photoactive layer, **3)** separation of the charges leading to the dissociation of the exciton, **4)** transport of the free charges to the electrodes and **5)** collection of charges at the electrodes.
- Figure 1.2** The sun irradiance as a function of wavelength. Data obtained from NREL.
- Figure 1.3** The charge transfer interface (type-II heterojunction). The exciton on the donor can be dissociated into an electron residing on the acceptor lowest unoccupied molecular orbital (LUMO) and a hole on the donor highest occupied molecular orbital (HOMO). Note that if the nanoparticle absorbs the incident radiation, charge transfer can take place with a hole transferred from the nanoparticle HOMO to the polymer HOMO with the electron residing on the nanoparticle LUMO.
- Figure 1.4** Typical current-voltage (IV) curve showing the main parameters that are evaluated when assessing the performance of a solar cell. The light curve occupies the fourth quadrant with the ends of the curve defined by the short-circuit current (J_{SC}) and open-circuit potential (V_{OC}).
- Figure 1.5** Origin of the V_{OC} along with the condition for charge transfer. These are parameters that can potentially be tailored through synthetic chemistry when designing hybrid devices.
- Figure 1.6** Absorption spectra of CdSe nanocrystals showing the change that occurs with crystallite size.
- Figure 1.7** Evolution of energy levels with system size. As the size increases from an individual atom to a bulk crystal, the density of states increases until a continuum of energy levels forms a band. The space between the bands is called the band gap which is found to increase when the system becomes smaller.
- Figure 1.8** Typical experimental setup for semiconductor nanoparticle synthesis. This method involves rapid injection of precursors into a coordinating solvent. Typically, a round-bottom flask with condenser is used along with a thermocouple to monitor the temperature.

- Figure 1.9** Nucleation and growth process of semiconductor nanoparticles. The two main events during crystal growth are the nucleation stage and the growth stage.
- Figure 1.10** Ligand choice dictates the chemical potential in the growth solution controlling particle shape. The polar facets of CdSe allow for anisotropic growth of the crystal leading to nanorods.
- Figure 1.11** TEM images showing anisotropic control over CdTe crystal growth. The formation of tetrapods with varying arm diameters is possible by manipulating precursor concentrations.
- Figure 1.12** Hyperbranched particles of CdTe formed by controlling the concentration of calcogenide precursor in solution.
- Figure 1.13** The basic design of a hybrid solar cell. The components from top to bottom include a metal top contact, the photoactive layer, electrode modifier layer (typically PEDOT:PSS), and a transparent conducting electrode (typically ITO).
- Figure 1.14** Two commonly employed architectures in polymer-based third-generation solar cell design. **A)** Planar architecture ideal for charge transport and **B)** BHJ architecture ideal for charge transfer. These two designs represent the tradeoff between carrier transport and charge transfer in PAL designs.
- Figure 1.15** The ideal PAL interdigitated architecture exhibiting excellent carrier transport as well as charge transfer throughout the film.
- Figure 1.16** Elongated particles lead to improved charge transport by forming well defined percolation pathways that require a smaller number of hopping events for the charges to reach the electrodes.
- Figure 1.17** **A)** External quantum efficiencies of three different aspect ratio CdSe nanorods **B)** current-voltage curves of the 7 nm x 60 nm nanorod device illuminated at 515 nm **C)** current-voltage curves of the 7 nm x 60 nm nanorod device under AM1.5G solar conditions **D)** Photocurrent spectra of two devices with nanorods at two different diameters.

- Figure 1.18** Hybrid solar cell devices made from hyperbranched semiconductor nanoparticles . The dimensions of the nanocrystals span the entire thickness of the device bypassing the defects which are detrimental to traditional spin-cast hybrid cells. Transmission electron micrographs show both **d)** CdSe and **e)** CdTe hyperbranched nanoparticles.
- Figure 1.19** Hybrid solar cell characteristics using hyperbranched CdSe nanoparticles. Hyperbranched particles are found to outperform nanorod devices in all parameters. Only the nanorod devices show a loading threshold.
- Figure 1.20** Synthesis of P3HT with amino end-functionality. The new ligand (**4**) can be used with CdSe nanoparticles for better dispersion in nanoparticle/polymer films.
- Figure 1.21** Plots of power conversion efficiency (AM 1.5) versus the volume ratio of CdSe in the active layer of the devices. Devices were made using both polymer **4** (solid lines) and polymer **1** (dashed lines) as shown in figure 1.20.
- Figure 1.22** AFM images showing the topography **a)** and phase **b)** of the CdSe/P3HT system with 90 weight % nanoparticles with dimensions 8 nm x 13 nm. The images show the difference between 1 vol% and 8 vol% pyridine in chloroform. Scan areas are 5x5 microns.
- Figure 1.23** The range of RMS roughness values obtained with varying ratios of pyridine to chloroform. The corresponding EQE values are also shown.
- Figure 1.24** PL decay curves for blends of CdSe and OC₁C₁₀-PPV polymer. Solvents used to spin cast the films were TCB (circles) and chloroform (squares). The pristine polymer film is shown for comparison (triangles).
- Figure 1.25** Synthetic protocol for creating P3HT-capped CdSe nanorods.
- Figure 1.26** Simplified picture of multiple exciton generation (MEG) in semiconductor nanoparticles. Absorption of a photon in excess of two times the band gap, E_g , produces multiple excitons.

- Figure 1.27** In their study, Zhu et al. found that regardless of quantum dot size or chemical treatment, the lowest excited electronic state of PbSe was always below the TiO₂ conduction band minimum. Therefore electron transfer from the PbSe to the TiO₂ could only be possible through hot-electron states.
- Figure 1.28** The two main packing types of the thiophene oligomer include the herringbone and cofacial arrangements.
- Figure 1.29** An example of the HOMO and LUMO interactions that lead to the formation of valence and conduction bands in extended systems of packed cofacial molecules.
- Figure 2.1** UV-vis spectra of PAA-g-MEA-QDs (A) and MPA-QDs (B) at various NaCl concentrations. (C) Normalized PL intensities of PAA-g-MEA-QDs (2) and MPA-QDs (b) under various NaCl concentrations. (D) Photographs of PAA-g-MEA-QDs (top) and MPA-QDs (bottom) under various concentrations of NaCl solutions.
- Figure 2.2** Electrostatic layer-by-layer assembly process for fabricating multilayer thin films. A) Steps 1 and 3 represent the adsorption of a polyanion and polycation, while steps 2 and 4 are the washing steps. B) Molecular picture for the first two adsorption steps. C) Chemical structure of the two polyanions.
- Figure 2.3** Absorption of CdSe nanoparticles with increasing bilayer number using the ELBL film growth process. Inset shows the absorbance measured at 439 nm as a function of the number of layers.
- Figure 2.4** A) ELBL assembly of CdTe nanoparticles with PDDA polymer. Successive dipping leads to the formation of multilayer thin films. B) The first bilayer composed of CdTe nanoparticles and PDDA. C) Incorporation of various nanocrystal sizes to the thin film in order to create cascaded energy transfer layers. D) Fully assembled device with graded energy gaps.
- Figure 2.5** Basic protocol to forming NRs with three different aspect ratios and the subsequent ligand exchange procedure used to render the NRs water-soluble.

- Figure 2.6** FTIR spectra of A) TOPO-capped CdSe nanorods and B) AET-capped CdSe nanorods. Decreases in the C-H and P=O stretching regions indicate the replacement of TOPO with AET.
- Figure 2.7** A) Optical image of stable AET-capped nanorod solutions made in this study and the TEM micrographs for samples B) NR1, C) NR2, and D) NR3. Insets show HR-TEM images of the three samples. The scale bars in B-D are 20 nm, whereas those in the insets are 2 nm.
- Figure 2.8** UV-vis and PL spectra for aqueous NR1, NR2, and NR3 (A-C, respectively). Excitation wavelength for emission spectra was 550 nm for NR1, 545 nm for NR2, and 620 nm for NR3.
- Figure 2.9** UV-vis spectra for PTEBS (red) and P3KHT (blue) polymer.
- Figure 2.10** Electronic band edge structure of the three nanorods and two photoconducting polymers as determined by cyclic voltammetry. Values correspond to the energies in electron volts.
- Figure 2.11** ELBL assembly of nanocomposite thin films composed of semiconductor NRs and polymer. Repeating the steps leads to controlled thickness on the nanometre scale.
- Figure 2.12** UV-vis experiment monitoring the absorbance of 5, 20, 40, and 60 bilayer films assembled using ELBL on glass with CdSe NR2 and PSS polyelectrolyte.
- Figure 2.13** UV-vis experiment monitoring the absorbance of 5, 20, 40, and 60 bilayer films assembled using ELBL on glass with CdSe NR2 and PTEBS polyelectrolyte.
- Figure 2.14** UV-vis experiment monitoring the absorbance of 5, 20, 40, and 60 bilayer films assembled using ELBL on glass with CdSe NR2 and P3KHT polyelectrolyte.
- Figure 2.15** Summary of the maximum absorbance with increasing bilayer number.

- Figure 2.16** AFM study showing the surface of PSS and NR2 films assembled on glass using ELBL after A) 0 bilayers, B) 10 bilayers, C) 20 bilayers, D) 30 bilayers, and E) 60 bilayers.
- Figure 2.17** Roughness of films after 10, 20, 30, and 60 bilayers for PSS, PTEBS, and P3KHT and NR2 systems.
- Figure 2.18** SEM cross-sections of (CdSe NR2/PSS)_n multilayer nanocomposite thin films on glass with 10, 30, and 60 bilayers.
- Figure 2.19** Cross-section SEM images of (A) (CdSe NR1/PTEBS)₆₀ and (D) (CdSe NR2/PTEBS)₆₀ nanocomposite films (assembled on ITO/ePEDOT:PSS substrate). TEM and HR-TEM cross-sectional analysis of NR1/PTEBS (B and C) and NR2/PTEBS (E and F) nanocomposite films. C and F show the crystal planes of NR1 (0.36 nm) and the moiré fringes of NR2 (0.86 nm).
- Figure 2.20** Auger analysis of ELBL thin film on silicon. Intimate mixing between components is shown, suggesting a bulk heterojunction architecture to the film.
- Figure 3.1.** Equivalent circuit diagram for an illuminated photovoltaic cell. In the simplest model, it can be thought of as a diode in parallel with a constant source of current. R_s and R_{sh} are the series and shunt resistances respectively. I_{out} represents the current and V_{out} the voltage in the external circuit. C is the capacitance.
- Figure 3.2.** The changes that occur in the current-voltage curves with A) increasing series resistance and B) decreasing shunt resistance.
- Figure 3.3.** AFM image showing the formation of a partial monolayer of CdSe quantum dots after spin-casting with the hole-transporting material N,N'-diphenyl-N,N'-bis(3-methylphenyl)-(1,10-biphenyl)-4,4'-diamine (TPD) onto an ITO substrate. Incomplete coverage led to poor performance in the optoelectronic devices.

- Figure 3.4.** The orientation of the nanorods within the photoactive layer can play a large role in the ability of current to be transported throughout the device. The larger the number of nanorods that lie vertically with respect to the electrode, the lower the number of hopping events that must occur.
- Figure 3.5.** Fabrication of photovoltaic devices from CdSe NR/polymer multilayer films assembled by ELBL. The green represents a negatively charged surface. Blue denotes the work function modifier while the remaining layers shows the fully assembly device.
- Figure 3.6.** Cross-section SEMs of (A) (CdSe NR1/PTEBS)₆₀ and (B) CdSe NR2/PTEBS)₆₀ completed device architecture using the ELBL technique. The labels in B) identify the layers within the device.
- Figure 3.7.** J-V characteristics of the illuminated (CdSe NR_x/polymer)₆₀ devices made in this study (x = 1, 2).
- Figure 3.8.** A) SEM image showing a NR1/PTEBS ELBL film at 45°. Variations in the surface lead to depressions in the film potentially leading to pinholes in the film. Pinholes are known to give low values for shunt resistance. B) Close-up view showing the depressions in the film.
- Figure 3.9.** A) SEM image showing a PTEBS/NR2 ELBL film at 45°. Variations in the surface lead to depressions in the film potentially leading to pinholes in the film. Pinholes are known to give low values for shunt resistance. B) Close-up view showing the depressions in the film.
- Figure 3.10.** A) SEM image showing a P3KHT/NR1 ELBL film at 45°. Variations in the surface lead to depressions in the film potentially leading to pinholes in the film. Pinholes are known to give low values for shunt resistance. B) Close-up view showing the depressions in the film.
- Figure 3.11.** A) SEM image showing a NR1/PTEBS ELBL film at 45°. The roughness shown in figure 3.8 leads to roughness in the aluminum top contact, potentially leading to high values of series resistance.

- Figure 3.12.** SEM cross-section of (CdSe NR3/PTEBS)₆₀ hybrid device. The overall device architecture is shown in C) while a close-up of the PAL is shown in D).
- Figure 3.13.** PL quenching experiments of PTEBS solutions with increasing NR1 content. A decrease in the PL intensity with increasing NR1 concentration is indicative of charge transfer from PTEBS to NR1.
- Figure 3.14.** PL quenching experiments of P3KHT solutions with increasing NR1 content. A decrease in the PL intensity with increasing NR1 concentration is indicative of charge transfer from P3KHT to NR1.
- Figure 3.15.** Nanoindent AFM used to investigate the first bilayers of ELBL thin film assembly. A) Bare ITO used as control to show an indentation of 1.9 nm. B) Same force applied to 2 bilayers of NR1/PSS showing an indent of 8.3 nm. The 2 bilayers show that the beginning of ELBL starts with a few localized spots instead of a uniform increase in thickness.
- Figure 4.1** B971/6-31+G(d,p) potential energy surface for dimer 12a' computed with and without carbon DCPs. The inclusion of DCPs (red) accurately predicts the dimer separation and binding energy.
- Figure 4.2** Schematic illustrating the energy splitting between the filled (electrons are black dots) dimer HOMO (green) and HOMO-1 (red) orbitals as a function of overlap between two filled, monomer orbitals (blue). When the orbitals are perfectly overlapping, as in the case of a, maximum splitting is nominally achieved. When overlap is less than ideal, as in the case of b, splitting is reduced (viz. $S_{\text{HOMO a}} > S_{\text{HOMO b}}$). Splitting between dimer LUMOs can be similarly illustrated, but with empty orbitals.
- Figure 4.3** A) Highest occupied and B) lowest unoccupied molecular orbitals of the T1 monomer. The colours of the orbitals represent their relative phases. C) The lowest unoccupied molecular orbital of a T2 shown for comparison. The atom coloring scheme yellow (sulphur), gray (carbon), white (hydrogen) is used throughout this chapter, unless otherwise indicated.

Figure 4.4 Two perspective views of a stacked T1 dimer with C_{2h} symmetry are shown in (A) and (B). Orbital splittings are evaluated for displacements along the directions i and ii in (A) and along iv in (B) and for rotation about an axis perpendicular to the plane of the molecules (indicated by iii). For displacements along i and ii, the initial monomer separation is 3.8 Å. For rotations about iii, monomer separation is maintained at 3.8 Å.

Figure 4.5 (Lower panel) Binding energy as a function of the displacement of one thiophene monomer in the T1 dimer along the direction “i” indicated in Figure 4.4A. (Upper panel) Energy splitting between two highest occupied molecular orbitals (S_{HOMO} , red) and the two lowest unoccupied molecular orbitals (S_{LUMO} , blue) as a function of displacement distance. Insets show the molecular orientation and representations of the dimer LUMO+1 orbitals for two displacements. The relative phases of the orbitals are indicated as green and red.

Figure 4.6 (Lower panel) Binding energy as a function of the displacement of one thiophene monomer in the T1 dimer along the direction “ii” indicated in figure 4.4B. (Upper panel) Energy splitting between two highest occupied molecular orbitals (S_{HOMO} , red) and the two lowest unoccupied molecular orbitals (S_{LUMO} , blue) as a function of displacement distance. Insets show the molecular orientation for two displacements of the dimer with representations of the corresponding highest occupied molecular orbitals. The relative phases of the orbitals are indicated as green and red.

Figure 4.7 (Lower panel) Binding energy as a function of the rotation of one thiophene monomer in the T1 dimer, according to “iii” indicated in Figure 4.4B. (Upper panel) Energy splitting between two highest occupied molecular orbitals (S_{HOMO} , red) and the two lowest unoccupied molecular orbitals (S_{HOMO} , blue) as a function of displacement distance. Insets show the molecular orientations for the indicated rotations. Representations of the highest occupied molecular orbitals for two rotations (red frame) and the lowest unoccupied molecular orbitals for one rotation (blue frame) are displayed in the insets. The relative phases of the orbitals are indicated as green and red.

Figure 4.8 (Lower panel) Binding energy with DCPs (black), and without DCPs (red), as a function of the displacement of one thiophene monomer in the T1 dimer along the direction “iv” indicated in Figure 4.4B. (Upper panel) Energy splitting between two highest occupied orbitals (S_{HOMO} , red) and the two lowest unoccupied molecular orbitals (S_{LUMO} , blue) as a function of displacement distance. Insets show the molecular orientations for two displacements along with representations of the highest occupied molecular orbitals. Note that there is a change in the dimer HOMO character upon decreasing the intermonomer distance below 4 Å, c.f. left and right orbital insets. The relative phases of the orbitals are indicated as green and red. The vertical black lines show the values that are predicted for S_{HOMO} and S_{LUMO} when dispersion is taken into account (solid) and when dispersion is not taken into account (dashed).

Figure 4.9 Two conformers of T1 dimers with selected associated dimer orbitals.

Figure 4.10 Orbital isosurfaces for three representative dimers of the optimized T2 system as found using DCP-DFT. Red dots are used to identify the same rings in each view of a dimer structure.

Figure 4.11 Orbital isosurfaces for two representative dimers of the optimized T3 system as found using DCP-DFT. Red dots are used to identify the same rings in each view of a dimer structure.

Figure 4.12 Perspective images showing (a) rotation, (b) slipping, and (c) breathing vibration modes in a T4 dimer. The carbon atoms in one monomer are coloured orange to help with differentiation.

Figure 5.1 Cross-sectional SEM images of high surface area nanoITO electrode.

Figure 5.2 A) Incomplete infiltration of PAL onto high surface area electrode.
B) Complete infiltration of PAL

Figure 5.3 SEM images of CA nanofibers assembled with (a) three, (b) four, (c) five, and d) six bilayers of PAA/PDADMAC.

- Figure 5.4** Alignment of CdSe nanorods using electric fields.
- Figure 5.5** Alignment of CdS nanorods using electric fields. Domain sizes exceeding $0.5 \mu\text{m}^2$ are important for device applications.
- Figure 5.6** Ordering induced in nanorods within the PAL of a hybrid device. The polymer matrix must be brought within its T_g in order to allow the nanorods mobility.
- Figure 5.7** Orbital analysis of HOMO and LUMOs between PTCI and PC. Symmetry allows certain configuration to undergo charge transfer while others do not.
- Figure 5.8** Bulk heterojunction of the thiophene/PCBM system as predicted by a course grained approach

List of Tables

Table 2.1	Experimentally determined band gaps of the three NR samples and two photoactive polymers as determined by UV-vis spectroscopy (E_g) and cyclic voltammetry (E_g').
Table 3.1	PV Characteristics of the Best Performing Examples of ELBL-Assembled Solar Cells Made in This Study Showing the Nanorod Aspect Ratio (AR), Power Conversion Efficiency (η), Open Circuit Potential (V_{OC}), Fill Factor (FF), and Short Circuit Current (J_{SC}).
Table 3.2	Series and shunt resistances of the polymer/NRx films fabricated in this study. (x = 1, 2 and 3). The series resistances are quite large suggesting poor transport throughout the devices. Shunt resistances are also present suggesting short-circuits throughout the film.
Table 4.1	Conformer Label and Selected Optimized Structures of T1 dimers. Binding Energy (BE, kcal/mol), Inter-Ring Separation (R, Å), Angle between Rings (θ , °) and Orbital Energy Splitting (S, eV) are also shown.
Table 4.2	Conformer Label and Selected Optimized Structures of T2 dimers. Binding Energy (BE, kcal/mol), Inter-Ring Separation (R, Å), Angle between Rings (θ , °) and Orbital Energy Splitting (S, eV) are also shown. Table 4.3 lists the remainder of the T2 dimers.
Table 4.3	Conformer Label and Selected Optimized Structures of T2 dimers. Binding Energy (BE, kcal/mol), Inter-Ring Separation (R, Å), Angle between Rings (θ , °) and Orbital Energy Splitting (S, eV) are also shown.
Table 4.4	Conformer Label and Selected Optimized Structures of T3 dimers. Binding Energy (BE, kcal/mol), Inter-Ring Separation (R, Å), Angle between Rings (θ , °) and Orbital Energy Splitting (S, eV) are also shown.
Table 4.5	Conformer Label and Selected Optimized Structures of T3 dimers. Binding Energy (BE, kcal/mol), Inter-Ring Separation (R, Å), Angle between Rings (θ , °) and Orbital Energy Splitting (S, eV) are also shown.
Table 4.6	Binding Energy (BE, kcal/mol), HOMO (S_{HOMO} , eV), and LUMO Splitting (S_{LUMO} , eV) Ranges for Various Structures of T4, T5, and T6 Dimers
Table 4.7	Vibration Mode, Frequency (cm^{-1}), and Changes in S_{HOMO} and S_{LUMO} (eV) at the Inner/Outer Vibration Turning Points for the T4A, T4D, T5B, and T6A Dimers.

List of Equations

$$1.3.1 \quad \eta = \frac{V_{OC} \times J_{SC} \times FF}{P_{in}}$$

$$1.3.2 \quad FF = \frac{I_{mpp} \times V_{mpp}}{J_{SC} \times V_{OC}}$$

$$1.5.2a \quad S_r = S_b \exp(2\sigma V_m / rRT)$$

$$1.5.2b \quad \frac{dr}{dt} = K \left(\frac{1}{r} + \frac{1}{\delta} \right) \left(\frac{1}{r^*} - \frac{1}{r} \right)$$

$$1.9.1 \quad E = E_o(\rho_o)$$

$$1.9.2 \quad \hat{H} = -\frac{1}{2} \sum_{i=1}^n \nabla_i^2 + \sum_{i=1}^n v(r_i) + \sum_j \sum_{i>j} \frac{1}{r_{ij}}$$

$$1.9.3 \quad v(r_i) = -\sum_{\alpha} \frac{Z_{\alpha}}{r_{i\alpha}}$$

$$1.9.4 \quad \int \rho_0(r) dr = n$$

$$\begin{aligned} 1.9.5 \quad E_{0,a} &\leq \left\langle \Psi_{0,b} | H_a | \Psi_{0,b} \right\rangle \\ E_{0,a} &\leq \left\langle \Psi_{0,b} | H_a - H_b + H_b | \Psi_{0,b} \right\rangle \\ E_{0,a} &\leq \left\langle \Psi_{0,b} | \nu_a - \nu_b | \Psi_{0,b} \right\rangle + E_{0,b} \\ E_{0,a} &\leq \int [\nu_a(r) - \nu_b(r)] \rho_0(r) dr + E_{0,b} \\ E_{0,b} &\leq \int [\nu_b(r) - \nu_a(r)] \rho_0(r) dr + E_{0,a} \\ E_{0,a} + E_{0,b} &\leq \int [\nu_a(r) - \nu_b(r)] \rho_0(r) dr + \int [\nu_b(r) - \nu_a(r)] \rho_0(r) dr + E_{0,b} + E_{0,a} \\ &\leq \int [\nu_b(r) - \nu_a(r) + \nu_a(r) - \nu_b(r)] \rho_0(r) dr + E_{0,b} + E_{0,a} \\ &\leq E_{0,b} + E_{0,a} \end{aligned}$$

$$1.9.6 \quad E[\rho(r)] = T_{ni}[\rho(r)] + V_{ne}[\rho(r)] + V_{ee}[\rho(r)] \\ + \Delta T[\rho(r)] + \Delta V_{ee}[\rho(r)]$$

$$1.9.7 \quad E[\rho(r)] = \sum_i^N \left(\left\langle \chi_i \left| -\frac{1}{2} \nabla_i^2 \right| \chi_i \right\rangle - \left\langle \chi_i \left| \sum_k^{nuclei} \frac{z_k}{r_i - r_k} \right| \chi_i \right\rangle \right) \\ - \sum_i^n \left\langle \chi_i \left| \frac{1}{2} \int \frac{p(r')}{r_i - r'} dr' \right| \chi_i \right\rangle + E_{xc}[\rho(r)]$$

$$1.9.8 \quad \rho = \sum_{i=1}^N \langle \chi_i | \chi_i \rangle$$

$$1.9.9 \quad h_i^{KS} \chi_i = \varepsilon_i \chi_i$$

$$1.9.10 \quad h_i^{KS} = -\frac{1}{2} \nabla_i^2 - \sum_k^{nuclei} \frac{z_k}{r_i - r_k} \\ + \int \frac{p(r')}{r_i - r'} dr' + V_{xc}$$

$$1.9.11 \quad V_{xc} = \frac{\delta E_{xc}}{\delta \rho}$$

$$1.9.12 \quad \theta_i^{KS} = \sum_{r=1}^b c_{ri} \chi_r$$

$$1.9.13 \quad h_{rs}^{KS} = \left\langle \chi_r \left| \hat{h}^{KS} \right| \chi_s \right\rangle$$

$$1.9.14 \quad \left\langle x^2 \right\rangle = nDt$$

$$1.9.15 \quad \mu = \frac{eD}{k_B T}$$

$$1.9.16 \quad \frac{1}{\mu} = \frac{1}{\mu_{low}} + \frac{1}{\mu_{high}}$$

$$1.9.17 \quad \mu_O = \mu_\infty \exp(-\Delta / k_B T)$$

$$1.9.18 \quad t = \frac{E_H - E_{H-1}}{2}$$

$$1.9.19 \quad t = \frac{E_{L+1} - E_L}{2}$$

$$1.9.20 \quad k_{ET} = \frac{4\pi^2}{h} \frac{1}{\sqrt{4\pi\lambda k_B T}} V^2 \exp\left(-\frac{\lambda}{4k_B T}\right)$$

$$3.1 \quad I(V) = I_O [e^{(qv/nkT)} - 1]$$

$$3.2 \quad I_{out} = \frac{R_{sh}}{R_s + R_{sh}} \left(I_O [e^{[q(V_{out} - I_{out} R_s)/nkT]} - 1] + \frac{V_{out}}{R_{sh}} \right)$$

$$4.1 \quad k_{ET} = \frac{4\pi^2}{h} \frac{1}{\sqrt{4\pi\lambda k_B T}} V^2 \exp\left(-\frac{\lambda}{4k_B T}\right)$$

$$5.1 \quad k_{ET} = \frac{4\pi^2}{h} \frac{1}{\sqrt{4\pi\lambda k_B T}} V^2 \exp\left(-\frac{(G^o + \lambda)^2}{4\lambda k_B T}\right)$$

$$5.2 \quad \Delta G_{dis}^o = E^{D^+} + E^{A^-} - E^{D^*} - E^A + \Delta E_{coul}$$

$$5.3 \quad \Delta E_{coul} = \sum_{D^+} \sum_{A^-} \frac{q_{D^+} q_{A^-}}{4\pi\epsilon_o \epsilon_s r_{D^+ A^-}} \\ - \sum_{D^*} \sum_A \frac{q_{D^*} q_A}{4\pi\epsilon_o \epsilon_s r_{D^* A}}$$

List of Abbreviations

AET	Aminoethanethiol
AFM	Atomic force microscopy
AR	Aspect Ratio
ATP	Adenosine triphosphate
BHJ	Bulk heterojunction
CdMe ₂	Dimethyl Cadmium
CT	Charge transfer
CV	Cyclic voltammetry
DFT	Density functional theory
EM	Electromagnetic
ePEDOT:PSS	Electropolymerized polyethylene dioxythiophene polystyrene sulfonate
EQE	External Quantum Efficiency
FF	Fill factor
FTIR	Fourier transform infrared
HOMO	Highest occupied molecular orbital
HPA	Hexylphosphonic acid
HR-TEM	High- resolution transmission electron microscopy
ITO	Indium tin oxide
JSC	Short-circuit current

LUMO	Lowest unoccupied molecular orbital
MEH-PPV	Poly(2-methoxy,5-(2'-ethyl)-hexyloxy-p-phenylenevinylene)
MEG	Multiple exciton generation
MO	Molecular orbital
η	Overall power conversion efficiency
NP	Nanoparticle
OC1C10-PPV	Poly(2-methoxy-5-(3',7'-dimethyl-octyloxy)-p-phenylenevinylene)
ODPA	Octyldecylphosphonic acid
OPV	Organic photovoltaic
P3HT	Poly-3-hexylthiophene
P3KHT	Poly[3-(potassium-6-hexanoate)thiophene-2,5-diyl]
PAL	Photoactive layer
PCBM	[6,6]-phenyl-C61-butyric acid methyl ester
PDDA	Polydiallyl dimethylammonium chloride
PEDOT:PSS	Polyethylenedioxythiophene polystyrene sulfonate
PES	Potential energy surface
Pin	Power input
PL	Photoluminescence
PSS	Polystyrene

PTEBS	Poly[2-(3-thienyl)-ethoxy-4-butylsulfonate]
SCNPs	Semiconductor nanoparticles
SEM	Scanning electron microscopy
TBOC	Tert-butoxycarbonyl
TCB	Trichlorobenzene
TCO	Transparent conducting oxide
TDPA	Tetradecylphosphonic acid
TEM	Transmission electron microscopy
T _g	Glass transition temperature
V _{oc}	Open-circuit potential

Chapter 1

General Introduction

This thesis describes the use of electrostatic layer-by-layer (ELBL) assembly to fabricate multilayer nanocomposite films composed of alternating polymer and nanoparticle layers. The synthesis of water-soluble semiconductor nanorods, the design of multilayers that pair nanorods with conducting polymer into photoactive films, and the integration of these films into solar cell devices will be presented. Computer modeling of thiophenes is studied in order to elucidate the fundamental mechanisms by which charge transport occurs throughout the polymer component of the film. These investigations strengthen our understanding of nanoscale materials and help shed light on the steps necessary to integrate them into efficient devices.

As an introduction, the first chapter will discuss the background behind the work presented in this thesis. An overview of semiconductor nanoparticle/polymer hybrid solar cells will be discussed as a case study in third-generation optoelectronics. This discussion will outline both the fundamental mechanisms behind their operation as well as the state-of-the-art chemical approaches to their design. The synthetic strategies used to fabricate semiconductor nanoparticles and the physical chemistry behind their unique properties will also be presented. An overview of some of the theory behind the computer modeling methods used in this thesis will be given along with the theoretical background to charge transport in organic semiconductor films.

1.1 Background

Enough energy hits the earth's surface every hour to power our planet for an entire year.^{1, 139} Solar power offers the potential for virtually limitless electrical energy and is considered by many to be the only viable alternative to fossil fuels. The ability to harness the power of the sun is seen in nature through the process of photosynthesis. Through millions of years of evolution, plants have developed the ability to convert the photons from the sun into stored chemical energy. Research has shed light onto the mechanisms by which plants are able to make this energy conversion possible.² Photosynthetic organisms are equipped with antenna systems that harvest solar radiation by absorbing the incident photons. Once absorbed, the energy is transferred to reaction centres where stable charge-separated states exist in the form of a trans-membrane electrochemical potential. It is through this potential that the production of molecules such as adenosine triphosphate (ATP) is made possible. The realization that solar radiation could be converted into useful energy inspired early scientists to attempt such feats in the laboratory.

Although the photovoltaic effect was discovered as early as 1839, it wasn't until 1954 that the first modern silicon solar cell was invented by Pearson, Fuller, and Chapin at Bell labs.³ These solar devices had an overall power conversion efficiency of approximately 6%. Since then, scientists have been actively working towards high efficiency solar cells. Today, commercially available silicon devices reach average efficiencies of ~17% with laboratory records reaching ~25% for single junction architectures.⁴ These efficiencies are

considered quite high and are approaching the theoretical limit for a silicon device (31%) as predicted by Shockley and Queisser.⁵ Despite these impressive efficiencies, the fabrication of silicon solar cells is much too costly to allow them to become a viable energy alternative to the much less expensive fossil fuels. The costs associated with conventional solar cell fabrication originate from the high temperature, high vacuum and numerous lithographic steps necessary to create the required cell architecture. In order for solar power to compete with other energy technologies, entirely new approaches must be investigated that convert solar energy into electricity. These new devices must be made of inexpensive materials and be processed and fabricated on a large scale.

Nanotechnology offers the potential to develop solar cells using inexpensive materials and fabrication methods. The ability to manipulate matter at the nanoscale opens the possibility towards a high degree of control over the physical and mechanical properties of the material. In the context of solar cell design, nanoparticles and polymers can be synthetically engineered to absorb incident sunlight at a range of desired wavelengths. Particle morphology can be tailored to allow for a variety of novel architectures while thermal treatments can influence film properties as the polymer matrix is brought above its glass transition temperature (T_g). Films composed of polymeric materials have the advantage of benefiting from their inherent flexibility. In fact, the field of plastic electronics is considered to be an area that may one day revolutionize the electronics industry.⁶ Roll-to-roll processing of these materials could allow for

the large-scale production of low-cost solar cells capturing a significant portion of the photovoltaic device market.⁷

Solar cells that utilize nanotechnology are termed “third-generation photovoltaics.” The last 20 years has seen much progress in utilizing nano-materials and characterization techniques to understand and develop low-cost photovoltaics with moderate efficiencies. The most successful examples of third-generation solar cells include dye-sensitized photoelectrochemical,⁸ small molecule thin film,⁹ polymer/fullerene planar and bulk heterojunction,¹⁰ and organic-inorganic hybrid devices.¹¹ The top performing polymer-based third-generation devices currently hold performance records of ~5-6%. In order to compete with current energy technologies, cell efficiencies must reach ~10%.

The hybrid solar cell combines organic semiconductor polymers with inorganic semiconductor nanoparticles. This approach to solar cell design marries the benefits of these two components. On the polymer end, flexibility and strong absorption in the visible region are beneficial to device performance. The incorporation of an inorganic component leads to better electron mobility throughout the film and also sensitizes the device to additional wavelengths. The performance of hybrid solar cells is not as sensitive to film stability as is the case for the dye-sensitized solar cell which relies on an iodine electrolyte to shuttle charges within the device. Although small molecule and polymer/fullerene cells currently hold the efficiency records, they generally only contain a single absorbing component in their photoactive layer. Unlike the ubiquitous C₆₀, which does not absorb in the visible region, semiconductor nanoparticles can be

tailored to absorb across the entire visible, and in some cases near-IR and IR, region. Therefore, in hybrid devices, both active components can lead to photocurrent. In addition to the fundamental benefits of these materials, the components are relatively cheap and can be processed from solution making scale-up a possibility for future applications.

Despite the recent progress in hybrid solar cell research, there remains a significant challenge in moving towards a thorough understanding of the parameters leading to better performing devices. This challenge involves developing a clear understanding of the molecular origins of the photocurrent from films composed of polymers and semiconductor nanoparticles. In addition, inorganic nanoparticles must be made compatible with conducting polymers while ensuring charge transfer across the polymer/nanoparticle interface. Control over film morphology is critical to achieving the ideal amount of phase separation between the components to ensure charge transport to the electrodes. Finally, fabricating devices and characterizing the photocurrent is essential to gaining insight into the chemistry needed to produce photoactive films.

This introduction will first look at the optoelectronic processes in hybrid solar cells followed by the basic design of a polymer-based third-generation photovoltaic cell. The electrical characterization of assembled films is discussed in the context of performance parameters and the relationship between these factors and their chemical origins are examined. An overview of the fundamentals behind the synthesis and resultant properties of semiconductor nanoparticles will be given using CdSe as a specific case study. Particle size and

shape, film morphology and surface chemistry will be discussed in order to gain an understanding of the chemical approaches that can be used to lead to specific improvements in device performance. Finally, some future directions currently being taken to surpass limitations in performance are discussed. It is hoped that this introduction will serve as a review of the current “toolbox” researchers are using towards achieving the dream of a rationally designed hybrid solar cell.

1.2 Optoelectronic Processes between Conducting Polymers and Semiconductor Nanoparticles

The fundamental mechanisms behind the generation of photocurrent in hybrid solar cells provide a picture of the molecular origins of device performance. Knowledge of these mechanisms is critical if the rational design of a hybrid solar cell with moderate to good performance is to become reality. The critical processes behind the generation of photocurrent are typically broken into five key steps as shown in Figure 1.1. Step 1 is the initial capture of light. At least one material in the photoactive layer must absorb radiation somewhere in the range of the solar spectrum. Absorption of light in both polymers and nanoparticles produce a particle known as the exciton. Excitons are Coulombically bound electron-hole pairs and are the source of charges that ultimately produce photocurrent. The exciton is neutral to electric fields and must diffuse to a charge-transfer interface in order to be dissociated into free carriers.

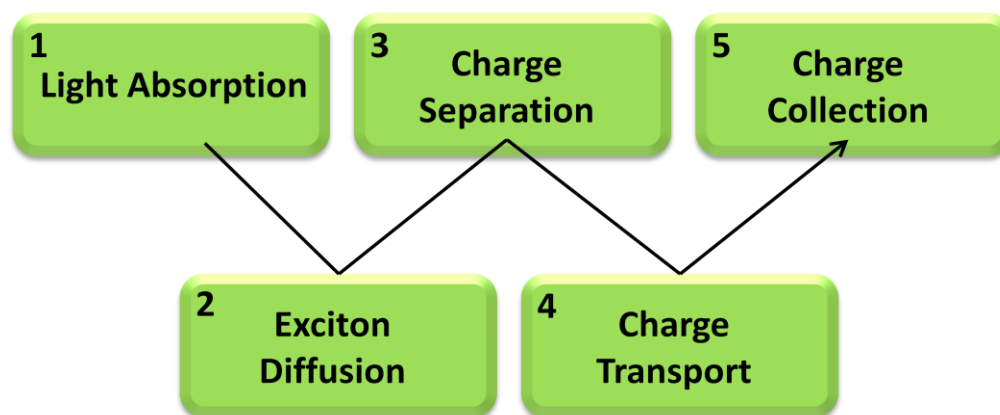


Figure 1.1. The five steps involved in solar energy conversion include, **1)** the initial absorption of the incident radiation and generation of the exciton, **2)** diffusion of the exciton throughout the photoactive layer, **3)** separation of the charges leading to the dissociation of the exciton, **4)** transport of the free charges to the electrodes and **5)** collection of charges at the electrodes.

From step 1 it can be seen that a necessary condition for hybrid solar cells is a photoactive layer composed of materials that absorb electromagnetic (EM) radiation in the region of the spectrum commensurate with solar radiation. Many conductive polymers, including the ubiquitous poly (3-hexylthiophene) (P3HT), absorb visible light and are therefore suited for solar cell applications. A distinct advantage to hybrid solar cells is that the semiconductor nanoparticles also absorb solar radiation. As mentioned previously, this allows both components of the film to contribute to photocurrent. Through the use of synthetic chemistry, polymers can be tailored to adjust their absorbance. Semiconductor nanoparticles can be treated as chemical reagents and exhibit size-dependent optical properties (vide infra), and therefore they too can be synthetically manipulated to absorb a

specified range of wavelengths. This gives a great deal of control over the absorption properties of the photoactive film.

Some of the existing limits to device performance originate in step 1 alone. Inspection of the sun's spectrum shows the wavelengths that lead to the irradiance available at the earth's surface (see Figure 1.2).

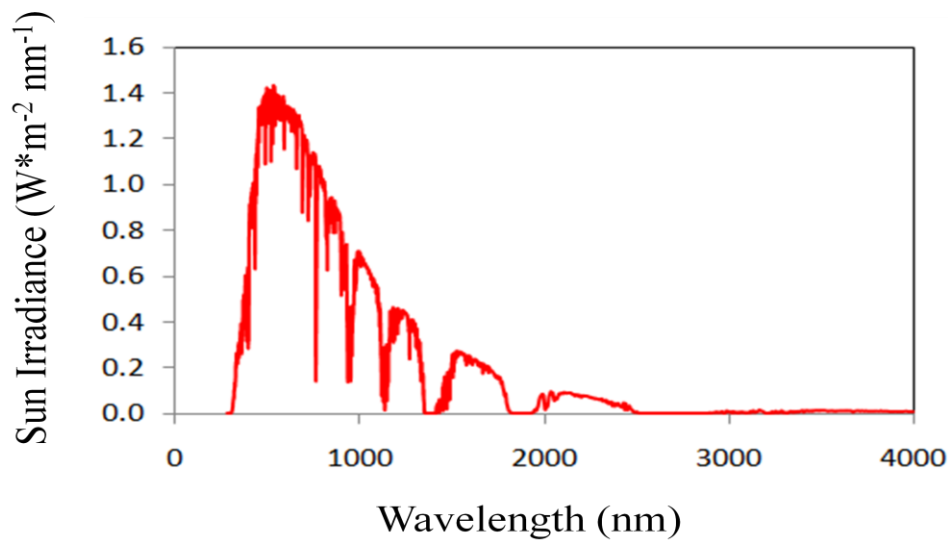


Figure 1.2. The sun irradiance as a function of wavelength. Data obtained from National Renewable Energy Laboratory (NREL).¹²

At the equator, solar radiation has an energy value of approximately 1000 W m^{-2} . This is typically called AM1 (Air Mass 1) and takes into account the absorption losses due to the atmosphere. To define the radiation at latitudes off of the equator, AM1.5G is used and is defined as the solar irradiance from the sun positioned 45° above the horizon.¹² This is the standard used when characterizing

the device performance of solar cells. As seen from Figure 1.2, although the irradiance extends to 4000 nm, the majority of the sun's energy lies below 2000 nm and thus a large fraction of the available photons are beyond the visible region. In terms of available energy, approximately one half of the sun's total power lies in the near-IR and IR parts of the spectrum. Consequently, a main thrust in solar cell research is the incorporation of photoactive materials that absorb in the red and near-IR range. A large synthetic effort has been applied to polymers in order to shift their absorption to towards longer wavelengths.¹³ Outlining these efforts is beyond the scope of this thesis and will not be discussed here.

Once the exciton is generated within the film, it has a finite lifetime before recombination annihilates the electron-hole pair. The distance the exciton can travel prior to recombination is termed the exciton diffusion length. This distance can range from 5-20 nm depending on the material.^{14, 15} The architecture of hybrid solar cells is highly dependent on this parameter as the morphology of the film must be structured to increase the chance of charge transfer (CT) prior to recombination (see section 1.6). Step 2 is therefore a critical step and involves the diffusion of the exciton throughout the photoactive layer towards a CT interface where the bound electron-hole pair can be dissociated into free carriers.

In order for the exciton to be dissociated into isolated charges, a driving force for separating the electron from the hole must exist within the film. As the exciton is virtually neutral to electric fields (it would take $\sim 10^6$ V/cm to separate a typical electron-hole pair), any difference in work function between the electrodes

is insufficient to overcome the Coulombic forces binding the electron and hole of the exciton. Such strong fields do not exist in these devices, and therefore a separate mechanism must cause the exciton to dissociate. This is accomplished by forming a CT interface between a donor material and an acceptor material. Step 3 therefore plays a critical role in the production of free carriers in the device and is the main criterion by which candidate materials are selected for making polymer-based third-generation solar cells. The electronic structure at the CT interface necessary to accomplish exciton dissociation is termed a type-II heterojunction and is shown in Figure 1.3. In order for charge transfer to be successful, the nanoparticle must have a high electron affinity relative to that of the polymer. In addition, the lowest unoccupied molecular orbital (LUMO) offset must be at least 0.3 eV to overcome the binding energy of an exciton.

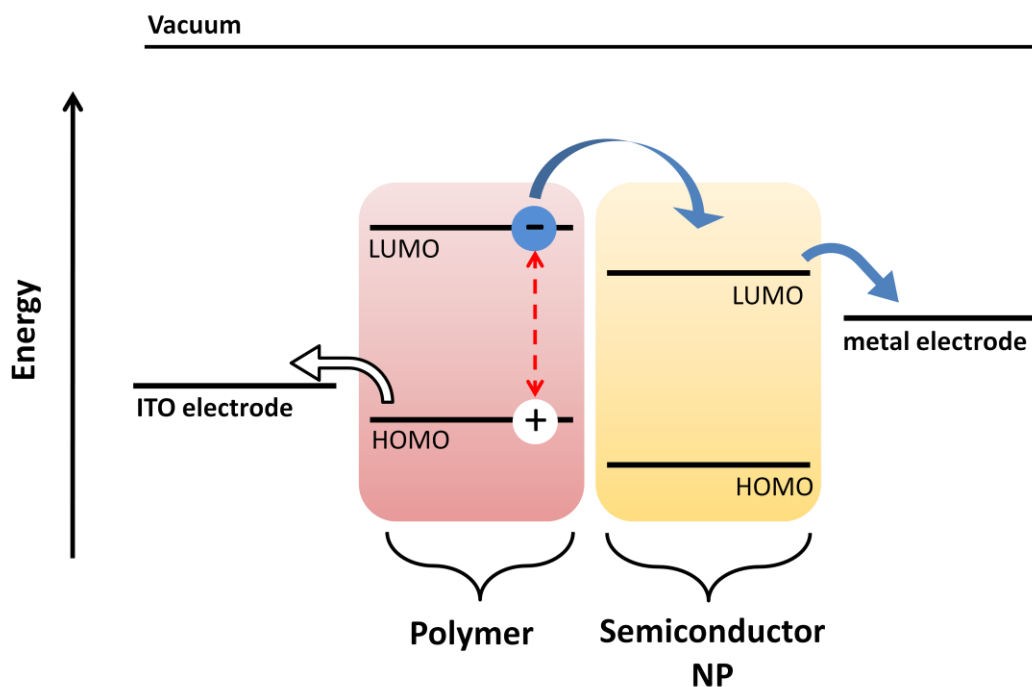


Figure 1.3. The charge transfer interface (type-II heterojunction). The exciton on the donor can be dissociated into an electron residing on the acceptor lowest unoccupied molecular orbital (LUMO) and a hole on the donor highest occupied molecular orbital (HOMO). Note that if the nanoparticle absorbs the incident radiation, charge transfer can take place with a hole transferred from the nanoparticle HOMO to the polymer HOMO with the electron residing on the nanoparticle LUMO.

Assuming exciton dissociation occurs at the interface, the free charge carriers must migrate to the electrodes in order for current to be extracted from the device (step 4). This requires good carrier mobility of both holes and electrons in the donor and acceptor components respectively. Hole mobilities in some of the more widely used conductive polymers are typically on the order of $0.01\text{--}1\text{ cm}^2\text{ V}^{-1}\text{ s}^{-1}$, while electron mobilities are several orders of magnitude lower.¹⁶

P3HT has the highest hole mobility for organic semiconductors and is currently used in the best performing OPV devices.¹⁷ Inorganics, on the other hand, are known for very high electron mobilities with values several orders of magnitude higher than that in organics. Therefore, the addition of inorganic nanoparticles to the semiconductor polymer matrix can be seen as a way of increasing electron mobility in the polymer matrix making up the photoactive layer (PAL).

The final step is the collection of the carriers at the electrodes (step 5). At the anode end, indium tin oxide (ITO), a transparent conducting oxide (TCO), is used to collect the holes transported through the polymer component. The cathode (typically composed of metals such as Al or Ag) collect the electrons transported through the nanoparticle acceptor phase. The energy levels of the electrodes must be aligned properly, relative to the donor and acceptor, in order to ensure efficient collection of the charges (see Figure 1.3).

1.3 Electrical Characterization of Photoactive Films

In order to gain insight into the chemistry and morphology of the hybrid thin film, electrical characterization is typically performed. As the purpose of bringing the material components together is to produce photocurrent, the characterization involves an investigation into the current-density/voltage response of an assembled device. Evaluating the overall quality of a hybrid solar cell is done in the same way as any photovoltaic device and involves a number known as the power conversion efficiency η (see equation 1.3.1). η is simply the ratio of the power output (P_{out}) over the power input (P_{in}). P_{in} represents the incident light power density and is standardized at 1000 W/m^2 . The spectral intensity distribution must match that of the sun's at the earth's surface at an incident angle of 45° thus conforming to the AM 1.5G spectrum.

$$1.3.1 \quad \eta = \frac{V_{OC} \times J_{SC} \times FF}{P_{in}}$$

$$1.3.2 \quad FF = \frac{J_{mpp} \times V_{mpp}}{J_{SC} \times V_{OC}}$$

The output power can be understood in terms of open-circuit voltage (V_{OC}) and short-circuit current (J_{SC}) along with a parameter known as the fill factor (FF) (see below). These are labelled in Figure 1.4 which shows typical current-density/voltage curves of a solar cell with and without illumination.

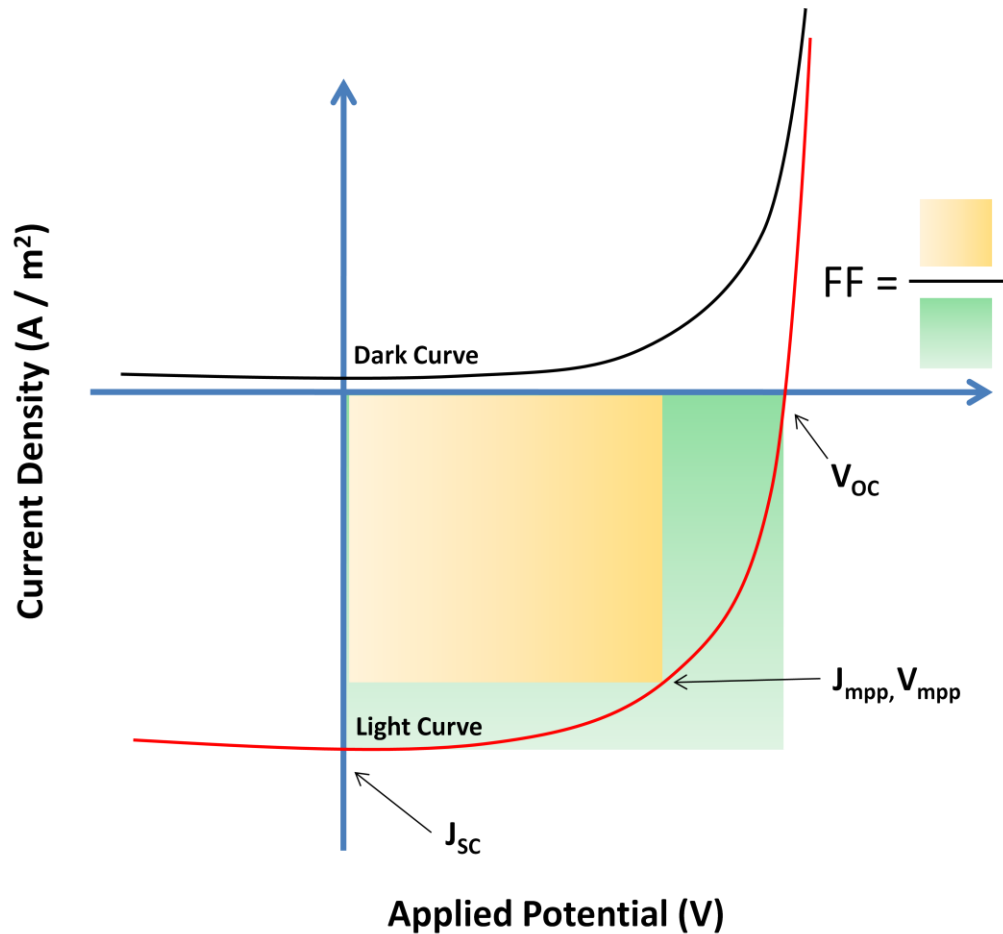


Figure 1.4 Typical current-voltage (IV) curve showing the main parameters that are evaluated when assessing the performance of a solar cell. The light curve occupies the fourth quadrant with the ends of the curve defined by the short-circuit current (J_{SC}) and open-circuit potential (V_{OC}).

The largest value for the output power is determined by the point where the product of the voltage and current is maximized. This is indicated in Figure 1.4 by the label J_{mpp} , V_{mpp} . The open circuit potential, which is the potential produced in the cell when the leads of the device are not in contact to any load, is indicated by the symbol V_{OC} . The short-circuit current density, J_{SC} , is the current produced by the device at zero applied voltage. A final parameter used to determine the overall power conversion efficiency is the fill factor (see equation 1.3.2). This is calculated by taking the largest square that can be made in the fourth quadrant inside the light curve (yellow box) divided by the largest square that can be made in the fourth quadrant at the points of J_{SC} and V_{OC} (green box). Fill factors can give an indication of the overall quality of the device and large values lead to high overall power conversion efficiencies as shown in equation 1.3.1.

1.4 Molecular Origins of Device Parameters

In order to rationally design third generation solar cells, there needs to exist a good understanding of the molecular origins behind the performance parameters used in the device analysis. The three main parameters are the V_{OC} , J_{SC} , and FF as described in the previous section. The V_{OC} is believed to originate from the difference in energy between the donor highest occupied molecular orbital (HOMO) and the acceptor lowest unoccupied molecular orbital (LUMO) as shown in Figure 1.5.¹⁸⁻²¹

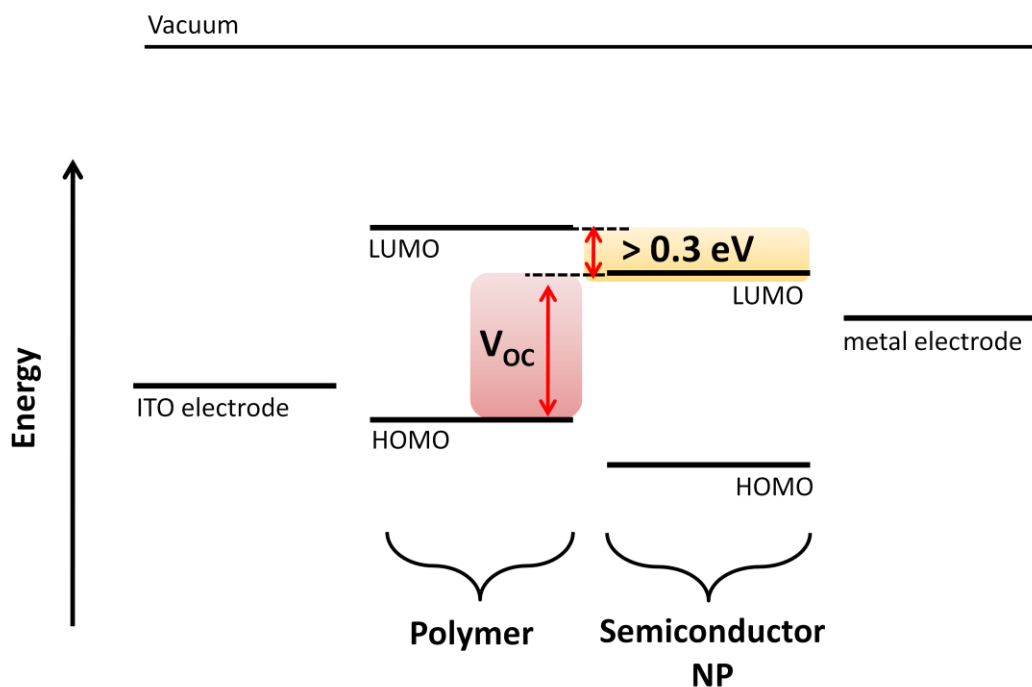


Figure 1.5 Origin of the V_{OC} along with the condition for charge transfer. These are parameters that can potentially be tailored through synthetic chemistry when designing hybrid devices.

In hybrid solar cells, this corresponds to the energy difference between the polymer HOMO and nanoparticle LUMO. Note that the nanoparticle LUMO can also be considered the conduction band edge (see section 1.5.1). Since nanoparticles can be synthetically tailored to adjust their electronic structure,¹⁴⁰ a potential handle on the value of the cell's V_{OC} is possible. This opens the door toward engineering an improvement in hybrid solar cell performance.

The value of J_{SC} depends on the amount of photocurrent extracted from the device. One factor affecting the amount of photocurrent generated is the number

of CT events occurring throughout the film. The more CT events that occur, the greater the number of free carriers in the PAL that can contribute to the J_{SC} . In order to ensure CT at the interface between polymer and nanoparticle, an energy difference of at least 0.3 eV must exist between the donor and acceptor LUMOs in order to overcome the binding energy of the exciton (see Figure 1.5).²²

The production of free carriers in the film does not guarantee a photocurrent outside of the device as the carriers must be transported throughout the film until they reach the anode and cathode. As a result, another factor influencing the value of J_{SC} is the mobility of carriers throughout the film. Holes are transported to the ITO anode while electrons move towards the metal cathode. Polymers are typically p-type materials and transport holes via a thermally activated hopping mechanism²³ (see section 1.8.2). Hole mobility in thin films of organic semiconductors depends on the packing of the polymer chains. In general, long range order throughout the film is conducive to good carrier transport.²⁴ P3HT has some of the highest recorded hole mobility values due to the presence of hexyl chains that cause the formation of two-dimensional conjugated sheets via interchain packing.²⁵ Therefore the structural order of the polymeric component in the film is important as better charge transport leads to higher J_{SC} values.²⁶

In the case of nanoparticles, good particle-particle contact is essential in order to ensure a good percolation pathway back to the cathode. Studies show that in the absence of good particle contact, J_{SC} values suffer in hybrid devices.²⁷ A primary issue are the insulating ligands used to make the particles processable. These capping compounds act as barriers to charge transfer and can inhibit the

mobility of carriers at the donor-acceptor interface. Finally, absorption in the photoactive layer indirectly influences J_{SC} values by virtue of the number of excitons generated within the film. The more photons absorbed by the donor and acceptor, the greater the number of CT events. FF depends on both J_{SC} and V_{OC} and can give insight into the general quality of the film and some of the competing mechanisms taking place. For example, a low FF has been attributed to lower CT rates relative to carrier recombination.²⁸

The three main parameters are often correlated and making an improvement in one may concomitantly improve or be detrimental to the others. Therefore, despite what is known about the molecular origins of hybrid solar cell parameters, improvement in the overall performance of a device is often difficult. Nevertheless, knowing the chemical source of the performance parameters, along with the electrical characterization of the devices, allows one to isolate what film property has led to an improvement. This ability brings researchers one step closer to the rational design of a hybrid solar cell.

An understanding of the optoelectronic processes between conducting polymers and semiconductor nanoparticles is only half of the researcher's "toolbox." Great progress has been made in understanding and controlling the synthesis of photoactive materials used to make the donor and acceptor components of hybrid films. Such control over material properties is critical to the success of any functioning device and this is the topic of the next section.

1.5 Semiconductor Nanoparticles

Semiconductor nanoparticles have unique optical and electrical properties that offer distinct advantages in solar energy conversion. Currently, the best performing polymer-based devices are the polymer/fullerene variety with the best example being composed of the polymer P3HT as donor and the fullerene derivative [6,6]-phenyl-C61-butyric acid methyl ester (PCBM) as acceptor. The structural symmetry in the fullerene of PCBM leads to a 6-fold degeneracy of the LUMO level and allows the structure to be reduced by up to 6 electrons. This ability to reduce electrons, relative to the donor polymer, makes it close to ideal for organic photovoltaic (OPV) devices. Another consequence of the structural symmetry, however, is transitions in the visible and near-IR regions of the solar spectrum are forbidden.²⁹ Thus only the polymeric component of the OPV photoactive layer can contribute to the photocurrent. In contrast, semiconductor nanoparticles can be chemically tailored to absorb across the entire visible range of the solar spectrum. In addition, nanocrystal morphology can be manipulated to allow for a variety of shapes and sizes. Since the optical and electrical properties of semiconductor nanoparticles are highly dependent on size and shape, band gap tuning becomes possible raising the level of control one has over solar cell design. Extremely thin films can lead to appreciable photocurrent due to many nanoparticles exhibiting a direct band gap resulting in large absorption coefficients. To fully appreciate the range of properties made accessible by these

materials, a brief background of their physical chemistry is necessary along with some discussion of the recent advances in nanoparticle synthesis.

1.5.1 Physical Chemistry of Semiconductor Nanoparticles

Since the pioneering work of Brus^{30 - 32} and Efros,³³ the physical science of semiconductor nanocrystals has attracted a great deal of attention. The interest in these materials stems from their extensive range of unique optical and electrical properties. The majority of these interesting features are based on a key physical phenomenon; the quantum size effect. It is through the quantum size effect that semiconductor nanoparticles exhibit the ability to have their properties tuned to meet the demands of a specific application. In order to see how this effect is useful in solar energy conversion, it is worth understanding how the phenomenon arises.

As the size of the particle decreases, the physical dimensions of the crystal eventually reach the spatial extent of the exciton. This is the distance between the electron and the hole, and is commonly referred to as the exciton Bohr radius. It is at this point that the changes that arise in the electronic structure of the crystal can be explained using the “particle-in-a-box” model from quantum mechanics. In this model, boundary conditions are imposed upon a wave function in the Schrödinger equation. Solutions to this problem give a relationship between energy and momentum whereby the energy values become discrete. Therefore,

energy discreteness is a natural consequence of boundary conditions applied to wave functions. In the case of nanoparticles, the wave functions are attributed to the electron and hole of the exciton, while the boundary conditions are dictated by the physical size of the crystal itself. The overall result is a concentration of the oscillator strength (the probability of a transition occurring from the ground state to the excited state to form the exciton) into a few distinct energy levels.

The discrete nature of the electronic transitions is apparent in the absorption spectra of nanoparticles as shown in Figure 1.6.⁸⁹ Strong excitonic peaks can be seen in the spectra for each sample. It is for this reason that quantum confined particles are often called artificial atoms. Also apparent in these spectra, is the shifting of the absorption onset with crystallite size. This energy dependence is another consequence of the physical boundary conditions on the excitonic wave functions and it can be shown that energy follows a $1/r^2$ relationship with crystal radius. In fact absorption spectroscopy can be used as a method to measure the size of the particle.

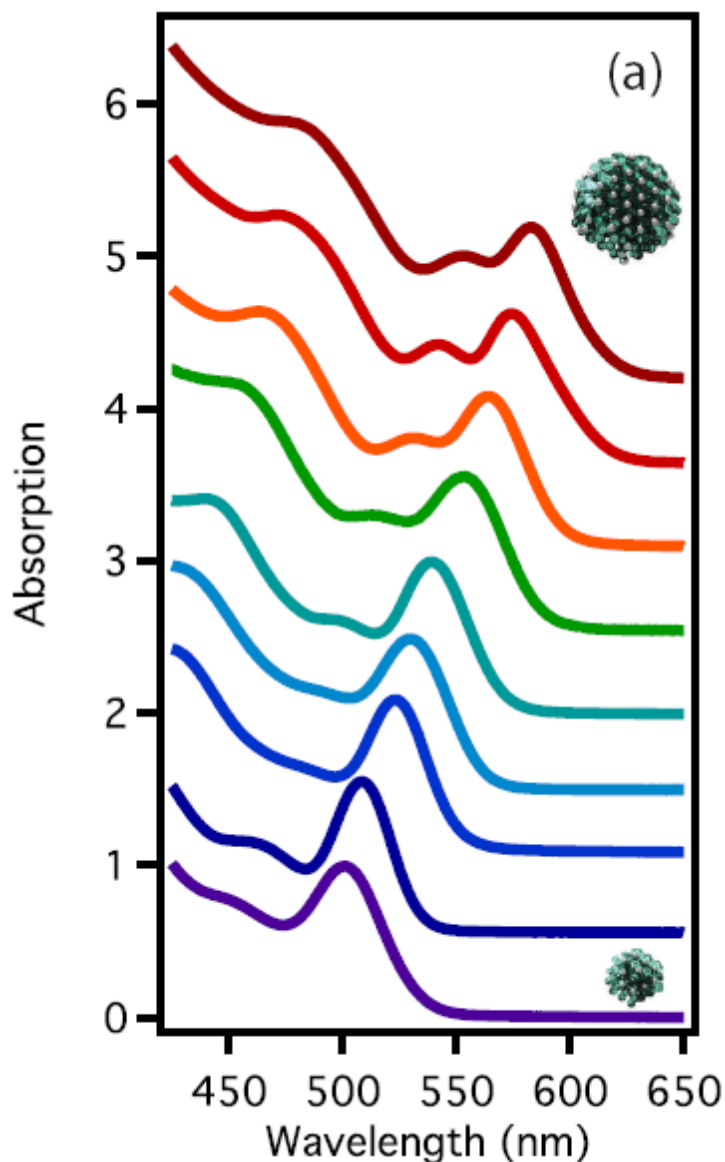


Figure 1.6 Absorption spectra of CdSe nanocrystals showing the change that occurs with crystallite size. Reprinted with permission from ref. 89. Copyright © 2009 SPIE.

Semiconductor nanoparticles are at the interface between a molecule and a bulk semiconductor (see Figure 1.7). As a result, the band gaps in semiconductor nanocrystals are larger than their corresponding bulk crystal. It can also be seen that the discreteness in the electronic structure at the band edges is similar to that

of a molecule. The density of states increases, however, as one moves up the band and a quasi-continuum of energy states is available to the nanocrystal much as in the bulk semiconductor. This increase in density of states is also apparent in the UV-Vis spectra as the number of high energy transitions increases (see Figure 1.6).

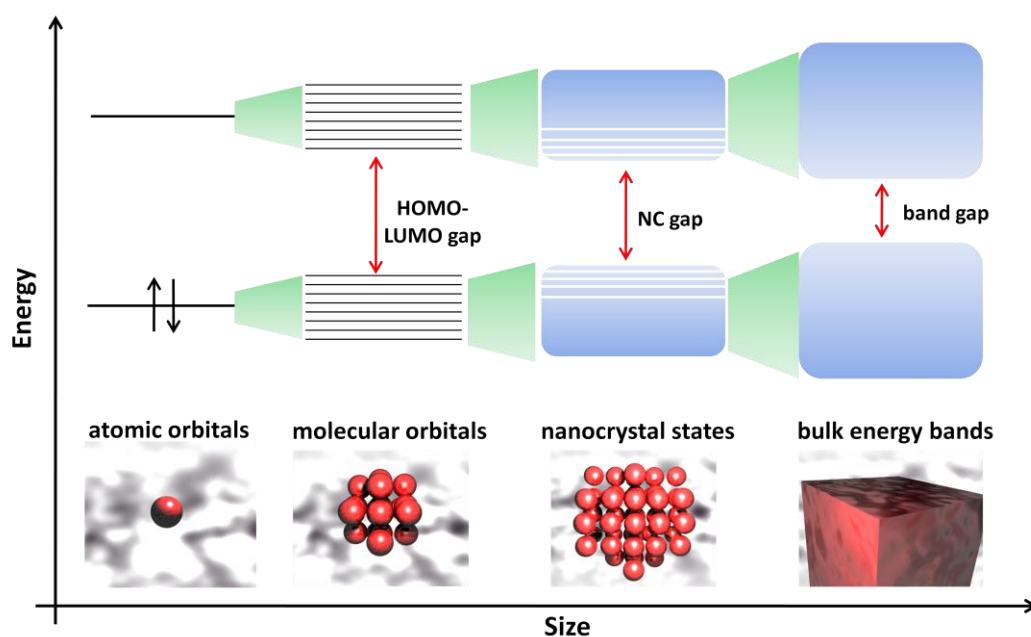


Figure 1.7. Evolution of energy levels with system size. As the size increases from an individual atom to a bulk crystal, the density of states increases until a continuum of energy levels forms a band. The space between the bands is called the band gap which is found to increase when the system becomes smaller.

Tailoring the absorption of the nanocrystal allows one to control where in the solar spectrum light will be absorbed. Devices can therefore be designed to

capture light at specific wavelengths. Band edges can be tailored to potentially design type-II heterojunctions with optimal energy offsets to optimize the charge-transfer driving force (see Figure 1.3). Open circuit potentials can be manipulated by setting the conduction band edge of a nanocrystal at certain positions relative to the polymer HOMO. From the above discussion it can be seen that semiconductor nanoparticles are much more than simple additives to conductive polymers to increase electron transport. Having control over the electronic structure of the acceptor material in third-generation photovoltaics offers potentially huge benefits to their rational design.

1.5.2 Nanoparticle Synthesis

The controllable synthesis of semiconductor nanoparticles with narrow size distribution presents one of the great accomplishments in materials science. It makes possible the design of semiconductor particles with desired properties and allows these crystals to be treated as chemical reagents. The latter attribute permits nanoparticles to be routinely dissolved in a variety of solvents, cast into thin films and interfaced with an array of other materials. Manipulating particle dimensions and morphology gives researchers control over their size and shape dependent properties. From a device design standpoint, this synthetic achievement is critical to the realization of low-cost optoelectronic devices with good performance.

This initial success has generated additional avenues of crystal design that go beyond the archetypal quantum dot morphology. A variety of anisotropic shapes has been synthesized opening the door towards a range of particles with novel physical properties and potential applications.^{34 – 41} Design inspiration evolves from a solid foundation of accepted laws and mechanisms that govern the rules of assembly. In order to successfully move towards the dream of rationally designed nanoparticles, an understanding of the underlying machinery governing their fabrication is essential. Therefore it is worth exploring some of the fundamental aspects of nanocrystal growth and the potentially useful properties that emerge.

As a case study, we look at the II-VI semiconductor nanocrystals CdSe and CdTe due to their importance in both fundamental studies of quantum confined systems as well as their incorporation into devices.^{11, 76, 77} We begin with a general preview of how these particles are made, followed by a closer look at the kinetics and thermodynamics behind their crystal growth. From this starting point we will see how this knowledge has guided the synthesis of novel shapes with fascinating properties.

CdSe Crystal Growth

Originally, CdSe was synthesized using the highly toxic dimethyl cadmium (CdMe_2) precursor along with tri-n-octylphosphine oxide (TOPO) as surfactant.³⁴ Due to the inherent difficulties with this approach, a new method involving the thermal decomposition of cadmium oxide with an organo-selenium precursor was developed.^{42, 43} In this process, the Se precursor (TOP:Se) is injected into a high

temperature bath of coordinating solvent. Crystal growth begins shortly after injection and the particles grow until the available monomer is depleted or the reaction is stopped by a rapid reduction in temperature. The typical experimental set up is shown in Figure 1.8 with the standard round bottom flask and condenser apparatus used for high temperature reflux chemistry.

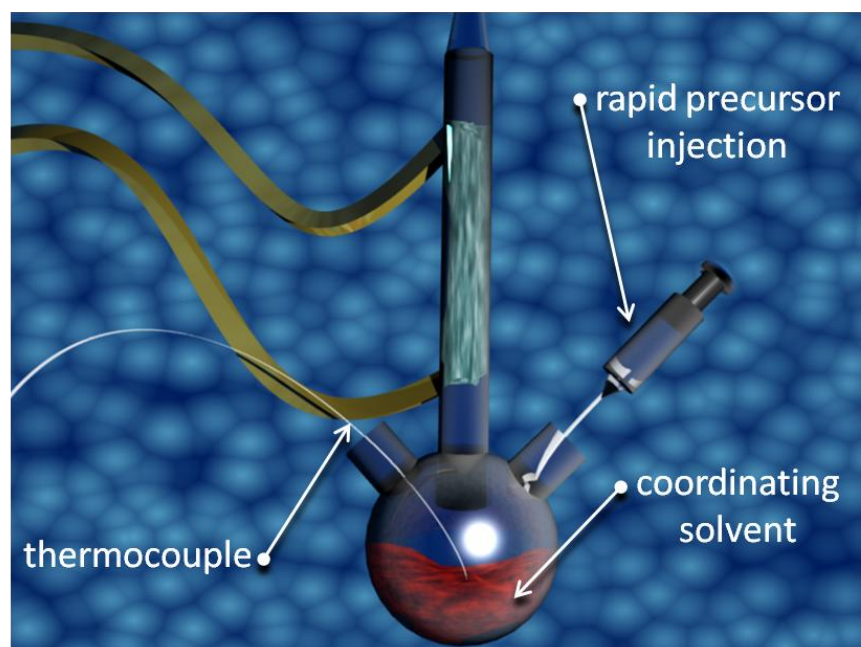


Figure 1.8 Typical experimental setup for semiconductor nanoparticle synthesis. This method involves rapid injection of precursors into a coordinating solvent. Typically, a round-bottom flask with condenser are used along with a thermocouple to monitor the temperature.

If the nanocrystals are allowed to grow for an extended period of time, a large distribution in crystal size will result.¹⁴¹ A size selection method such as

selective precipitation can then be used to sort particles of different diameter. A better method involves separating the nucleation stage from the growth stage, which can be accomplished by ensuring a rapid injection of precursors followed by a quick reduction in temperature. This has the advantage of capturing the particles in a specific stage of growth known as the size focusing regime.

The kinetics of crystal growth has been studied extensively using a variety of experiments and have shed light on how these materials assemble.^{44 – 50} The typical method of hot injection can be understood in terms of the separate nucleation and growth events mentioned above. Rapid injection of the selenium precursors ensures a sharp rise in precursor concentration above the nucleation threshold. For a finite amount of time, the solution exists in a supersaturated state shortly after which a nucleation burst relieves the supersaturation.⁵⁰ (see Figure 1.9). Immediately following injection of the selenium precursor, nucleation takes place and continues until the monomer concentration drops below the critical threshold.

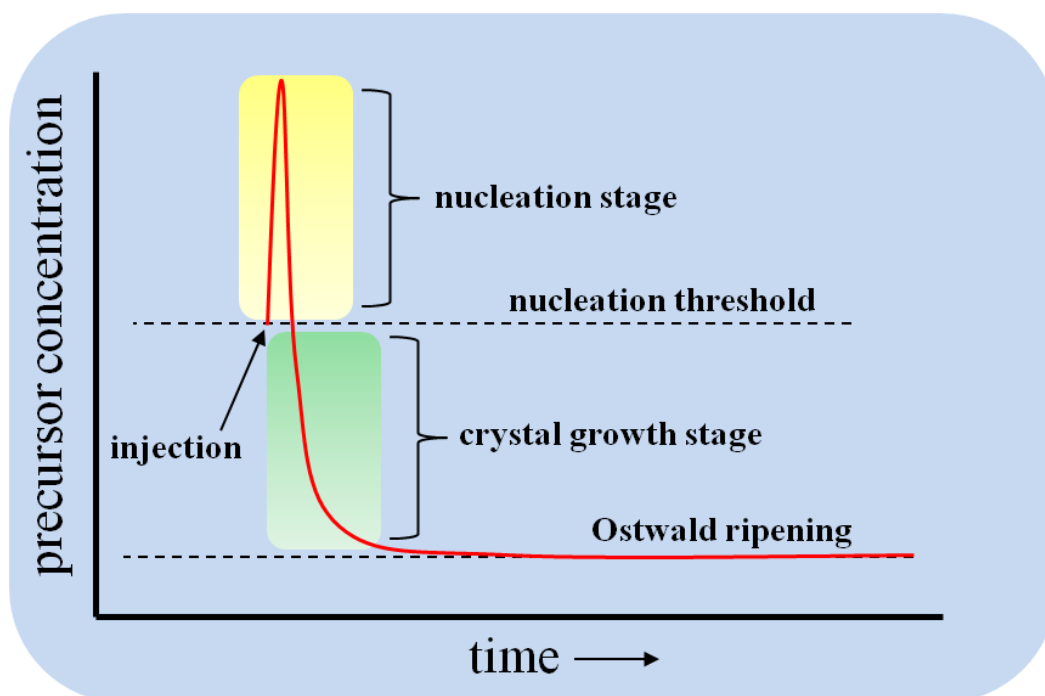


Figure 1.9. Nucleation and growth process of semiconductor nanoparticles. The two main events during crystal growth are the nucleation stage and the growth stage. Reprinted with permission from ref. 50. Copyright © 2000 Annual Reviews.

Although little is known about the nucleation stage, studies of crystal growth have led to a degree of control over particle radius and size distribution. In the growth stage, diffusion of monomer to the particle surface is assumed to be rate limiting and a size dependent growth rate can be obtained from the Gibbs-Thomson equation^{45, 51} (see equation 1.5.2a).

$$1.5.2a \quad S_r = S_b \exp(2\sigma V_m / rRT)$$

$$1.5.2b \quad \frac{dr}{dt} = K \left(\frac{1}{r} + \frac{1}{\delta} \right) \left(\frac{1}{r^*} - \frac{1}{r} \right)$$

S_r = nanocrystal solubility

S_b = bulk crystal solubility

σ = surface energy

r = radius

V_m = molar volume

δ = diffusion layer thickness

r^* = critical radius

If the exponential term in equation 1 is minimal ($\ll 1$), an expression for the diffusion controlled growth rate with particle radius gives equation 1.5.2b, where K, R and T are the Boltzmann constant, gas constant and temperature respectively. The fate of growing nanocrystals can be understood with the

concept of the critical radius. At a given monomer concentration, there always exists a critical size below which particles exhibit negative growth rates (dissolve). Above the critical size, particles grow with a size dependent rate. As can be seen from equation 1.5.2b, smaller particles grow faster than large ones as a result of the difference in surface energies. Focusing of the size distribution takes place, and eventually the monomer concentration is depleted and the critical size increases just above the average particle size. At this stage, smaller particles start to dissolve while the larger ones continue to grow. This is termed Ostwald ripening, and it serves to defocus the size distribution. This is typically detrimental, although this process has been taken advantage of when preparing nanocrystal size series.³⁴ Addition of extra precursor shifts the critical size to a smaller value resulting in a refocusing of the size distribution. By controlling the Cd to Se ratio in the starting precursor concentrations, the focusing time can be manipulated and higher control over crystal growth obtained.

Crystal growth is a dynamic process with ligands adsorbing and desorbing from the crystal surface, permitting controlled growth. Understanding how ligands interact with crystal facets of varying surface energy gives insight into how one might manipulate the growth process to obtain crystals of varying shape. Anisotropic systems are considered more useful for device applications than their quantum dot counterparts. For example, elongated CdSe nanorods cause a drastic improvement in device performance due to a superior conduction pathway to the electrodes.¹¹

The classic model for controlling the shape of nanocrystals is the Gibbs-Curie-Wulff theorem.⁵² It suggests that the surface energy of each facet of the crystal determines particle growth. More recent studies, however, suggest growth occurs far from any thermodynamic equilibrium and that high monomer concentrations are needed to control particle shape. The crystallization is still based on the Gibbs-Thomson equation, however new theories recast the nanocrystal solubility in terms of chemical potential.⁴⁸ Thus, particle morphology is principally determined by the concentration of monomers in solution, as a high concentration ensures a large chemical potential. At moderate potential, intraparticle ripening takes place leading to rice shaped particles. This occurs when the potential in the solution becomes lower than the chemical potential of the CdSe polar facet. Atoms thus diffuse from this facet to the sides of the crystal leading to a oval shaped particles. If nanorods are desired, the chemical potential in the solution must be kept higher than that of the polar facets during the entire growth process (see Figure 1.10). This is accomplished by the use of strong metal-binding ligands such as tetradecylphosphonic acid (TDPA) and hexylphosphonic acid (HPA). By making strong complexes to cadmium, the monomer concentration can be kept high and rods will form. The use of HPA will tend to form a predominance of rod-shaped particles compared to TDPA due to the difference in their diffusion coefficients.

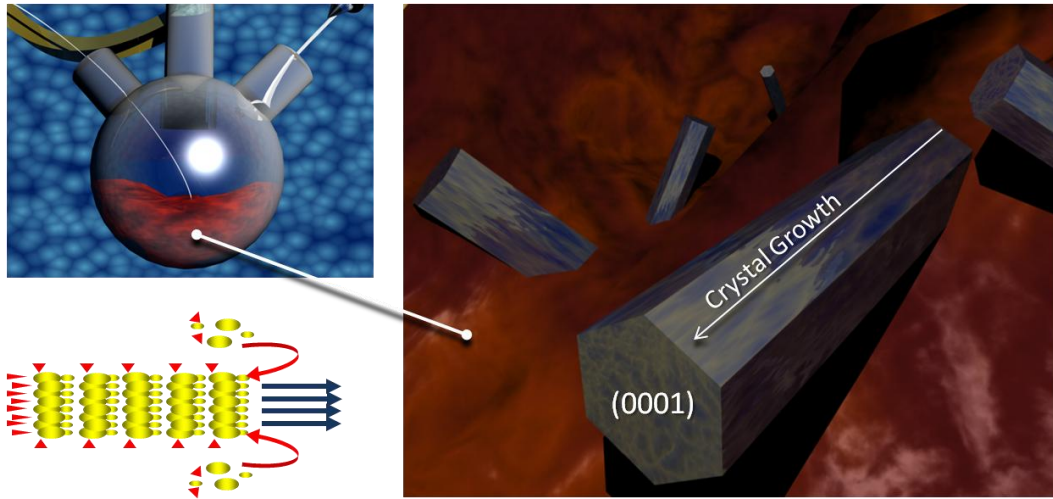


Figure 1.10 Ligand choice dictates the chemical potential in the growth solution controlling particle shape. The polar facets of CdSe allow for anisotropic growth of the crystal leading to nanorods.

Particles of complexity beyond nanorods are possible through the control of reaction conditions. This opens the possibility towards other optical and electrical properties that may prove important for solar cell design. For example, Manna et al. have shown CdTe can be grown into tetrapod shapes by taking advantage of the polytypism that exists with this crystal at various temperatures³⁷ (see Figure 1.11). CdTe can exist in both the zinc blende and wurtzite crystal structures. The (111) facets of the zinc blende structure are atomically identical to the (0001) facets of the wurtzite structure. This allows CdTe to grow with a zinc blende core and branching wurtzite arms. Since there is an energy difference between the zinc blende and wurtzite crystal structures, one crystal type will be preferred during

nucleation and the other during growth. In the case of CdTe, the energy difference between these two structures provides a handle on the synthetic control over crystal formation. By using alkyl chain phosphonic acids, wurtzite growth is favoured at higher temperatures as these are known to stabilize the non-polar facets of the crystal. Therefore, following zinc blende nucleation, wurtzite arms are allowed to extend from the core.

Higher levels of control stem from the ability to independently tune the length and diameter of the arms by the manipulation of growth kinetics. Higher ratios of Cd/Te lead to an increase in arm length since growth is primarily determined by the concentration of Cd precursor. The use of n-octyldecylphosphonic acid (ODPA) in large amounts relative to Cd leads to larger arm diameters. This is due to the ability of ODPA to decrease the reactivity of the Cd precursor allowing the diameter of the arm to grow. In addition to CdTe, other important materials have been grown into tetrapod shapes including cadmium sulphide,^{36, 53} manganese sulphide⁵⁴ and zinc oxide,⁵⁵ increasing the number of potentially useful structures for a variety of applications.

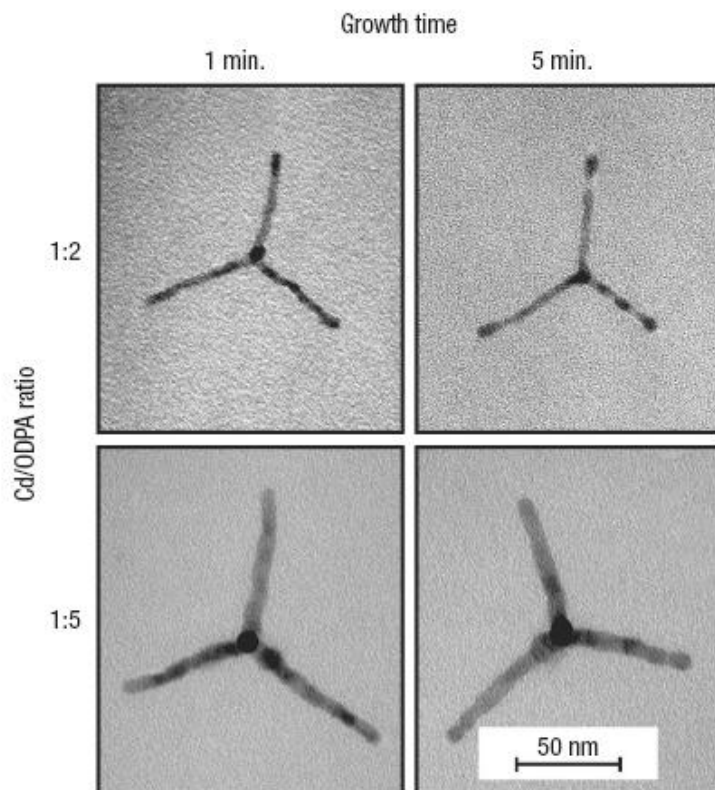


Figure 1.11. TEM images showing anisotropic control over CdTe crystal growth. The formation of tetrapods with varying arm diameters is possible by manipulating precursor concentrations. Reprinted with permission from ref. 37. Copyright © 2003 Nature.

Highly branched semiconductor nanoparticles can be synthesized by controlling the conditions during the reaction (see Figure 1.12). For example, Kanaras et al. varied the reaction parameters in order to strongly favour branching during nanocrystal growth.⁴¹ Specifically, the concentration of calcogenide precursor was adjusted in order to create hyperbranched CdSe and CdTe. The mechanism by which hyperbranching occurs can be explained in terms of the

concentration of nuclei relative to the available monomer in solution. At low Te concentrations, very few nuclei form and the ratio of monomer to nuclei is high. This leads to fast growth resulting in kinetically favoured branches to form. At high Te concentration, the ratio of monomer to nuclei is low and slower growth results in less branching. The authors also noted that ligand chain length influenced the degree of branching in the nanoparticles. Short chain phosphonic acids increased the number of arms whereas the longer chain acids had the opposite effect due to their ability to stabilize the wurtzite branches.

The above discussion has shown the variety of semiconductor nanoparticle shapes that can be formed and the mechanisms governing their growth. The diversity of particles has the potential to serve unique functions in solar cell design due to the strong correlation between crystal shape and particle properties. In the next section we will look at how particle shape can directly influence the performance of hybrid solar cells, and dramatically improve the researcher's "toolbox" for designing third-generation photovoltaics.

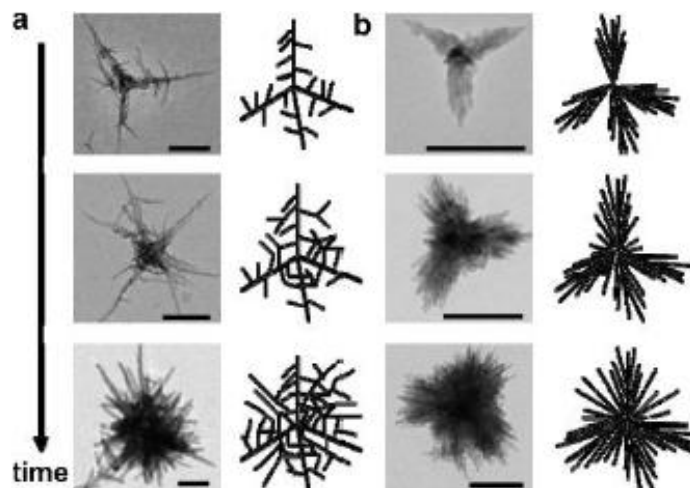


Figure 1.12 Hyperbranched particles of CdTe formed by controlling the concentration of calcogenide precursor in solution. Reprinted with permission from ref. 41. Copyright © 2005 American Chemical Society.

1.6 Design Principles for Polymer-Based Third-Generation Photovoltaics

The basic design of a hybrid solar cell device is shown in Figure 1.13. This architecture is typical for all polymer-based third-generation photovoltaic devices and begins with a transparent conducting electrode. As solar cells must allow incident radiation into the photoactive layer, this electrode faces the sun during the operation of the cell. The most common material used for this electrode is indium tin oxide (ITO) and is used in many optoelectronic devices including LEDs,⁵⁶ liquid crystal displays,⁵⁷ and solar cells.⁵⁸

ITO has a work function in the range of 4.5 – 5.4 eV which depends on the surface treatment.⁵⁹ ITO typically acts as the hole collecting anode of the device (except in reverse cells where ITO functions as the cathode). Although devices can be fabricated with the photoactive layer deposited directly onto the ITO, almost all devices employ the semiconducting polymer polyethylene dioxythiophene polystyrene sulfonate (PEDOT:PSS). This polymer serves to modify the work function of the ITO bringing its level closer to the majority of hole transporting polymers used in hybrid solar cells. It also helps to flatten the natively rough ITO and allows for subsequent layers to form smooth thin films.

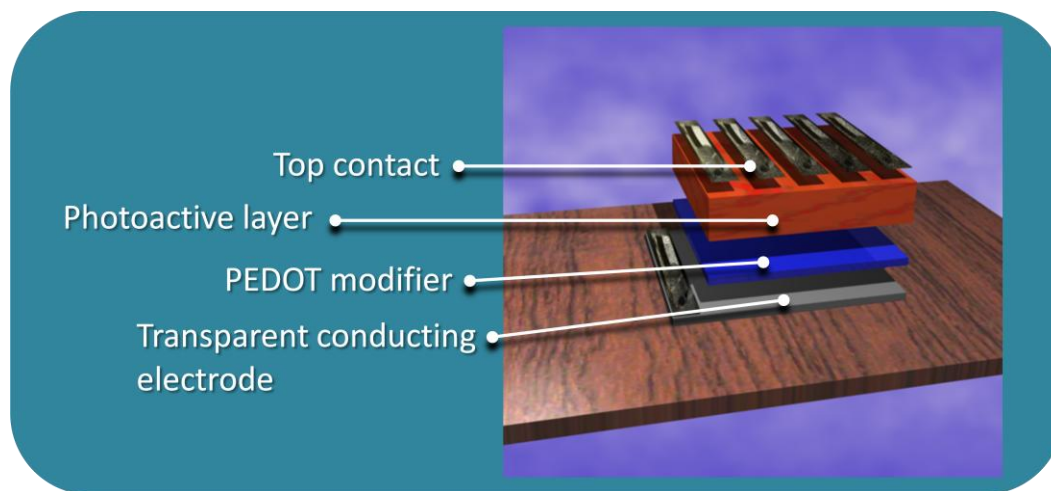


Figure 1.13 The basic design of a hybrid solar cell. The components from top to bottom include a metal top contact, the photoactive layer (PAL), electrode modifier layer (typically PEDOT:PSS), and a transparent conducting electrode (typically ITO).

The PAL is a critical component of any third- generation solar cell and is where the majority of the rational design takes place. Many techniques have been developed to deposit the PAL including spin casting,⁶⁰ layer-by-layer,⁶¹ vapour-phase deposition,⁶² doctor-blading⁶³ and inkjet printing.⁶⁴ Regardless of the technique, it is generally accepted that the PAL must be as smooth as possible to avoid pinholes throughout the film. Such features are known to lower the shunt resistance leading to poor performance (see Chapter 3).

One of the most important features of the PAL is its overall architecture. There are two types commonly employed in polymer-based third-generation photovoltaics known as the bilayer and bulk heterojunction (BHJ) designs (see Figures 1.14a and b). Each type has two distinct advantages to its layout. In the bilayer structure, excellent carrier mobility can be expected as the electrons and holes move solely through their native phases. A much lower degree of recombination can be expected and carrier transport is limited only by the mobility of the polymer in the case of holes and of the packed nanoparticles in the case of electrons. Bilayer hybrid solar cells typically give lower overall power conversion efficiencies due to the extraction of current being limited by the exciton diffusion length.⁶⁵ Any generation of excitons beyond ~20 nm (the typical maximum diffusion length) from the CT interface recombine prior to charge transfer. Therefore, although the bilayer design provides an excellent architecture for charge transport, a smaller number of CT events can be expected, limiting the device performance.

The second type of design is the BHJ architecture. This is the most popular design in polymer-based photovoltaics as it has been shown to lead to the highest performing devices.^{66, 67} The reason behind its high efficiency stems from the large number of CT events possible throughout the film. The BHJ consists of an interpenetrating network of donor and acceptor material as shown in Figure 1.14b. This PAL architecture ensures that most of the excitons generated throughout the film will reach a CT interface before recombining. The ideal BHJ would thus have a phase separation between donor and acceptor components on the order of the typical exciton diffusion length. Although this design provides excellent film morphology in terms of increasing the frequency of CT events, it is far from ideal for charge transport. The interpenetrating network of photoactive components increases the chance of carriers recombining with the opposite charge as they move towards the electrode. These two PAL designs suggest an ideal film architecture. This film would consist of a controlled network of interdigitated donor and acceptor components as shown in Figure 1.15. There is much effort in photovoltaics research to create this architecture; however this ultimate design has yet to be realized.

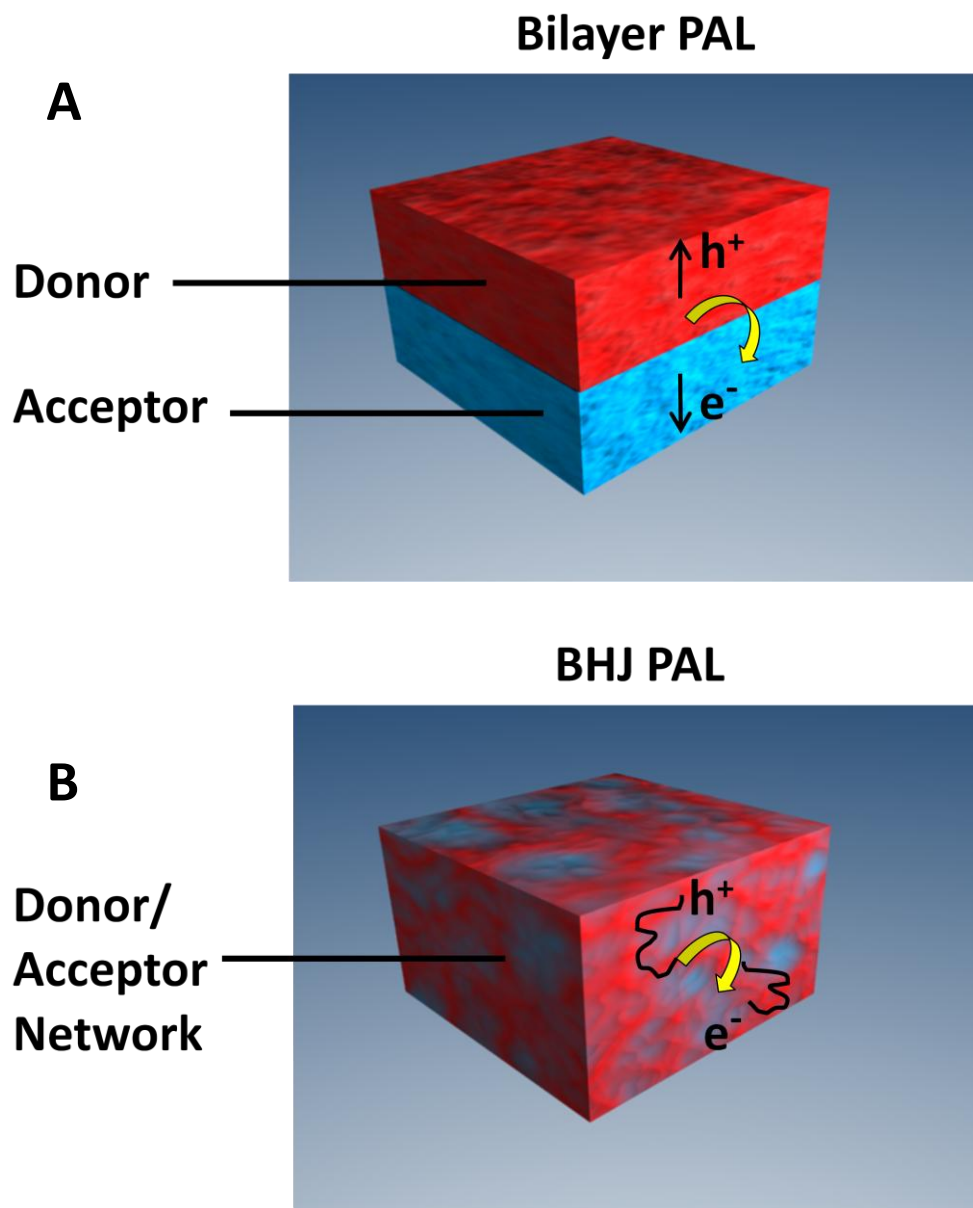


Figure 1.14 Two commonly employed architectures in polymer-based third-generation solar cell design. **A)** Planar architecture ideal for charge transport and **B)** BHJ architecture ideal for charge transfer. These two designs represent the tradeoff between carrier transport and charge transfer in PAL design.

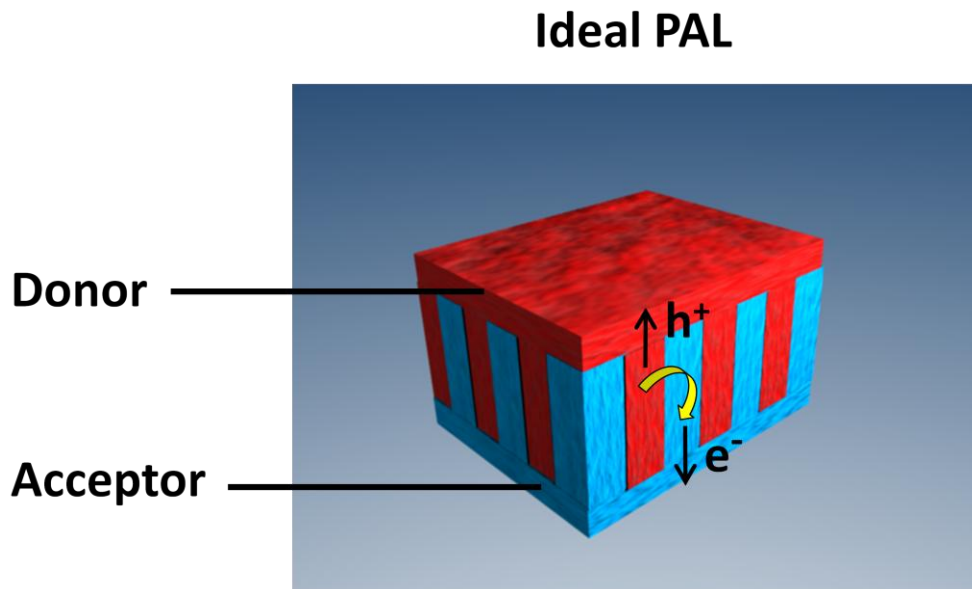


Figure 1.15 The ideal PAL interdigitated architecture exhibiting excellent carrier transport as well as charge transfer throughout the film.

1.7 Semiconductor Nanoparticles in Hybrid Solar Cells

The existence of a type-II heterojunction between a conducting polymer and an electron acceptor is the main criterion used in pairing donors and acceptors in third-generation devices. In the case of hybrid solar cells, the acceptor component is a semiconductor nanoparticle, of which five top candidates currently exist. These are CdSe, CdTe, PbSe, PbS and ZnO. TiO₂ has been paired with conducting polymers,^{68–71} however, it is much more ubiquitous in dye-sensitized solar cells.⁷² As a case study of the variety of techniques used to enhance device performance, we will again look at CdSe. It will be shown how particle shape,

surface chemistry and fabrication procedure lead to specific improvements in device performance. Through this approach, knowledge of how to rationally design hybrid devices through the use of chemistry will be presented.

The most successful semiconductor nanoparticle used in hybrid solar cells is CdSe. Charge transfer between CdSe and conductive polymer was investigated by Greenham et al. in 1996 by pairing the nanoparticle with poly(2-methoxy,5-(2'-ethyl)-hexyloxy-*p*-phenylenevinylene) (MEH-PPV).⁷³ Devices were assembled in the standard fashion and external quantum efficiencies up to 12% recorded at 514 nm were reported. External quantum efficiency (EQE) is defined as the number of electrons extracted from the device per incident photon, while internal quantum efficiency is the number of excitons generated per incident photon. Both are important parameters in evaluating the ability of an assembled device to generate electron-hole pairs and produce photocurrent.

The surface of the particle plays a large role in device performance. Most synthetic procedures for fabricating semiconductor nanoparticles leave a bulky, long-chain organic ligand (typically TOPO) on the exterior of the crystal. This serves to prevent the aggregation of particles in solution and remove surface states that are known to degrade PL efficiency. In devices, however, the ligands act as barriers to charge transfer and are detrimental to the performance of hybrid solar cells. Greenham et al. showed that when the surface of CdSe was chemically treated with pyridine, the bulky TOPO ligands were effectively removed as evidenced by the quenching of the polymer photoluminescence (PL) in the composite films. PL quenching is indicative of fast charge transfer at the

nanoparticle/polymer interface as the polymer is no longer provided with a radiative decay pathway on the timescale of electron transfer.⁷⁴

Another factor affecting device performance is the phase segregation that occurs between donor and acceptor. As mentioned in the previous section, phase segregation on the scale of nanometres ensures that the majority of excitons meet a charge transfer interface within their lifetime. Through the use of transmission electron microscopy (TEM), Greenham et al. showed that phase segregation on the nanoscale was possible in CdSe/MEH-PPV films. In addition, it was shown that particle loading was essential in order to form the necessary percolation pathways to the electrodes. Composite films composed of 5 nm CdSe particles with 90% by mass loading led to devices with a V_{OC} of 0.5 V and a fill factor of 0.26. Short-circuit currents were fairly low suggesting a lack of efficient percolation pathways. Absorption in the film stopped at 650 nm and therefore extended beyond the absorption available by the polymer alone. As mentioned in the optoelectronic processes section of this thesis, both components in hybrid solar cells can contribute to the photocurrent, marking a distinct advantage to these systems. In this study, it was determined that 37% of incident solar energy contributed to the photocurrent. The overall power conversion efficiency of the device was 0.1%. This study proved that CdSe nanoparticles interfaced with a conducting polymer could lead to the production of photocurrent.

In a similar study, Ginger et al. showed efficient charge transfer between CdSe nanoparticles and the two polymers MEH-PPV and MEH-CN-PPV.⁷⁵ The PL quenching was found to be insensitive to the size of the nanoparticle,

supporting the previous observation that CdSe nanoparticles and certain conducting polymers form excellent type-II heterojunctions. To improve on the device performance, nanoparticles of various shapes have been incorporated into photoactive thin films. In the next section, the role that particle morphology plays in device performance will be discussed.

1.7.1 Particle Size and Shape

The shape and size of semiconductor nanoparticles play a large role in the performance of hybrid solar cells. The physical properties of quantum confined structures are modulated when particle dimensions change; a feature that can be used to enhance device performance. For example, the range of wavelengths absorbed in composite thin films can be extended in order to capture more incident radiation. Shape alone can also have dramatic effects, such as the use of elongated nanoparticles to form efficient percolation pathways, increasing charge transport. When the complexity in particle shape is increased even further, near-ideal PAL architectures are created along with an increased ability to characterize film properties (*vide infra*).

Huynh et al., showed that the elongation of CdSe nanoparticles could be used to improve the response of hybrid solar cells in the CdSe / P3HT system.⁷⁶ Spherical quantum dots are considered non-ideal for hybrid thin films as they form inefficient percolation pathways to the cathode of the device. Percolation is the phenomenon that occurs when a sufficient concentration of nanoparticles has

been reached in the film, such that a pathway exists for the carriers to reach the electrodes. As charge transport occurs via hopping from particle to particle, the number of hopping events must be minimized. Elongation of the nanoparticle significantly improves device performance by decreasing the number of these hopping events (see Figure 1.16).

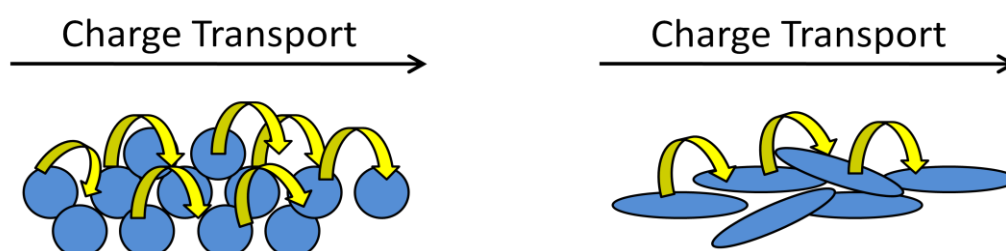


Figure 1.16 Elongated particles lead to improved charge transport by forming well defined percolation pathways that require a smaller number of hopping events for the charges to reach the electrodes.

The devices were composed of 8 x 13 nm nanorods with regioregular P3HT. It was shown that the majority of nanorods oriented themselves along their polar c-axes within the polymer forming percolation pathways. External quantum efficiencies of 16% were obtained and V_{OC} values reached as high as 0.57 V. The device had a fill factor of 0.49. Quantum efficiencies were found to increase by a factor of 4 compared to devices made from quantum dots. Despite the improvement in performance, the short-circuit current had a linear dependence

with light intensity which is consistent with a model of recombination at a fixed number of sites. This was explained as dead ends in the nanoparticle pathway leading to recombination of electrons with holes in the polymer. They obtained internal quantum efficiencies of 2.7%, and a monochromatic conversion efficiency of 2.2% at 480 nm.

A limiting factor in the fabrication of CdSe nanorod / polymer hybrid solar cells is the low solubility of high aspect ratio inorganic nanorods into the organic polymer matrix. Large phase segregation can occur over time due to the polar CdSe nanocrystals being chemically dissimilar to the relatively nonpolar organic polymer. This incompatibility is worse with high aspect ratio nanocrystals due to the increased surface area of the particle and the strong polarization along its c-axis. In addition to the risk of forming large-scale phase segregation, charge transfer is impeded due to a poor interface between nanocrystal and polymer.

A breakthrough was made in 2002, when Huynh et al. used a binary solvent mixture of pyridine and chloroform to load a high concentration of CdSe nanorods into a P3HT thin film.¹¹ Pyridine is known to be a good solvent for CdSe, as shown in the previous studies. Nonpolar organic semiconductors such as P3HT, however, are soluble in solvents such as chloroform and chlorobenzene.⁷⁷ When the ratio is set properly, a binary mixture of pyridine and chloroform can allow for good compatibility between high aspect ratio CdSe and P3HT. The nanorods in this study were of three different aspect ratios with the best performance attributed to those with dimensions 7 nm x 60 nm (see Figure 1.17). Devices made from these films gave external quantum efficiencies of 54%.

Under AM1.5G solar conditions, an overall power conversion efficiency of 1.7% was reported with a V_{OC} of 0.7 V and a FF of 0.4. Much of the performance increase was attributed to less hopping between particles although band transport may compete with hopping as the nanorods were of considerable length. As in the previous study, most nanorods were found to be directed along the route for electron transport. The thickness of the PAL was approximately 200 nm, thus the 60 nm long nanorods could penetrate through a significant portion of the thin film. This should lead to much better transport throughout the device. In addition to the increase in electron transport, the CdSe/polymer film absorbed from 300 nm to 720 nm, covering a significant portion of the incident radiation. In addition, the length of the nanorods may have led to increased delocalization of the exciton along the c-axis. This could have allowed for easier charge transfer from the less-bound electron-hole pair.

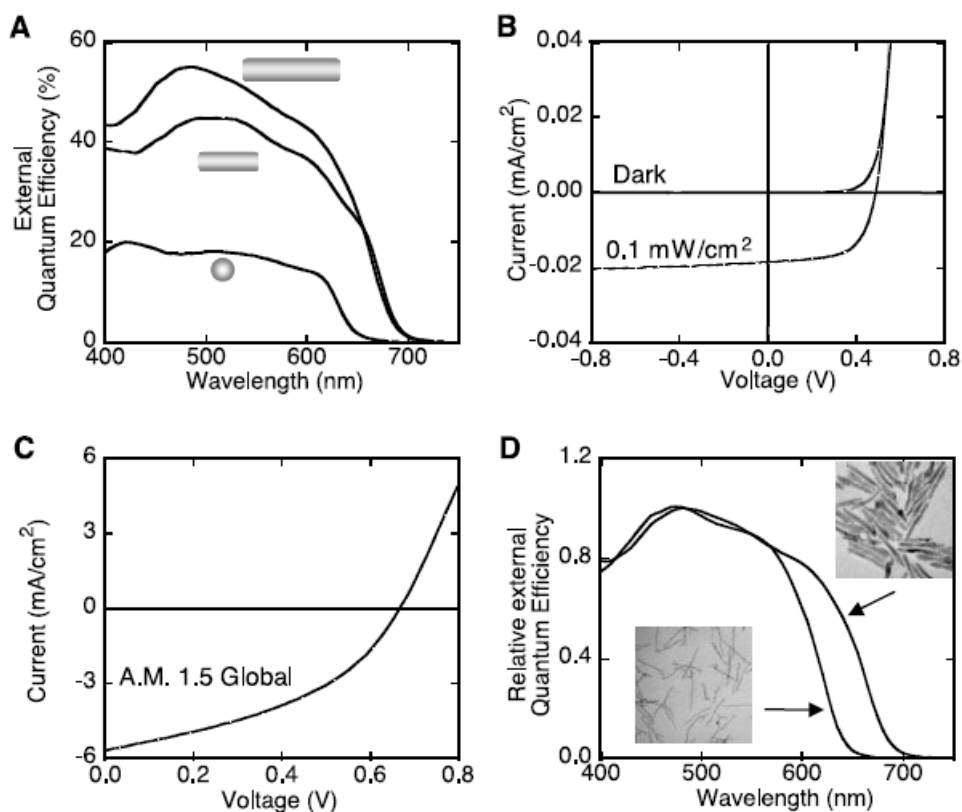


Figure 1.17 **A)** External quantum efficiencies of three different aspect ratio CdSe nanorods **B)** current-voltage curves of the 7 nm x 60 nm nanorod device illuminated at 515 nm **C)** current-voltage curves of the 7 nm x 60 nm nanorod device under AM1.5G solar conditions **D)** Photocurrent spectra of two devices with nanorods at two different diameters. Reprinted with permission from ref. 11. Copyright © 2002 Science.

Particles of higher shape complexity can lead to improvements in device performance as shown by Sun et al. in 2003.⁷⁸ Tetrapod shaped CdSe nanoparticles were incorporated into devices using poly(2-methoxy-5-(3',7'-dimethyl-octyloxy)-*p*-phenylenevinylene) (OC1C10-PPV) as the polymer.

Device efficiencies reached 1.8%, with the boost in performance attributed to the increased charge transport perpendicular to the plane of the film. This can be understood from the fact that tetrapods are unable to lie flat in the PAL film, with the result that one arm of the particle will be oriented in the direction of electron transport. When compared to devices made from nanorods with the exact same conditions and particle loading, the tetrapod devices gave consistently higher values for EQE. Specifically, an EQE of 45% was obtained under 0.39 mW cm^{-2} illumination at 480 nm while the nanorod device gave an EQE almost a factor of 2 smaller. The EQE also showed absorption outside the range of the polymer alone, showing that hole transfer from nanoparticle to polymer contributed to device performance. Under AM1.5G conditions the tetrapod CdSe/polymer devices gave a V_{OC} of 0.65 V, J_{SC} of -7.30 mA cm^{-2} and a FF of 0.35.

Hyperbranched particles were incorporated into CdSe/polymer devices by Gur et al. in 2007.⁷⁹ The hyperbranched nanocrystal phase controls the morphology of the film in these devices, and as a result the photoactive layer is insensitive to solubility and processing variations as is the case when CdSe of lower shape complexity is used. In addition, hyperbranched particles span the entire device thickness and thus the transport of electrons to the anode is possible through the built-in percolation pathway throughout the film (see Figure 1.18). Despite the use of P3HT as a polymer, no binary solvent was used in the processing. This was possible since hyperbranched particles have increased solubility in the polymer matrix due to their inability to form aggregates with

themselves. This leads to better dispersion of the nanocrystals within the polymer matrix and a lower degree of large-scale phase separation between the donor and acceptor components.

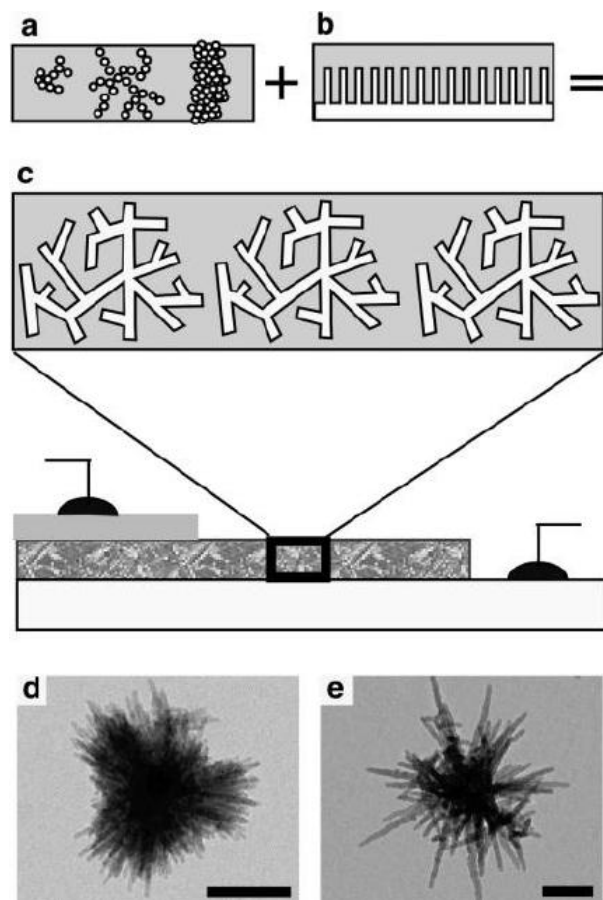


Figure 1.18 Hybrid solar cell devices made from hyperbranched semiconductor nanoparticles. The dimensions of the nanocrystals span the entire thickness of the device bypassing the defects which are detrimental to traditional spin-cast hybrid cells. Transmission electron micrographs show both **d)** CdSe and **e)** CdTe hyperbranched nanoparticles. Reprinted with permission from ref. 79. Copyright © 2007 American Chemical Society.

Figure 1.19 shows the various device characteristics for different concentrations of nanorod and branched CdSe with P3HT polymer. In the case of nanorods, a significant level of loading is required in order for the V_{OC} to reach appreciable levels. In hybrid devices, V_{OC} is found to be proportional to nanoparticle loading since a good percolation pathway is needed to establish the open-circuit potential. A similar trend is seen in the J_{SC} and can also be explained by the need for an efficient pathway for the charges to move through the nanocrystal phase. In contrast to nanorods, the V_{OC} in the hyperbranched samples reach its maximum value of 0.6V with very low levels of loading. Hyperbranched particles contain a built in percolation pathway such that each cluster of CdSe can contribute to the photocurrent. In addition to the advantages associated with the improved thin film architecture, spectral analysis showed that the hyperbranched particles contributed more to the photocurrent than the nanorods.

The electrical characteristics fit with the model of a parallel circuit in that the voltage remains constant with the addition of particles while the current is additive. From this analysis, the authors suggest that each particle acts as an individual hybrid solar cell connected in parallel to create the full device.

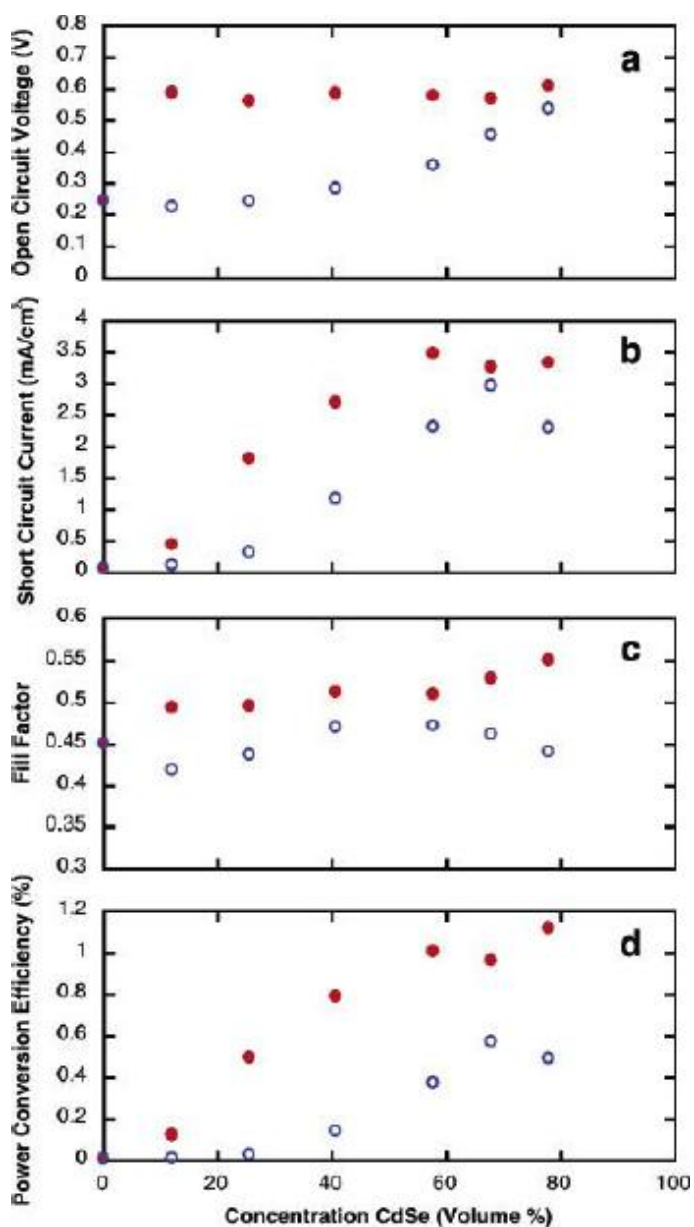


Figure 1.19 Hybrid solar cell characteristics using hyperbranched CdSe nanoparticles. Hyperbranched particles are found to outperform nanorod devices in all parameters. A) V_{OC} of both hyperbranched (solid) and nanorod (open) devices. B) J_{SC} of both devices. C) FF of both devices. D) η of both devices. Only the nanorod devices show a loading threshold. Reprinted with permission from ref. 79. Copyright © 2007 American Chemical Society.

1.7.2 Film Morphology

Film morphology plays a large role in the efficient generation and extraction of free carriers in hybrid devices. As was shown in Figure 1.15, an ideal film architecture is one in which a highly interpenetrating network of donor and acceptor exists throughout the bulk of the film. Although such a perfect design has yet to be realized in hybrid solar cells, much progress has been made to create films that offer distinct advantages when optimizing device parameters.

The amount of dispersion nanocrystals exhibit in nanoparticle/polymer composite films plays a decisive role in the overall morphology of the PAL. Synthetic approaches can be used to interface nanoparticles with polymers to offer a level of control over dispersion not obtainable through simple mixing and annealing techniques. In one example, Liu et al. synthesized end-functional P3HT to enhance the performance of hybrid devices by increasing the dispersion of the CdSe nanorods without the introduction of insulating surfactants.⁸⁰ Figure 1.20 shows the synthesis of P3HT with amino end-functionality. When a co-solution of compound **4** and CdSe nanorods was spin-cast into thin films, a high degree of homogeneity could be seen through TEM analysis. This increased amount of dispersion over typical CdSe/P3HT films provided more interfacial surface area for charge transfer. Figure 1.21 shows the dependence of device performance on CdSe loading for both the precursor polymer (**1**) and the amino-functionalized P3HT (**4**). It can be seen that the use of amino end-functionalized P3HT leads to much higher performance in the device. The authors suggest that the amino groups on the thiophene replace the weakly bound pyridine ligands on

the CdSe surface. Another advantage to using this type of polymer is that the loading of CdSe needed to obtain good performance is lower than that of typical hybrid solar cells. This allows the films to be more “plastic” in nature thus having more desirable mechanical properties.⁸¹

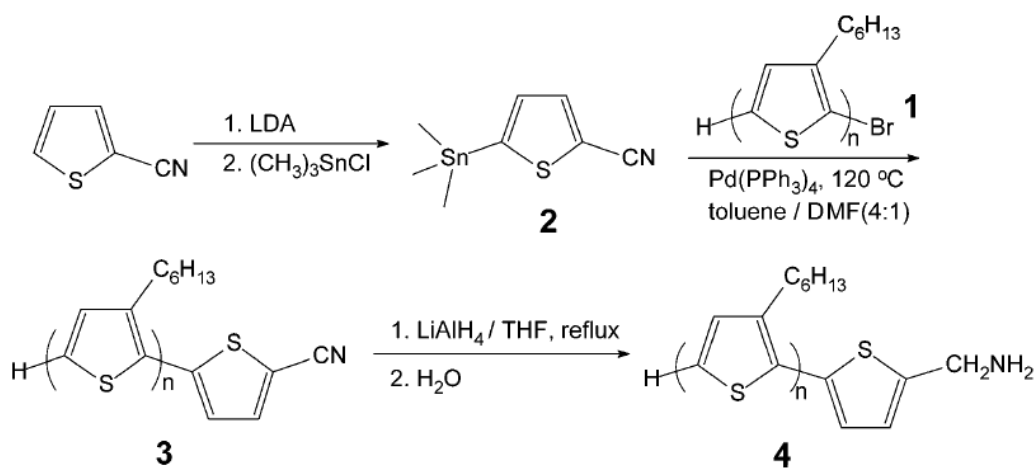


Figure 1.20. Synthesis of P3HT with amino end-functionality. The new ligand (**4**) can be used with CdSe nanoparticles for better dispersion in nanoparticle/polymer films. Reprinted with permission from ref. 80. Copyright © 2004 American Chemical Society.

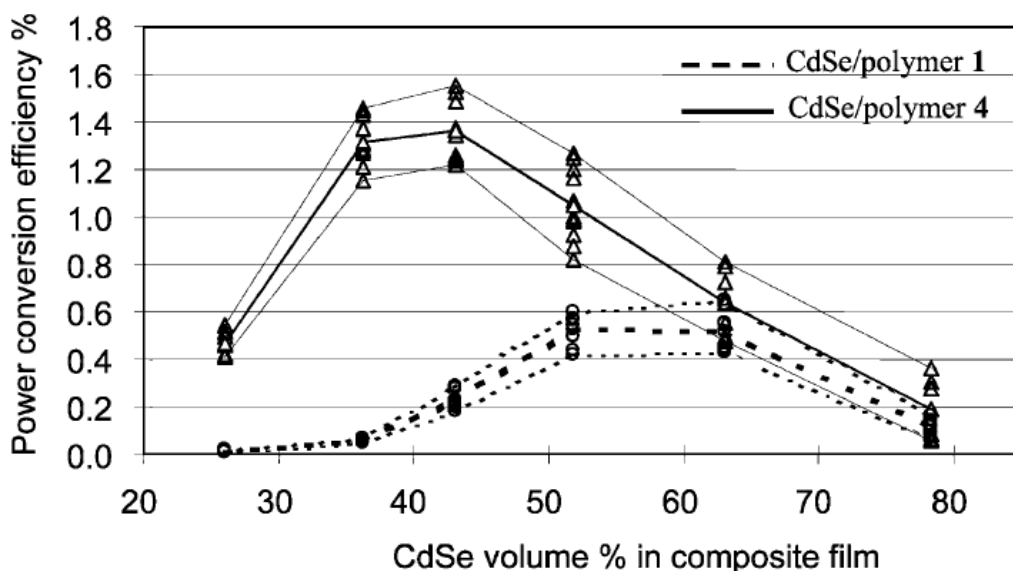


Figure 1.21. Plots of power conversion efficiency (AM 1.5) versus the volume ratio of CdSe in the active layer of the devices. Devices were made using both polymer **4** (solid lines) and polymer **1** (dashed lines) as shown in Figure 1.20. Reprinted with permission from ref. 80. Copyright © 2004 American Chemical Society.

In an effort to enhance charge separation and transport in CdSe/P3HT thin films, Wu et al. used a chemical vapour annealing technique to replace the bulky ligands on CdSe while preserving their solubility in the polymer matrix.⁸² The annealing was carried out with the solvent benzene-1,3-dithiol and gave devices with an overall power conversion efficiency of 1.56%. The V_{OC} was 0.577 and the J_{SC} 5.823 mA/cm². When exposing the fully fabricated device to the same vapour annealing conditions as the original photoactive layer, the short-circuit

current was increased to 9.7 mA/cm^2 and the overall power conversion efficiency jumped to 2.65%. This corresponds to an increase of 66% and 70% for J_{SC} and V_{OC} respectively. The fill factor was found to increase from 0.47 to 0.50. The improvement in device performance was attributed to the benzene-1,3-dithiol molecules diffusing into the blended film and replacing the bulky alkylphosphonic acid ligands. This leads to improved charge separation and transport. TOPO has exceptional compatibility with polymers (due to its long alkyl chain) and thus excellent particle dispersion is present. As the chemical vapour annealing is a post-fabrication procedure, the insulating TOPO can be removed while preserving the dispersion of particles and locking in the morphology.

Huynh et al. looked at the effect of varying the pyridine/chloroform ratio, in the binary solvent mixture, on the film morphology of CdSe nanorod / P3HT films.⁸³ This ratio can be used to control the dispersion of high aspect ratio CdSe nanorods in the P3HT phase with phase segregation ranging between the micron to nanoscale. This ability has implications for device performance, as the right amount of phase segregation is the one that is on the order of the exciton diffusion length (see section 1.6). Figure 1.22 shows the difference between films cast with 1 vol% and 8 vol% pyridine in chloroform. Both the topography and phase AFM images show that an increase in the amount of pyridine decreases the roughness of the film.

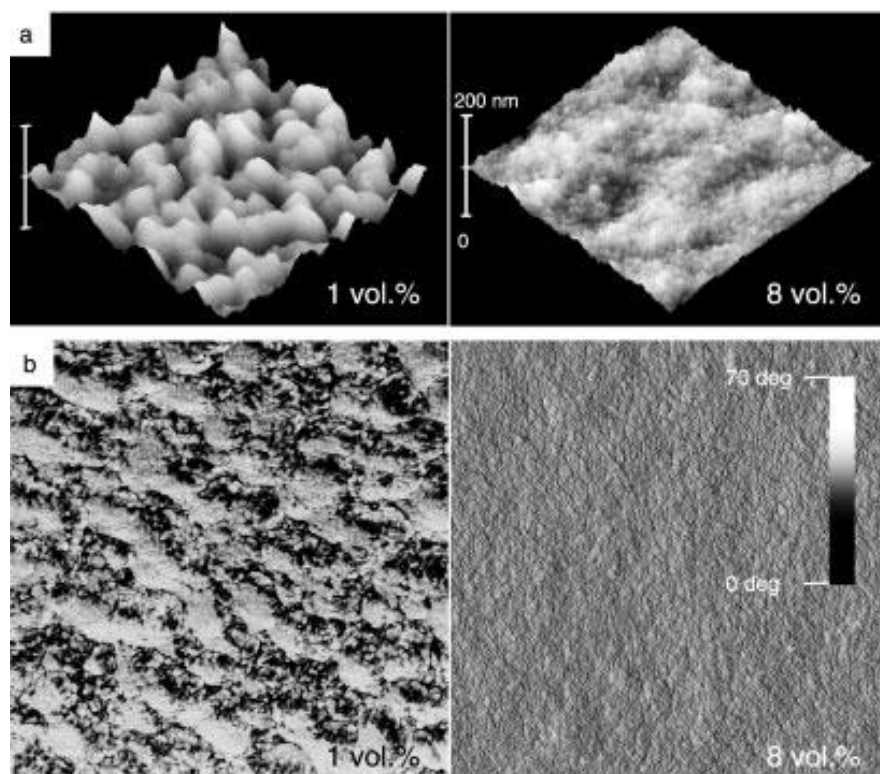


Figure 1.22. AFM images showing the topography a) and phase b) of the CdSe/P3HT system with 90 weight % nanoparticles with dimensions 8 nm x 13 nm. The images show the difference between 1 vol% and 8 vol% pyridine in chloroform. Scan areas are 5x5 microns. Reprinted with permission from ref. 83. Copyright © 2003 Wiley.

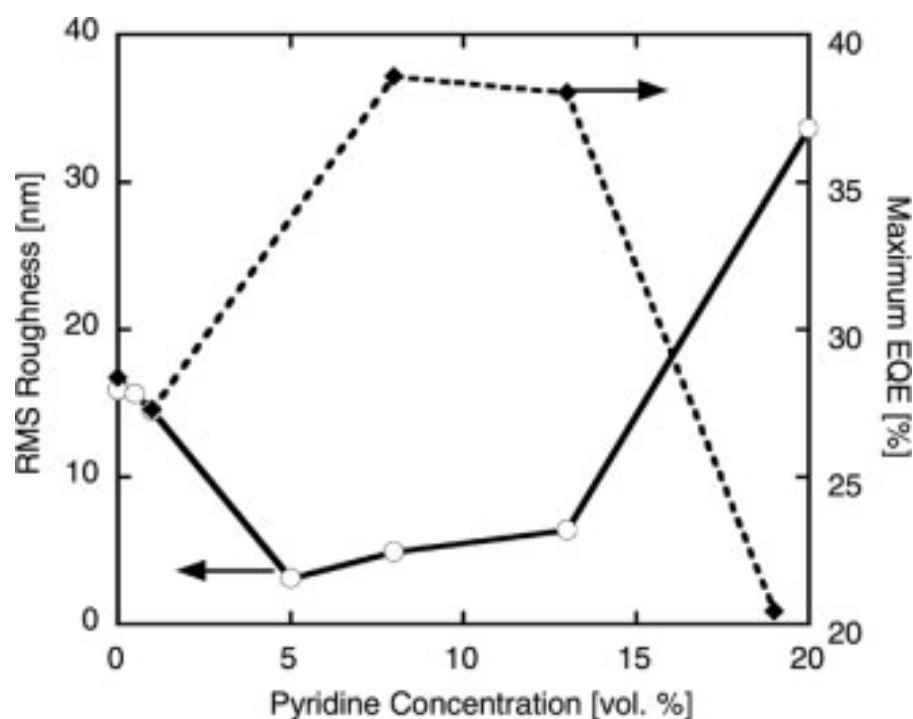


Figure 1.23. The range of RMS roughness values obtained with varying ratios of pyridine to chloroform. The corresponding EQE values are also shown. Reprinted with permission from ref. 83. Copyright © 2003 Wiley.

Three regimes based on the amount of pyridine incorporated into the binary solvent mixture are defined. In the first regime, low pyridine concentrations cause flocculation of the nanoparticles, leading to large scale phase segregation in the films. This is expected, as pyridine is needed to increase the solubility of the inorganic nanoparticles in the polymer phase. The second regime increases the amount of pyridine making the nanoparticles much more soluble in the polymer. As long as the pyridine does not go beyond a critical threshold, the polymer is still

sufficiently soluble due to a significant amount of chloroform still in the binary solvent mixture. This allows for an intimate mixing of the two types of semiconductor and is expected to lead to good device performance. In the third regime, the pyridine concentration becomes too high for the polymer to stay soluble and large scale phase segregation is the result.

Figure 1.22 shows the RMS roughness and corresponding EQE values for all three regimes. EQE values increased by a factor of 1.4 in going from regime I to regime II and decreased when going from regime II to regime III. An inverse dependence of EQE on RMS film roughness was found with the highest EQE values corresponding to the smoothest films having the smallest degree of phase segregation. Interestingly, it was found that the V_{OC} and fill factor did not change with pyridine concentration.

The amount of pyridine needed to ensure good dispersion depends on the surface to volume ratio of the nanoparticles. 12 vol % pyridine was needed for CdSe nanorods with dimensions 3 nm x 100 nm whereas 4 vol% were needed for rods 40 nm x 60 nm. Further improvements in film morphology and device performance were obtained with thermal annealing. The improvements were attributed to the removal of the pyridine ligand and better phase segregation. The advantage of controlling film morphology is evidenced through the high external quantum efficiency of 59% at 450 nm in the smooth films.

The effect of polymer choice on phase segregation has been shown by Sharma et al., where lower RMS roughness values were reported in CdSe/polymer films when using P3HT instead of MEH-PPV.⁸⁴ The inferior morphology of the MEH-PPV/CdSe film was attributed to the difference in conjugation length of the polymer, phase segregation between the two components and the surface roughness of the film.

Sun et al. have shown that vertical segregation of CdSe tetrapods lead to improved performance due to the achievement of a close-to-ideal bilayer architecture in the photoactive layer.⁸⁵ Through the use of the high boiling point solvent 1,2,4-trichlorobenzene (TCB), a unique film morphology is achieved through the slow evaporation of the solvent. Device performance at AM1.5G conditions were 0.76, -6.42, 0.44 and 2.8% for the V_{OC} , J_{SC} , FF and overall power conversion efficiency respectively. The large V_{OC} and J_{SC} values in these devices are characteristic of a vertical phase separation of the donor and acceptor components leading to a bilayer device architecture (see Figure 1.14a). The bilayer design is good for electron transport due to their continuous pathways for carrier transport. This architecture also avoids the build-up of space charge that occurs in blend films at high intensities, thus bimolecular recombination throughout the film should be significantly reduced. Despite the phase segregation in the vertical dimension, AFM analysis showed very little lateral phase segregation, indicative of good particle dispersion throughout the film.

Evidence for vertical segregation is seen in the time-resolved PL studies (see Figure 1.23). Charge transfer within the PAL leads to a decrease in the lifetime of the exciton relative to the pristine polymer film. As can be seen in Figure 1.23, the shortest lived excitons are correlated with the CdSe /polymer films cast from chloroform. These films give an intermixed blend morphology with a large amount of surface area for charge transfer to take place. When TCB is used, a lower number of excitons are close to the charge transfer interface and less quenching occurs in the film. This change in film morphology has led to one the highest performing tetrapod devices to date.

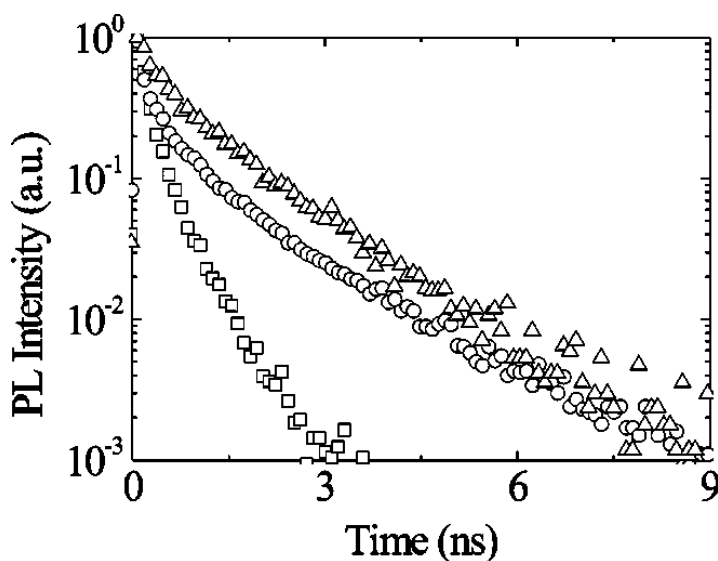


Figure 1.24. PL decay curves for blends of CdSe and OC₁C₁₀-PPV polymer. Solvents used to spin cast the films were TCB (circles) and chloroform (squares). The pristine polymer film is shown for comparison (triangles). Reprinted with permission from ref. 85. Copyright © 2005 American Institute of Physics.

Another example of using a high boiling point solvent to control film morphology uses TCB to form P3HT nanofibers in the CdSe/polymer system.⁸⁶ This nanofibrillar morphology increased hole transport in the film and produced devices with 2.6% overall power conversion efficiencies. This is the highest reported CdSe nanorod/polymer device reported to date. The fibrils in these films were found to extend over several microns.

In addition to film morphology, the chemistry on the surface of the nanoparticles is critical to device performance. The next section explores some of the approaches that are currently in use to fabricate CdSe nanoparticles with ideal surface chemistry.

1.7.3 Particle Surface Chemistry

The performance of hybrid solar cells depends on the interfacial chemistry occurring between device components. Whether it is charge transfer (CT) from polymer to nanoparticle, nanoparticle to polymer, or nanoparticle to nanoparticle, surface chemistry plays a vital role. The commensurability of the nanoparticles with the polymer also depends on the nature of the particle's surface. As a result, much effort has been applied to controlling the capping ligands attached to the surface of CdSe in order ensure sufficient communication between photoactive species.

Shortening the capping ligand has been shown to improve the performance parameters in hybrid cells. Longer chain lengths act as a barrier to charge transfer, limiting the amount of photocurrent that can be extracted from the

device. In addition, interparticle hopping can be expected to suffer with longer chain ligands. Most syntheses of CdSe nanoparticles leave the particle capped with a long alkyl chain surfactant such as TOPO. As discussed in previous sections, one common method to remove TOPO is to treat the particles with pyridine. Although pyridine does not bind well to the surface of CdSe, refluxing displaces the TOPO by mass action leaving pyridine-capped crystals. Despite this technique being used for devices with moderate photoactivity, much work remains in achieving a good dispersion of nanoparticles into a matrix of conducting polymer.

In one approach, the native TOPO ligand on the CdSe surface was replaced with the *tert*-butyl *N*-(2-mercaptoethyl)carbamate ligand.⁸⁷ When exposed to UV radiation, the *tert*-butoxycarbonyl (*t*BOC) group of the carbamate group releases isobutene and carbon dioxide causing the chain length to decrease and the dispersibility of the particles to improve. Seo et al. used this strategy with heat treatment to develop CdSe/polymer devices with impressive gains in performance. The authors found that short-circuit current density was improved by a factor of 60, while the power conversion efficiency increased by an order of magnitude. The improvement in device performance was attributed to increased charge transport between nanoparticles due to the decreased length in capping ligands.

In another approach, a hexanoic acid-assisted washing procedure was used to treat non ligand-exchanged quantum dots.⁸⁸ In this paper, the authors measured a V_{oc} of 623 mV, J_{sc} of 5.8 mA/cm², and a fill factor of 0.56. The overall power

conversion efficiency of the device was 2%. They found that the optimum loading was 85-89%. Thus they found that if the QD/polymer ratio is too low, there are not enough QDs to minimize the hopping distances between dots. Therefore electrons cannot be extracted from the device as no good percolation pathway exists. On the other hand, if the polymer component is too low, there is not enough absorption in the PAL and hole transport suffers. Therefore there exists an optimum loading percentage in these devices. The hexanoic acid is used to remove the insulating HDA sphere due to the salt formation of HDA. Thus the reduced insulating sphere barriers improved the charge transfer between P3HT and CdSe as well as increasing electron mobility by creating a percolation pathway with tightly-packed nanoparticles.

In some elegant work by Emrick et al., P3HT has been covalently attached to the surface of CdSe nanorods.⁹⁰ This bypasses the need for an intermediate ligand on the surface for solubility and significantly reduces the barrier to charge transfer. Figure 1.25 shows the attachment procedure. In order to create the P3HT-functionalized nanorods, arylbormide-functionalized phosphine oxides and thiols were synthesized to act as ligands for the surface of CdSe. These ligands were then used to couple to vinyl-terminated P3HT to fabricate P3HT-hybrid nanocomposites. The photophysics of the composite material were modulated by the direct attachment of P3HT to the CdSe surface.

It is interesting to note that this seemingly ideal material has not led to improved device performances since its publication. This is not surprising however when one takes into account all of the correlated effects that lead to well

performing devices. Although there is both intimate contact between P3HT and the CdSe and proof of complete CT at the interface, the charges still need to be extracted at the electrodes. The attachment of P3HT may still hinder the direct attachment of nanorods to themselves, thus inhibiting the formation of a good percolation pathway to the electrodes.

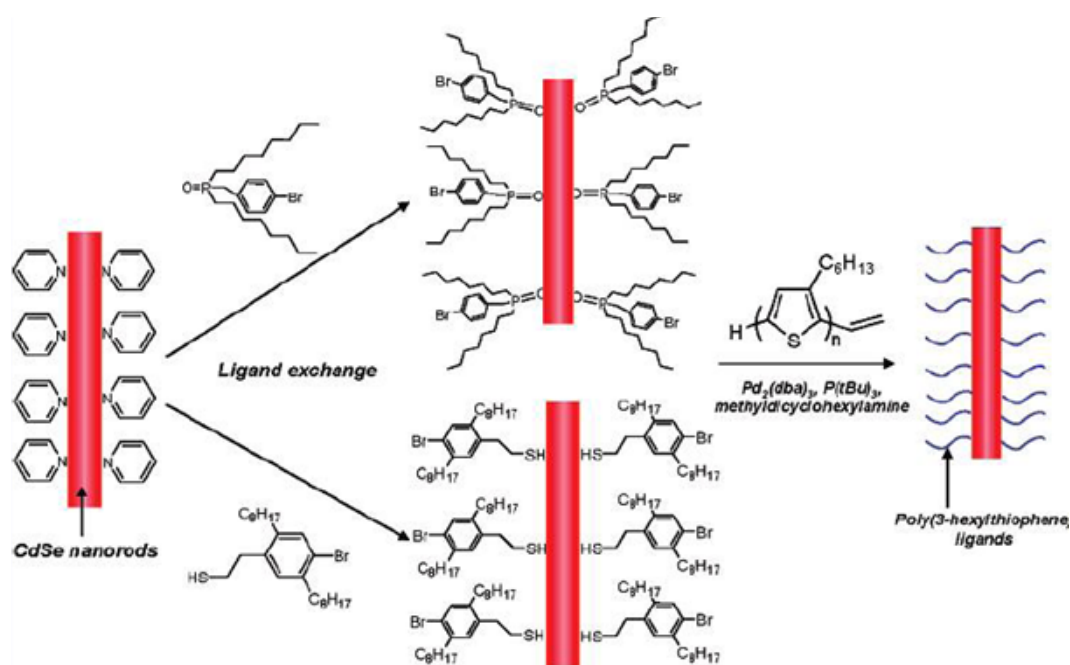


Figure 1.25. Synthetic protocol for creating P3HT-capped CdSe nanorods. Reprinted with permission from ref. 90. Copyright © 2007 American Chemical Society.

The preceding sections have shown the variety of methods that can be used to enhance device performance in nanoparticle/polymer solar cells. The

techniques typically involve control over particle surface chemistry and overall film morphology. In the next section, we look at some of the more radical approaches to improving device performance in nanoparticle-based devices. Although these approaches are mostly theoretical, some recent experiments have shown them to be potentially useful in surpassing current performance limits.

1.7.4 Future Applications

Multiple Exciton Generation

Crystalline silicon currently holds the record for single junction solar cell efficiency at ~25% under standard AM1.5G radiation.⁹¹ The limiting factor in these cells is that only ~33% of incident sunlight is converted into electricity as dictated by the Shockley-Queisser limit.⁹² The majority of losses in efficiency occur when photons with energies greater than the band gap are absorbed and converted to heat within the cell via phonon scattering. Studies suggest that if the carriers could be extracted without heat loss, the efficiency of single junction cells could reach 67% under standard AM1.5G radiation.⁹³

The process by which this high efficiency may one day be possible occurs in some semiconductor nanoparticles and is termed multiple exciton generation (MEG). To understand MEG, we can look at the band diagram in Figure 1.26.⁹⁴ A photon of energy greater than 2 times the band gap of the semiconductor could theoretically be converted into multiple excitons using simple conservation of

energy arguments. Nozik speculated that a process called inverse-Auger recombination (impact ionization) along with a phenomenon known as the phonon bottleneck, which was known to occur in bulk semiconductors, may be highly efficient in quantum confined nanocrystals.^{95, 96} Since the formation of excitons is the critical first step in third-generation devices, such a highly efficient process could be extremely useful in solar energy technology. These theories have since been confirmed and it is believed that this process is extremely efficient in certain nanoparticles. To differentiate the process from what occurs in bulk systems, it has been termed multiple exciton generation (MEG). The nanoparticles that have been shown to exhibit MEG include PbSe,¹⁰⁵ PbS,¹⁰³ CdSe¹⁰⁶, PbTe,¹⁰⁷ and InAs.¹⁰⁸

The majority of studies on MEG are centred around PbSe nanocrystals. This is due to its relatively large exciton Bohr radius (46 nm), which results in quantum confined features at larger sizes than other semiconductor nanoparticles.⁹⁷ In one study, a quantum efficiency of 700% (seven excitons per photon) was measured in PbSe.⁹⁸

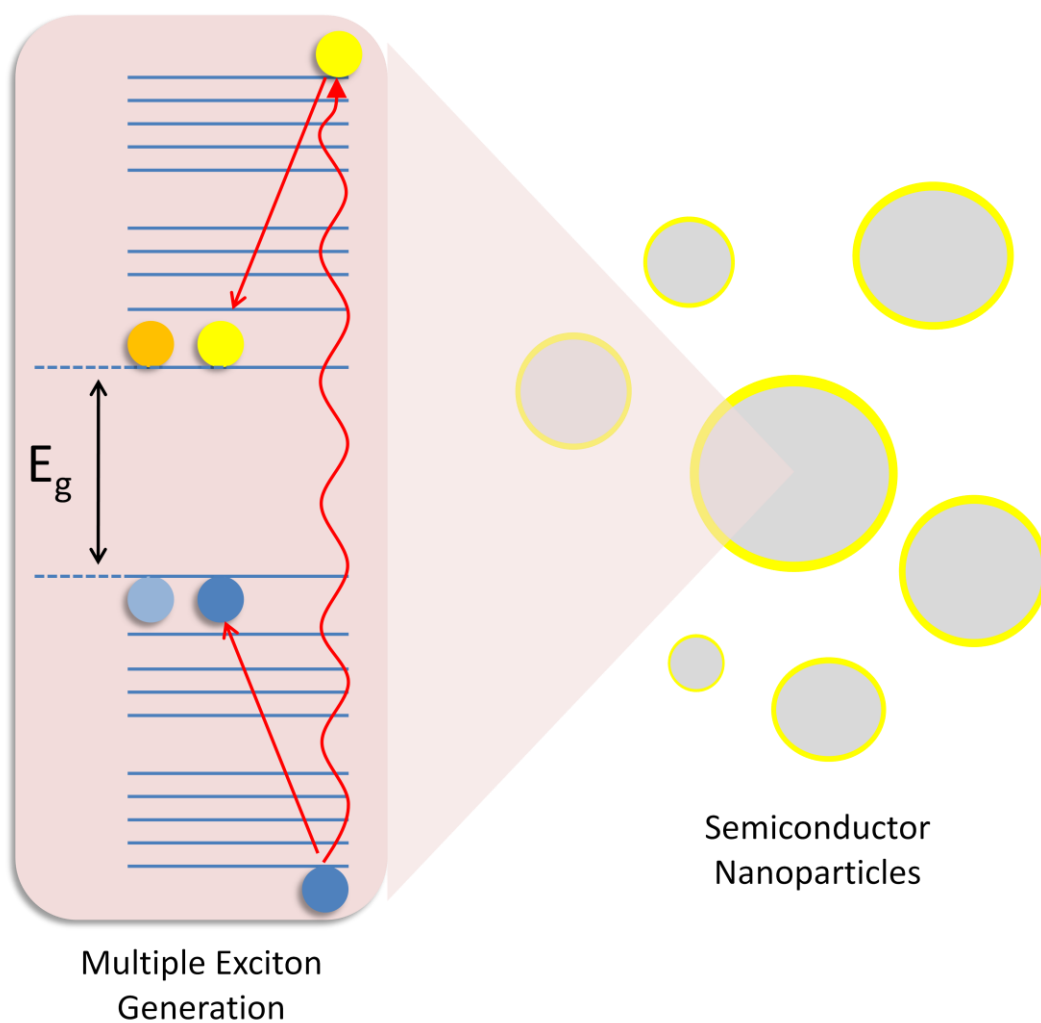


Figure 1.26 Simplified picture of multiple exciton generation (MEG) in semiconductor nanoparticles. Absorption of a photon in excess of two times the band gap, E_g , produces multiple excitons.

Much research has gone into MEG,^{94, 98 - 101} and several models have been proposed to explain the process including the virtual exciton state model,¹⁰² coherent superposition of multiexcitons and highly excited single excitons¹⁰³ and impact ionization.¹⁰⁴

Although no actual solar device has been proven to benefit from MEG, there is progress being made in packed films of semiconductor nanoparticles. The challenge to extracting carriers subsequent to the MEG process is that charge separation must occur on time scales longer than that of MEG (10^{-13} - 10^{-12} s) but shorter than the biexciton lifetime (10^{-10} s).¹⁰⁹ Biexciton recombination is the mechanism by which multiple excitons undergo annihilation and it is this process that MEG must compete with in order to contribute to the photocurrent.

Carrier mobility in nanoparticle films increases drastically when the particles are coupled close together.^{110 - 113} One factor leading to such improvements in the electrical characteristics of packed nanoparticle films is the delocalization of the exciton. Nozik et al. have studied the effect that delocalized excitons in PbSe nanoparticle films have on the MEG quantum yield.¹⁰⁹ In order to create layers of close packed PbSe, films were fabricated by spin-casting from solution and subsequently treating with hydrazine. It was shown that the biexciton lifetime in films actually increased relative to the isolated particles in solution, with the result attributed to the delocalization of the excitonic wave function. This resulted in extended exciton states which require more time to undergo Auger recombination whereby a biexciton decays into a single exciton. This is an advantage to the potential charge carrier extraction from MEG in nanoparticle films. Another fascinating result was reported by Prasad et al. that showed increased carrier extraction in PbSe films attributed to MEG.¹⁰¹

Although much work remains, the prospect of extracting charges from the MEG process in solar cell devices holds great promise for improved device efficiency.

Hot Electron Transfer

Another method used to capture the energy above the band gap in the semiconductor nanoparticles is called hot electron transfer. In a recent study by Zhu et al., hot carriers were successfully transferred from PbSe to TiO₂ prior to the detrimental thermalization process (see Figure 1.27).¹¹⁴ Proper ligands were chosen in order to facilitate this electron transfer process. Using a core-shell passivation method, Guyot-Sionnest et al. have shown that the thermalization process in CdSe quantum dots capped with a ZnSe shell can be slowed to > 1ns.¹¹⁵ They found that the relaxation time of the hot carriers could be manipulated with the thickness of the ZnSe passivating layer. This holds great promise for synthetically tailoring relaxation times and moving a step closer to extracting charges from either MEG or hot electron transfer in solar cell devices.

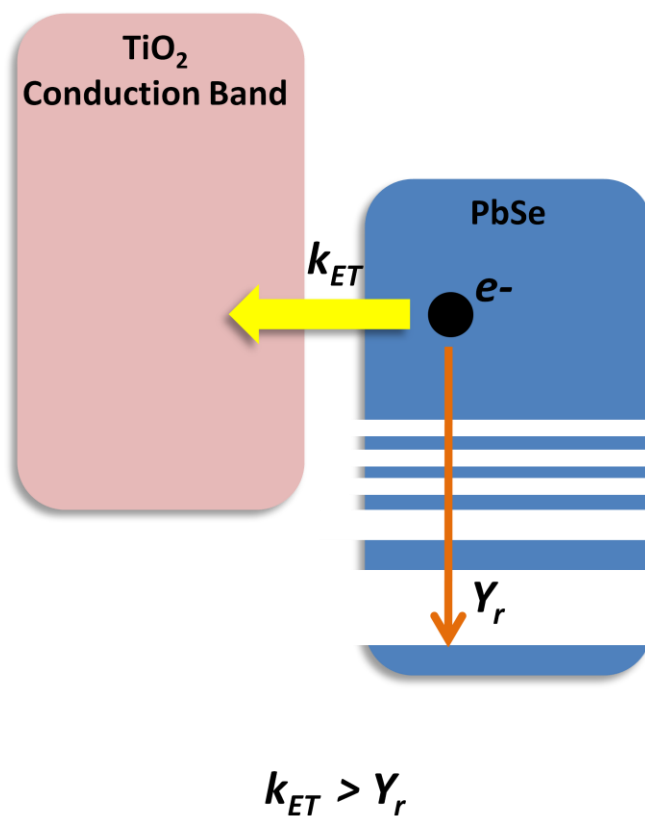


Figure 1.27. In their study, Zhu et al. found that regardless of quantum dot size or chemical treatment, the lowest excited electronic state of PbSe was always below the TiO₂ conduction band minimum. Therefore electron transfer from the PbSe to the TiO₂ could only be possible through hot-electron states. Reprinted with permission from ref. 114. Copyright © 2010 Science.

1.8 Computational Studies of Charge Transport in Thiophenes

Intrinsically, the mobility of carriers in inorganic materials is several orders of magnitude higher than in organics. As a result, charge transport in hybrid optoelectronic devices is largely limited by the polymeric component of the photoactive layer. Carrier mobility is one of the key parameters to the operation of a solar cell and understanding the fundamental mechanisms by which charge is transported in these materials is critical to the rational design of third-generation solar devices.

Thiophenes are to date the best examples of high performance hole conducting material for polymer-based third-generation devices. Hole mobilities up to $0.1 \text{ cm}^2/\text{V}\cdot\text{s}$ have been measured in these materials. Their high mobility is a consequence of the π - π stacking forced by the side chains of the polymer. Despite the plethora of experimental data on the packing of thiophenes in thin films, it is difficult to gain a truly molecular understanding of the origins behind their charge transport. Subtle structure-function relationships exists that cannot be probed by experimental means. In order to understand the factors leading to good transport in these polymeric components, a tool that goes beyond the limits of our experimental instruments is required.

Computational chemistry offers insight into many of the physical phenomena found in chemical systems. Using the foundations of quantum and

Newtonian mechanics, and the recent explosion in computing power, computational chemistry gives researchers a means to explore the subtle molecular parameters that govern macroscopic behaviour such conductivity in thin films. A variety of methods now exist with different levels of complexity. Knowing which method is appropriate involves a thorough understanding of the physical phenomena being explored and the fundamentals behind the various methods available. As many methods scale exponentially with the number of atoms in the system, a serious consideration is the computational cost of the methods being used. Despite the rapid progress in computing power, all but the simplest calculations require significant computational resources.

Density functional theory (DFT) is one of the most widely used methods in computational chemistry. Originally created for physicists studying condensed matter systems, DFT is now used to study the physical properties of a variety of atoms and molecules. One of the biggest advantages to the use of DFT is its ability to handle relatively large systems with a fairly high degree of accuracy. At its core, DFT uses a quantum mechanical description of the molecular system and is therefore capable of delivering accurate results using a reasonable amount of computational resources.

This section begins with an introduction to DFT and how it differs from some of the more conventional methods in computational chemistry. A basic outline of how the method is used and how properties of molecules are derived will be given. Following the introduction to DFT, a discussion on charge transport in organic semiconductors is presented. A basic understanding of some

of the molecular origins to carrier mobility is critical to the modeling of these systems. Finally, the approach known as the “energy-splitting-in-dimer” method will be introduced. This method is used in Chapter 4 to investigate the carrier transport properties of thiophenes; the polymeric component to the multilayer thin films described in Chapters 2 and 3.

1.8.1 Density Functional Theory – An Introduction

As mentioned in the introduction of this section, DFT is able to offer fairly accurate results with a lower computational cost than many other methods. Much of the motivation behind the development of DFT stems from the unsettling nature of the wave function. In reality, it is not known if there exists a truly physical manifestation of the wave function. What is known is that it is a mathematical equation that offers a great deal of information about a quantum mechanical system. In a many-electron molecule, this information actually lacks any direct physical meaning despite its powerful predictive and explanatory ability.

A breakthrough came when it was realized that the ground-state molecular energy wave function, and all other properties, could be determined by the ground-state electron probability density. What makes this discovery so powerful, is that the probability density connects a real physical property (density)

to the elusive wave function. The relationship can be expressed as shown in equation 1.9.1.

Therefore we can say that the electronic energy E_0 is a functional of the density ρ_0 .

$$1.9.1 \quad E = E_0(\rho_0)$$

It was shown by Kohn and Hohenberg that the ground state electron probability density determines the external potential and the number of electrons, and can therefore be used to determine the ground state wave function. This can be understood through the Hohenberg-Kohn theorem. The purely electronic Hamiltonian is shown in equation 1.9.2. The electronic Hamiltonian is the energy operator used in the Schrödinger equation to solve for the energy of the molecule. The external potential acting on electron i is shown in equation 1.9.3.

$$1.9.2 \quad \hat{H} = -\frac{1}{2} \sum_{i=1}^n \nabla_i^2 + \sum_{i=1}^n v(r_i) + \sum_j \sum_{i>j} \frac{1}{r_{ij}}$$

$$1.9.3 \quad v(r_i) = -\sum_{\alpha} \frac{Z_{\alpha}}{r_{i\alpha}}$$

Determining the number of electrons is straightforward by simply integrating over all space and using the normalization of the wave function (equation 1.9.4).

$$1.9.4 \quad \int \rho_0(r) dr = n$$

Determining the external potential is more challenging. It requires both the charges and positions of nuclei. In order to accomplish this it was necessary to prove that the ground state density determines the external potential. This can be accomplished via *reductio ad absurdum* (proof by contradiction) using the Hohenberg-Kohn Theorem.

The Hohenberg-Kohn Theorem

We start by assuming two different external potentials (see equations 1.9.5), each consistent with the same nondegenerate ground-state densities \mathbf{V}_a and \mathbf{V}_b and the two corresponding Hamiltonian operators \mathbf{H}_a and \mathbf{H}_b . Each Hamiltonian has an associated ground-state wave function and eigenvalue \mathbf{E}_0 . The variational theorem of molecular orbital theory dictates that the expectation value of the Hamiltonian \mathbf{a} over the wave function \mathbf{b} must be higher than the ground-state energy of \mathbf{a} . Note that the final result is not possible. Therefore by contradiction it can be shown that the non-degenerate ground state density must determine the external potential and thus the Hamiltonian. With the Hamiltonian known the wave function can be determined. From the connection

of the density to the wave function, we can see that there is a tremendous amount of information coded in the density. At this point we need to know how to predict the density of the system. To do this there must be a way to optimize that density.

Equations 1.9.5

$$E_{0,a} \leq \langle \Psi_{0,b} | H_a | \Psi_{0,b} \rangle$$

$$E_{0,a} \leq \langle \Psi_{0,b} | H_a - H_b + H_b | \Psi_{0,b} \rangle$$

$$E_{0,a} \leq \langle \Psi_{0,b} | \nu_a - \nu_b | \Psi_{0,b} \rangle + E_{0,b}$$

$$E_{0,a} \leq \int [\nu_a(r) - \nu_b(r)] \rho_0(r) dr + E_{0,b}$$

$$E_{0,b} \leq \int [\nu_b(r) - \nu_a(r)] \rho_0(r) dr + E_{0,a}$$

$$\begin{aligned} E_{0,a} + E_{0,b} &\leq \int [\nu_a(r) - \nu_b(r)] \rho_0(r) dr + \int [\nu_b(r) - \nu_a(r)] \rho_0(r) dr + E_{0,b} + E_{0,a} \\ &\leq \int [\nu_b(r) - \nu_a(r) + \nu_a(r) - \nu_b(r)] \rho_0(r) dr + E_{0,b} + E_{0,a} \\ &\leq E_{0,b} + E_{0,a} \end{aligned}$$

Fortunately, the density obeys a variational principle just like molecular orbital (MO) theory. To summarize at this point, we know that the density determines the external potential, the external potential determines the Hamiltonian, and the Hamiltonian determines the wave function. Therefore with

the Hamiltonian and wave function in hand we can calculate the energy of the system.

It should be noted that at this point there is still no simplification over MO theory since the solution still relies on solving the Schrödinger equation. This, as usual, is prohibitively difficult due to the issue of electron-electron interaction. In order to deal with this problem, the Kohn-Sham self-consistent field methodology was developed which is the topic of the next section.

Kohn-Sham Self-Consistent Field Methodology

The Kohn-Sham methodology allows one to account for the electron-electron interactions inherent to molecular systems. To start, a fictitious system of non-interacting electrons is considered. It is assumed that this fictitious system has an overall ground-state density that is the same as some real system of interest where the electrons do interact. The energy functional can thus be divided into separate components to facilitate the analysis since we are dealing with a non-interacting system. Equation 1.9.6 shows the energy functional with the appropriate potential and kinetic energy terms.

$$\begin{aligned} 1.9.6 \quad E[\rho(r)] = & T_{ni}[\rho(r)] + V_{ne}[\rho(r)] + V_{ee}[\rho(r)] \\ & + \Delta T[\rho(r)] + \Delta V_{ee}[\rho(r)] \end{aligned}$$

The five terms on the right hand side of the equation stand for the kinetic energy of the electrons $T_{ne}[\rho(r)]$, the potential energy of the electrons with the nuclei $V_{ne}[\rho(r)]$, the potential energy of the electron-electron interaction $V_{ee}[\rho(r)]$, the kinetic energy correction for interacting electrons $\Delta T[\rho(r)]$, and all non-classical corrections for the electron-electron repulsion energy $\Delta V_{ee}[\rho(r)]$. Equation 1.9.6 can be rewritten within an orbital expression for the density as shown in equation 1.9.7.

1.9.7

$$E[\rho(r)] = \sum_i^N \left(\left\langle \chi_i \left| -\frac{1}{2} \nabla_i^2 \right| \chi_i \right\rangle - \left\langle \chi_i \left| \sum_k^{nuclei} \frac{Z_k}{r_i - r_k} \right| \chi_i \right\rangle \right) - \sum_i^n \left\langle \chi_i \left| \frac{1}{2} \int \frac{\rho(r')}{r_i - r'} dr' \right| \chi_i \right\rangle + E_{xc}[\rho(r)]$$

Note that the difficult terms on the far right of equation 1.9.6 have been lumped into the exchange correlation energy ($E_{xc}[\rho(r)]$) on the right of equation 1.9.7. N represents the numbers of electrons and χ_i are the Kohn-Sham orbitals. Using the density for a Slater-determinantal wave function, which is an exact eigenfunction for the non-interacting system, we get equation 1.9.8.

$$1.9.8 \quad \rho = \sum_{i=1}^N \langle \chi_i | \chi_i \rangle$$

Therefore we can find the orbitals that minimize E in equation 1.9.7. The orbitals must satisfy the eigenvalue equation shown in 1.9.9, with the Kohn-Sham one electron operator defined in equation 1.9.10. The exchange correlation potential is defined in equation 1.9.11.

$$1.9.9 \quad h_i^{KS} \chi_i = \epsilon_i \chi_i$$

$$1.9.10 \quad h_i^{KS} = -\frac{1}{2} \nabla_i^2 - \sum_k^{nuclei} \frac{z_k}{r_i - r_k} + \int \frac{p(r')}{r_i - r'} dr' + V_{xc}$$

$$1.9.11 \quad V_{xc} = \frac{\delta E_{xc}}{\delta \rho}$$

Using the above definitions one can go about solving for the lowest energy.

The steps are as follows:

- 1) Start with an initial guess for the density
- 2) From the initial guess for density, an initial estimate of $V_{xc}(\mathbf{r})$ is found
(using whatever functional has been chosen i.e. LDA)
- 3) This initial estimate to $V_{xc}(\mathbf{r})$ is used in the Kohn-Sham equations to solve
for the initial estimate of the **Kohn-Sham orbitals**
- 4) These can be expanded in terms of a set of **basis functions** of the type
shown in equation 1.9.12.
- 5) This will yield equations that resemble the Hartree-Fock-Roothan
equations except that the Fock matrix elements are replaced by Kohn-
Sham matrix elements of the type shown in equation 1.9.13.
- 6) The initially found **Kohn-Sham orbitals** are used to get improved
electron density
- 7) then used to get improved V_{xc} ,
- 8) then used in the **KS equations** to get improved **KS orbitals** and so on.

$$1.9.12 \quad \theta_i^{KS} = \sum_{r=1}^b c_{ri} \chi_r$$

$$1.9.13 \quad h_{rs}^{KS} = \left\langle \chi_r \left| \hat{h}^{KS} \right| \chi_s \right\rangle$$

The iterations are continued until there is no further significant change in the density and the KS orbitals. Thus it can be seen that this is an iterative process and thus as with MO calculations, a self consistent field (SCF) method.

1.8.2 Charge Transport in Organic Semiconductors

One of the most important issues in solar cell design is the charge transport of carriers throughout the organic component of the hybrid device.¹¹⁷ Charge transport is typically understood via carrier mobility, which can be thought of as a purely diffusive phenomenon and described by the simple diffusion equation shown in 1.9.13.

$$1.9.14 \quad \langle x^2 \rangle = nDt$$

$\langle x^2 \rangle$ represents the mean square displacement of the charges, D the diffusion coefficient, t the time and n for the dimensionality of the system. The charge mobility can be related to the diffusion coefficient through the so-called Einstein equation as shown in equation 1.9.14 where k_B is the Boltzmann constant and e is the electron charge. The carrier velocity can be considered a drift phenomenon and is typically expressed in units of velocity over electric field (i.e. $\text{cm}^2/\text{V}\cdot\text{s}$).

$$1.9.15 \quad \mu = \frac{eD}{k_B T}$$

One of the most important factors influencing charge transport is molecular packing. Thiophene oligomers will often pack into the so-called herringbone motif as shown in Figure 1.28. High carrier mobility would not be expected due to the large angle between molecular planes. The co-facial arrangement also shown in Figure 1.28 is considered much more beneficial for charge transport due to the favourable alignment of the frontier orbitals necessary for charge transfer (vide infra). Interestingly, the herringbone arrangement can lead to high mobility as will be discussed in Chapter 4.

Mobility of carriers is typically not constant throughout the bulk of the film unless the organic material is grown to be pure crystalline. The addition of nanoparticles to thiophenes is known to affect the packing arrangement of the polymer and lead to variations in crystallinity throughout the film.¹³⁸ In hybrid solar cells, one can expect the majority of the organic phase to be in a semi-crystalline state with a fairly high degree of disorder. A variety of chain lengths and torsion angles are available to the conjugated material and it is assumed that a Gaussian distribution of HOMO/LUMO energy levels exists throughout the film.^{118, 119} Mobility can be thought to occur very well in certain regions of the film, while on other regions the transport is quite low. These regions can be modeled in series and the mobility expressed as shown in equation 1.9.15.¹²⁰

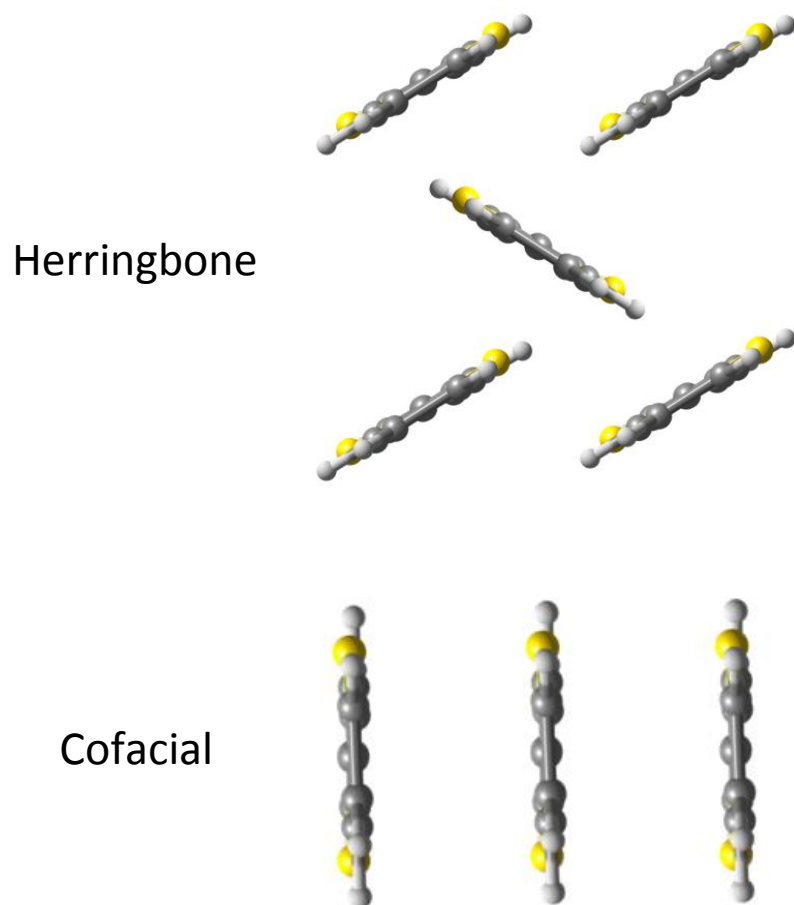


Figure 1.28. The two main packing types of the thiophene oligomer include the herringbone and cofacial arrangements.

$$1.9.16 \quad \frac{1}{\mu} = \frac{1}{\mu_{low}} + \frac{1}{\mu_{high}}$$

In single crystals of organic material, the conductivity is found to decrease with the temperature, just as is the case for metals. This is typical for any kind of

band transport and comes from the scattering phonons within the material. Phonons are quasiparticles of lattice vibration within the crystal which are quantized. Therefore there is a coupling between phonon modes in the material and the carriers.¹²¹ In highly disordered systems, such as that expected in the polymer matrix of hybrid devices, transport occurs via a thermally activated hopping mechanism. Thus an increase in temperature is found to increase the conductivity. This can be understood by the fact that the increase in temperature provides the energy necessary to overcome the barriers created by the energetic disorder of the system. This barrier can be seen in the simple Arrhenius equation as shown in equation 1.9.16 where Δ is the barrier caused by the amount of disorder in the film.

$$1.9.17 \quad \mu_O = \mu_\infty \exp(-\Delta / k_B T)$$

In inorganic semiconductors, the electron-phonon interactions are typically much smaller than the electronic interactions and are seen as perturbations to normal carrier transport. Organic semiconductors on the other hand have electron-phonon interactions comparable to the electronic interactions and this leads to the formation of polarons. Polarons can be thought of as electronic charges dressed in a cloud of phonons.^{122, 123}

1.8.3. *Modeling Charge Transport: The Energy Splitting in Dimer Method*

Determining the electronic coupling between molecules is of key importance in areas of biology, chemistry and physics.^{124 - 128} It involves the determination of the matrix element between two species involved in electron transfer. The energy splitting in dimer method has been used extensively^{129 - 135} and originates from the realization that at the transition point, excess charge is equally delocalized between the two molecules. At this point the energy difference between the two states corresponds to two times the transfer integral; $2t_{ab}$. Therefore it can be said that $t_{ab} = (E_2 - E_1) / 2$. Although a full treatment of the charge transfer would require the geometry at the transition point (the so-called avoided crossing point) of the charged dimer, in practice the calculations are simplified by using the neutral dimer geometry. A further simplification is to apply Koopmans theorem and rely on the one-electron approximation. Using this approximation, the absolute value of the transfer integral can be expressed as shown in equations 1.9.17 and 1.9.18 for hole and electron transport respectively.

$$1.9.18 \quad t = \frac{E_H - E_{H-1}}{2} \quad \text{Hole transport}$$

$$1.9.19 \quad t = \frac{E_{L+1} - E_L}{2} \quad \text{Electron transport}$$

E_L and E_{L+1} are the energy of the LUMO and LUMO+1 respectively while E_H and E_{H-1} are the energy of the HOMO and HOMO-1 respectively. These are taken from the closed-shell configuration of the neutral state of the dimer. Due to its simplicity, this approach is the most widely used method for the evaluation of transfer integrals in organic semiconductors. Studies show that the splitting in dimer approach compares well to other high level methods.¹³⁶

In the limit of semiclassical electron transfer theory, the hopping rate for charge transfer can be approximated by the following expression:

$$1.9.20 \quad k_{ET} = \frac{4\pi^2}{h} \frac{1}{\sqrt{4\pi\lambda k_B T}} V^2 \exp\left(-\frac{\lambda}{4k_B T}\right)$$

The key parameters are the electron transfer integral V^2 and the reorganization energy λ .¹³⁷ The transfer integral gives the degree of overlap between wave functions on neighbouring molecules. To see how this degree of overlap can be interpreted as bandwidths, Figure 1.29 shows the formation of valence and conduction bands in the limit of an extended system. They are the result of the overlap between HOMO and LUMO orbitals of two interacting molecules that make a dimer (see Chapter 4 of thesis for a more detailed description).

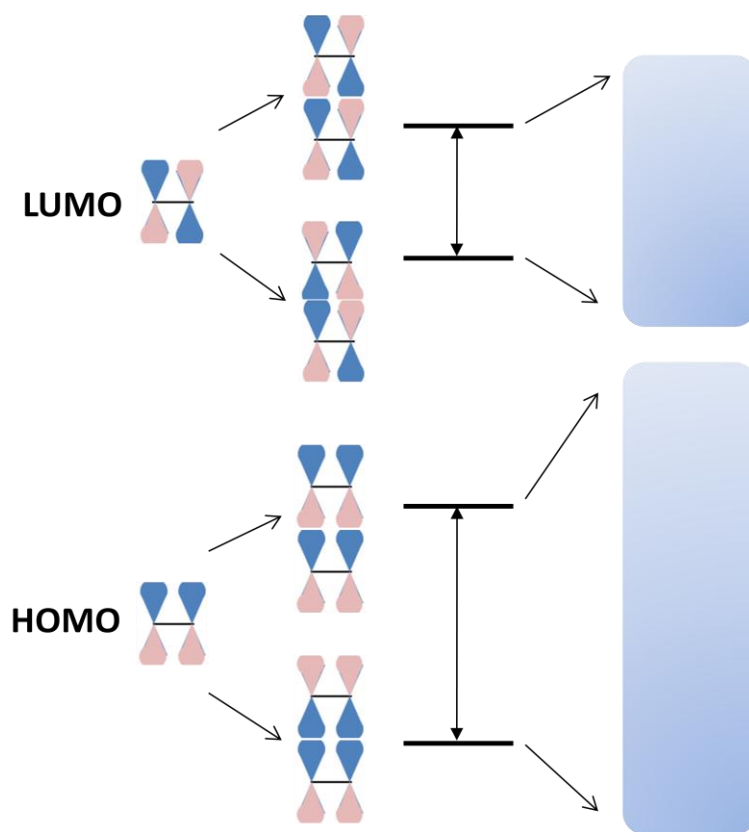


Figure 1.29. An example of the HOMO and LUMO interactions that lead to the formation of valence and conduction bands in extended systems of packed cofacial molecules. Reprinted with permission from ref. 137. Copyright © 2002 PNAS.

1.9 Organization of Thesis

Following the concepts discussed in the introduction, this thesis presents the synthesis of nanocomposite thin films from semiconductor nanoparticles and conducting polymer. Chapter 2 is dedicated to the fabrication of stable and water-soluble nanorods and their incorporation into multilayer thin films using electrostatic layer-by-layer (ELBL) assembly. Characterization of the optical and electrical properties of the films and their individual components sheds light on their potential for optoelectronics applications.

In Chapter 3, the photoelectrical properties of the nanocomposite films are characterized by integrating the ELBL films into functional solar cell devices. A series of cells are constructed with three different nanorod morphologies and two distinct anionic conductive polymers. Using the one-diode model, the current-voltage characteristics of the devices are analyzed and discussed in the context of film morphology and particle surface chemistry. [Chapters 2 and 3 were reproduced in part with permission from: McClure, S.A.; Worfolk, B.J.; Rider, D.A.; Tucker, R.T.; Fordyce, J.A.M.; Fleischauer, M.D.; Harris, K.D.; Brett, M.J.; Buriak, J.M. ACS Appl. Mater. Interf. **2010**, 2, 219 – 229. Copyright © 2010 American Chemical Society.]

Chapter 4 presents a fundamental investigation into the charge transport properties of the polymeric component of the aforementioned films. Thiophene dimers are studied using density functional theory (DFT) with dispersion correcting potentials (DCPs) to account for the long range order inherent to assembled thin films. The contribution that molecular motion makes to the spread in band widths is calculated and the role this plays in poor carrier transport is discussed. [Chapter 4 was reproduced in part with permission from: McClure, S.A.; Buriak, J.M.; DiLabio, G.A. *J. Phys. Chem. C*, **2010**, 114, 10952. Copyright © 2010 American Chemical Society.]

Finally, Chapter 5 will give the Chapter Summaries along with potential directions of research commensurate with this thesis.

1.10 References

1. Wurfel, P. Physics of Solar Cells: From Principles to New Concepts;
Wiley-VCH, Darmstadt, Germany, **2005**.
2. Amerongen, H.; Valkunas, L.; Grondelle, R. Photosynthetic Excitons;
World Scientific Publishing, New Jersey, **2000**.
3. Chapin, D. M.; Fuller, C. S.; and Pearson, G. L. J. Appl. P. **1954**, 25, 676 -
677.
4. Green, M.; Emery, K.; Hishikawa, Y.; Warta, W. Prog. Photovolt. **2009**,
17, 85 - 94.
5. Queisser, H.J.; Shockley, W.J. Appl. Phys. **1961**, 32, 510 - 519.
6. Rogers, J.A.; Bao, Z. J. POLYM. SCI. PART A: POLYM. CHEM. **2002**,
40, 3327 - 3334
7. Brabec, C.J. Sol. Ener. Mat. Sol. Cells. **2004**, 83, 273 - 292
8. O'Regan, B.; Gratzel, M. Nature, **1991**, 353, 737 - 740
9. Riede, M.; Mueller, T.; Tress, W.; Schueppel, R.; Leo, K.
Nanotechnology, **2008**, 19, 424001
10. Coffey, D.C.; Reid, O.G.; Rodovsky, D.B.; Bartholomew, G.P.; Ginger,
D.S. Nano Lett. **2007**, 7, 738 - 744

11. Huynh, W.U.; Dittmer, J.J.; Alivisatos, A.P. *Science*. **2002**, *295*, 2425 - 2427
12. National Renewable Energy Laboratory (NREL), MS ExcelTM spreadsheet file downloaded from <http://rredc.nrel.gov/solar/spectra/am1.5/S>.
13. Bundgaard, E.; Krebs, F.C. *So. Ener. Mat. Sol. Cells*. **2007**, *91*, 954
14. Savenije, T.J.; Warmn, J.M.; Goossens, A. *Chem. Phys. Lett.* **1998**, *287*, 148 - 153
15. Halls, J.J.M.; Pichler, K.; Friend, R.H.; Moratti, S.C.; Holmes, A.B. *Synth. Met.* **1996**, *77*, 277 - 280
16. Yan, H.; Chen, Z.; Zheng, Y.; Newman, C.; Quinn, J.R.; Dotz, F.; Kastler, M.; Facchetti, A. *Nature*. **2009**, *457*, 679 - 687
17. Sirringhaus, H.; Tessler, N.; Friend, R.H. *Science*. 1998, *280*, 1741 - 1744
18. Gregg, B.A.; Hanna, M.C. *J. Apply. Phys.* **2003**, *93*, 3605 - 3616
19. Brabec, C.J.; Cravino, A.; Meissner, D.; Sariciftci, S.; Fromherz, T.; Rispen, M.T.; Sanchez, L.; Hummelen, J.C. *Adv. Funct. Mater.* **2001**, *11*, 374 - 380
20. Scharber, M.C.; Muhlbacher, D.; Koppe, M.; Denk, P.; Waldauf, C.; Heeger, A.J.; Brabec, C.J. *Adv. Mater.* **2006**, *18*, 789 - 794
21. Frohne, H.; Shaheen, S.E.; Brabec, C.J.; Muller, D.C.; Sariciftci, N.S.; Meerholz, K. *Chem. Phys. Chem.* **2002**, *9*, 795 - 799

22. Po, R.; Maggini, M.; Camaioni, N. *J. Phys. Chem. C*. **2010**, *114*, 695 - 706
23. Skotheim, T.A.; Elsenbaumer, R.L.; Reynolds, J.R. *Handbook of Conducting Polymers*; Marcel Dekker Inc., New York, New York, **1998**.
24. Fichou, D. *J. Mat. Chem.* **2000**, *10*, 571 - 588
25. Sirringhaus, H.; Brown, P.J.; Friend, R.H.; Nielsen, M.M.; Bechgaard, K.; Langeveld-Voss, B.M.W.; Spiering, A.J.H.; Janssen, R.A.J.; Meijer, E.W.; Herwig, P.; de Leeuw, D.M. *Nature*. **1999**, *401*, 685 - 688
26. Geens, W.; Martens, T.; Poortmans, J.; Aernouts, T.; Manca, J.; Lutsen, L.; Heremans, P.; Borghs, S.; Mertens, R.; Vanderzande, D. *Thin Solid Films*. **2004**, *451-452*, 498 - 502
27. Greenham, N.C.; Peng, X.; Alivisatos, A.P. *Phys. Rev. B*. **1996**, *54*, 17629 - 17637
28. Maria, A.; Cyr, P.W.; Klem, E.J.D.; Levina, L.; Sargent, E.H. *Appl. Phys. Lett.* **2005**, *87*, 213112
29. Cheng, Y.J.; Yang, S.H.; Hsu, C.S. *Chem. Rev.* **2009**, *109*, 5868 - 5923
30. Rossetti, R.; Nakahara, S.; Brus, L.E. *J. Chem. Phys.* **1983**, *79*, 1086 - 1088
31. Brus, L.E. *J. Chem. Phys.* **1983**, *79*, 5566 - 5571
32. Brus, L.E. *J. Chem. Phys.* **1984**, *80*, 4403 - 4409
33. Efros, A.L.; Efros, A.L. *Sov. Phys. Tech. Semicond.* **1982**, *16*, 1209–1214
34. Murray, C.B.; Norris, D.J.; Bawendi, M.G. *J. Am. Chem. Soc.* **1993**, *115*, 8706 - 8715

35. Peng, X.; Manna, L.; Yang, W.; Wickham, J.; Scher, E.; Kadavanich, A.; Alivisatos, A.P. *Nature*. **2000**, *404*, 59 - 61
36. Jun, Y.W.; Lee, S.M.; Kang, N.J.; Cheon, J. J. *Am. Chem. Soc.* **2001**, *123*, 5150 - 5151
37. Manna, L.; Milliron, D.J.; Meisel, A.; Scher, E.C.; Alivisatos, A.P. *Nature*. **2003**, *2*, 382 - 385
38. Shieh, F.; Saunders, A.E.; Korgel, B.A. *J. Phys. Chem. B*. **2005**, *109*, 8538 - 8542
39. Asokan, S.; Krueger, K.M.; Colvin, V.L.; Wong, M.S. *Small*. **2007**, *3*, 1164 - 1169
40. Manna, L.; Scher, E.C.; Alivisatos, A.P. *J. Am. Chem. Soc.* **2000**, *122*, 12700 - 12706
41. Kanaras, A.G.; Sonnichsen, C.; Liu, H.; Alivisatos, A.P. *Nano Lett.* **2005**, *5*, 2164 - 2167
42. Peng, Z.A.; Peng, X. *J. Am. Chem Soc.* **2001**, *123*, 183 - 184
43. Qu, L.; Peng, A.; Peng, X. *Nano Lett.* **2001**, *1*, 333 - 337
44. Liu, H.; Owen, J.S.; Alivisatos, A.P. *J. Am. Chem Soc.* **2007**, *129*, 305 - 312
45. Peng, X.; Wickham, J.; Alivisatos, A.P. *J. Am. Chem Soc.* **1998**, *120*, 5343 - 5344

46. Peng, Z.A.; Peng, X. J. Am. Chem. Soc. **2001**, *123*, 1389 - 1395
47. Qu, L.; Yu, W.W.; Peng, X. Nano Lett. **2004**, *4*, 465 - 469
48. Peng, Z.A.; Peng, X. J. Am. Chem. Soc. **2002**, *124*, 3343 - 3353
49. Bullen, C.R.; Mulvaney, P. Nano. Lett. **2004**, *4*, 2303 - 2307
50. Murray, C.B.; Kagan, C.R.; Bawendi, M.G. Annu. Rev. Mater. Sci. **2000**, *30*, 545 - 610
51. Sugimoto, T. Adv. Coll. Inter. Sci. **1987**, *28*, 65 - 108
52. Markov, I.V. Crystal Growth for Beginners: Fundamentals of Nucleation, Crystal Growth and Epitaxy; World Scientific, Singapore, **2004**.
53. Chen, M.; Xie, Y.; Lu, J.; Xiong, Y.; Zh Y.; Liu, X. J. Mater. Chem. **2002**, *12*, 748 - 753
54. Jun, Y.W.; Jung, Y.Y.; Cheon, J. J. Am. Chem. Soc. **2002**, *124*, 615 - 619
55. Dai, Y.; Zhang, Y.; Li, Q.K.; Nan, C.W. Chem. Phys. Lett. **2002**, *358*, 83 - 86
56. Kuo, C.H.; Chang, S.J.; Chen, S.C. J. Cryst. Growth. **2005**, *285*, 295 - 299
57. Osada, T.; Kugler, T.; Broms, P.; Salaneck, W.R. Synth. Met. **1998**, *96*, 77 - 80
58. You, Z.Z.; Dong, J.Y. Vacuum. **2007**, *81*, 819 - 825
59. Sharma, A.; Haldi, A.; Potscavage, W.J.; Hotchkiss, P.J.; Marder, S.R.; Kippelen, B. J. Mater. Chem. **2009**, *19*, 5298 - 5302
60. Ross, R.B.; Cardona, C.M.; Swain, F.B.; Guldi, D.M.; Sankaranarayanan, S.G.; Van Keuren, E.; Holloway, B.C.; Drees, M. Adv. Funct. Mater. **2009**, *19*, 2332

61. McClure, S.A.; Worfolk, B.J.; Rider, D.A.; Tucker, R.T.; Fordyce, J.A.M.; Fleischauer, M.D.; Harris, K.D.; Brett, M.J.; Buriak, J.M. ACS Appl. Mater. Interf. **2010**, *2*, 219 - 229
62. Yang, F.; Shtein, M.; Forrest, S.R. Nature Mat. **2005**, *4*, 37 - 41
63. Seemann, A.; Egelhaaf, H.J.; Brabec, C.J.; Hauch, J.A. Org. Elect. **2009**, *10*, 1424 - 1428
64. Hoth, C.N.; Choulis, S.A.; Schilinsky, P.; Brabec, C.J. Adv. Mater. **2007**, *19*, 3973 - 3978
65. Unger, E.L.; Ripaud, E.; Leriche, P.; Cravino, A.; Roncali, J.; Johansson, E.M.J.; Hagfeldt, A.; Boschloo, G. J. Phys. Chem. C. **2010**, *114*, 11659 - 11664
66. Park, S.H.; Roy, A.; Beaupre, S.; Cho, S.; Coates, N.; Moon, J.S.; Moses, D.; Leclerc, M.; Lee, K.; Heeger, A.J. Nature Photonics. **2009**, *3*, 297 - 303
67. Blom, P.W.M.; Mihailetschi, V.D.; Koster, L.J.A.; Markov, D.E. Adv. Mater. **2007**, *19*, 1551 - 1566
68. Arango, A.C.; Johnson, L.R.; Bliznyuk, V.N.; Schlesinger, Z.; Carter, S.A.; Horhold, H. Adv. Mater. **2000**, *12*, 1689 - 1692
69. Sloof, L.H.; Wienk, M.M.; Kroon, J.M. Thin Solid Films. **2004**, *451-452*, 634 - 638

70. Ravirajan, P.; Haque, S.A.; Poplavskyy, D.; Durrant, J.R.; Bradley, D.D.C.; Nelson, J. *Thin Solid Films*. **2004**, *451* - 452, 624 - 629
71. Kwong, C.Y.; Choy, W.C.H.; Djuricic, A.B.; Chui, P.C.; Cheng, K.W.; Chan, W.K. *Nanotechnology*. **2004**, *15*, 1156 - 1161
72. Gratzel, M. J. *Photochem. Photobio. C Photochem. Rev.* **2003**, *4*, 145 - 153
73. Greenham, N.C.; Peng, X.; Alivisatos, A.P. *Phys. Rev. B*. **1996**, *54*, 17628 - 17637
74. Huang, J.; Ho, Z.; Kekuda, D.; Chang, Y.; Chu, C.; Ho, K. *Nanotechnology*. **2009**, *20*, 025202
75. Ginger, D.S.; Greenham, N.C. *Phys. Rev. B*. **1998**, *59*, 10623 - 10629
76. Huynh, W.U.; Peng, X.; Alivisatos, A.P. *Adv Mater.* **1999**, *11*, 923 - 927
77. Joung, M.J.; Kim, C.A.; Kang, S.Y.; Baek, K.H.; Kim, G.H.; Ahn, S.D.; You, I.K.; Ahn, J.H.; Suh, K.S. *Synthetic Metals*. **2005**, *149*, 73 - 77
78. Sun, B.; Marx, E.; Greenham, N.C. *Nano Lett.* **2003**, *3*, 961 - 963
79. Gur, I.; Fromer, N.A.; Chen, C.P.; Kanaras, A.G.; Alivisatos, A.P. *Nano Lett.* **2007**, *7*, 409 - 414
80. Liu, J.; Tanaka, T.; Sivula, K.; Alivisatos, A.P.; Frechet, M.J. *J. Am. Chem. Soc.* **2004**, *126*, 6550 - 6551
81. McCumiskey, E.J.; Chandrasekhar, N.; Taylor, C.R. *Nanotechnology*. **2010**, *21*, 225703

82. Wu, Y.; Zhang, G. *Nano. Lett.* **2010**, *10*, 1628 – 1631
83. Huynh, W.U.; Dittmer, J.J.; Libby, W.C.; Whiting, G.L.; Alivisatos, A.P.
Adv. Funct. Mater. **2003**, *13*, 73 - 79
84. Sharma, S.N.; Kumar, U.; Vats, T.; Arora, M.; Singh, V.N.; Mehta, B.R.;
Jain, K.; Kakkar, R.; Narula, A.K. *Eur. Phys. J. Apply. Phys.* **2010**, *50*,
20602
85. Sun, B.; Snaith, H.J.; Dhoot, A.S.; Westenhoff, S.; Greenham, N.C. J.
Apply. Phys. **2005**, *97*, 014914
86. Sun, B.; Greenham, N.C. *Phys. Chem. Chem. Phys.* **2006**, *8*, 3557 - 3560
87. Seo, J.; Kim, W.J.; Kim, S.J.; Lee, K.; Cartwright, A.N.; Prasad, P.N.
Appl. Phys. Lett. **2009**, *94*, 133302
88. Zhou, Y.; Riehle, F.S.; Yuan, Y.; Schleiemacher, H.F.; Niggeman, M.;
Urban, G.A.; Kruger, M. *Appl. Phys. Lett.* **2010**, *96*, 013304
89. Huxter, V.M.; Scholes, G.D. *J. Nanophot.* **2009**, *3*, 032504
90. Zhang, Q.; Russel, T.P.; Emrick, T. *Chem. Mater.* **2007**, *19*, 3712 - 3716
91. Green, M.A.; Emery, K.; Hishikawa, Y.; Warta, W. *Prog. Photovolt: Res.*
Appl. **2009**, *17*, 85 – 94
92. Shockley, W.; Queisser, H.J. *J. Appl. Phys.* **1960**, *32*, 510 - 519
93. Ross, R.T.; Nozik, A.J. *J. Appl. Phys.* **1962**, *53*, 3813 - 3818
94. Beard, M.C.; Ellingson, R.J. *Laser Phot. Rev.* **2008**, *2*, 377 - 399
95. Nozik, A.J. *Annu. Rev. Phys. Chem.* **2001**, *52*, 193 - 231
96. Nozik, A.J. *Physica E* **2002**, *14*, 115 - 120

97. Koole, R.; Allan, G.; Delerue, C.; Meijerink, A.; Vanmaekelbergh, D.; Houtepen, A.J. *Small* **2008**, *4*, 127 - 133
98. Schaller, R.D.; Sykora, M.; Pietryga, J.M.; Klimov, V.I. *Nano Lett.* **2006**, *6*, 424 - 429
99. Klimov, V.I. *J. Phys. Chem. B* **2006**, *110*, 16827 - 16845
100. Hanna, M.C.; Nozik, A.J. *J. Appl. Phys.* **2006**, *100*, 074510
101. Kim, S.J.; Kim, W.J.; Sahoo, Y.; Cartwright, A.N.; Prasad, P.N. *Appl. Phys. Lett.* **2008**, *92*, 031107
102. Schaller, R.D.; Agranovich, V.M.; Klimov, V.I. *Nature Physics* **2005**, *1*, 189 - 194
103. Ellingson, R.J.; Beard, M.C.; Johnson, J.C.; Yu, P.; Micic, O.I.; Nozik, A.J.; Shabaev, A.; Efros, A.L. *Nano Lett.* **2005**, *5*, 865 - 871
104. Franceschetti, A.; An, J.M.; Zunger, A. *Nano Lett.* **2006**, *6*, 2191 - 2195
105. Schaller, R.D.; Klimov, V.I. *Phys. Rev. Lett.* **2004**, *92*, 186601
106. Schaller, R.D.; Sykora, M.; Jeong, S.; Klimov, V.I. *J. Phys. Chem. B* **2006**, *110*, 25332 - 25338
107. Murphey, J.E.; Beard, M.C.; Norman, A.G.; Ahrenkiel, P.; Johnson, J.C.; Yu, P.; Micic, O.I.; Ellingson, R.J.; Nozik, A.J. *J. Am. Chem. Soc.* **2006**, *128*, 3241 - 3247

108. Pijpers, J.J.H.; Hendry, E.; Milder, M.T.W.; Fanciulli, R.; Savolainen, J.; Herek, J.L.; Vanmaekelbergh, D.; Ruhman, S.; Mocatta, D.; Oron, D.; Aharoni, A.; Banin, U.; Bonn, M. J. Phys. Chem. C **2007**, *111*, 4146 - 4152
109. Luther, J.M.; Beard, M.C.; Song, Q.; Law, M.; Ellingson, R.J.; Nozik, A.J. Nano Lett. **2007**, *7*, 1779 - 1784
110. Murphy, J.E.; Beard, M.C.; Nozik, A.J. J. Phys. Chem. B **2006**, *110*, 25455 - 25461
111. Wehrenberg, B.L.; Yu, D.; Ma, J.; Guyot-Sionnest, P. J. Phys. Chem. B **2005**, *109*, 20192 - 20199
112. Wehrenberg, B.L.; Guyot-Sionnest, P.; J. Am. Chem. Soc. **2003**, *125*, 7806 - 7807
113. Talapin, D.V.; Murray, C.B. Science, **2005**, *310*, 86 - 89
114. Tisdale, W.A.; Williams, K.J.; Timp, B.A.; Norris, D.J.; Aydil, E.S.; Zhu, X.Y. Science, **2010**, *328*, 1543 - 1547
115. Pandey, A.; Guyot-Sionnest, P.; Science **2008**, *322*, 929 - 932
116. Quantum Chemistry Textbook
117. Coropceanu, V.; Cornil, J.; da Silva Filho, D.A.; Olivier, Y.; Silbey, R.; Bredas, J. Chem. Rev. **2007**, *107*, 926 - 952
118. Blom, P. W. M.; deJong, M. J. M.; vanMunster, M. G. Phys. Rev. B **1997**, *55*, R656

119. Sirringhaus, H. *Adv. Mater.* **2005**, *17*, 2411
120. Horowitz, G.; Hajlaoui, M. E. *Adv. Mater.* **2000**, *12*, 1046
121. Karl, N.; Kraft, K. H.; Marktanner, J.; Munch, M.; Schatz, F.; Stehle, R.; Uhde, H. M. *J. Vac. Sci. Technol., A* **1999**, *17*, 2318
122. Pope, M.; Swenberg, C. E.; Pope, M. *Electronic Processes in Organic Crystals and Polymers*, 2nd ed.; Oxford University Press: New York, **1999**.
123. Silinsh, E.; Čápek, V. *Organic Molecular Crystals: Interaction, Localization, and Transport Phenomena*; American Institute of Physics: New York, **1994**.
124. Newton, M.D. *Chem. Rev.* **1991**, *91*, 767 - 792
125. Marcus, R.A. *Rev. Mod. Phys.* **1993**, *65*, 599 - 610
126. Creutz, C.; Newton, M.D.; Sutin, N. *J. Photochem. Photobiol. A: Chem.* **1994**, *82*, 47 - 59
127. Hush, N.S. *Coord. Chem. Rev.* **1985**, *64*, 135 - 157
128. Barbara, P.F.; Meyer, T.J.; Ratner, M.A. *J. Phys. Chem.* **1996**, *100*, 13148 - 13168
129. Lemaire, V.; da Silva Filho, D.A.; Coropceanu, V.; Lehmann, M.; Geerts, Y.; Pirls, J.; Debije, M.G.; van de Craats, A.M.; Senthilkumar, K.; Siebbeles, D.A.; Warman, J.M.; Bredas, J.; Cornil, J. *J. Am. Chem. Soc.* **2004**, *126*, 3271 - 3279

130. Hutchison, G.R.; Ratner, M.A.; Marks, T.J. *J. Am. Chem. Soc.* **2005**, *127*, 16866 - 16881
131. Kwon, O.; Coropceanu, V.; Gruhn, N.E.; Durivage, J.C.; Laquindanum, J.G.; Katz, H.E.; Cornil, J.; Bredas, J.L. *J. Chem. Phys.* **2004**, *120*, 8186 - 8194
132. Huang, J.; Kertesz, M. *Chem. Phys. Lett.* **2004**, *390*, 110 - 115
133. Cornil, J.; Calbert, J. P.; Bredas, J.L. *J. Am. Chem. Soc.* **2001**, *123*, 1250 - 1251
134. Cheng, Y.C.; Silbey, R.J.; da Silva Filho, D.A.; Calbert, J.P.; Cornil, J.; Bredas, J.L. *J. Chem. Phys.* **2003**, *118*, 3764 - 3774
135. da Silva Filho, D.A.; Kim, E.G.; Bredas, J.L. *Adv. Mater.* **2005**, *17*, 1072 - 1076
136. Blancafort, L.; Voityuk, A.A. *J. Phys. Chem. A* **2006**, *110*, 6426 - 6432
137. Bredas, J.L.; Calbert, J.P.; da Silva Filho, D.A.; Cornil, J. *PNAS*, **2002**, *99*, 5804 - 5809
138. Hu, Z.; Gesquiere, A.J. *Chem. Phys. Lett.* **2009**, *476*, 51 – 55
139. Lewis, N.S.; Nocera, D.G. *PNAS* **2006**, *103*, 15729 - 15735.
140. Rogach, A. *Semiconductor Nanocrystal Quantum Dots: Synthesis, Assembly, Spectroscopy and Applications*; SpringerWienNewYork, Austria, 2008.

141. Luan, W.; Yang, H.; Tu, S.T.; Wang, Z. *Nanotechnology* 2007 18, 175603.

Chapter 2

Electrostatic Layer-by-Layer Assembly of CdSe Nanorod/Polymer Thin Films

2.1. Introduction

In Chapter 1, a variety of methods and techniques used to synthesize photoactive nanoparticles and fabricate functional devices were discussed. In this chapter, the surface chemistry of CdSe nanorods is manipulated to produce water-soluble and charged species. These particles are then paired with anionic conducting polymers using electrostatic layer-by-layer (ELBL) assembly. The resulting thin films are fabricated with controlled thickness and a bulk heterojunction architecture; features critical to their implementation into functional devices. As a background to the relevant topics in this chapter, Chapter 2 Discussion begins with an introduction to the synthesis of water soluble nanoparticles and their incorporation into technologically relevant films using the ELBL assembly method. The experimental technique of photoluminescence spectroscopy will also be briefly introduced. [Chapter 2 was reproduced in part with permission from: McClure, S.A.; Worfolk, B.J.; Rider, D.A.; Tucker, R.T.; Fordyce, J.A.M.; Fleischauer, M.D.; Harris, K.D.; Brett, M.J.; Buriak, J.M. ACS Appl. Mater. Interf. 2010, 2, 219 – 229. Copyright © 2010 American Chemical Society]

Water-Soluble Nanoparticles

To fabricate ELBL thin films, the components must be water-soluble and bear an electrostatic charge. When the desired product is a photoactive layer for optoelectronics, the challenge goes beyond mere solution solubility. The components must retain their photoactive properties and have the ability to contribute to device operation. There are currently two methods for creating water-soluble nanoparticles. One method uses hydrophilic ligands to stabilize the nanoparticles during crystal growth.¹⁻⁴ Despite this *in situ* method being facile, shapes other than spherical dots remains a challenge although a few examples do exist.³ In the second method, the procedure involves a post synthesis protocol. Since the surface chemistry is not manipulated until after the original colloidal growth of the particles, a variety of morphologies can be made charged and water-soluble.⁵⁻⁸ Substitution of hydrophobic for hydrophilic ligands renders the particles miscible in a variety of hydrophilic solvents.^{4, 9, 10, 11}

Liu et al. used a multidentate polymer ligand along with ligand exchange to impart water-solubility to CdSe quantum dots.⁸⁵ The authors synthesized mercaptoethylamine grafted poly(acrylic acid) ligand (PAA-g-MEA), whose chelating ability allowed for increased stability relative to the monothiol ligand mercaptopropionic acid (MPA). The PAA-g-MEA capped particles were tested for stability by varying the ionic strength of the nanoparticle solutions using increasing concentrations of NaCl. Figure 2.1 shows the comparison between the PAA-g-MEA-capped quantum dots and the MPA-capped particles. As can be

seen from the absorption spectra of the PAA-g-MEA-capped quantum dots, the baselines remain horizontal with no absorption tail at longer wavelengths. Horizontal baselines indicate a lack of scattered light from colloidal dispersions normally associated with aggregated particles. In contrast, the MPA-capped particles show substantial scattering due to aggregation. PAA-g-MEA particles were stable throughout the entire ionic strength range. The solutions in this study were found to be stable (with no flocculation) for periods up to a month. Figure 2.1C shows the PL intensity remaining high following ligand exchange when the PAA-g-MEA ligands are used at a variety of ionic strengths. The preservation of physical properties following the ligand exchange process is essential for applications requiring the unique optical and electrical properties of the nanoparticles.

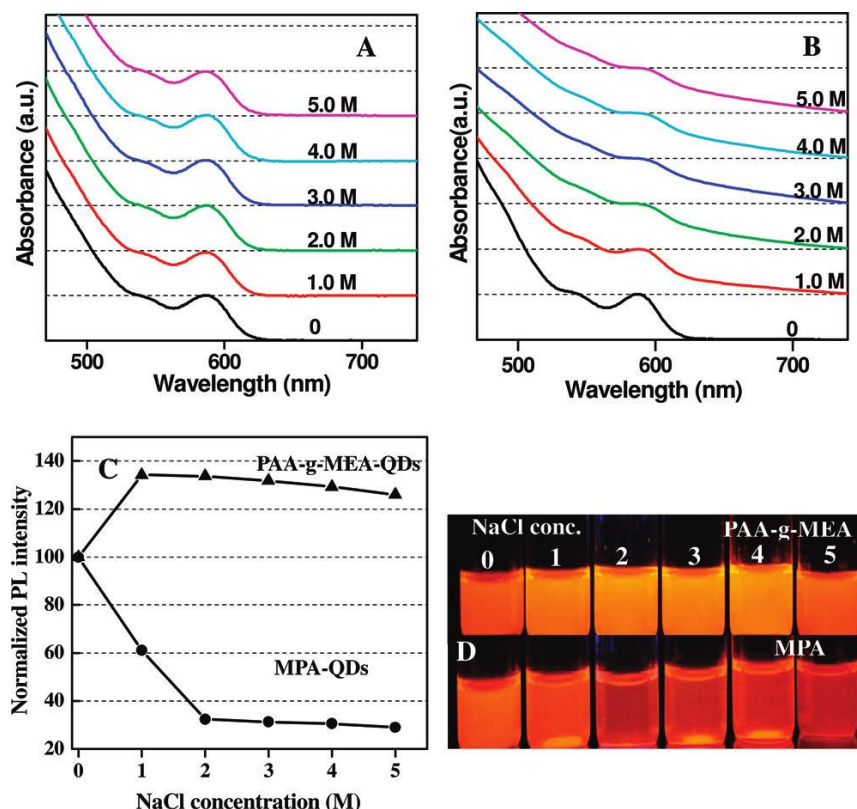


Figure 2.1. UV-vis spectra of PAA-g-MEA-QDs (A) and MPA-QDs (B) at various NaCl concentrations. (C) Normalized PL intensities of PAA-g-MEA-QDs (2) and MPA-QDs (b) under various NaCl concentrations. (D) Photographs of PAA-g-MEA-QDs (top) and MPA-QDs (bottom) under various concentrations of NaCl solutions. Reprinted with permission from ref. 85. Copyright © 2010 American Chemical Society.

Electrostatic Layer-by-Layer Assembly of Thin Films

Layer-by-Layer (LBL) assembly has proven to be a robust and facile method for fabricating multilayer thin films. Nanoscale control over film growth and incorporation of technologically relevant materials makes this approach attractive to thin film researchers.^{12 - 14} The process can take advantage of hydrogen bonding,¹⁵⁻¹⁷ van der Waals forces,¹⁸ covalent bonding,¹⁹⁻²¹ and

electrostatic interactions.^{22, 23} The latter is used in Electrostatic Layer-by-Layer (ELBL) assembly and involves the combination of anionic and cationic components in combination with a substrate of interest. It is a simple and low-cost method to fabricating multilayer thin films that are well-defined at the nanoscale.²⁴ The method has been used to produce films of polyelectrolytes,²⁵⁻²⁸ DNA,²⁹⁻³¹ proteins,^{32,33} viruses,³⁴ conducting polymers,^{26,35-37} and nanoparticles.³⁸⁻⁴² In terms of applications, light emitting diodes,²⁶ fuel cell membrane electrodes,⁴³ fast energy transfer nanocrystal bilayers,^{44 - 47} thin film diodes,⁴⁸ donor/acceptor tunnelling layers,⁴⁹ chemical as well as biological sensors,^{50 - 54} memory elements,^{55, 56} photodetectors,⁵⁷ and photovoltaics^{58, 59} have all been produced.

Figure 2.2 shows the process for fabricating ELBL thin films using solutions of polyelectrolyte as the source of positive and negative charge.⁶⁰ The substrate used must bear either a native or chemically modified charged layer. Glass, silicon and ITO are common substrates as they naturally bear a negative charge, although modifiers such as aminopropyltrimethoxysilane can be used to impart a more uniform charge layer on the surface. Repeated dipping causes the material to build up sequentially while wash solutions ensure that material non-selectively bound to the surface is removed, improving the quality of the overall film. The number of bilayers dictates the thickness of the film. Since the film is fabricated using nanoscale components, thickness is increased on the order of nanometres. This has important implications when using ELBL assembly for device fabrication (vide infra).

Using nanoparticles as the building blocks in ELBL assembly permits the fabrication of a variety of functional thin films. Nanoparticle films can be formed by pairing charged and water-soluble particles with a polymeric counter charge such as a polyelectrolyte. Repeated dipping between the nanocrystal and polyelectrolyte solutions allows for bilayers of densely packed nanoparticle films to form. Film growth is typically tracked using spectroscopic techniques such as UV-vis spectroscopy (see Figure 2.3). As each bilayer forms, the amount of absorbing material increases and a near-linear trend in absorbance is typically observed.⁶¹

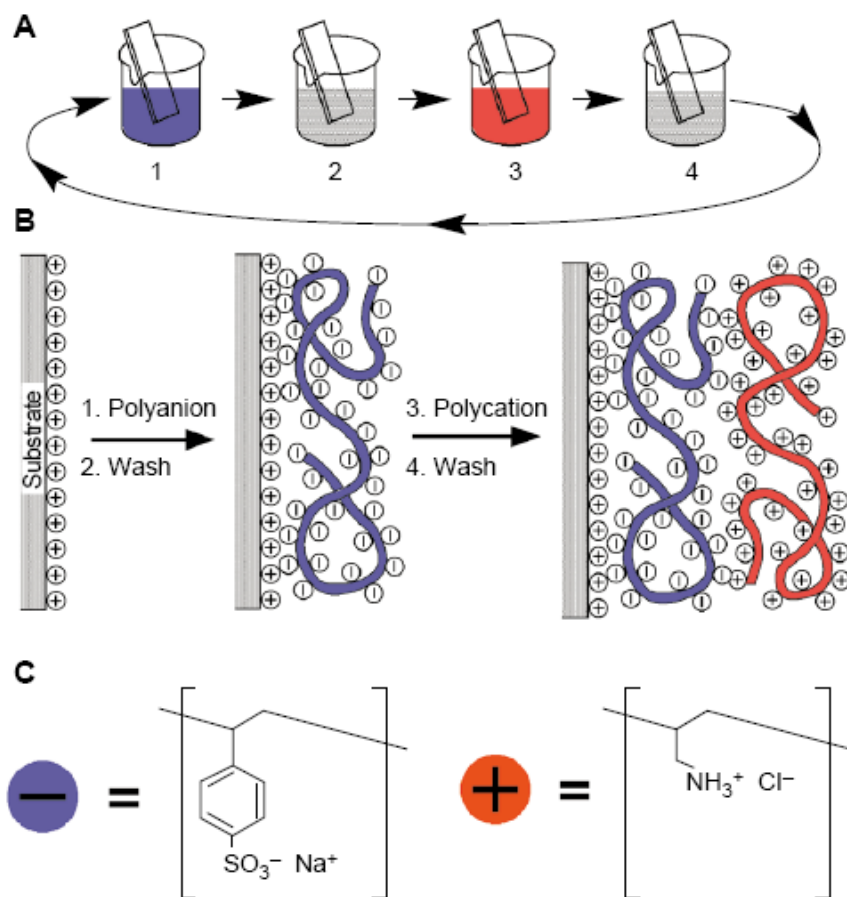


Figure 2.2. Electrostatic layer-by-layer assembly process for fabricating multilayer thin films. **A)** Steps 1 and 3 represent the adsorption of a polyanion and polycation, while steps 2 and 4 are the washing steps. **B)** Molecular picture for the first two adsorption steps. **C)** Chemical structure of the two polyanions. Reprinted with permission from ref. 60. Copyright © 1997 Science.

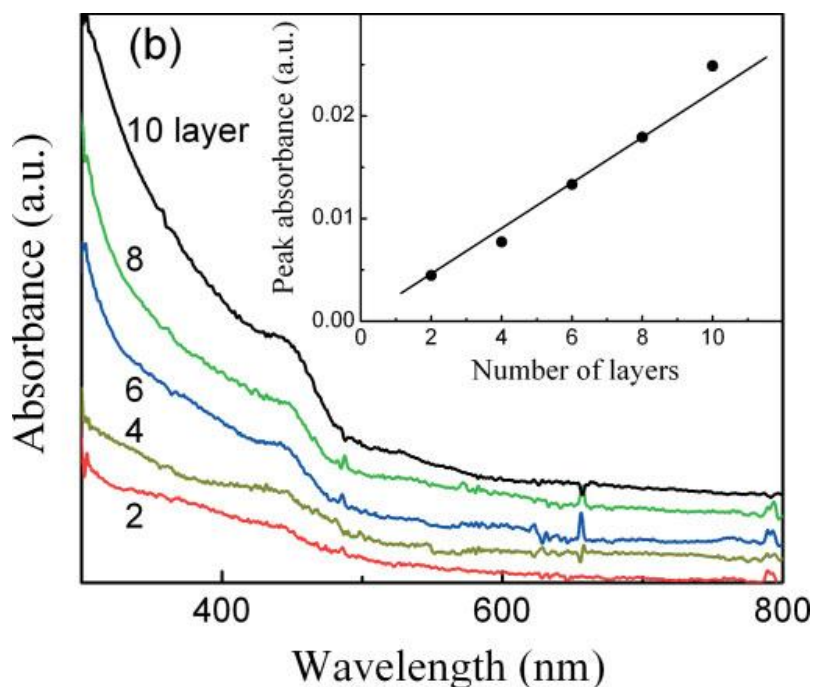


Figure 2.3. Absorption of CdSe nanoparticles with increasing bilayer number using the ELBL film growth process. Inset shows the absorbance measured at 439 nm as a function of the number of layers. Reprinted with permission from ref. 61. Copyright © 2007 Wiley.

Rogach et al. used the ELBL process to assemble thin films of thioglycolic acid (TGA) capped CdTe nanocrystals and poly(diallyldimethylammonium chloride) (PDDA) polyelectrolyte (see Figure 2.4).⁴⁷ Using glass as the substrate, densely packed films of CdTe were assembled which showed high PL quantum efficiencies. The authors fabricated a size grading such that the excitons funnelled by a stepwise passing of the excitation energy within the film. The close proximity of the nanocrystals allowed for exciton migration from the layer of smaller particles to the layer of larger particles in a so-called cascaded energy transfer process. This example shows how quantum confined semiconductor

nanoparticles can be incorporated into functional thin films using ELBL assembly.

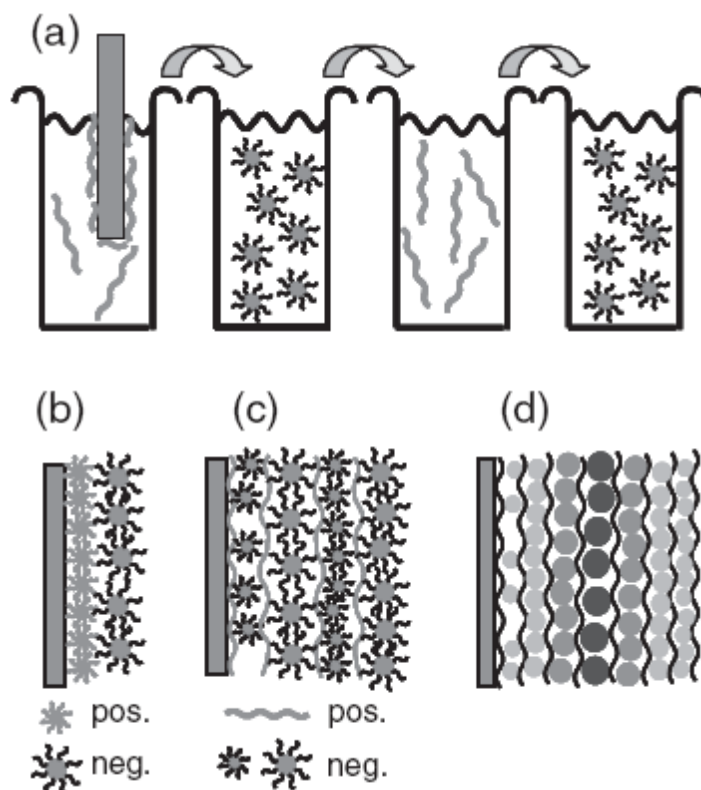


Figure 2.4. A) ELBL assembly of CdTe nanoparticles with PDDA polymer. Successive dipping leads to the formation of multilayer thin films. B) The first bilayer composed of CdTe nanoparticles and PDDA. C) Incorporation of various nanocrystal sizes to the thin film in order to create cascaded energy transfer layers. D) Fully assembled device with graded energy gaps. Reprinted with permission from ref. 47. Copyright © 2005 Wiley.

Photoluminescence Spectroscopy

A key experimental technique used to study the optical properties of photoactive molecules is photoluminescence spectroscopy (PL). In single beam experiments (as used in this thesis), light intensity is measured before and after a sample is inserted into the instrument (spectrophotometer). Using a monochromator with a diffraction grating produces the range of incident wavelengths used to irradiate the sample of interest. This results in discrete frequencies passing through the sample with the transmitted light intensity measured by a photodiode detector. The transmittance value for each wavelength is compared to the transmission through a reference sample resulting in a PL spectrum.

The following section discusses how the ELBL process can be used to build photoactive layers from semiconductor nanorods and conducting polymers. This will provide the PAL for integration into functional devices as shown in Chapter 3.

2.2 Results and Discussion

Water-Soluble CdSe Nanorods

Three organic-soluble nanorods (NRs) were synthesized according to a modified literature procedure and subsequently treated to a ligand exchange.^{62, 63} Figure 2.5 shows the basic protocol by which the original TOPO ligand was

replaced by the hydrophilic aminoethane thiol (AET) capping group (from the AET·HCL salt). The reasoning behind using AET as the ligand is twofold; it is hydrophilic, thus imparting water-solubility to the nanoparticle and is also a short-chain ligand which is a requirement for its use in CT systems.⁶⁴ The improvement in CT, resulting from the use of short-chain ligands, was discussed in the General Introduction section of this thesis. To confirm the success of the ligand exchange procedure, Fourier Transform Infrared (FTIR) spectroscopy was performed on a dried sample of the AET-capped CdSe NRs. Figure 2.6 shows the FTIR results highlighting the disappearance of the C-H and P=O stretching regions indicative of TOPO. Further confirmation is obtained through the ease at which the NRs dissolve in aqueous media. Figure 2.7A shows the optical images of the three NR samples in water forming stable solutions. All samples were stable for periods up to a month and remained optically clear with no sign of precipitation.

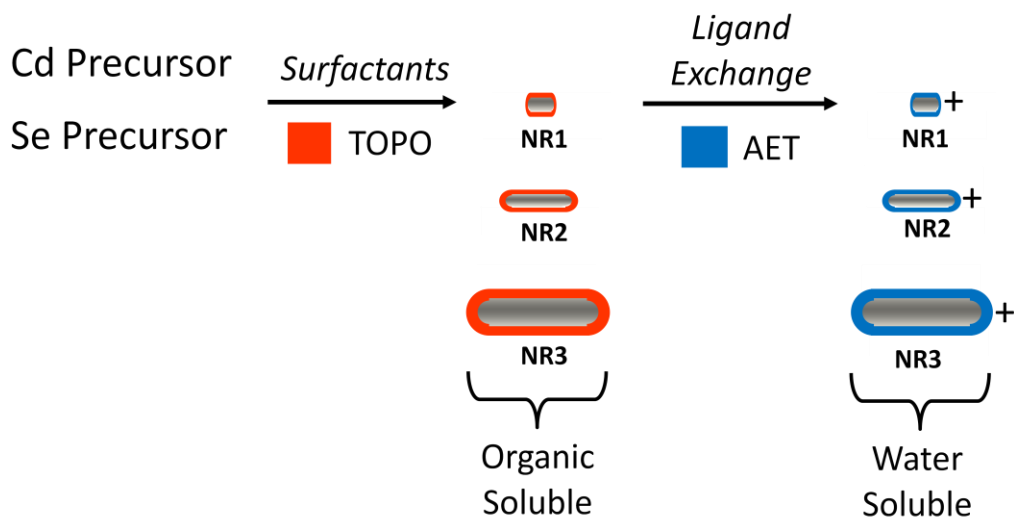


Figure 2.5. Basic protocol to forming NRs with three different aspect ratios and the subsequent ligand exchange procedure used to render the NRs water-soluble.

In order to investigate the size and morphology of the AET-stabilized NRs, TEM was performed on dried samples as shown in Figure 2.6B-D. The average length by diameter dimensions of the nanorods were 5.5×4.3 , 12.5×3.5 , and 31.0×7.3 nm for NR1, NR2 and NR3, respectively (50 particles were chosen in each respective SEM image to calculate the average aspect ratios). These give aspect ratios of 1.3, 3.6 and 4.2 for the three samples. The crystal planes of the wurtzite structure can be seen from high-resolution TEM (HR-TEM) analysis. Single crystal NRs have excellent charge transport characteristics due to their covalent bonding,⁶⁵ and are thus important for use in optoelectronics applications. The optical and electrical properties of the NR samples were investigated by UV-vis and PL spectroscopy and are presented in Figure 2.8.

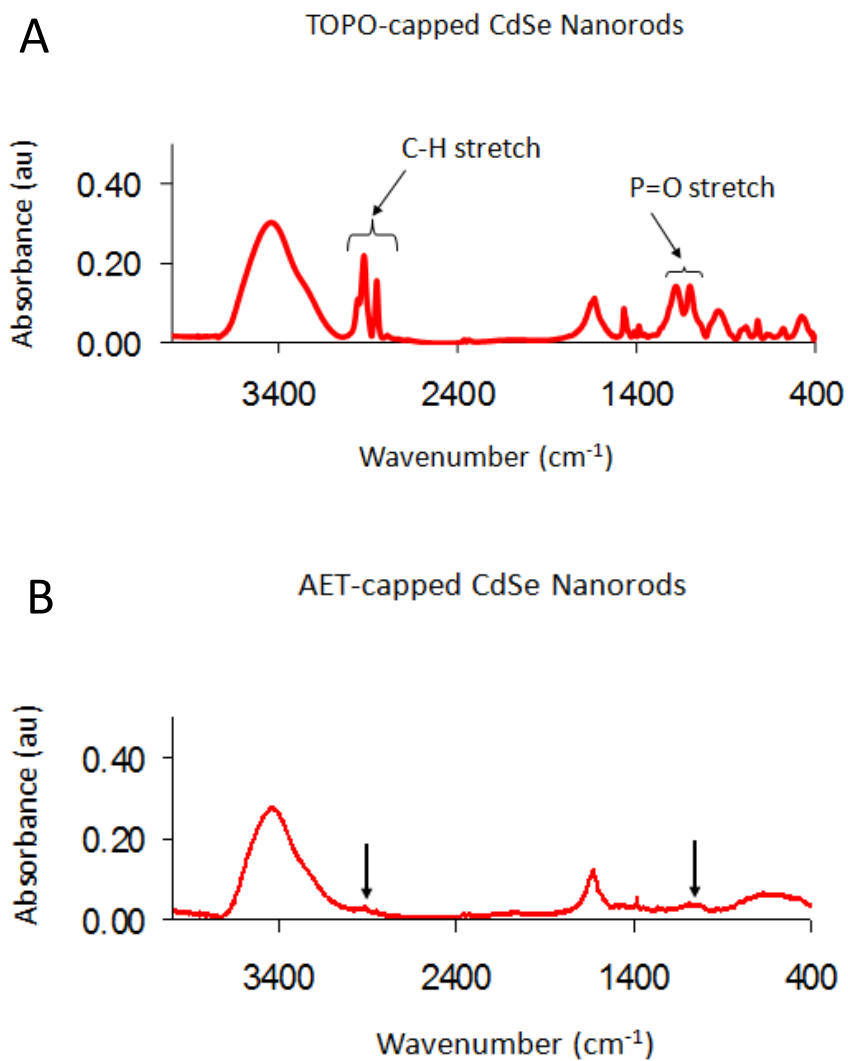


Figure 2.6. FTIR spectra of **A)** TOPO-capped CdSe nanorods and **B)** AET-capped CdSe nanorods. Decreases in the C-H and P=O stretching regions indicate the replacement of TOPO with AET.

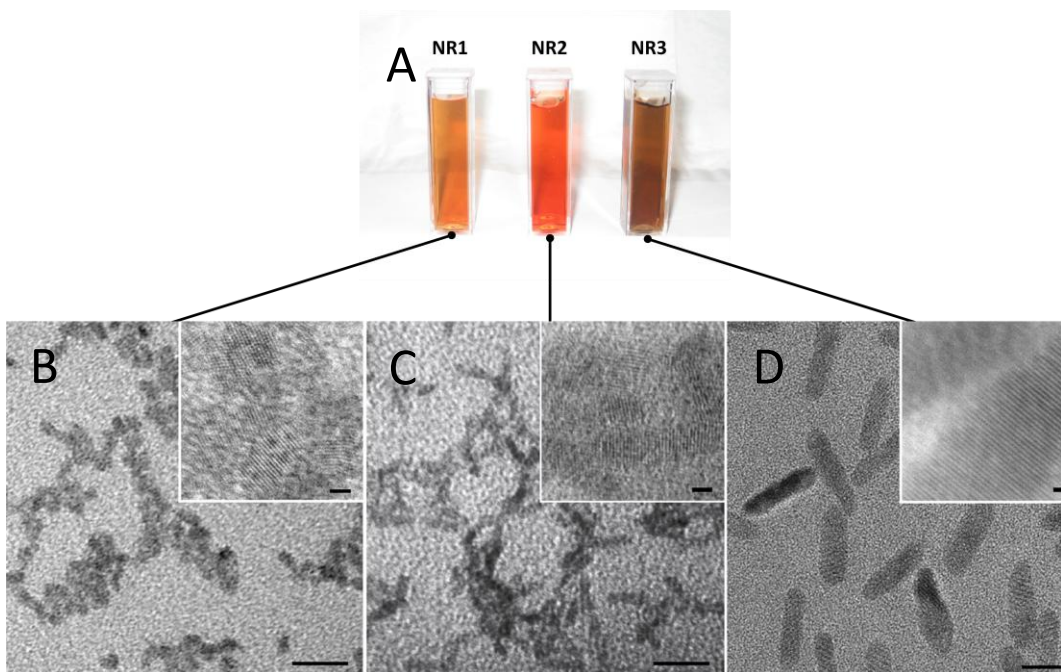


Figure 2.7. A) Optical image of stable AET-capped nanorod solutions made in this study and the TEM micrographs for samples B) NR1, C) NR2, and D) NR3. Insets show HR-TEM images of the three samples. The scale bars in B-D are 20 nm, whereas those in the insets are 2 nm.

Distinct excitonic peaks can be seen in the UV-vis spectra, indicating the quantum confined nature of the NRs.⁶⁶ The absorption is found to shift with the change in aspect ratio of the rod, typical of quantum confined systems. The trend differs from what might be expected for NRs of increasing aspect ratio. For instance, a red-shifted absorption relative to NR1 might be expected for NR2 due to its higher aspect ratio. Upon close inspection of the NR dimensions, however, it can be seen that NR2 has a smaller diameter, despite its longer length. Quantum confinement can be expected within the diameter as its dimensions are

on the order of the exciton Bohr radius of CdSe (5.7 nm).⁶⁷ The UV-vis spectra of both PTEBS and P3KHT polymers are shown in Figure 2.9. Both absorb in the visible region with PTEBS and P3HKT covering the spectrum up to 600 nm and 700 nm respectively.

At this point, it can be concluded that the components are appropriate for the ELBL assembly of photoactive materials. In order to assess their viability for use in hybrid solar cell devices, the electronic structure of the materials must be determined. This is the critical step in developing devices with the necessary CT interface. As discussed in the general introduction of this thesis, a requirement for CT is an energy level offset that must exist to drive the electron transfer necessary to create free charges. Cyclic voltammetry (CV) can be used to determine band edges and gaps in both semiconductor polymers and nanoparticles.^{68, 69} Table 2.1 shows the comparison between band gaps determined from UV-Vis spectroscopy and cyclic voltammetry. There is fairly close agreement between the two experimental methods suggesting the absorption onset can be used to probe the energy of the excitonic transition in both NRs and photoactive polymers.

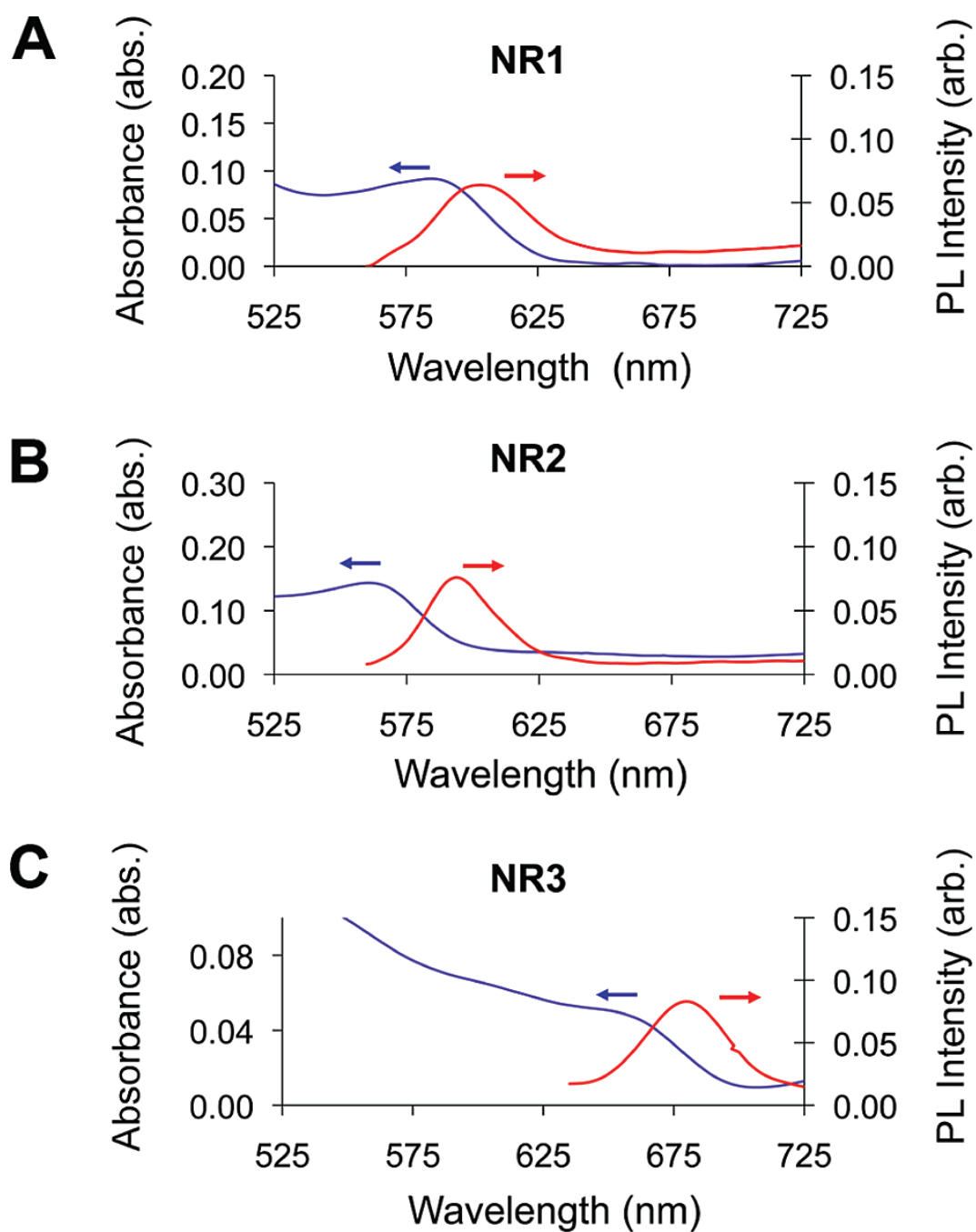


Figure 2.8. UV-vis and PL spectra for aqueous NR1, NR2, and NR3 (A-C, respectively). Excitation wavelength for emission spectra was 550 nm for NR1, 545 nm for NR2, and 620 nm for NR3.

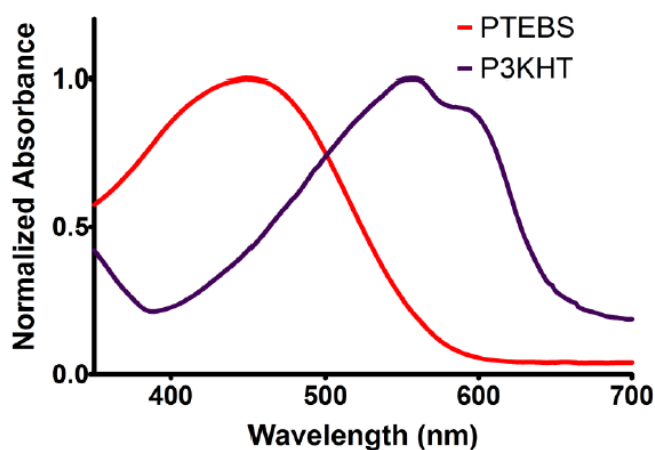


Figure 2.9. UV-vis spectra for PTEBS (red) and P3KHT (blue) polymer.

Figure 2.10 shows the band edges of the materials as determined by cyclic voltammetry. [Note the term “band edges” is more appropriate for NRs. In polymers, frontier molecular orbitals (HOMOs and LUMOs) are the appropriate term. For simplicity, however, band edges will be used for both NRs and polymers.] All nanorod samples gave conduction band edge values between -4.16 and -4.48 eV, while the valence band edges are between -6.16 and -6.25 eV. Band edges for PTEBS and P3KHT lie between 5.40 and 5.57 eV for the HOMO and 3.51 and 3.54 eV for the LUMO.

Table 2.1. Experimentally determined band gaps of the three NR samples and two photoactive polymers as determined by UV-vis

Material	E_g (eV)	E_g' (eV)
NR1	1.96	2.02
NR2	2.07	2.02
NR3	1.77	1.77
PTEBS	2.06	2.03
P3KHT	1.82	1.89

spectroscopy (E_g) and cyclic voltammetry (E_g').

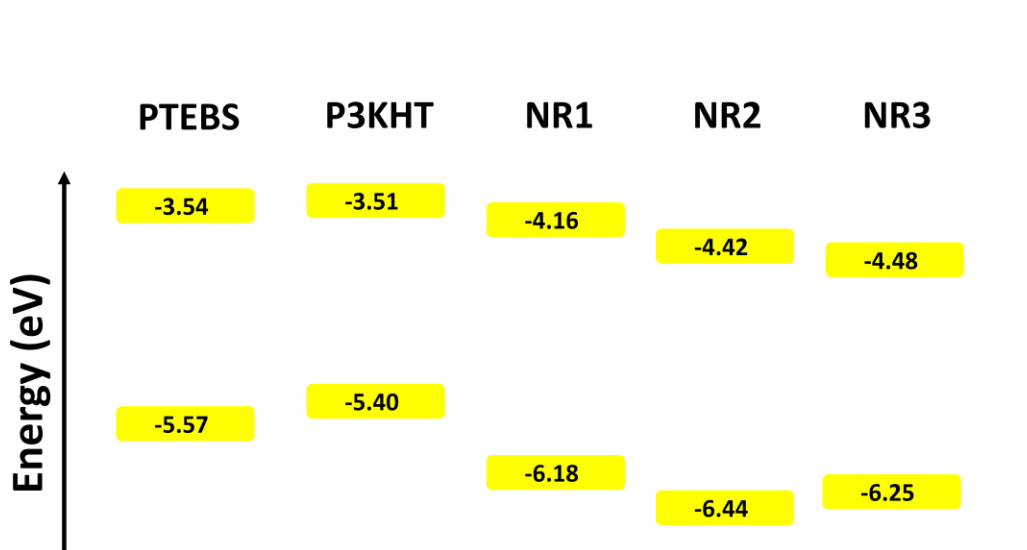


Figure 2.10. Electronic band edge structure of the three nanorods and two photoconducting polymers as determined by cyclic voltammetry. Values correspond to the energies in electron volts.

Electrostatic Layer-by-Layer Assembly of CdSe / Conducting Polymer Nanocomposite Thin Films

The construction of multilayer thin films via ELBL requires the components to be charged and water-soluble. The AET-capped NRs bear positive charge in aqueous media due to the protonation of the amine group in water. The AET-capped NRs can be paired with polymers that bear the opposite charge. Figure 2.11 shows the ELBL procedure using AET-capped NRs with anionic polymers. To investigate the growth of multilayer films composed of AET-capped NRs, NR samples were initially paired with the well-established polyelectrolyte (sodium 4-styrenesulfonate) (PSS). PSS has been used to form various LBL motifs for a variety of applications.^{60, 70, 71} Figure 2.12 depicts the optical characterization of the successive bilayer build-up on a glass substrate for PSS and CdSe NR2 components. The optical density of the film increases with bilayer number n . The characteristic excitonic peak of the embedded NRs occurs at approximately 580 nm, a value that closely matches that found in aqueous solution (see Figure 2.8). This feature can be used to track the growth of the (CdSe NR2/PSS) $_n$ film, as has been shown in previous studies of nanorod/polymer systems.^{72 - 76} As can be seen, successive layers lead to the expected increase in optical density. The results are summarized in Figure 2.15 with the absorbance plotted against bilayer number. The absorption trend is close to linear with slight deviations at the early stages of film growth. The photoactive polymers PTEBS and P3KHT are anionic and form stable solutions in water. They were also paired with the NR2 samples with the results shown in Figures

2.13 and 2.14 respectively. The increase in optical density with bilayer number for the $(\text{CdSe NR2/PTEBS})_n$ film is similar to that of PSS (see Figure 2.11). The $(\text{CdSe NR2/P3KHT})_n$ film growth is presented in Figure 2.13 and shows a stronger absorbance with bilayer number.

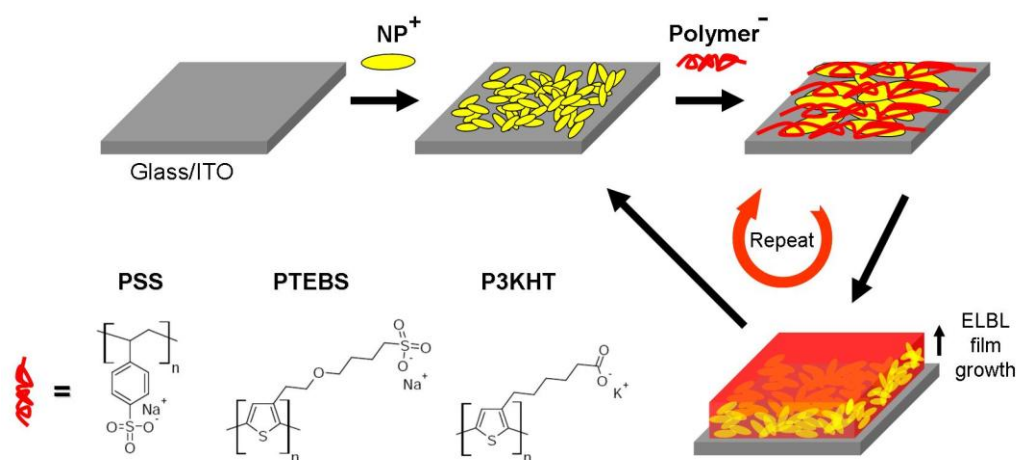


Figure 2.11. ELBL assembly of nanocomposite thin films composed of semiconductor NRs and polymer. Repeating the steps leads to controlled thickness on the nanometre scale.

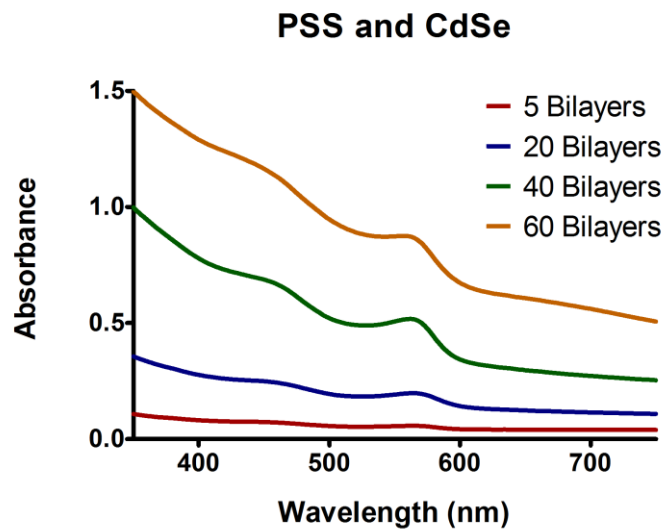


Figure 2.12. UV-vis experiment monitoring the absorbance of 5, 20, 40, and 60 bilayer films assembled using ELBL on glass with CdSe NR2 and PSS polyelectrolyte.

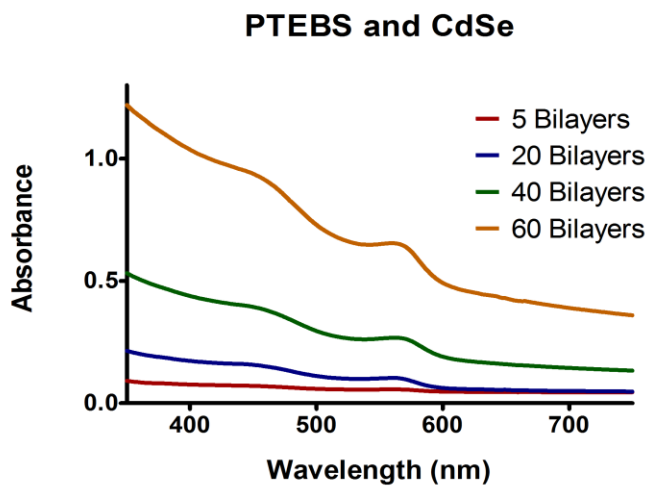


Figure 2.13. UV-vis experiment monitoring the absorbance of 5, 20, 40, and 60 bilayer films assembled using ELBL on glass with CdSe NR2 and PTEBS polyelectrolyte.

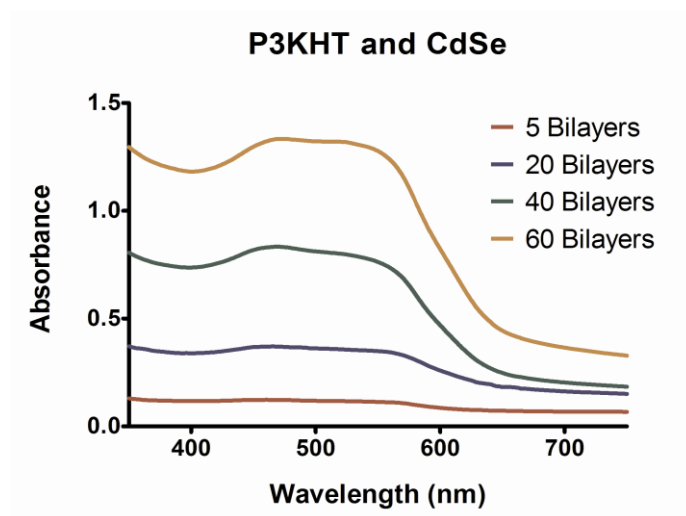


Figure 2.14. UV-vis experiment monitoring the absorbance of 5, 20, 40, and 60 bilayer films assembled using ELBL on glass with CdSe NR2 and P3KHT polyelectrolyte.

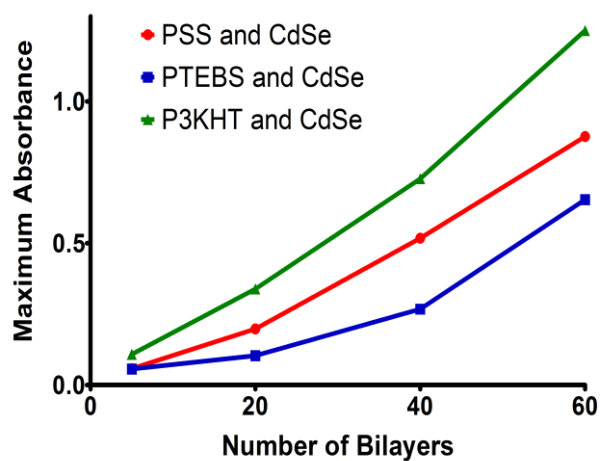


Figure 2.15. Summary of the maximum absorbance with increasing bilayer number.

To determine the surface roughness of the multilayer films, AFM analysis was performed for the $(\text{CdSe NR2/PSS})_n$ system with 0, 10, 20, 30, and 60 bilayers (see Figure 2.16). The dependence of RMS roughness on bilayer number is plotted in Figure 2.17. The increasing roughness with bilayer number suggests that the deviation from linearity in the optical density plots in Figure 2.15 was caused by increases in surface area. As the number of layers increase, more material is deposited to the film leading to larger changes in optical density as a higher number of bilayers is targeted. A similar trend was observed for the growth of the $(\text{CdSe NR2/PTEBS})_n$ film.

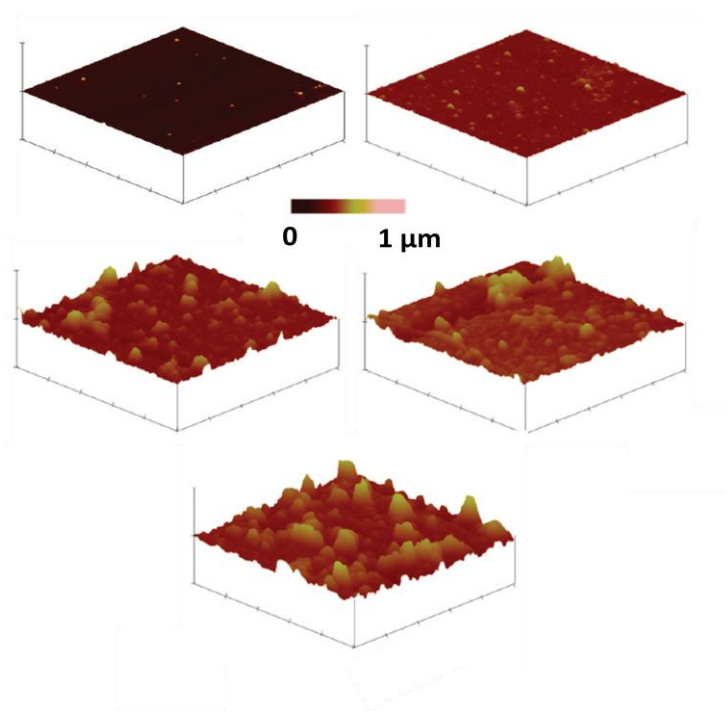


Figure 2.16. AFM study showing the surface of PSS and NR2 films assembled on glass using ELBL after **A)** 0 bilayers, **B)** 10 bilayers, **C)** 20 bilayers, **D)** 30 bilayers, and **E)** 60 bilayers.

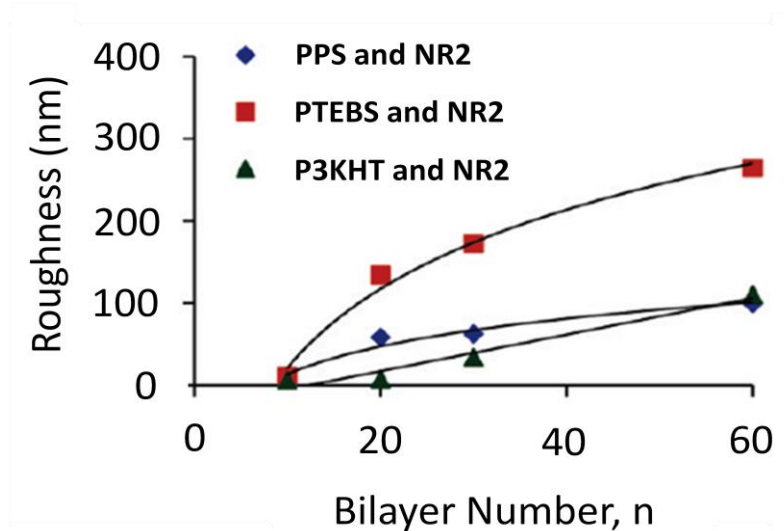


Figure 2.17. Roughness of films after 10, 20, 30, and 60 bilayers for PSS, PTEBS, and P3KHT and NR2 systems.

P3KHT contains carboxylic acid residues and the solution needed to be buffered to an alkaline pH of 9 in order to produce quality multilayer films. At pH values lower than 8, the polymer was found to precipitate from solution and the films delaminated from the substrate; possibly due to the low ionic charge of the polymer. Increasing the pH of the solution would result in a higher number of deprotonated polymer side-chains and hence an increase in the overall negative charge on the polymer. In addition, the disruption of hydrogen bonding in the P3KHT may be the mode for solution phase aggregation and hence precipitation.^{77, 78} Using these experimental conditions, (CdSe NR2/P3KHT)_n films could be reproducibly constructed. The optical characterization is shown in 2.14 along with the trend in film growth in 2.15. As with the other systems, an increase in the optical density with bilayer number is observed.

To further investigate the thin films, multilayers were fabricated on glass and characterized in cross-section using SEM. Figure 2.18 shows the tilted, cross-sectional SEM images of the (CdSe NR/PSS)_n films with 10, 30 and 60 bilayers. From these images it can be seen that the thickness of the composite films can be controlled on the nanoscale. As mentioned in the introduction of the thesis, typical photoactive layers range from 150 – 200 nm. A trade-off exists between absorption and charge transport with thick films having high absorption and thin films having better transport to the electrodes. Control over the assembly of photoactive components is therefore critical if the films are to be implemented in device designs. The TEM analysis shows that the constructed films were continuous with an increase in thickness based on the bilayer number *n*. Films thicknesses measure approximately 33, 80 and 140 nm for *n*=10, 30 and 60 respectively in the (CdSe NR/PSS)_n film. Using these thickness values, each bilayer is approximately 2-3 nm thick. Interestingly, the smallest NR dimension is 3 nm in width. Discrepancies between the average bilayer thickness and the NR dimensions can be rationalized by assuming interpenetrating components throughout the film. Therefore, a bilayer does not correspond to a distinct two-layer system with abrupt interfaces. These thicknesses are rough averages as the ELBL films have fairly high rms roughness values (see Figure 2.17).

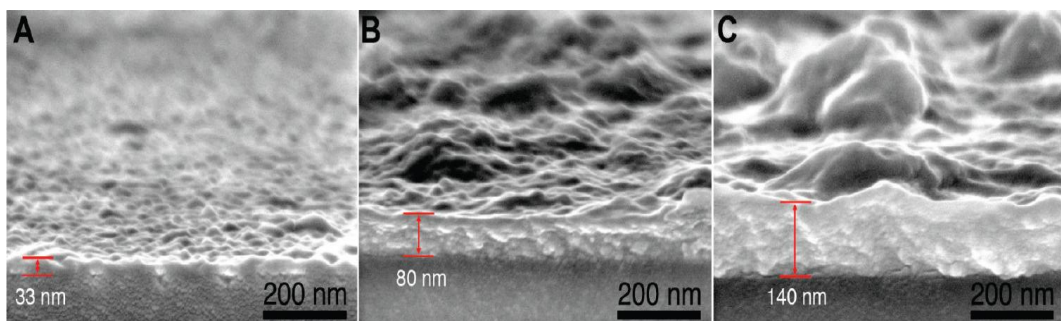


Figure 2.18. SEM cross-sections of (CdSe NR2/PSS) n multilayer nanocomposite thin films on glass with 10, 30, and 60 bilayers.

With the assembly of NRs and polyelectrolyte successfully demonstrated using the (CdSe NR/PSS) $_n$ system, the process was extended to polymers and substrates that have technological relevance for applications in optoelectronics. Polyethylenedioxythiophene polystyrene sulfonate (PEDOT:PSS) coated ITO, a commonly used transparent conducting electrode, also successfully functions as a platform onto which ELBL assembly can be performed. PEDOT:PSS is semiconductor polymer blend of cationic and conducting PEDOT, charge balanced with by anionic and insulating PSS. There is an overcompensation of negative charge due to excess PSS associated with the PEDOT (by London dispersion forces). This material has been widely employed as a hole-collecting interfacial layer at the ITO surface due to its stable and high work function and electron-blocking properties.⁷⁹ Conventional films of PEDOT:PSS spin coated onto ITO were found to dissolve during the ELBL assembly process. In order to overcome this limitation, electrochemically prepared PEDOT:PSS (ePEDOT:PSS) was incorporated into the thin film fabrication. ePEDOT:PSS has been shown to provide fully functional and water-insoluble films on ITO.⁸⁰

ELBL multilayer films, with an ePEDOT interfacial layer, were fabricated from CdSe nanorods and PTEBS polymer. The cross-sectional SEM images are shown in Figure 2.19 A and D. The two films consisted of (CdSe NR1/PTEBS)₆₀ and (CdSe NR2/PTEBS)₆₀ assemblies, and were 180 and 250 nm thick respectively. In both cases, the ePEDOT:PSS was 30 nm thick. In addition to the SEM analysis, TEM and HR-TEM images were acquired by embedding the nanocomposite films in epoxy and sectioning off thin slices. Figure 2.19 shows the TEM results with the CdSe NRs as darker domains embedded in the PTEBS matrix. Close inspection reveals the lattice planes of the NRs as shown in Figure 2.19C. The lines seen in Figure 2.18F are moiré fringes despite appearing as lattice planes.⁸¹ Both of these features confirm the presence of nanocrystalline CdSe throughout the bulk of the film. NRs appear to be approximately within 5 nm of one another. To further confirm the intimate mixing the NRs and photoactive polymer, a (CdSe NR/PTEBS)₆₀ film was fabricated on silicon and analyzed by scanning Auger microscopy (see Figure 2.20). This technique allows for elemental mapping in the cross-section of the film. There are fairly consistent levels of C, S, Cd and Se throughout the bulk. This characterization, in combination with the TEM analysis, points to the formation of a bulk heterojunction architecture^{82 - 84} in the ELBL assembled films of PTEBS and CdSe NRs (see section 1.6 in General Introduction).

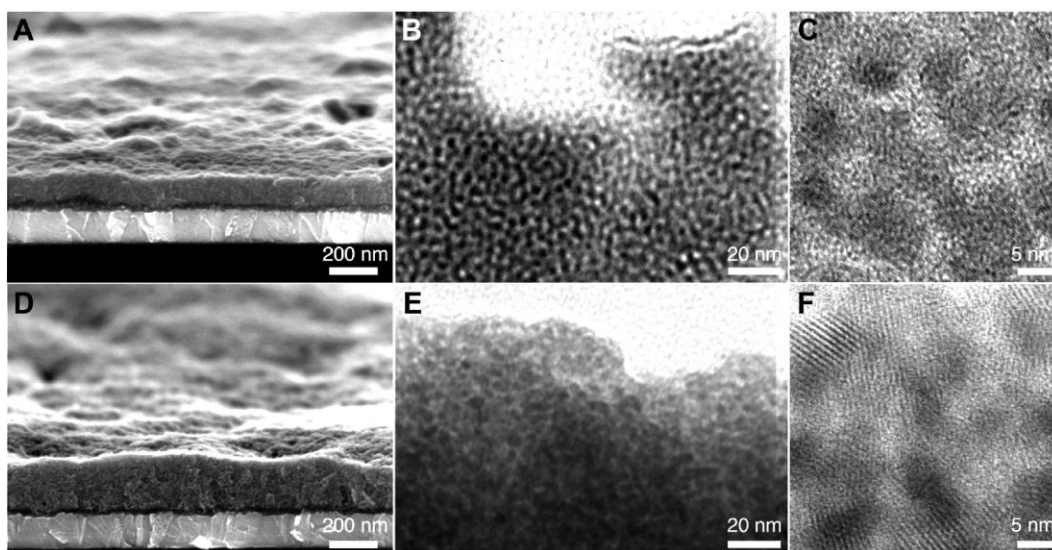


Figure 2.19. Cross-section SEM images of (A) (CdSe NR1/PTEBS)60 and (D) (CdSe NR2/PTEBS)60 nanocomposite films (assembled on ITO/ePEDOT:PSS substrate). TEM and HR-TEM cross-sectional analysis of NR1/PTEBS (B and C) and NR2/PTEBS (E and F) nanocomposite films. C and F show the crystal planes of NR1 (0.36 nm) and the moiré fringes of NR2 (0.86 nm). Moiré fringes form when two sets of parallel lines are inclined with respect to one another resulting in an interference pattern. In the case of nanocrystals, atomic planes form the “parallel lines”.

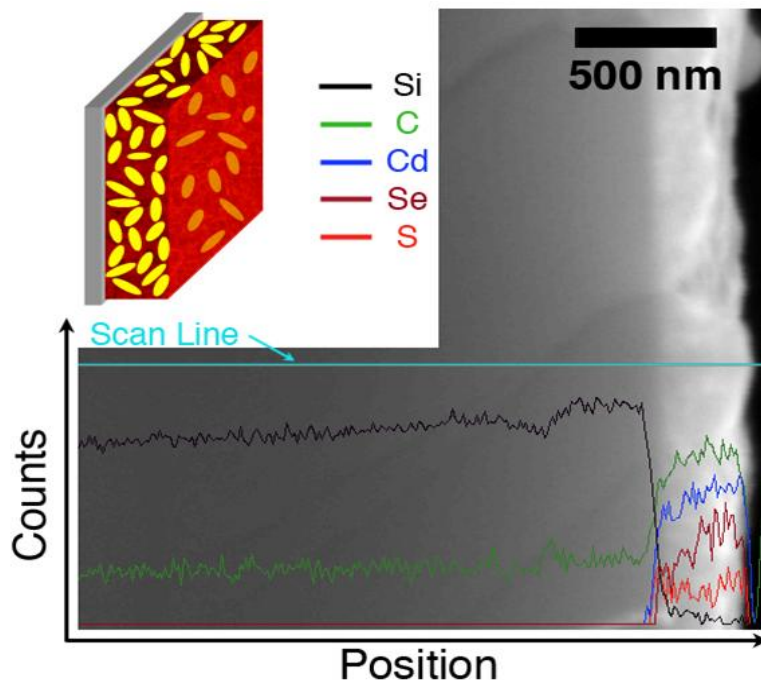


Figure 2.20. Auger analysis of ELBL thin film on silicon. Intimate mixing between component is shown suggesting a bulk heterojunction architecture to the film.

2.3 Conclusion

In this chapter, a facile and versatile all-aqueous method for fabricating CdSe nanorod/polymer nanocomposite thin films was discussed. Using ligand exchange chemistry, water-soluble CdSe nanorods were synthesized with varying lengths and properties. The nanorods were incorporated into multilayer thin films with controlled thickness on the order of nanometres using ELBL assembly. Surface analysis showed that the film roughness increases with thickness. The presence of a polymer/nanorod bulk heterojunction was shown with cross-sectional SEM, TEM, and scanning Auger analysis.

2.4 *Experimental Section*

Materials and General Instrumentation.

Tetradecylphosphonic acid (TDPA) and hexylphosphonic acid (HPA) were used as received from Strem Chemicals Inc.; trioctylphosphine oxide (TOPO), trioctylphosphine (TOP), cadmium oxide (CdO), selenium, aminoethanethiol · hydrochloride (AET), high and low molecular weight poly(sodium 4-styrenesulfonate) (PSS) (M_n PSS, $M_n = 1\,000\,000$) (M_n PSS, $M_n = 70\,000$), poly(diallyldimethylammonium chloride) (PDDA) ($M_n = 400\,000$ - $500\,000$), and 3,4-ethylenedioxythiophene (EDOT) were used as received from Sigma-Aldrich. PTEBS (ADS2000P) was acquired from American Dye Source whereas P3KHT was acquired from Rieke Metals Inc. and both used without further purification. The P3KHT was buffered with phosphate buffer solution (PBS) at a pH of 9. Methanol, ethanol, isopropanol, acetone, toluene, and dichloromethane solvents were used as received from Sigma-Aldrich. Indium tin oxide (ITO) coated glass substrates ($8\text{--}12\ \Omega/\text{square}$) were purchased from Delta Technologies, Ltd. Absorption spectra were recorded on an Agilent UV-vis spectrometer and the solution photoluminescence (PL) was characterized with a PTI (Photon Technology International) fluorescence spectrophotometer. Surfaces were characterized by atomic force microscopy (AFM) using a Nanoscope IV (Digital Instruments/Veeco) instrument, operated in tapping mode with commercially available Si cantilevers (Mikromasch, freq.) $300\ \text{kHz}$).

Synthesis of NR1 CdSe Nanorods.

The synthesis of TOPO-capped CdSe NRs follows a modified protocol as outlined by Gur et al. and Wang et al.^{86, 87} In brief, 710 mg of tetradecylphosphonic acid (TDPA), 3.00 g of trioctylphosphine oxide (TOPO) and 200 mg of CdO were added to a round-bottom flask and degassed at 120 °C for 30 min under an argon atmosphere. A selenium precursor was made by adding 73 mg of selenium metal to 416 mg of TOP and heating until dissolved. Once dissolved, the mixture was cooled to room temperature. The temperature of the degassing round-bottom flask was then increased to 320 °C to decompose the CdO. The decomposition was accompanied by a transition to a clear and colourless solution. The temperature was further reduced to 280 °C, and the selenium precursor was injected while stirring vigorously. The colour of the reaction solution was monitored as it changed from yellow to dark brown indicating increasing aspect ratio nanorods. In the case of NR1, the reaction was stopped when the solution turned red. Once the desired particle length had been reached, the flask was immersed in a water bath to quench the reaction. To purify the nanorods, 3-4 mL of anhydrous toluene was added to the flask. The solution was cleaned using precipitation and centrifugation. The nonsolvent used to precipitate the crystals was methanol. Once added, the mixture was centrifuged for 2 min. The pellets were redispersed in toluene and reprecipitated with methanol. The purification procedure was repeated three times to remove excess TOPO ligand.

Synthesis of NR2 CdSe Nanorods.

The synthesis of NR2 is analogous to NR1 with the following modifications: 710 mg of tetradecylphosphonic acid (TDPA), 3.00 g of trioctylphosphine oxide (TOPO), and 80 mg of hexylphosphonic acid (HPA) were used as surfactants. In the case of NR2, the reaction was stopped when the solution turned red.

Synthesis of NR3 CdSe Nanorods.

The synthesis of NR3 is analogous to NR1 with the following modifications: 710 mg of tetradecylphosphonic acid (TDPA), 3.00 g of trioctylphosphine oxide (TOPO), and 160 mg of hexylphosphonic acid (HPA) were used as surfactants. Following the trioctylphosphine injection, the temperature was increased to 320 °C followed by the selenium precursor injection. In the case of NR3, the reaction was stopped when the solution turned dark brown.

AET-CdSe Nanorods.

The ligand exchange process follows a procedure similar to Haremza et al.⁸⁸ with minor modifications; 3.2 g of AET was added to a round-bottom flask along with the TOPO-capped nanorods. To this, 20 mL of dichloromethane was added and the solution refluxed at 60 °C overnight under argon in the dark for 12-18 h. At this point, 20 mL of ethanol was added to precipitate the nanorods from the solution and the reflux was continued for an additional hour. To purify the nanorods, the suspension was then centrifuged for 2 min to create AET-CdSe

nanorod pellets. The nanorods were then dispersed in methanol with agitation. The purification procedure was repeated six times followed by drying under vacuum. Millipore water was added to the dried pellets, and then the solution was filtered using 0.200 μm cellulose acetate filters to give optically clear and stable solutions. These solutions were then stored at 4 °C in the dark until use.

Electrostatic Layer-by-Layer Assembly (ELBL).

The layer-by-layer assembly process was performed using a custom robotic dipper equipped with two Velmex translation axes for lateral and vertical directional movement. The entire ELBL apparatus was contained in a box prepurged with nitrogen at a flow rate of 62 sccm for 10 min. The nitrogen flow was maintained for the duration of the run. The temperature within the box was 29 °C. The robotic dipper was kept in the dark for the duration of the film fabrication. Glass, ITO or silicon substrates were cleaned by sequential 10 min ultrasonication in acetone and isopropyl alcohol. Prior to use, the substrates were further cleaned by exposure to 10 min oxygen plasma at ~ 0.1 mTorr (Harrick Plasma, PDC 32G, 18W). To generate a single bilayer the following cycle was performed: The negatively charged substrates were immersed in AET-CdSe nanorod solutions that had an optical density of approximately 2.6 for 5 min. The substrate was then removed and rinsed three times using Millipore water (18 M Ω). Following the rinsing, the substrates were then immersed in solutions of polyelectrolyte (HMn PSS, PTEBS, or P3KHT), at concentrations of 0.5-1 mg/mL, for 5 min, to complete the cycle. These cycles were repeated until the

desired number of bilayers was achieved. The pH of all solutions was kept neutral except for P3KHT which was buffered to pH 9 with PBS.

SEM Cross-Sectioned Samples.

ELBL films deposited on glass or ITO were cleaved with the assistance of a carbide blade and were affixed to SEM mounts with carbon tape. Thin films deposited on glass were sputter-coated with 50 Å of chromium. A Hitachi FE S-4800 SEM was used to image all samples with an accelerating voltage of 10 KV.

TEM.

Dilute solutions of AET-CdSe nanorods were drop-cast on to 200 mesh copper grids and allowed to dry. A JEOL JEM 2100 TEM with an accelerating voltage of 200 kV was used to image the NRs.

TEM Cross-Sectioned Samples.

Completed devices were embedded in epoxy (Spurs resin) and cured at (70 °C for 8 h). The solid product was then cracked by sequential dipping in liquid nitrogen and water to remove the glass substrate from the film. This film was then sliced into thin cross-sections using a microtome equipped with a diamond blade. The sliced cross-sections were floated onto carbon-coated copper TEM grids and analyzed using a JEOL JEM 2100 TEM at an accelerating voltage of 200 kV.

Cyclic Voltammetry.

Cyclic voltammetry was carried out using a Princeton Applied Research Model 2273 potentiostat employing a standard three-electrode electrochemical cell. All potentials are reported relative to a Ag/Ag⁺ reference electrode recorded at a scan rate of 50 mV/s. Experiments were carried out at room temperature in acetonitrile containing 0.1 mol L⁻¹ tetra(*n*-butyl)ammonium hexafluorophosphate (*n*Bu₄NPF₆) as the supporting electrolyte. The counterelectrode was platinum, and the working electrode consisted of a platinum disk (0.071 cm²) coated with a dried film of the material of interest. Bandgaps were determined by depositing a few drops of polymer or nanoparticle solution onto the electrode surface and drying in air. The electrodes were immersed in the acetonitrile solution in a standard three-electrode electrochemical cell as described above. Oxidation and reduction peaks were taken as the HOMO and LUMO levels respectively of the photoactive material.

2.5 *References*

1. Xing, R. M.; Wang, X. Y.; Yan, L. L.; Zhang, C. L.; Yang, Z.; Wang, X. H.; Guo, Z. J. *Dalton Trans.* **2009**, *10*, 1710–1713.
2. Gaponik, N.; Talapin, D. V.; Rogach, A. L.; Hoppe, K.; Shevchenko E. V.; Kornowski, A.; Eychmüller, A.; Weller, H. J. *Phys. Chem. B* **2002**, *106* (29), 7177–7185.
3. Schulz-Drost, C.; Sgobba, V.; Guldi, D. M. J. *Phys. Chem. C* **2007**, *111* (27), 9694–9703.
4. Fang, Z.; Liu, L.; Xu, L. L.; Yin, X. G.; Zhong, X. H. *Nanotechnology* **2008**, *19* (23), 235603.
5. Alivisatos, A. P. *Science* **1996**, *271* (5251), 933–937.
6. Manna, L.; Scher, E. C.; Alivisatos, A. P. J. *Am. Chem. Soc.* **2000**, *122* (51), 12700–12706.
7. Peng, Z. A.; Peng, X. G. J. *Am. Chem. Soc.* **2001**, *123* (1), 183–184.
8. Peng, X. G.; Manna, L.; Yang, W. D.; Wickham, J.; Scher, E.; Kadavanich, A.; Alivisatos, A. P. *Nature* **2000**, *404* (6773), 59–61.
9. Artemyev, M.; Kisiel, D.; Abmriotko, S.; Antipina, M. N.; Khomutov, G. B.; Kislov, V. V.; Rakhnyanskaya, A. A. J. *Am. Chem. Soc.* **2004**, *126*, 10594–10597.

10. Sukhanova, A.; Baranov, A. V.; Klinov, D.; Oleinikov, V.; Berwick, K.; Cohen, J. H. M.; Pluot, M.; Nabiev, I. *Nanotechnology* **2006**, *17*, 4223–4228.
11. Haremza, J. M.; Hahn, M. A.; Krauss, T. D. *Nano Lett.* **2002**, *2* (11), 1253–1258.
12. Decher, G. *Science* **1997**, *277* (5330), 1232–1237.
13. Caruso, F. *Adv. Mater.* **2001**, *13* (1), 11–12.
14. Schreiber, F. *Prog. Surf. Sci.* **2000**, *65* (5-8), 151–256.
15. Hammond, P. T. *Adv. Mater.* **2004**, *16* (15), 1271–1293.
16. Hao, E. C.; Lian, T. Q. *Langmuir* **2000**, *16* (21), 7879–7881.
17. De Girolamo, J.; Reiss, P.; Pron, A. J. *Phys. Chem. C* **2008**, *112* (24), 8797–8801.
18. Sato, M.; Sano, M. *Langmuir* **2005**, *21* (24), 11490–11494.
19. Cui, J.; Huang, Q. L.; Wang, Q. W.; Marks, T. J. *Langmuir* **2001**, *17* (7), 2051–2054.
20. Tian, Y.; He, Q.; Tao, C.; Li, J. B. *Langmuir* **2006**, *22* (1), 360–362.
21. Liang, Z. Q.; Dzienis, K. L.; Xu, J.; Wang, Q. *Adv. Funct. Mater.* **2006**, *16* (4), 542–548.

22. Lvov, Y.; Ariga, K.; Ichinose, I.; Kunitake, T. J. Am. Chem. Soc. **1995**, *117* (22), 6117–6123.
23. Lee, S. H.; Balasubramanian, S.; Kim, D. Y.; Viswanathan, N. K.; Bian, S.; Kumar, J.; Tripathy, S. K. Macromolecules **2000**, *33* (17), 6534–6540.
24. Decher, G.; Schlenoff, J. B. Multilayer Thin Films: Sequential Assembly of Nanocomposite Materials, Wiley-VCH: Weinheim, Germany, **2003**; p 524
25. Wang, X. Y.; Kim, Y. G.; Drew, C.; Ku, B. C.; Kumar, J.; Samuelson, L. A. Nano Lett. **2004**, *4* (2), 331–334
26. Ho, P. K. H.; Kim, J. S.; Burroughes, J. H.; Becker, H.; Li, S. F. Y.; Brown, T. M.; Cacialli, F.; Friend, R. H. Nature **2000**, *404* (6777), 481–484.
27. Bertrand, P.; Jonas, A.; Laschewsky, A.; Legras, R. Macromol. Rapid Commun. **2000**, *21* (7), 319–348.
28. Shiratori, S. S.; Rubner, M. F. Macromolecules **2000**, *33* (11), 4213–4219.
29. Jordan, C. E.; Frutos, A. G.; Thiel, A. J.; Corn, R. M. Anal. Chem. **1997**, *69* (24), 4939–4947.
30. Pei, R. J.; Cui, X. Q.; Yang, X. R.; Wang, E. K. Biomacromolecules **2001**, *2* (2), 463–468.

31. Johnston, A. P. R.; Read, E. S.; Caruso, F. *Nano Lett.* **2005**, *5* (5), 953–956.
32. Caruso, F.; Niikura, K.; Furlong, D. N.; Okahata, Y. *Langmuir* **1997**, *13* (13), 3427–3433.
33. Caruso, F.; Mohwald, H. J. *Am. Chem. Soc.* **1999**, *121* (25), 6039–6046.
34. Yoo, P. J.; Nam, K. T.; Qi, J. F.; Lee, S. K.; Park, J.; Belcher, A. M.; Hammond, P. T. *Nat. Mater.* **2006**, *5* (3), 234–240.
35. Mwaura, J. K.; Pinto, M. R.; Witker, D.; Ananthakrishnan, N.; Schanze, K. S.; Reynolds, J. R. *Langmuir* **2005**, *21* (22), 10119–10126.
36. Ramey, M. B.; Hiller, J. A.; Rubner, M. F.; Tan, C. Y.; Schanze, K. S.; Reynolds, J. R. *Macromolecules* **2005**, *38* (2), 234–243.
37. Pinto, M. R.; Kristal, B. M.; Schanze, K. S. *Langmuir* **2003**, *19* (16), 6523–6533.
38. Kim, J.; Lee, S. W.; Hammond, P. T.; Shao-Horn, Y. *Chem. Mater.* **2009**, *21* (13), 2993–3001.
39. Lowman, G. M.; Nelson, S. L.; Graves, S. A.; Strouse, G. F.; Buratto, S. K. *Langmuir* **2004**, *20* (6), 2057–2059.

40. Zhang, Q.; Atay, T.; Tischler, J. R.; Bradley, M. S.; Bulovic, V.; Nurmikko, A. V. *Nat. Nanotechnol.* **2007**, 2 (9), 555–559.
41. Kim, H. S.; Sohn, B. H.; Lee, W.; Lee, J. K.; Choi, S. J.; Kwon, S. J. *Thin Solid Films* **2002**, 419 (1-2), 173–177.
42. Wang, S. B.; Li, C.; Shi, G. Q. *Sol. Energy Mater. Sol. Cells* **2008**, 92 (5), 543–549.
43. Taylor, A. D.; Michel, M.; Sekol, R. C.; Kizuka, J. M.; Kotov, N. A.; Thompson, L. T. *Adv. Funct. Mater.* **2008**, 18 (19), 3003–3009.
44. Franzl, T.; Koktysh, D. S.; Klar, T. A.; Rogach, A. L.; Feldmann, J.; Gaponik, N. *Appl. Phys. Lett.* **2004**, 84 (15), 2904–2906.
45. Franzl, T.; Shavel, A.; Rogach, A. L.; Gaponik, N.; Klar, T. A.; Eychmuller, A.; Feldmann, J. *Small* **2005**, 1 (4), 392–395.
46. Franzl, T.; Klar, T. A.; Schietinger, S.; Rogach, A. L.; Feldmann, J. *Nano Lett.* **2004**, 4 (9), 1599–1603.
47. Klar, T. A.; Franzl, T.; Rogach, A. L.; Feldmann, J. *Adv. Mater.* **2005**, 17 (6), 769–773.
48. Cassagneau, T.; Mallouk, T. E.; Fendler, J. H. *J. Am. Chem. Soc.* **1998**, 120 (31), 7848–7859.
49. Gross, D.; Susa, A. S.; Klar, T. A.; Da Como, E.; Rogach, A. L.; Feldmann, J. *Nano Lett.* **2008**, 8 (5), 1482–1485.

50. Beissenhirtz, M. K.; Scheller, F. W.; Lisdat, F. *Anal. Chem.* **2004**, 76 (16), 4665–4671.
51. Slater, J. M.; Paynter, J.; Watt, E. J. *Analyst* **1993**, 118 (4), 379–384.
52. Decher, G.; Lehr, B.; Lowack, K.; Lvov, Y.; Schmitt, J. *Biosens. Bioelectron.* **1994**, 9 (9-10), 677–684.
53. Anzai, J.; Takeshita, H.; Kobayashi, Y.; Osa, T.; Hoshi, T. *Anal. Chem.* **1998**, 70 (4), 811–817.
54. Zheng, L. Z.; Yao, X.; Li, J. H. *Curr. Anal. Chem.* **2006**, 2 (3), 279–296.
55. Das, B. C.; Batabyal, S. K.; Pal, A. J. *Adv. Mater.* **2007**, 19 (23), 4172–4176.
56. Sahu, S.; Majee, S. K.; Pal, A. J. *Appl. Phys. Lett.* **2007**, 91, 14–143108.
57. Tu, C. C.; Lin, L. Y. *Appl. Phys. Lett.* **2008**, 93, 16–163107.
58. Masuda, K.; Ogawa, M.; Ohkita, H.; Bente, H.; Ito, S. *Sol. Energy Mater. Sol. Cells* **2009**, 93 (6-7), 762–767.
59. Kniprath, R.; McLeskey, J. T.; Rabe, J. P.; Kirstein, S. J. *Appl. Phys.* **2009**, 105, 12–124313.
60. Decher, G. *Science* **1997**, 277, 1232–1237

61. Das, B.C.; Batabyal, S.K.; Pal, A.J. *Adv. Mater.* **2007**, *19*, 4172 - 4176
62. Gur, I.; Fromer, N. A.; Geier, M. L.; Alivisatos, A. P *Science* **2005**, *310* (5747), 462–465.
63. Wang, W.; Banerjee, S.; Jia, S. G.; Steigerwald, M. L.; Herman, I. P. *Chem. Mater.* **2007**, *19* (10), 2573–2580.
64. Landi, B. J.; Castro, S. L.; Ruf, H. J.; Evans, C. M.; Bailey, S. G.; Raffaele, R. P. *Sol. Energy Mater. Sol. Cells* **2005**, *87*, 733–746.
65. Canali, C.; Nava, F.; Ottaviani, G.; Paorici, C. *Solid State Comm.* **1972**, *11*, 105 - 107.
66. Murray, C. B.; Kagan, C. R.; Bawendi, M. G. *Annu. Rev. Mater. Sci.* **2000**, *30*, 545–610.
67. Blom, P.W.M.; Mihailetschi, V.D.; Koster, L.J.A.; Markov, D.E. *Adv. Mater.* **2007**, *19*, 1551 - 1566.
68. Inamdar, S. N.; Ingole, P. P.; Haram, S. K. *ChemPhysChem* **2008**, *9* (17), 2574–2579.
69. Kucur, E.; Riegler, J.; Urban, G. A.; Nann, T. J. *Chem. Phys.* **2003**, *119* (4), 2333–2337.
70. Decher, G.; Hong, J. D.; Schmitt, J. *Thin Solid Films* **1992**, *210* (1-2), 831–835.
71. Srivastava, S.; Kotov, N. A. *Acc. Chem. Res.* **2008**, *41* (12), 1831–1841.

72. Hao, E. C.; Lian, T. Q. *Langmuir* **2000**, *16* (21), 7879–7881
73. Kim, D.; Okahara, S.; Shimura, K.; Nakayama, M. J. *Phys. Chem. C* **2009**, *113* (17), 7015–7018.
74. Mohanta, K.; Majee, S. K.; Batabyal, S. K.; Pal, A. J. *J. Phys. Chem. B* **2006**, *110* (37), 18231–18235.
75. Zhai, L.; McCullough, R. D. *Adv. Mater.* **2002**, *14* (12), 901–905.
76. Zucolotto, V.; Gattas-Asfura, K. M.; Tumolo, T.; Perinotto, A. C.; Antunes, P. A.; Constantino, C. J. L.; Baptista, M. S.; Leblanc, R. M.; Oliveira, O. N. *Appl. Surf. Sci.* **2005**, *246* (4), 397–402.
77. McCullough, R. D.; Ewbank, P. C.; Loewe, R. S. *J. Am. Chem. Soc.* **1997**, *119* (3), 633–634.
78. Kim, B. S.; Chen, L.; Gong, J. P.; Osada, Y. *Macromolecules* **1999**, *32* (12), 3964–3969.
79. Roman, L. S.; Mammo, W.; Pettersson, L. A. A.; Andersson, M. R.; Inganäs, O. *Adv. Mater.* **1998**, *10* (10), 774–777.
80. Rider, D. A.; Harris, K. D.; Wang, D.; Bruce, J.; Fleischauer, M. D.; Tucker, R. T.; Brett, M. J.; Buriak, J. M. *ACS Appl. Mater. Interfaces* **2009**, *1* (2), 279–288.
81. Reyes-Gasga, J.; Tehuacanero, S.; Yacaman, M. J. *Microsc. Res. Tech.* **1998**, *40* (1), 2–9.

82. Saunders, B. R.; Turner, M. L *Adv. Colloid Interface Sci.* 2008, **138** (1), 1–23.
83. Coakley, K. M.; McGehee, M. D. *Chem. Mater.* **2004**, *16*, 4533–4542.
84. Blom, P. W. M.; Mihailetschi, V. D.; Koster, L. J. A.; Markov, D. E. *Adv. Mater.* **2007**, *19* (12), 1551–1566.
85. Liu, L.; Guo, X.; Li, Y.; Zhong, X. *Inorg. Chem.* 2010, *49*, 3768 - 3775.
86. Gur, I.; Fromer, N. A.; Geier, M. L.; Alivisatos, A. P *Science* **2005**, *310*, 462–465.
87. Wang, W.; Banerjee, S.; Jia, S. G.; Steigerwald, M. L.; Herman, I. P. *Chem. Mater.* **2007**, *19*, 2573–2580.
88. Haremza, J. M.; Hahn, M. A.; Krauss, T. D. *Nano Lett.* **2002**, *2* (11), 1253–1258.

Chapter 3

Hybrid Solar Cells from Nanocomposite Thin Films

3.1. Introduction

In Chapter 2 we considered the ELBL assembly of nanocomposite thin films from water-soluble CdSe NRs and polythiophenes. The components were photoactive and their electronic structure suggested they may be useful for optoelectronics applications. The most obvious of these is the hybrid solar cell. The construction of devices is important for two reasons. First, they allow for the electrical characterization of the films using current-voltage curves. These data provide insight into the quality of the assembled films and allow for specific properties to be investigated. For example, variation in the short-circuit current (J_{SC}) may be affected by nanorod orientation, while deviations in ideal diode behaviour may point to resistances in the film caused by imperfect film chemistry. Therefore, the testing of devices can be seen as an electrochemical characterization of the ELBL thin films to gain understanding of their chemistry and overall architecture. Second, device fabrication provides a proof-of-concept for realizing the dream of functional devices from designed nano-materials. Although overall performance is quite limited, the photoactivity shown in these films opens the door to further active research in this area.

Chapter 3 was reproduced in part with permission from: McClure, S.A.; Worfolk, B.J.; Rider, D.A.; Tucker, R.T.; Fordyce, J.A.M.; Fleischauer, M.D.; Harris, K.D.; Brett, M.J.; Buriak, J.M. ACS Appl. Mater. Interf. 2010, 2, 219 – 229. Copyright © 2010 American Chemical Society.]

In this chapter, we look at the fabrication of hybrid solar cell devices and their electrical characterization. The motivation behind this chapter is to connect the chemistry of the assembled thin films from Chapter 2 to the electrical characteristics described by the current-voltage analysis. To begin, an introduction to the diode model for describing the assembled devices will be given. The relationship between this model and nanorod/polymer hybrid devices will be discussed along with simple equations that allow understanding of these cells in terms of film properties.

A PV cell made from nanocrystals and polymer can be described using a model where a diode is in series with a resistor and in parallel with the photocurrent source, a capacitor and a shunt resistor.¹ Figure 3.1 shows the equivalent circuit diagram. The IV characteristics are determined largely by the series and shunt resistances. Low series resistance allows high currents to flow through the cell while high shunt resistance suggests a lack of shorts or photocurrent leakages within the device. Contributions to the series resistance include poor contacts between nanoparticles and between the photoactive material and the electrodes. Shunt resistances are a result of pinholes in the films that allow for short-circuits to exist. The ideal solar cell (with high fill factor) would

have a series resistance that approaches zero and a shunt resistance that approaches infinity.

In Chapter 1, Figure 1.4 showed a typical IV curve for solar cell characterization. These current-voltage characteristics can be described most simply by the Shockley equation as shown by equation 3.1.^{1,2} In order to account for the series and shunt resistances described above, the equation can be recast as shown in equation 3.2. The parameters include the saturation current (I_0), the electric charge (q), the output current (I_o), the output voltage (V_o), the series and shunt resistances (R_s and R_{sh}), the ideality factor (n), the Boltzmann constant (k) and temperature (T). The ideality factor ranges between 1 (a perfect diode) and 2 (recombination processes).

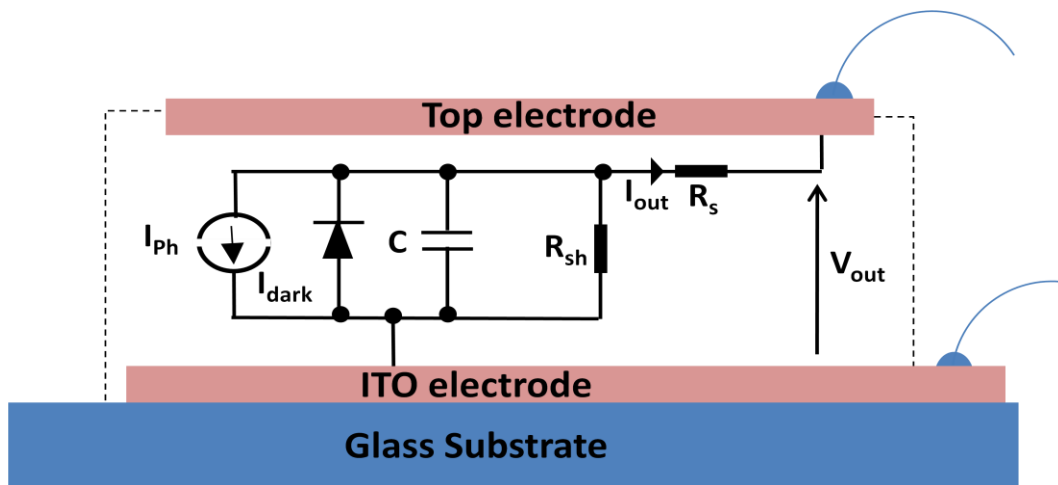


Figure 3.1. Equivalent circuit diagram for an illuminated photovoltaic cell. In the simplest model, a diode is in parallel with a constant source of current. R_s and R_{sh} are the series and shunt resistances respectively. I_{out} represents the current and V_{out} the voltage in the external circuit. C is the capacitance. Reprinted with permission from ref. 1. Copyright © 2003 American Physical Society.

$$3.1 \quad I(V) = I_o [e^{(qv/nkT)} - 1]$$

$$3.2 \quad I_{out} = \frac{R_{sh}}{R_s + R_{sh}} \left(I_o [e^{[q(V_{out} - I_{out}R_s)/nkT]} - 1] + \frac{V_{out}}{R_{sh}} \right)$$

It should be noted that the model can be further refined by taking into account the space charges that appear at high voltages. Since deviations from equation 3.2 do not typically occur until voltages surpass 0.7 V in hybrid nanoparticle/polymer devices ³ the space-charge limited model will not be considered here.

The resistances from the contacts and the PAL affect the shape of the IV curve. Figure 3.2 shows the changes in slope that occur when the cells deviate from high shunt resistance and low series resistance. An increase in series resistance causes the current-dominated section of the IV curve to move towards the origin of the graph. As mentioned earlier, the contributions to the series resistance include the contact resistances between material and electrodes and resistances within the PAL. In order for there to be good contact between the material and the electrodes, excellent chemical compatibility at the interface must exist. Incomplete coverage in the first few layers of film growth can be detrimental to the number of holes extracted at the ITO anode, while poor deposition of the top metal contact reduces the number electrons available at the cathode. In one study, Coe et al. fabricated LED devices from small molecules

and CdSe quantum dots. A variety of CdSe concentrations were spin-cast onto ITO anodes and analyzed using AFM.⁴ Figure 3.3 shows the AFM result with an unoptimized CdSe concentration used in the film deposition. As can be seen, island growth of the photoactive material leads to incomplete coverage on the electrode. In this study, incomplete coverage leads to poor performance in the devices due to a decreased number of charge transfer events at this interface.

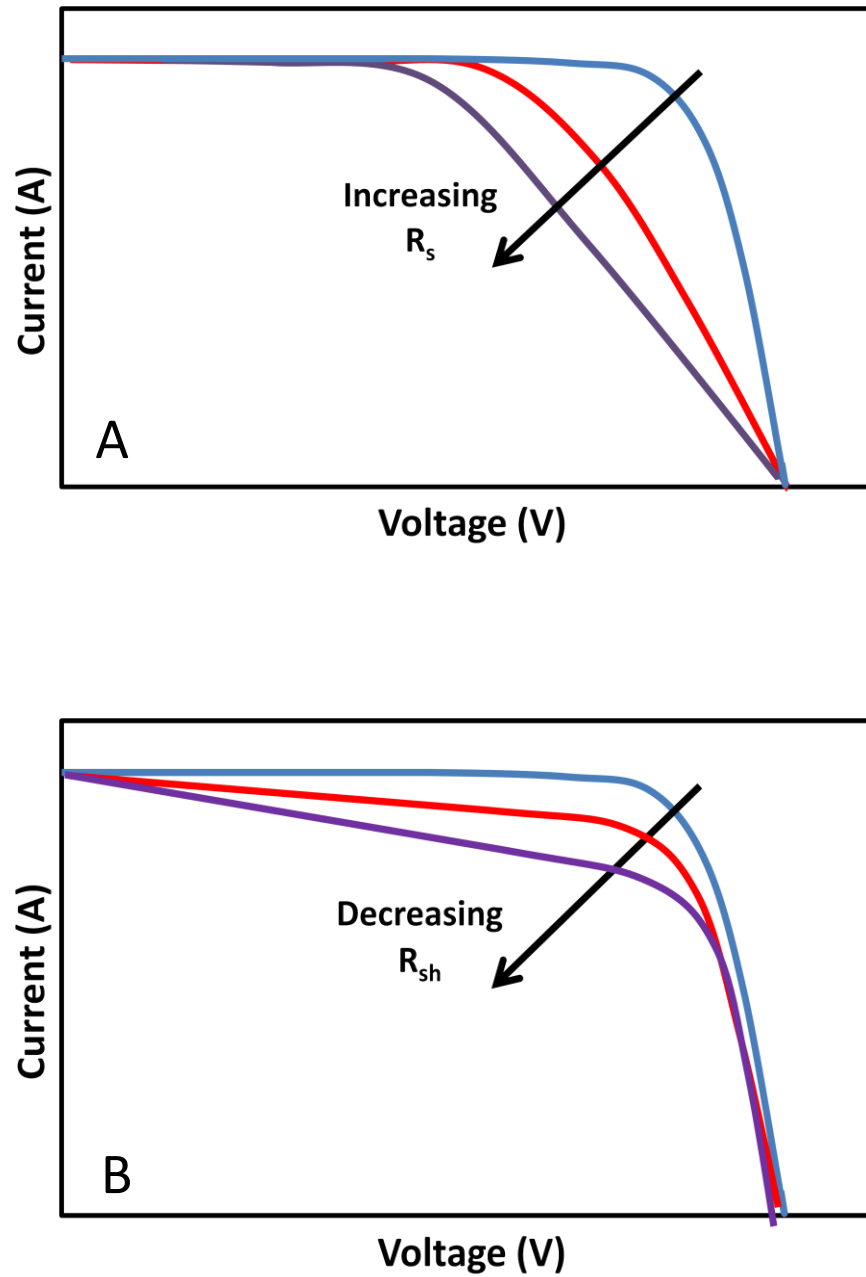


Figure 3.2. The changes that occur in the current-voltage curves with **A)** increasing series resistance and **B)** decreasing shunt resistance.

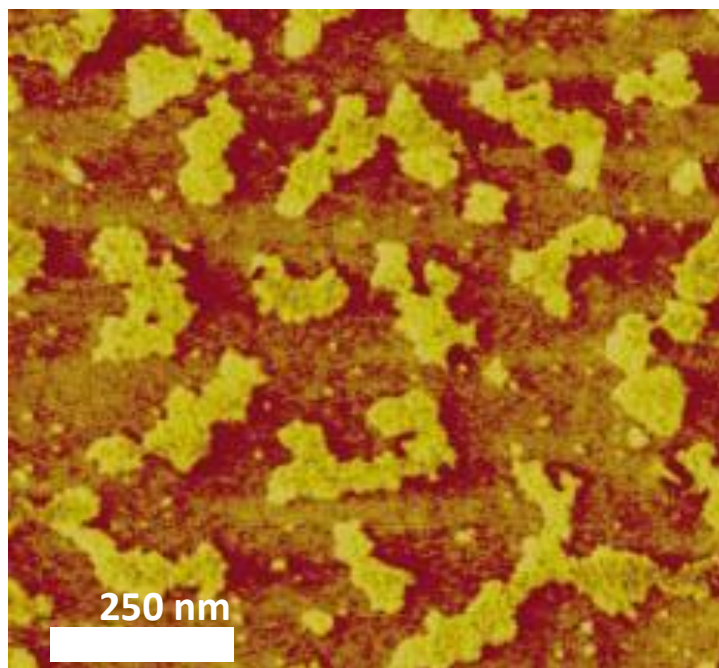


Figure 3.3. AFM image showing the formation of a partial monolayer of CdSe quantum dots after spin-casting with the hole-transporting material N,N'-diphenyl-N,N'-bis(3-methylphenyl)-(1,1'-biphenyl)-4,4'-diamine (TPD) onto an ITO substrate. Incomplete coverage led to poor performance in the optoelectronic devices. Reprinted with permission from ref. 4. Copyright © 2002 Nature.

An increase in series resistance can also be the result of poor nanoparticle contact within the photoactive layer. This arises from the physical separation of the nanoparticles within the polymer matrix and also from the ligand shell surrounding each nanoparticle. Longer chain ligands provide a larger barrier to charge and energy transfer, decreasing the mobility of charges and increasing the series resistance within the device. Chang et al. showed a factor-of-3 improvement in excitation transfer efficiency when exchanging longer chain ligands with shorter chain ligands.⁵ Exposure to oxygen during annealing can

also lead to increased series resistances as the oxide layer on the nanoparticles act as an insulating barrier. In another study, Zhao et al. showed that the oxide formed on PbS nanoparticles increased the series resistance in quantum dot solar cells.⁶

Series resistances are also affected by the orientation of the nanorods. In Chapter 1, it was shown that nanorods that lie vertically with respect to the electrode from a close-to-ideal architecture for charge transport. The larger the number of nanorods with this vertical orientation, the lower the number of hopping events needed in order for electrons to reach the cathode (see Figure 3.4).

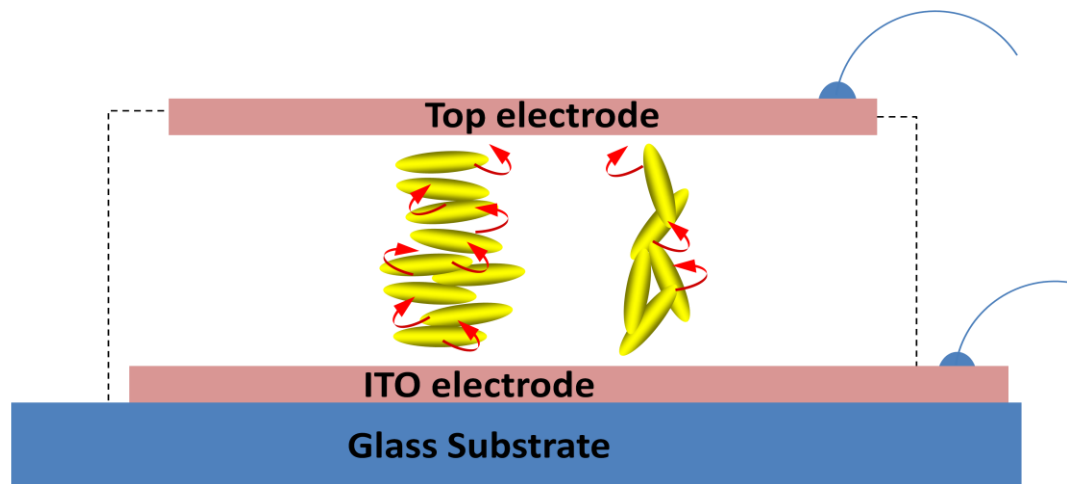


Figure 3.4. The orientation of the nanorods within the PAL can play a large role in the ability of current to be transported throughout the device. The larger the number of nanorods that lie vertically with respect to the electrode, the lower the number of hopping events that must occur.

An increase in shunt resistance causes the voltage-dominated section of the curve to move towards the origin (see Figure 3.2B). Contributions to the shunt resistance include short-circuits in the film caused by pinholes from incomplete coverage or severe surface roughness. When the first few layers of film growth appear as in Figure 3.3 high roughness in the film can be expected, leading to large variations in film uniformity.

3.2. Results and Discussion

Photovoltaic Devices Fabricated using ELBL with CdSe Nanorods and Conducting Polymer

In Chapter 2, optical and electrochemical characterization of the polythiophenes and NRs suggested the assembly of these components may lead to thin films with photovoltaic properties. The electrostatically stabilized and intermixed morphology between the donor polythiophenes and the acceptor CdSe NRs provides a large interfacial surface area for charge transfer. In addition, the offset of the band edges suggests a type- II heterojunction should exist between these materials.⁷ In order to investigate the photovoltaic properties of the ELBL assembled thin films, hybrid devices were fabricated using the general device architecture ITO/ePEDOT:PSS/(CdSe NR/polythiophene)₆₀/Al. The protocol for device fabrication is shown in Figure 3.5. Al cathodes were deposited directly onto the ELBL thin films by thermal evaporation. The bilayer number of 60 was chosen as this resulted in film thicknesses of ~200 nm; a number determined to be

optimal for this type of system.⁸ The devices fabricated include (CdSe NR1/PTEBS)₆₀, (CdSe NR2/PTEBS)₆₀, (CdSe NR3/PTEBS)₆₀, (CdSe NR1/P3KHT)₆₀, and (CdSe NR2/P3KHT)₆₀.

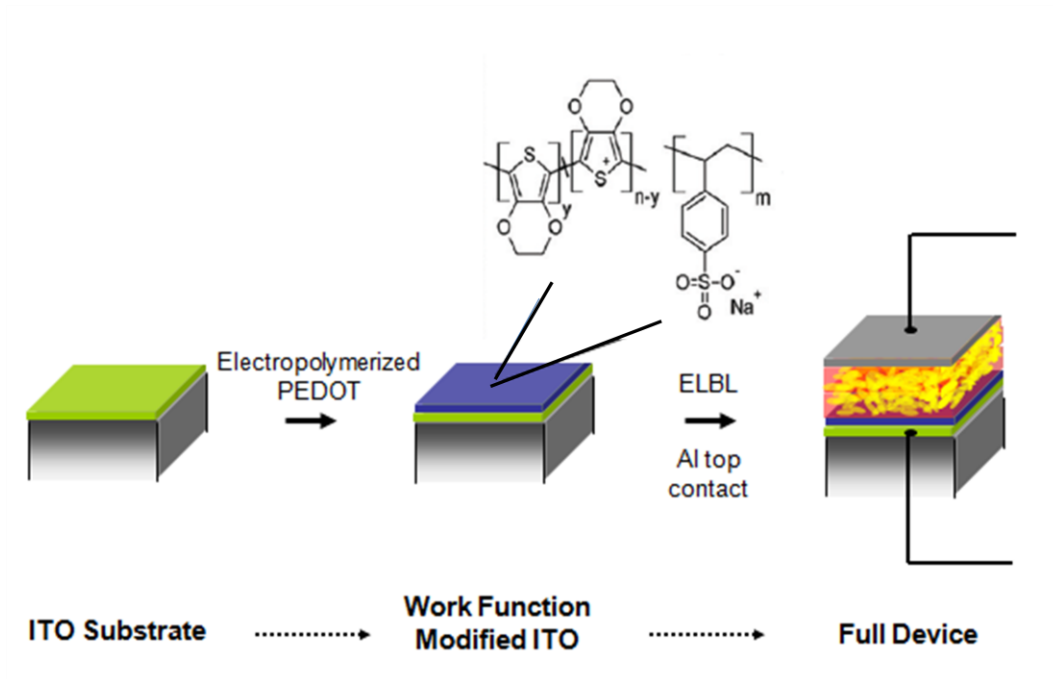


Figure 3.5. Fabrication of photovoltaic devices from CdSe NR /polymer multilayer films assembled by ELBL. The green represents a negatively charged surface. Blue denotes the work function modifier, while the remaining layers show the fully assembled device.

Figure 3.6 shows representative SEM cross-sections of (CdSe NR1/PTEBS)₆₀, and (CdSe NR2/PTEBS)₆₀, multilayer devices. The individual layers can be seen and include the ITO electrode, ePEDOT:PSS interfacial modifier, the PAL fabricated using ELBL, and the Al top contact. The devices were tested under AM1.5G solar conditions. The current-voltage curves for all devices are shown in Figure 3.7 and the results summarized in table 3.1

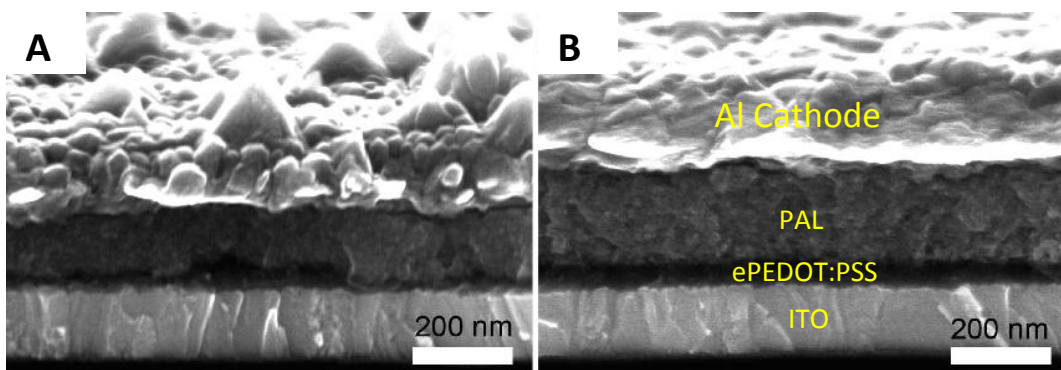


Figure 3.6. Cross-section SEMs of (A) (CdSe NR1/PTEBS)₆₀ and (B) CdSe NR2/PTEBS)₆₀ completed device architecture using the ELBL technique. The labels in B) identify the layers within the device.

The data represent the highest efficiency values from 10 regions on two substrates and are representative of the generally observed trend. All devices show a photovoltaic response in the fourth quadrant of the IV curve (see section 1.3 in General Introduction). The parameters used to investigate device properties are the short-circuit current (J_{SC}), open-circuit potential (V_{OC}), fill factor (FF) and overall power conversion efficiency (η) as shown in Table 3.1. In the NRx/PTEBS films ($x = 1, 2$ and 3), the J_{SC} increases with nanorod aspect ratio (AR). As discussed in the General Introduction of this thesis, J_{SC} depends on charge transport throughout the film.²³ A larger AR in the NRs is commensurate with an increase in their length. Longer NRs should transport charges more readily by virtue of the decreased number of hopping events the charges require to

reach the electrodes. Transport in nanocrystal films has been observed to be thermally activated similar to transport in polymers (see Chapters 1 and 4).^{9,24} One important aspect of charge transport in nanoparticles is energetic disorder arises from the size distribution of the particles while the geometric disorder arises from particle separation.¹⁰ The space between particles is a result of both the polymer matrix and the ligands capping the nanocrystals. Ligands are known to decrease carrier transport in nanoparticle films.^{25 - 28} Although the trend in J_{SC} is seen for the PTEBS system, the values are identical for P3KHT. The improvement in this set may be a result of the larger V_{OC} for the NR2 over the NR1. The improved performance of the higher AR devices may be the result of better charge transport, although such a strong conclusion requires further experimental support. The general trend, however, suggests the higher AR nanorods may be beneficial to ELBL device performance.

An increase in NR length may also help dissociate the exciton during charge transfer due to the increased spatial extent along the c-axis.¹¹ This would lead to the increased production of free charges and the potential for enhanced photocurrent.

It is interesting to note that the trend in electronic structure shown in Figure 2.9 from the cyclic voltammetry data do not correlate with the V_{OC} values measured here. There exists debate about the origin of V_{oc} in third- generation solar cells and this discrepancy may point to other factors affecting the open-circuit potential in these devices. For example, film morphology and particle loading have been found to effect V_{OC} values in polymer/fullerene OPVs.^{12, 13, 14,}

¹⁵ The variation in nanoparticle/polymer PAL architecture may convolute such predicted V_{OC} trends.

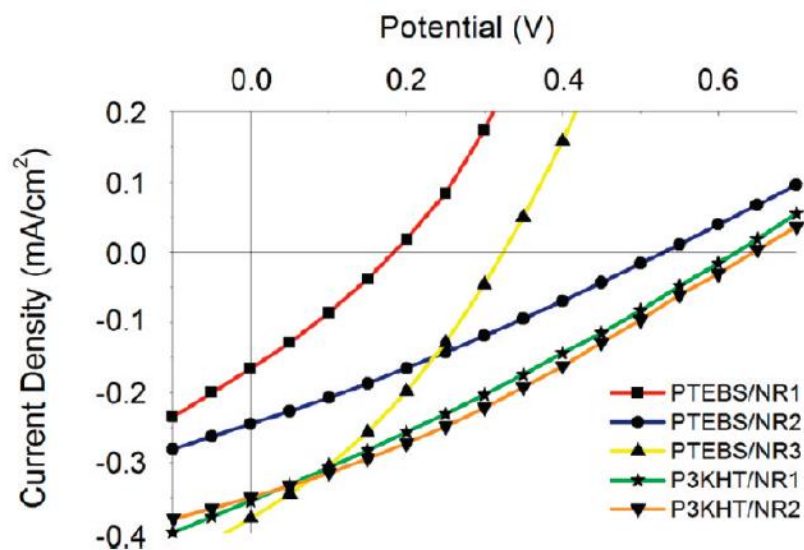


Figure 3.7. J - V characteristics of the illuminated $(\text{CdSe NR}_x/\text{polymer})_{60}$ devices made in this study ($x = 1, 2, 3$)

Table 3.1. PV Characteristics of the Best Performing Examples of ELBL-Assembled Solar Cells Made in This Study Showing the Nanorod Aspect Ratio (AR), Power Conversion Efficiency (η), Open Circuit Potential (V_{OC}), Fill Factor (FF), and Short Circuit Current (J_{SC}).

Material	AR	$J_{SC}(\text{mA}/\text{cm}^2)$	$V_{OC}(\text{V})$	FF	$\eta(\%)$
NR1	1.3	-0.17	0.18	0.29	0.010
NR2	3.6	-0.23	0.44	0.28	0.030
NR3	4.2	-0.38	0.32	0.32	0.042
NR1	1.3	-0.35	0.62	0.28	0.064
NR2	3.6	-0.35	0.65	0.30	0.071

Table 3.2. Series and Shunt Resistances of the Polymer/NRx Films Fabricated in this Study. (x = 1, 2 and 3). (The series resistances are quite large, suggesting poor transport throughout the devices. Shunt resistances are also significant suggesting short-circuits throughout the film.)

Material	Series Resistance (Ohm/cm^2)	Shunt Resistance (kOhm/cm^2)
PTEBS / NR1	69.91	0.06
PTEBS / NR2	589.21	2.01
PTEBS / NR3	82.15	0.66
P3KHT / NR1	285.35	1.66
P3KHT / NR2	384.56	3.56

Using the one-diode device model, series and shunt resistances can be determined from the shapes of the IV curves. In order to determine the series and shunt resistances of the five devices in this study, the slopes were taken at both ends of the curves and the resistances calculated as reported in table 3.2. The PTEBS/NR1 device shows low series and shunt resistance (relative to this group of five samples). In the case of the series resistance, fewer contact resistances should be present throughout the device relative to the other samples. Despite this low series resistance, the device has the lowest overall power conversion efficiency. This demonstrates the complexity of CT thin films and the challenge in achieving good performance. The origin of the lower overall efficiency is likely due to the relatively low shunt resistance. As mentioned in the Introduction of this chapter, low shunt resistance is crucial to establishing good photocurrent from the device. The low shunt resistance in the PTEBS/NR1 film may be the result of the rough film causing leakage current in the device. Figure 3.8 shows the SEM cross-section of the PTEBS/NR1 film. The overall variations in the film can be seen in Figure 3.8A. The material protrudes high above the average height of the film. In other areas, depressions can be seen as shown in the close-up in Figure 3.8B .

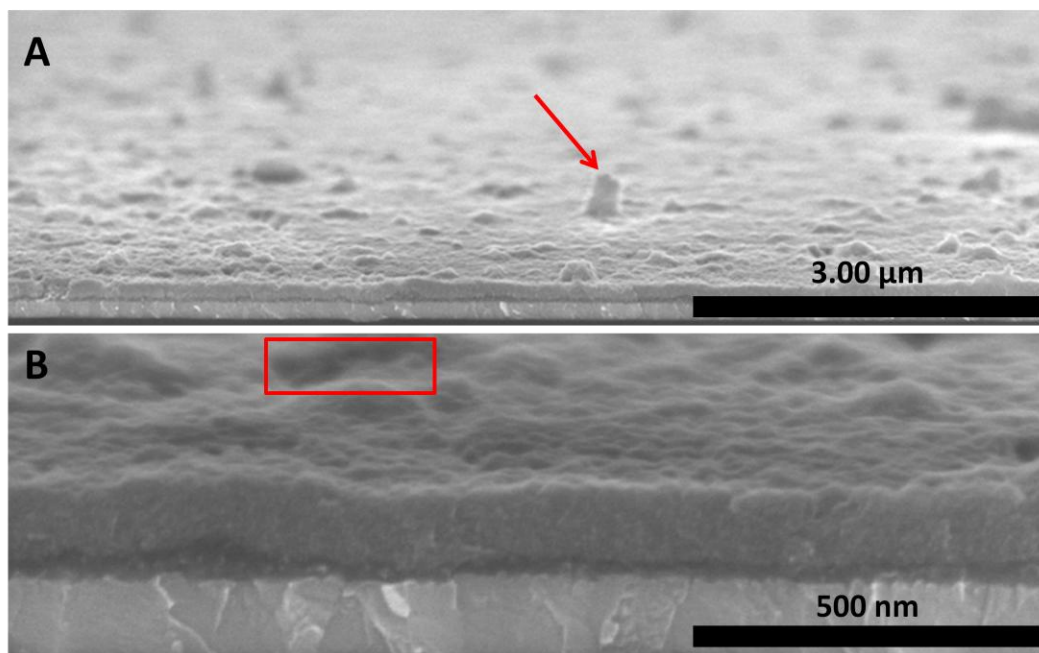


Figure 3.8. **A)** SEM image showing a NR1/PTEBS ELBL film at 45 °. Variations in the surface lead to depressions in the film potentially leading to pinholes throughout the multilayers. Pinholes lead to low values for shunt resistance. **B)** Close-up view showing the depressions in the film.

The series resistance in the PTEBS/NR2 device is much larger. One might expect this should lead to poorer performing devices. However the shunt resistance is two orders of magnitude larger in these films. Figure 3.9A shows the 45° view of the surface of the film. As can be seen in the SEM, the surface appears smoother than the PTEBS / NR1 film. The extra material above the surface does not appear in these films.

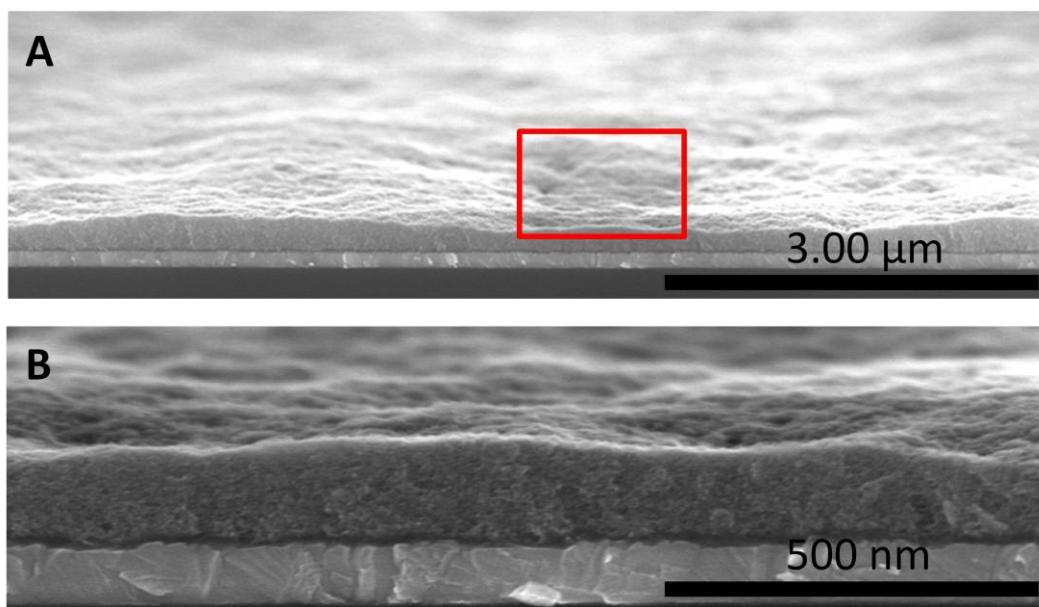


Figure 3.9. A) SEM image showing a PTEBS/NR2 ELBL film at 45 °. Variations in the surface lead to depressions in the film potentially leading to pinholes throughout the multilayers. B) Close-up view showing the depressions in the film.

Figure 3.10 shows the P3KHT/NR1 film. Its shunt resistance is somewhat intermediate in value compared to the other devices as is the amount of extra material on the surface of the film as can be seen in the SEM image. Efficient charge transfer and transport in the PAL is insufficient to ensure devices that perform well. The collection of charges at the electrodes is also vital to the extraction of carriers during a solar cell's operation. Figure 3.11 shows the SEM of the Al top contact. The film roughness seen in Figures 2.13 and 3.8 lead to rough metal contacts and as a result the collection of electrons at the cathode can be expected to suffer. The top layer in Figure 3.11 shows the roughness of the Al

top contact. The Al is deposited by thermal evaporation which may introduce additional defects into the ELBL assembled films.

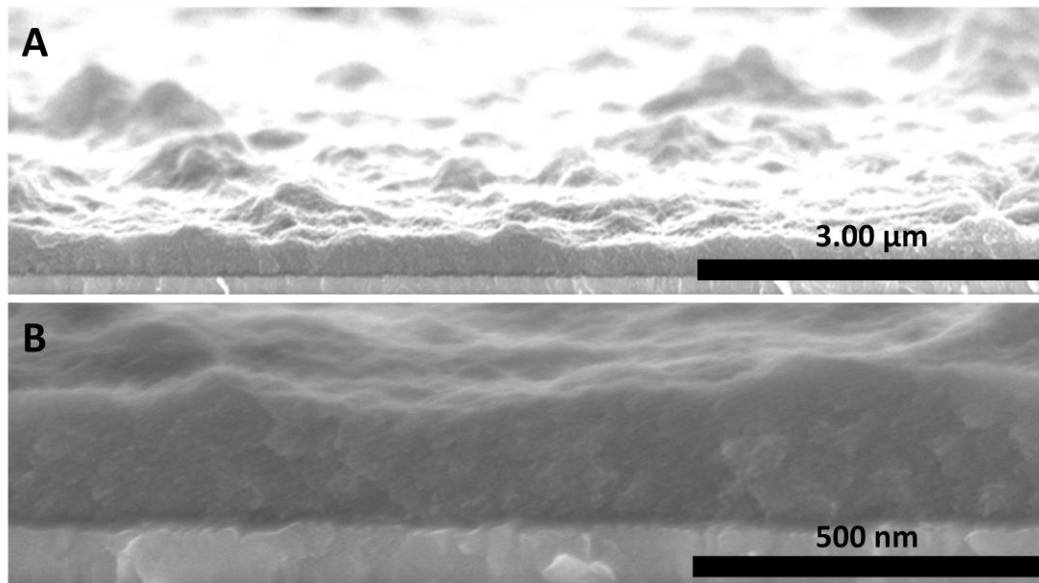


Figure 3.10. A) SEM image showing a P3KHT/NR1 ELBL film at 45 °. Variations in this film are intermediate between the films in Figures 3.8 and 3.9. B) Close-up view showing the depressions in the film.

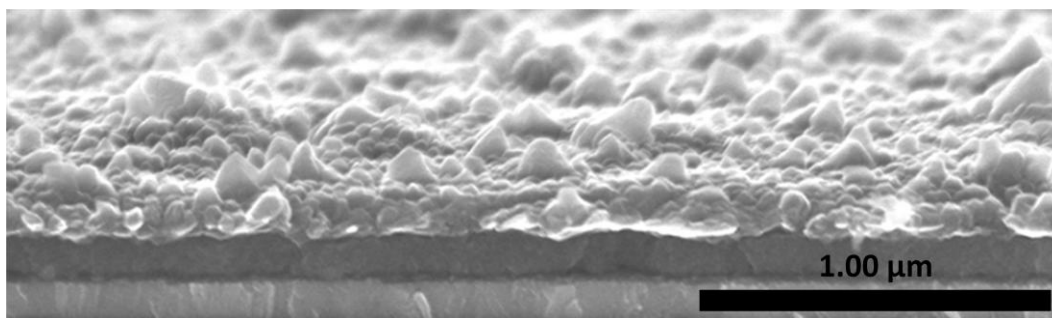


Figure 3.11. A) SEM image showing a NR1/PTEBS ELBL film at 45 °. The roughness shown in Figure 3.8 leads to roughness in the aluminum top contact, potentially leading to high values of series resistance.

CT in hybrid devices is also influenced by the orientation of the nanorods relative to the ITO substrate. Figure 3.12 shows the SEM cross-section analysis of the (CdSe NR3/PTEBS)₆₀ hybrid device with a high-resolution image of the PAL. These images are representative of the other NRx/polymer devices fabricated in this study.

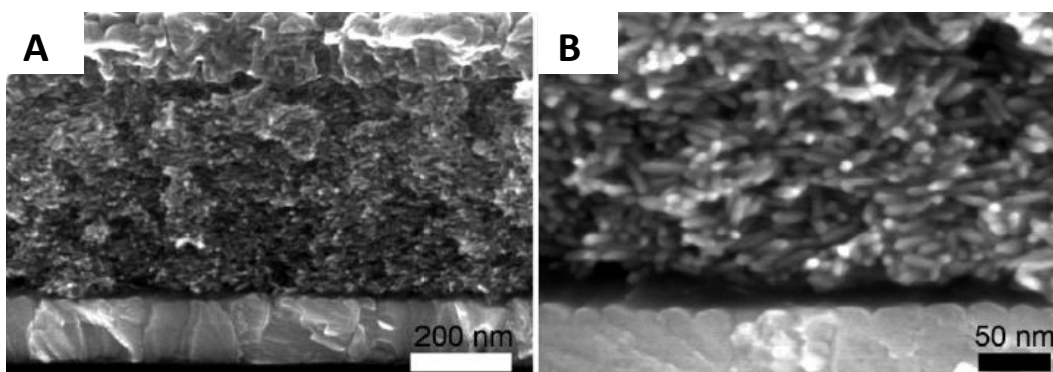


Figure 3.12. SEM cross-section of (CdSe NR3/PTEBS)₆₀ hybrid device. The overall device architecture is shown in **A**) while a close-up of the PAL is shown in **B**).

The majority of the nanorods lie parallel to the electrode surface. In Chapter 1, the importance of film morphology was discussed, and emphasized the need to have a close-to-ideal PAL architecture. In hybrid devices composed of NRs, this would equate to NRs lying vertically with respect to the electrode. The orientation of the NRs in these devices leads to relatively low J_{SC} values, and may explain the poor overall power conversion efficiencies.

J_{SC} also depends on the efficiency with which CT takes place between the NRs and photoactive polymer. The electronic structure of the materials was investigated in Chapter 2 (Figure 2.9) and suggested that the required type-II heterojunction exists between the materials. To probe the CT between donor and acceptor, PL quenching experiments were conducted. PL quenching can be used to qualitatively confirm the existence of the type-II heterojunction.¹⁷⁻²² As the concentration of acceptor is increased, a solution containing both materials should exhibit a decrease in the PL intensity of the donor. This is a result of charge transfer occurring faster than the radiative decay of the donor exciton. As can be seen in Figure 3.13, increasing the concentration of NR1, in a solution of PTEBS polymer, causes the characteristic PTEBS PL peak to decrease. Charge transfer between these materials appears to be efficient and thus should not play a limiting role in the performance of the devices. Figure 3.14 shows the PL quenching experiments for the P3KHT system, confirming charge transfer between the components. The P3KHT devices show better performance compared to the PTEBS films. This is most likely due to the broader absorption range of the P3KHT polymer relative to PTEBS.

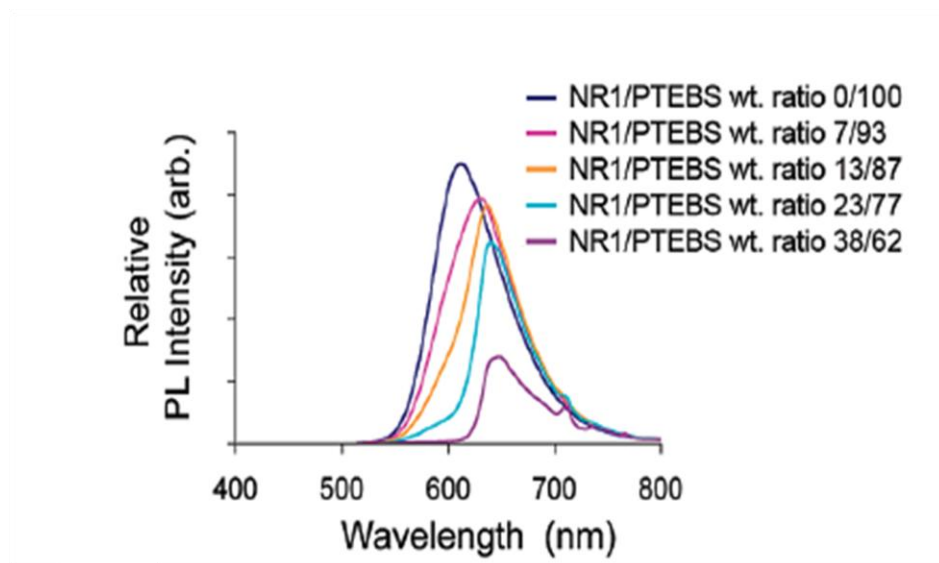


Figure 3.13. PL quenching experiments of PTEBS solutions with increasing NR1 content. A decrease in the PL intensity with increasing NR1 concentration is indicative of charge transfer from PTEBS to NR1.

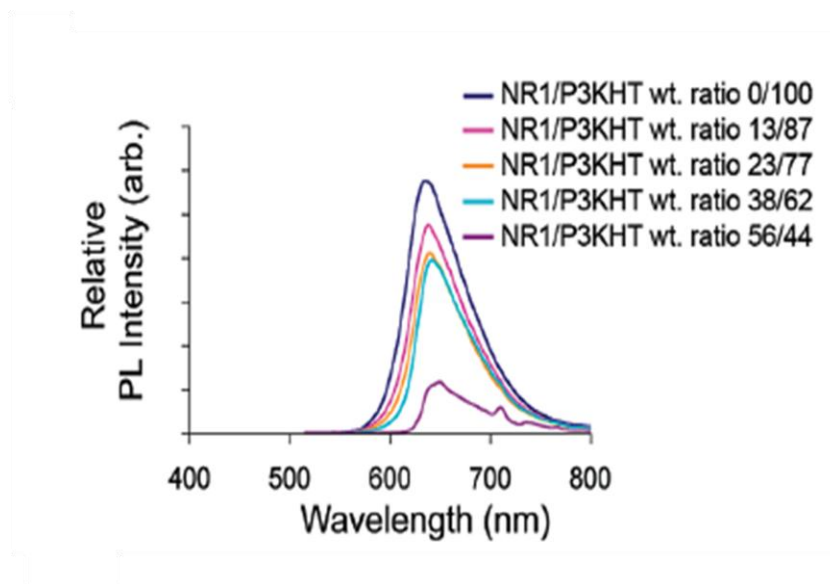


Figure 3.14. PL quenching experiments of P3KHT solutions with increasing NR1 content. A decrease in the PL intensity with increasing NR1 concentration is indicative of charge transfer from P3KHT to NR1.

Tapping-mode AFM was used to indent the first few bilayers in ELBL NR/polymer films. As shown in Figure 3.15, the first few bilayers of the ELBL film are non-uniform with island growth being evident. Island growth in the first few bilayers of ELBL assembly has been seen in other studies.²⁹ This may lead to poor electrical contact at the electrode/PAL interface. It may also be responsible for the high degree of roughness seen in subsequent layers. Modification of the ITO electrode with monolayers may improve the growth of these first few layers and enhance the electrical connection to the PAL.^{36 - 40} In addition, other ligand exchange procedures on the nanoparticles may improve early film growth.^{30 - 35}

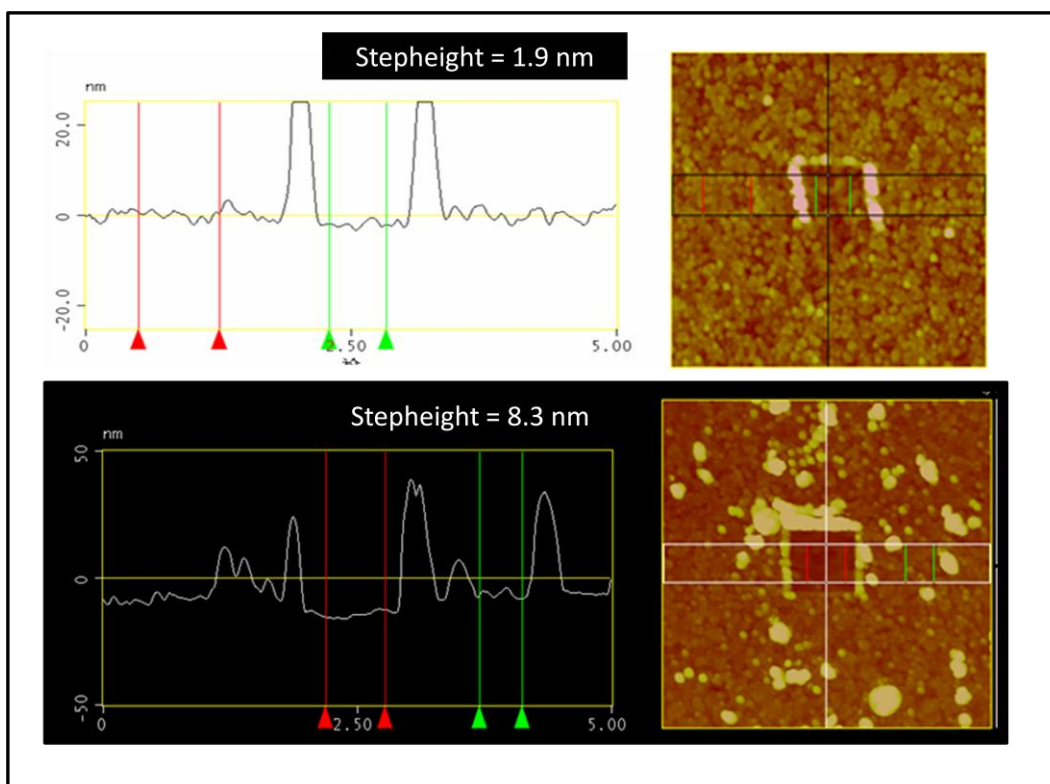


Figure 3.15. Nanoindent AFM used to investigate the first bilayers of ELBL thin film assembly. **A)** Bare ITO used as control to show an indentation of 1.9 nm. **B)** Same force applied to 2 bilayers of NR1/PSS showing an indent of 8.3 nm. The 2 bilayers show that the beginning of ELBL starts with a few localized spots instead of a uniform increase in thickness.

3.3 Conclusion

Optoelectronic devices were fabricated by employing ELBL on transparent conducting electrodes. IV characterization was done to assess the quality of the multilayer thin films and to provide a proof-of-concept for optoelectronics applications. The production of photocurrent was evident in all

films with a possible increase in performance using higher aspect ratio NRs. Employing a polymer with broader absorption was also found to enhance the overall performance of the devices. Series and shunt resistances were calculated from the IV curves using the one-diode model. Many of the devices suffered from poor shunt resistance which was attributed to the pinholes throughout the ELBL films as evidenced by SEM analysis. In addition, the first few bilayers of ELBL film growth were found to occur via an island growth mechanism which suggests a poor connection of the PAL to the electrical contacts in the device.

3.4 Experimental Section

Photovoltaic Devices.

Devices were fabricated on ITO substrates using the ELBL procedure to generate the photoactive layer. Prior to the ELBL film deposition, polyethylenedioxythiophene:poly(styrenesulfonate) (ePEDOT:PSS) was electrochemically grown from EDOT and LMn PSS on the ITO at a thickness of approximately 20-30 nm according to literature procedures.¹⁶ Onto the active layer, 200 nm of Al was deposited by thermal evaporation at a rate of 10 ± 1 Å/s under high vacuum conditions (5×10^{-4} Pa base pressure, 2×10^{-3} Pa deposition pressure) to complete the device. Photovoltaic device testing was performed at ambient atmosphere and temperature under simulated AM 1.5G irradiation using a xenon-lamp-based solar simulator (Oriel 91191 1000W Solar Simulator), with a nominal device irradiation of 100 mW/cm². The actual irradiance at our test position used for all experiments was calibrated using an NREL-calibrated reference cell of known efficiency (12% efficiency at 25 °C) and found to be 95 mW/cm². Device characterization was performed using a computer-controlled Keithley 2400 source meter. Fabricated devices were held at a negative bias without illumination to “burn out” short circuit contacts between the ITO anode and Al cathode, and get the devices to exhibit rectifying behaviour. The total energy dispersed during the burn out ranged from submillijoule to a significant fraction of a joule. Series and shunt resistance were determined by fitting a linear

function to the illuminated current density-voltage curves over regions of forward and reverse bias, respectively.

SEM Cross-Sectioned Samples.

ELBL films deposited on glass or ITO were cleaved with the assistance of a carbide blade and were affixed to SEM mounts with carbon tape. Thin films deposited on glass were sputter-coated with 50 Å of chromium. A Hitachi FE S-4800 SEM was used to image all samples with an accelerating voltage of 10 KV.

Scanning Auger.

Scanning Auger samples were prepared on a cleaned (ultrasonication with acetone and IPA) silicon substrate using the ELBL procedure. Samples were kept in nitrogen atmosphere until testing. Samples were run on a JAMP 9500F (JEOL) Auger Microscope.

Solution Photoluminescence.

Solution PL was performed with a PTI (Photon Technology International) fluorescence spectrophotometer. Excitation was performed at 500 nm using a Xe lamp at 75 W power. Samples were prepared such that the PTEBS and P3KHT concentrations were held at 1.0 and 0.5 mg/mL respectively, while the CdSe quantum dots were loaded with progressively higher concentrations. The spectra were obtained immediately following the loading of the CdSe. Normalization of the PL spectra was done to allow for comparison between the peaks.

3.5 *References*

1. Huynh, W.U.; Dittmer, J.J.; Teclamar, N.; Milliron, D.J.; Alivisatos, A.P.; Barnham, K.W.J. *Phys. Rev. B.* **2003**, *67*, 115326.
2. J. Simon and J.-J. Andre', *Molecular Semiconductors* (Springer-Verlag, Heidelberg, **1985**).
3. S. Tagmouti, A. Outzourhit, A. Oueragli, M. Khaidar, M. Elyacoubi, R. Evrard, and E. L. Ameziane, *Thin Solid Films* **2000**, *379*, 272 - 278.
4. Coe, S.; Woo, W.K.; Bawendi, M.; Bulovic, V. *Nature* **2002**, *420*, 800 - 803.
5. Chang, T.W.F.; Musikhin, S.; Bakueva, L.; Levina, L.; Hines, M.A.; Cyr, P.W.; Sargent, E.H. *Appl. Phys. Lett.* **2004**, *84*, 4295 - 4297.
6. Zhao, N.; Osedach, T.P.; Chang, L.Y.; Geyer, S.M.; Wanger, D.; Binda, M.T.; Arango, A.C.; Bawendi, M.G.; Bulovic, V. *ACS Nano* **2010**, *7*, 3743 - 3752.
7. Franciosi, A.; VandeWalle, C. G. *Surf. Sci. Rep.* **1996**, *25* (1-4), 1–140.
8. Huynh, W. U.; Dittmer, J. J.; Libby, W. C.; Whiting, G. L.; Alivisatos, A. P. *Adv. Funct. Mater.* **2003**, *13*, 73–79.
9. Ginger, D.S.; Greenham, N.C. *J. Appl. Phys.* **2000**, *87*, 1361 - 1368.
10. Schlamp, M.C.; Peng, X.; Alivisatos, A.P. *J. Appl. Phys.* **1997**, *82*, 5837 - 5842.
11. Gur, I.; Fromer, N. A.; Geier, M. L.; Alivisatos, A. P. *Science* **2005**, *310* (5747), 462–465.

12. Reyes-Reyes, M.; Kim, K.; Carroll, D.L. Appl. Phys. Lett. **2005**, 87, 083506.
13. Vanlaeke, P.; Swinnen, A.; Haeldermans, I.; Vanhoyland, G.; Aernouts, T.; Cheyns, D.; Deibel, C.; D'Haen, J.; Heremans, P.; Poortmans, J.; Manca, J.V. Sol. Ener. Mater. Sol. Cells **2006**, 90, 2150 - 2158.
14. Chirvase, D.; Parisi, J.; Hummelen, J.C.; Dyakonov, V. Nanotechnology **2004**, 15, 1317 - 1323.
15. van Duren, J.K.J.; Yang, X.; Loos, J.; Bulle-Lieuwma, C.W.T.; Sieval, A.B.; Hummelen, J.C.; Janssen, R.A.J. Adv. Funct. Mater. **2004**, 14, 425 - 434.
16. Rider, D. A.; Harris, K. D.; Wang, D.; Bruce, J.; Fleischauer, M. D.; Tucker, R. T.; Brett, M. J.; Buriak, J. M. ACS Appl. Mater. Interfaces **2009**, 1, 279–288.
17. Wang, H.S.; Su, M.S.; Wei, K.H. J. Poly. Sci: Part A: Poly. Chem. **2010**, 48, 3331 - 3339.
18. Aldakov, D.; Jiu, T.; Zagorska, M.; Bettignies, R.; Jouneau, P.H.; Pron, A.; Chandezon, F. Phys. Chem. Chem. Phys. **2010**, 12, 7497 - 7505.
19. Kumar, U.; Kumari, K.; Sharma, S.N.; Kumar, M.; Vankar, V.D.; Kakkar, R.; Kumar, V. Coll. Poly. Sci. **2010**, 288, 841 - 849.
20. Deng, D.; Shi, M.; Chen, F.; Chen, L.; Jiang, X.; Chen, H. Solar Energy **2010**, 84, 771 - 776.

21. Zhao, D.; Tang, W.; Ke, L.; Tan, S.W.; Sun, Z.W. ACS Appl. Mater. Interf. **2010**, 2, 829 - 837.
22. Kim, J.S.; Park, Y.; Lee, D.Y.; Lee, J.H.; Park, J.H.; Kim, J.K.; Cho, K. Adv. Funct. Mater. **2010**, 20, 540 - 545.
23. Geens, W.; Martens, T.; Poortmans, J.; Aernouts, T.; Manca, J.; Lutsen, L.; Heremans, P.; Borghs, S.; Mertens, R.; Vanderzande, D. Thin Solid Films **2004**, 451 - 452, 498 - 502.
24. Sampaio, J.F.; Beverly, K.C.; Heath, J.R. J. Phys. Chem. B. **2001**, 105, 8797 - 8800.
25. Drndic, M.; Jarosz, M.V.; Morgan, N.Y.; Kastner, M.A.; Bawendi, M.G. J. Apply. Phys. **2002**, 92, 7498 - 7503.
26. Romero, H.E.; Drndic, M. Phys. Rev. Lett. **2005**, 95, 156801.
27. Law, M.; Luther, J.M.; Song, Q.; Hughes, B.K.; Perkins, C.L.; Nozik, A.J. J. Am. Chem. Soc. **2008**, 130, 5974 - 5985.
28. Talapin, D.V.; Murray, C.B. Science **2005**, 310, 86 - 89.
29. Lobo, R.F.M.; Pereira-da-Silva, M.A.; Raposo, M.; Faria, R.M.; Oliveira Jr, O.N. Nanotechnology, **2003**, 14, 101 - 108.
30. Huynh, W.U.; Dittmer, J.J.; Libby, W.C.; Whiting, G.L.; Alivisatos, A.P. Adv. Funct. Mater. **2003**, 13, 73 - 79.
31. Kovalenko, M.V.; Spokoyny, B.; Lee, J.S.; Scheele, M.; Weber, A.; Perera, S.; Landry, D.; Talapin, D.V. J. Am. Chem. Soc. **2010**, 132, 6686 - 6695.

32. Han, L.; Qin, D.; Jiang, X.; Liu, Y.; Wang, L.; Chen, J.; Cao, Y.
Nanotechnology, **2006**, *17*, 4736 - 4742.
33. Aldakov, D.; Chandezon, F.; Bettignies, R.D.; Firon, M.; Reiss, P.;
Pron, A. Eur. Phys. J. Appl. Phys. **2007**, *36*, 261 - 265.
34. Chen, J.; Song, J.L.; Sun, X.W.; Deng, W.Q.; Jiang, C.Y.; Lei, W.;
Huang, J.H.; Liu, R.S. Appl. Phys. Lett. **2009**, *94*, 153115.
35. Milliron, D.J.; Alivisatos, A.P.; Pitois, C.; Edler, C.; Frechet,
J.M.J. Adv. Mater. **2003**, *15*, 58 - 61.
36. Campbell, I.H.; Kress, J.D.; Martin, R.L.; Smith, D.L.; Barashkov,
N.N.; Ferraris, J.P. Appl. Phys. Lett. **1997**, *71*, 3528 - 3530.
37. Appleyard, S.F.J.; Willis, M.R. Optical Materials **1998**, *9*, 120 -
124.
38. Hatton, R.A.; Willis, M.R.; Chesters, M.A.; Rutten, F.J.M.; Briggs,
D. J. Mater. Chem. **2003**, *13*, 38 - 43.
39. Cui, J.; Huang, Q.; Veinot, J.G.C.; Yan, H.; Marks, T.J. Adv.
Mater. **2002**, *14*, 565 - 569.
40. Guo, J.; Koch, N.; Schwartz, J.; Bernasek, S.L. J. Phys. Chem. B
2005, *109*, 3966 - 3970.

Chapter 4

Transport Properties of Thiophenes

4.1 Introduction

Chapters 2 and 3 dealt with the fabrication of nanocomposite films for hybrid solar cell applications. Characterization of the device performance showed low J_{SC} values which was attributed to poor carrier mobility. Although the overall architecture of the nanorods in the PAL play a significant role, it is often hole mobility that limits the performance in these devices. Hole mobility is determined by the molecular packing of the polymeric component of the thin film. In this thesis, thiophenes make up the hole transporting constituent in the ELBL multilayers. Despite the experimental efforts to understand carrier transport in thiophenes, there is still much that is unknown. As a tool to go beyond the limitations of experimental research, this chapter looks at using computational chemistry to elucidate the fundamentals behind charge transport in thiophene organic semiconductors.

[Chapter 4 was reproduced in part with permission from: McClure, S.A.; Buriak, J.M.; DiLabio, G.A. *J. Phys. Chem. C*, 2010, 114, 10952. Copyright © 2010 American Chemical Society.]

Carrier Transport in Thiophenes

Thiophenes are an important class of materials that have generated an enormous amount of scientific interest due to their unique optical and electrical properties. High carrier mobility¹ and ease of processing make thiophenes very attractive for optoelectronic applications such as field effect transistors,² light emitting diodes,³ and photovoltaics.⁴ At room temperature, conductivity in thin films composed of aggregates of conjugated thiophenes (i.e., polythiophenes) is known to occur via a hopping mechanism.⁵⁻⁷ In these cases, carrier mobility can be modeled as an electron transfer reaction between adjacent molecules in the film.⁸ As such, the rules governing CT from molecule to molecule follow the semiclassical Marcus theory of electron-transfer,^{8,9} where the overall rate constant is expressed as

$$4.1 \quad k_{ET} = \frac{4\pi^2}{h} \frac{1}{\sqrt{4\pi\lambda k_B T}} V^2 \exp\left(-\frac{\lambda}{4k_B T}\right)$$

where h is Planck's constant, k_B is Boltzmann's constant, V is the electronic coupling matrix element or transfer integral between two molecules, and λ is the reorganization energy associated with the geometry change that occurs during the CT process. It has been shown that this approximation is appropriate for determining the rate of CT in systems such as oligomeric thiophenes.¹⁰ As can be seen from equation 4.1, the reorganization energy, λ is an important contributor to the CT rate constant. Also important is the transfer integral V . The transfer

integral is related to the orbital overlap between interacting molecules. The overlap dictates the bandwidths formed in, and therefore carrier transport properties of, materials composed of these molecules. This thesis will focus on the orbital overlap in a series of thiophene dimers.

Some theoretical studies concerning CT in organic systems use the “splitting-in-dimer” method. This method assumes that the transfer integral evaluated for dimer systems can give insight into those present in extended systems.¹¹⁻¹⁵ Specifically, V for hole transfer processes can be approximated by evaluating the energy difference between the orbitals that result from the overlap between the highest occupied molecular orbitals (HOMOs) of two interacting molecules. Similarly, for electron transfer processes, V is related to the energy difference between the orbitals that result from the overlap between the lowest unoccupied molecular orbitals (LUMOs) of two interacting molecules. These energy differences, referred to as energy splittings, give an indication of the widths of valence (HOMO) and conduction (LUMO) bands in bulk systems and thus reflect carrier mobility. The evaluation of energy splittings from a single dimer represents a very simple and effective means of approximating V for an extended system. A principle assumption here is that the structure of the isolated dimer is representative of the structure of the molecules in a bulk film. Keeping this assumption in mind, this approach will be used to evaluate splittings that occur in dimers of oligothiophenes.

There exists a clear structure-function relationship in polythiophene

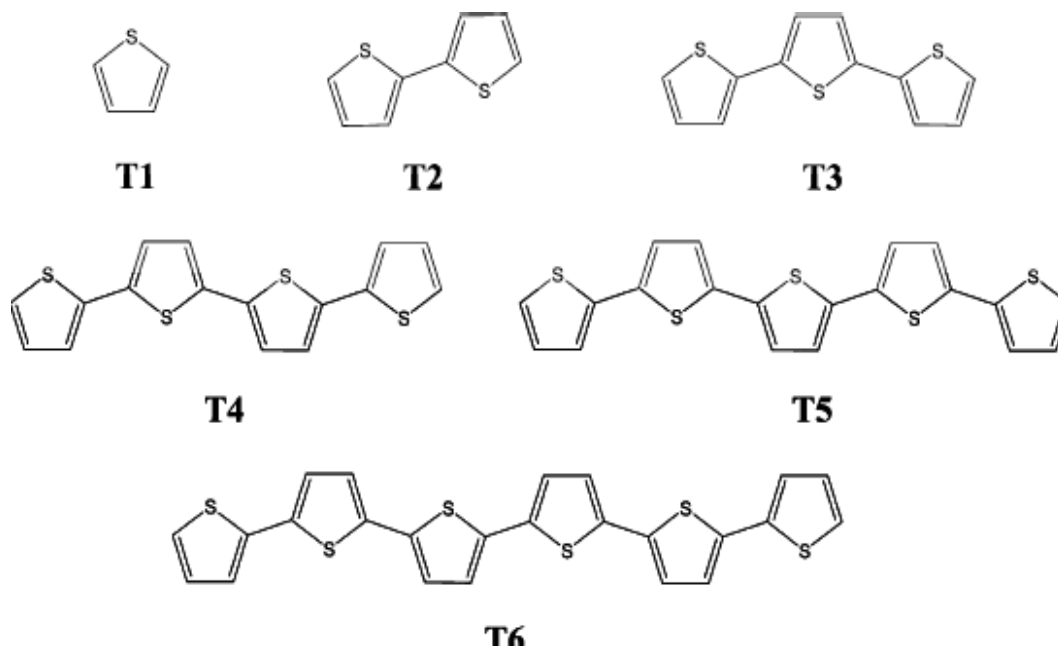
electronics. The magnitude of the energy splitting is determined by orbital overlap that in turn is dictated by the structure of the polythiophene dimer itself. The determination of structure, however, is not straightforward for these systems. The dimer structures are bound through noncovalent interactions between the monomers. In the case of polythiophene dimers, noncovalent bonding is dominated by π -stacking (dispersion) and dipole-dipole interactions.^{17,18} The accurate evaluation of binding energies in large, noncovalently bonded systems is notoriously time-consuming for conventional wave function techniques³⁶ and is impossible for commonly used density functional theory (DFT) methods (e.g., B3LYP),²⁵ which do not contain the correct dispersion physics.^{19,20}

To address the shortcomings of DFT with respect to the treatment of noncovalent interactions, recently developed dispersion-correcting potentials (DCPs) have been developed.^{21,27} DCPs have been shown to predict the structure and binding energies of noncovalently bound systems in very good agreement with high-level wave function theory results, in particular for dimers composed of simple thiophenes and benzothiophenes.²² In this thesis, a DFT-DCP approach was developed to handle thiophene systems. Orbital coefficients were optimized to achieve the highest accuracy in structure prediction between non-covalently bound thiophene dimers. The use of DCPs in conjunction with DFT allows for the treatment of relatively large systems.

In this thesis, the DCPs developed for thiophenes are used to compute low-energy, (meta)stable structures of oligothiophene dimers, whose monomers range in size from one to six thiophenes, as outlined in Scheme 1. Evaluations of

orbital splittings provide insight into the relationship between the strength of binding within a particular dimer structure and its electronic behaviour, viz., carrier transport. Finally, the effects of low-energy, normal mode vibration within a dimer on the orbital splitting is presented.

This chapter will show how the ability to determine accurate structures for oligothiophene dimers provides insight into their structure-function characteristics. From the crystal engineering standpoint, such ability allows for a more rational approach to the future design of thin film systems with optimized and well-known electronic behaviour.



SCHEME 1: Thiophenes studied in this work ranging from T1 to T6.

4.2 Computational Details

Dispersion-Correcting Potentials.

DCPs are atom-centered potentials that are designed to predict accurate binding energies for noncovalently bonded systems, especially those with significant dispersion interactions.²¹ Formally, DCPs are specific to the DFT method/basis sets for which they were developed. However, DFT methods with similar long-range behaviour (e.g., B971²³/PBE24 or B3^{25a}LYP^{25b}/PW91²⁶) have DCP coefficients that are quite similar. It can also be said that DCPs for a given functional are nearly basis set independent for basis sets of 6-31+G(d,p) quality or higher.

For a family of dispersion-bound hydrocarbon dimers, DFT-calculated binding energies have errors in the range of 50-90%, depending upon the functional and basis set used.²⁰ By incorporating DCPs in the DFT calculations, errors in calculated binding energies are reduced to ca. 8-37%.^{21,27} The structures of noncovalently bound dimers are also well predicted using DFT-DCP approaches. Figure 4.1 shows the advantage of using DCPs in non-covalent interaction calculations. In this work, it was shown that for a series of simple thiophene dimers (T1, see Scheme 1), DCPs can be used with the B971 and PBE functionals to obtain binding energies to within ca. 12% of high-level theory results.²²

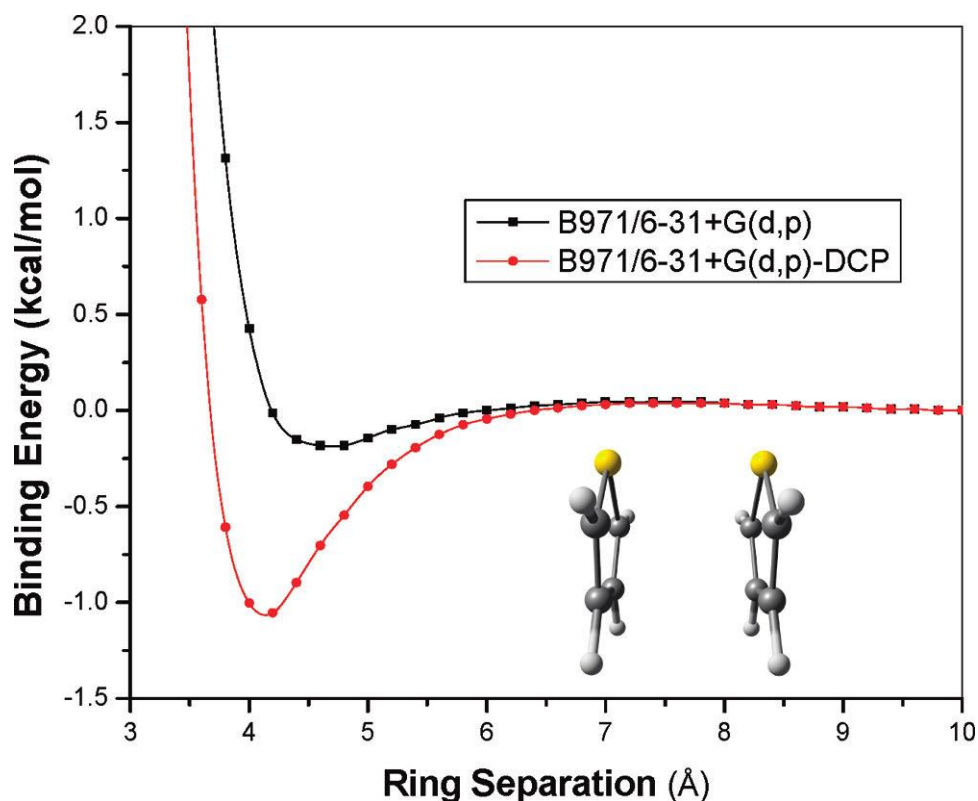


Figure 4.1. B971/6-31+G(d,p) potential energy surface for dimer **12a'** computed with and without carbon DCPs. The inclusion of DCPs (red) accurately predicts the dimer separation and binding energy.

The fact that DCPs are atom-centered potentials means that they can be used in any computational chemistry code that can handle effective-core potential input, and the overly repulsive behaviour of most functionals with respect to dispersion binding can be corrected using the DCP approach without the need for programming. Therefore DCPs can be used with the full features of computational chemistry codes, viz., geometry optimizations, frequency calculations, implicit solvation, etc. A recent review of dispersion-corrected density-functional theory

methods shows that the DCP approach is competitive with other techniques, including the M0 family of functionals.²⁸

Geometry Optimizations and Frequency Calculations.

For all calculations, we used the PBE²⁴ density-functional with 6-31+G(d,p) basis sets. PBE was chosen (over, for example, B971) for reasons of efficiency, expecting the pure funcan

ctional to make the calculations on the larger thiophene dimers faster. This approach is summarized as PBE/6-31+G(d,p)-DCP. Self-consistent field(SCF) convergence criteria were set to 10^{-6} hartree. The Gaussian-03 package was used for all of the calculations.²⁹

Dimers composed of interacting oligomers of unsubstituted thiophenes one (T1) to six (T6) units long were studied (see Scheme 1). Dimer structures were built using optimized monomer structures. For each dimer, several starting structures were constructed by placing the monomers in different positions. Monomers were arranged in various slipped-parallel, cofacial, T-shaped, and tilted T-shaped orientations and then subjected to energy minimization. All dimer structures were verified as being true (local) minima on their respective potential energy surfaces by vibration frequency analysis.

Visualizations of structures and molecular orbitals were performed using the Chemcraft program.³⁰ In some cases, the Spartan Program³¹ was used to evaluate certain geometric parameters.

Orbital Energy Splittings in Dimers.

As described above, the orbital energy splittings (hereafter S) are the energy differences between the dimer bonding (or antibonding) orbitals formed from the overlap of the monomer HOMOs (or LUMOs). Figure 1 illustrates the case for the overlap between two monomer HOMOs (blue) that result in the formation of the dimer HOMO-1 (red) and HOMO (green). (HOMO-1 refers to the occupied orbital that is energetically immediately below the highest occupied molecular orbital. LUMO+1 refers to the unoccupied orbital that is energetically immediately above the lowest unoccupied molecular orbital). That is, upon formation of a thiophene dimer, the two HOMOs of the monomers overlap and produce two dimer orbitals. These dimer orbitals nominally represent the bonding and antibonding overlap of the monomer HOMOs and are, respectively, the dimer HOMO-1 and dimer HOMO. Likewise, the overlap between two monomer LUMOs nominally results in a bonding-type dimer orbital (the dimer LUMO) and an antibonding-type dimer orbital (the dimer LUMO+1). Figure 4.2 is a simple illustration showing how S changes as a function of overlap between two (model) orbitals. To identify the orbitals in this connection derived from the calculations in this thesis, visual inspection of the orbital isosurfaces were performed. This verified that splitting values were generally derived from the HOMO/HOMO-1 and LUMO/LUMO+1 orbital pairs.

Additional calculations were performed to evaluate the effects of zero-point vibration on energy splittings. Three low-energy vibrations associated with

the relative slipping, rotation, and breathing motions of monomers with selected dimers were identified. For each mode, the structures for the turning points of the vibration were found and energy splittings were evaluated. The turning-point structures were found by displacing the monomers in a particular dimer structure along the selected vibration mode. The extent of the displacement is such that the energy of the displaced structure is higher than that of the minimum energy structure by $1/2V$, where V is the energy of the vibration mode (see Figure 4.3).

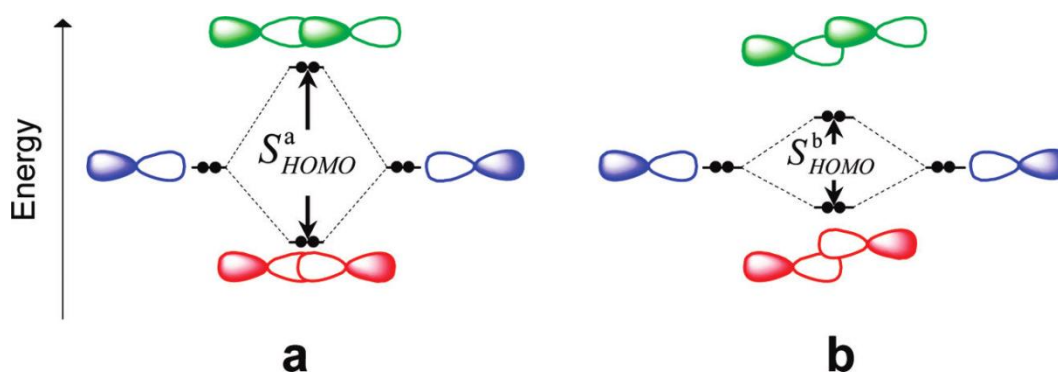


Figure 4.2. Schematic illustrating the energy splitting between the filled (electrons are black dots) dimer HOMO (green) and HOMO-1 (red) orbitals as a function of overlap between two filled, monomer orbitals (blue). When the orbitals are perfectly overlapping, as in the case of *a*, maximum splitting is nominally achieved. When overlap is less than ideal, as in the case of *b*, splitting is reduced (viz. $S_{HOMO}^a > S_{HOMO}^b$). Splitting between dimer LUMOs can be similarly illustrated, but with empty orbitals.

4.3 Results and Discussion

Orbital Splittings in a T1 Dimer Model.

To investigate the transport properties of thiophenes, a detailed analysis of the binding energy (BE) and orbital splittings were performed for the simplest system in this study, the T1 dimer. These analyses will prove useful in understanding some of the key interactions in the larger thiophene dimers and will be discussed later on in this thesis.

Examination of the orbitals on the T1 monomer shows that the HOMO density resides on the carbon-carbon bonds with a nodal plane down the centre of the ring (see Figure 4.3A). The LUMO is more complex with two nodal planes and orbital density on all five atoms making up the ring (see Figure 4.3B). It is important to point out that these orbital representations are very similar to those for the longer oligothiophene monomers. This is due to the fact that orbitals on the oligomer resemble repeating monomer orbitals and thus these simple T1 models can offer insight into larger systems. An important difference, however, is that the LUMO orbitals in the oligothiophenes have density on the C-C bonds between adjacent rings (see Figure 4.3c).

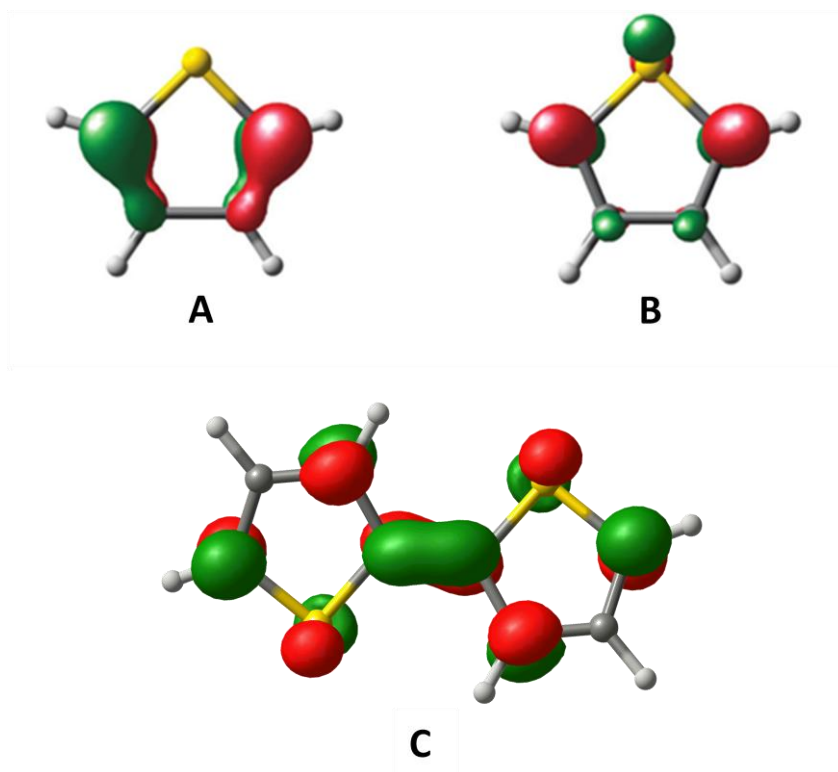


Figure 4.3. A) Highest occupied and B) lowest unoccupied molecular orbitals of the T1 monomer. The colours of the orbitals represent their relative phases. C) The lowest unoccupied molecular orbital of a T2 shown for comparison. The atom coloring scheme yellow (sulphur), gray (carbon), white (hydrogen) is used throughout this chapter, unless otherwise indicated.

To understand how orbital splittings change with the overlap in the T1 dimer, calculations were performed on the C_{2h} symmetric T1 system. In this arrangement, the thiophene rings are perfectly stacked as shown in Figure 4.1. Although this arrangement is not stable on the dimer potential energy surface (PES), it will serve as a model for understanding how various intradimer structures lead to different orbital splittings (S). Figure 4.4 shows the various

displacements used to calculate the orbital splittings in the T1 system. With the planes defined by the monomer atoms fixed at a distance of 3.8 Å, S values were computed at geometries corresponding to the lateral displacement of one monomer along a direction (i) parallel to and (ii) perpendicular to the C_2 rotation axis (see Figure 4.4A). Under the same fixed-plane separation conditions, S values corresponding to the relative rotation of one monomer were also computed, Figure 4.4B iii. In addition, the splittings as a function of monomer separation in the stacked structure, viz., along the direction indicated in Figure 4.4B iv were calculated.

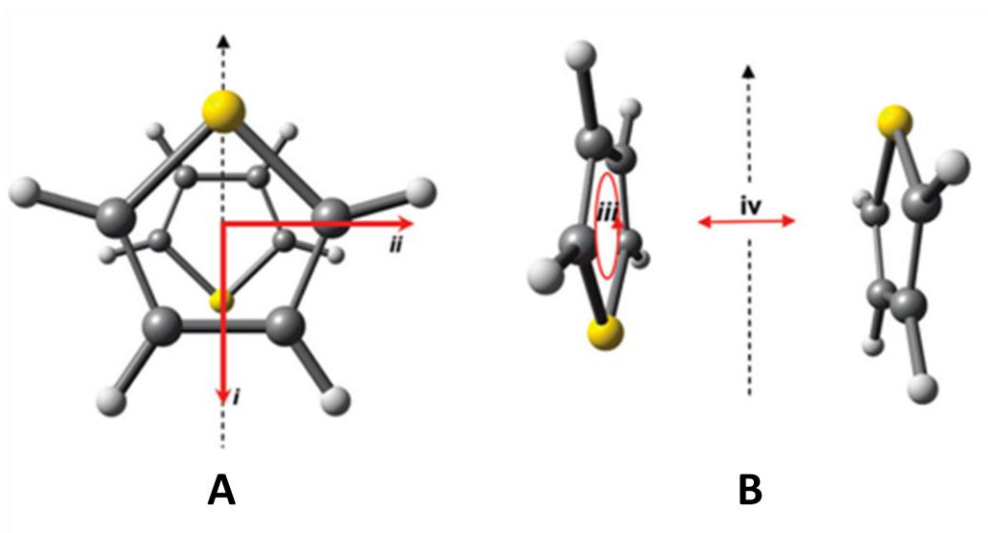


Figure 4.4. Two perspective views of a stacked T1 dimer with C_{2h} symmetry are shown in (A) and (B). Orbital splittings are evaluated for displacements along the directions i and ii in (A) and along iv in (B) and for rotation about an axis perpendicular to the plane of the molecules (indicated by iii). For displacements along i and ii, the initial monomer separation is 3.8 Å. For rotations about iii, monomer separation is maintained at 3.8 Å.

The results of the displacement of one thiophene in the T1 dimer system along direction “i” as indicated in Figure 4.4A is shown in Figure 4.5. The lower panel of the Figure plots the BE vs. displacement. It can be seen that the slipped-parallel conformation is preferred over the perfectly stacked arrangement (vide infra). The overall binding in the dimer is increased when the displacement is changed from 0 to 1.9 Å. This is consistent with the theoretical results obtained in the work done by Tsuzuki et al.¹⁶

The orbital splittings can be seen in the top panel of Figure 4.5. At approximately 0.4 Å the HOMO splitting is at a maximum. There is a general exponential decrease in splitting on either side of this maximum which can be understood by considering the bonding overlap in the HOMO-1 and the antibonding overlap in the dimer HOMO with increased (or decreased) displacement (not shown in Figure 4.5). Figure 4.2 in the introduction can be used to understand the effect of decreased overlap on orbital splitting. The S_{HOMO} decreases fairly slowly since some overlap in the dimer HOMO/HOMO-1 is maintained over a large displacement range. The values do not reach zero until ca. 8.0 Å.

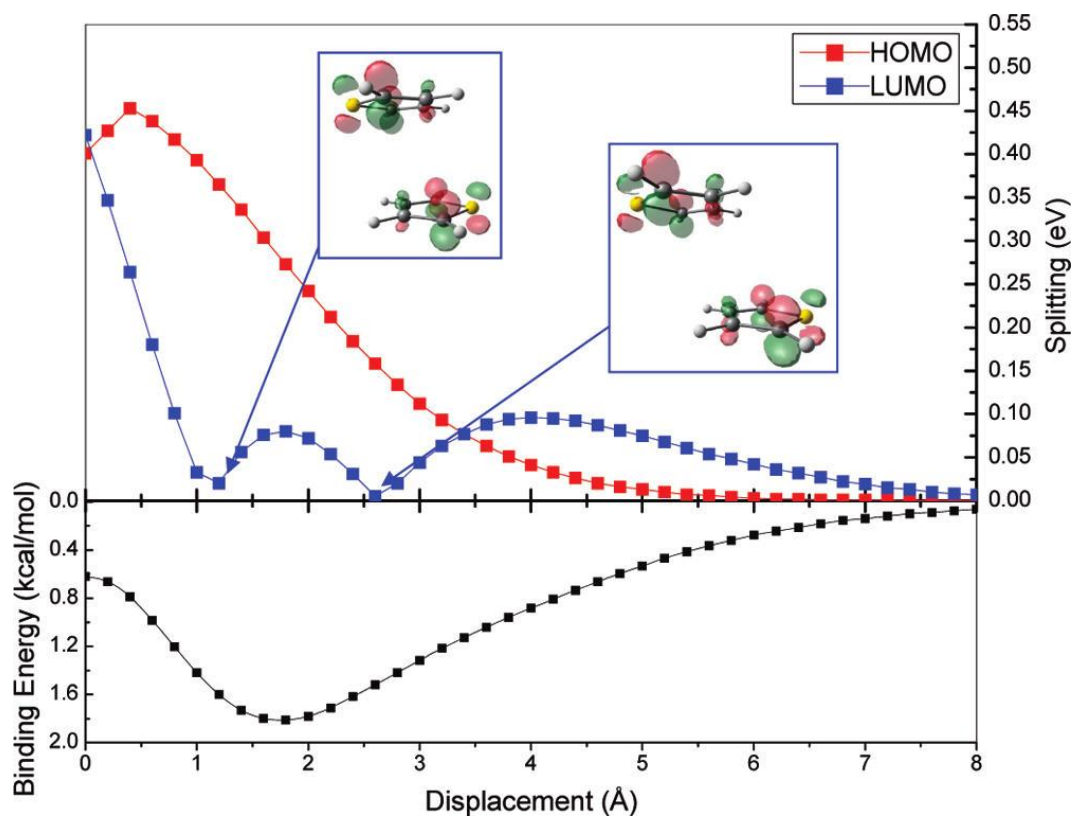


Figure 4.5. (Lower panel) Binding energy as a function of the displacement of one thiophene monomer in the T1 dimer along the direction “i” indicated in Figure 4.4A. (Upper panel) Energy splitting between two highest occupied molecular orbitals (S_{HOMO} , red) and the two lowest unoccupied molecular orbitals (S_{LUMO} , blue) as a function of displacement distance. Insets show the molecular orientation and representations of the dimer LUMO+1 orbitals for two displacements. The relative phases of the orbitals are indicated as green and red.

The changes in S_{LUMO} are more complicated due to the T1 monomer LUMO having multiple nodes (see Figure 4.3 and 4.5 insets). The S_{LUMO} is at a maximum at zero displacement. The dimer LUMO (LUMO+1) is derived from

the fully bonding (antibonding) overlap of the T1 monomer LUMOs. At 1.2 Å, the S_{LUMO} drops to zero (see left-most inset in Figure 4.5). The rapid decrease in value can be understood from the fact that the dimer LUMO takes on antibonding character with increased displacement. The insets in Figure 4.5 show that a small displacement from the stacked configuration moves the positive (green) lobe of the p-type orbital of the S atom on one of the rings away from the negative (red) lobes of the carbon atoms of the second ring. This results in the reduction of antibonding overlap in the dimer LUMO+1 orbital. Beyond displacements of 2.6 Å, the S_{LUMO} increases to a maximum value at approximately 4.0 Å. This is due to the bonding (antibonding) character in the LUMO (LUMO+1) being restored. A second point of nearly zero splitting between the LUMO and LUMO+1 orbitals occurs at about 2.5 Å along the “i” direction (see right-most inset in Figure 4.5).

The displacement of the T1 thiophene dimer along the direction “ii” was calculated for BE and splitting with the results shown in Figure 4.6. These results show that a slipped-parallel conformation is the lowest energy configuration. This motif is the most stable of any of the π -stacked structures adopted by the T1 dimer. At approximately 1.9 Å, binding in the dimer is at a maximum with an energy of ~1.9 kcal/mol (see lower panel of Figure 4.6). These results are consistent with previous work on similar systems.^{16, 22, 32}

Splitting values were calculated for the displacement along direction “ii” and are shown in the upper panel of Figure 4.6. At zero displacement, S_{HOMO} is a maximum and the HOMO-1 has maximum bonding overlap. The insets show the dimer HOMO orbitals at zero displacement (left-most inset) as well as at 2 Å.

Specifically, in the dimer HOMO-1, the negative and positive lobes of one monomer HOMO overlap with the negative and positive lobes of the HOMO of the second monomer. At zero displacement, the dimer HOMO has maximum antibonding overlap. As one monomer is displaced along the “ii” direction (see Figure 4.4A), the bonding overlap in the HOMO-1 decreases through an increase in distance between monomer orbital lobes of the same phase. In addition, a decrease in distance between monomer orbital lobes with different phases increases the HOMO-1 bonding overlap. At a displacement of ca. 1.9 Å, the bonding and antibonding contributions to the dimer HOMO-1 and HOMO orbitals are about equal and the orbital splitting is zero. Increasing the displacement beyond 1.9 Å restores some bonding (antibonding) character in the dimer HOMO-1 (HOMO) orbitals through the partial overlap of the monomer orbitals (see Figure 4.6, right-most inset). We note that (arbitrary) phase labels of one of the monomer orbitals are flipped in this dimer orientation relative to the perfectly stacked structure. The expected exponential decrease in S_{HOMO} occurs over the displacement range of 3-6 Å. S_{LUMO} tends to decrease slowly to zero in an exponential fashion with displacement.

Figure 4.7 shows the BE (lower panel) and orbital splittings (upper panel) as a function of the rotation angle of one monomer relative to the other monomer in the dimer. The BE decreases from ca. 1.2 kcal/mol at 0° to ca. 0.6 kcal/mol at 180°. The energy difference can be understood by considering the relative orientation of the monomer dipoles in the dimer. At 0°, the monomer dipoles are antialigned whereas they are fully aligned at 180°. Antialigned molecular dipoles

are generally (but not always, vide infra) more energetically favoured than aligned dipoles.

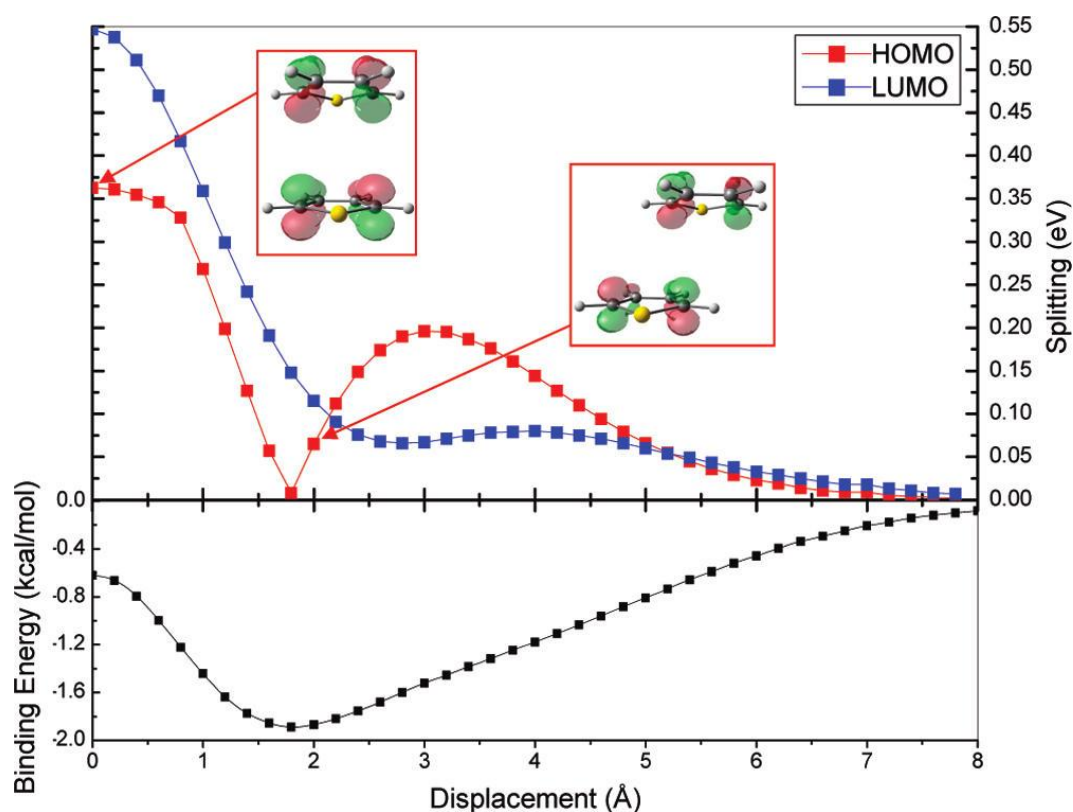


Figure 4. 6. (Lower panel) Binding energy as a function of the displacement of one thiophene monomer in the T1 dimer along the direction “ii” indicated in Figure 4.4B. (Upper panel) Energy splitting between two highest occupied molecular orbitals (S_{HOMO} , red) and the two lowest unoccupied molecular orbitals (S_{LUMO} , blue) as a function of displacement distance. Insets show the molecular orientation for two displacements of the dimer with representations of the corresponding highest occupied molecular orbitals. The relative phases of the orbitals are indicated as green and red.

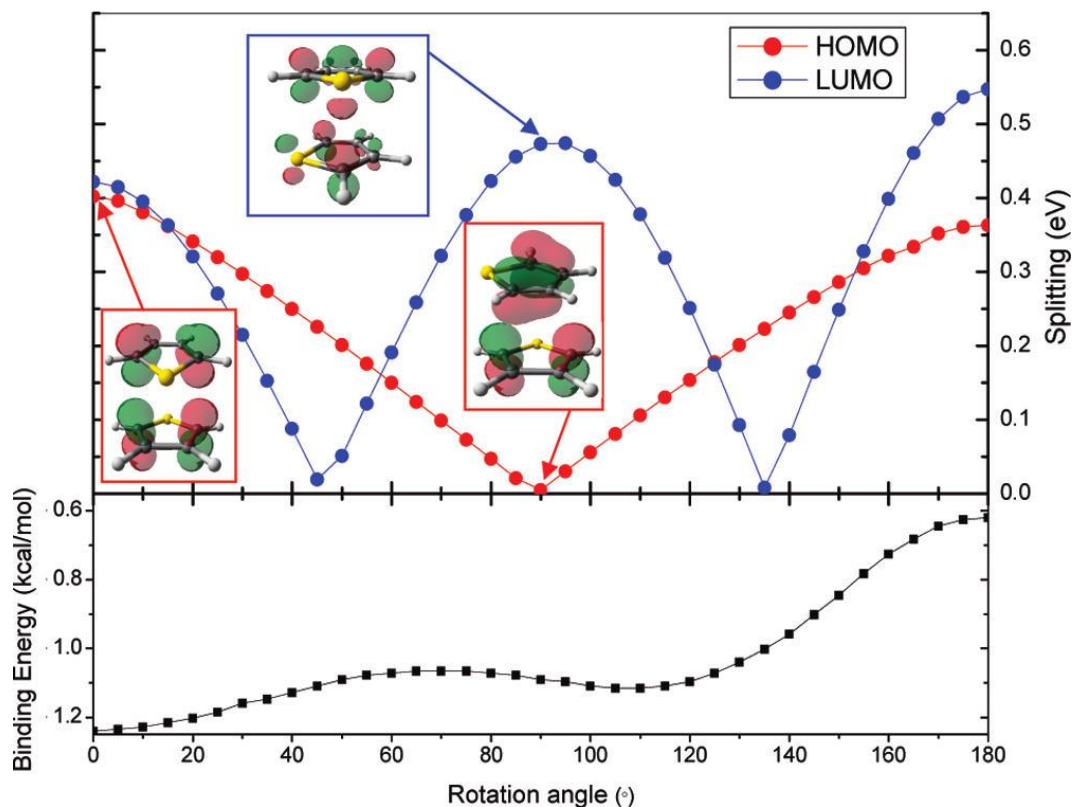


Figure 4.7. (Lower panel) Binding energy as a function of the rotation of one thiophene monomer in the T1 dimer, according to “iii” indicated in Figure 4.4B. **(Upper panel)** Energy splitting between two highest occupied molecular orbitals (S_{HOMO} , red) and the two lowest unoccupied molecular orbitals (S_{HOMO} , blue) as a function of displacement distance. Insets show the molecular orientations for the indicated rotations. Representations of the highest occupied molecular orbitals for two rotations (red frame) and the lowest unoccupied molecular orbitals for one rotation (blue frame) are displayed in the insets. The relative phases of the orbitals are indicated as green and red.

Maxima for S_{HOMO} occur at orientations of 0 and 180° with the former structure having the larger splitting value (see leftmost inset). This implies that better orbital overlap of the monomer HOMOs is achieved in the dipole antialigned structure. Both the 0 and 180° structures correspond to orientations in which the HOMO-1 (HOMO) dimer orbitals have maximum bonding (antibonding) character as a function of rotation angle. The splitting values decrease monotonically to zero at 90°, in which the bonding and antibonding overlaps roughly cancel in both the HOMO and HOMO-1 of the dimer. The red-framed, central inset in Figure 4.7 shows how this cancellation can occur: The negative lobe of the orbital on one monomer (forefront of inset) overlaps with both the positive and negative lobes of the orbital on the second monomer. Similarly, the positive lobe of the orbital on one monomer (at rear of inset) overlaps with both the positive and negative lobes of the orbital on the second monomer.

S_{LUMO} has maxima at 0, 90, and 180° structures in which the dimer LUMO (LUMO+1) has bonding (antibonding) character. The blue-framed inset at the right in Figure 4.7 shows the LUMO for the 90° structure. The minima in S_{LUMO} at ca. 45° and 135° correspond to structures in which the dimer LUMO (LUMO+1) is antibonding (bonding) in nature. Note that to maintain the most energetically favourable orbital overlap, changes in the (arbitrary) orbital phases for one monomer must occur in certain regions of rotation angle. These phase “flips” occur near 45° and 135°.

For completeness, we show in Figure 4.8 the BE and splitting curves as a function of dimer separation along the direction “iv” shown in Figure 4.4B. When dispersion is included in the calculation (see Figure 4.8, lower panel, black curve), the minimum in BE along this coordinate is ca. 1.3 kcal/mol. This binding causes the monomers to be separated by 4 Å. When dispersion is not included (see Figure 4.8, lower panel, red curve), the minimum in the dimer BE along this coordinate is only 0.1 kcal/mol. This weaker binding results in a larger minimum energy monomer separation of ca. 4.75 Å. As indicated by the vertical lines in Figure 4.8, the larger binding that arises from the inclusion of dispersion results in significantly larger orbital splittings than when dispersion is absent from the computational treatment.

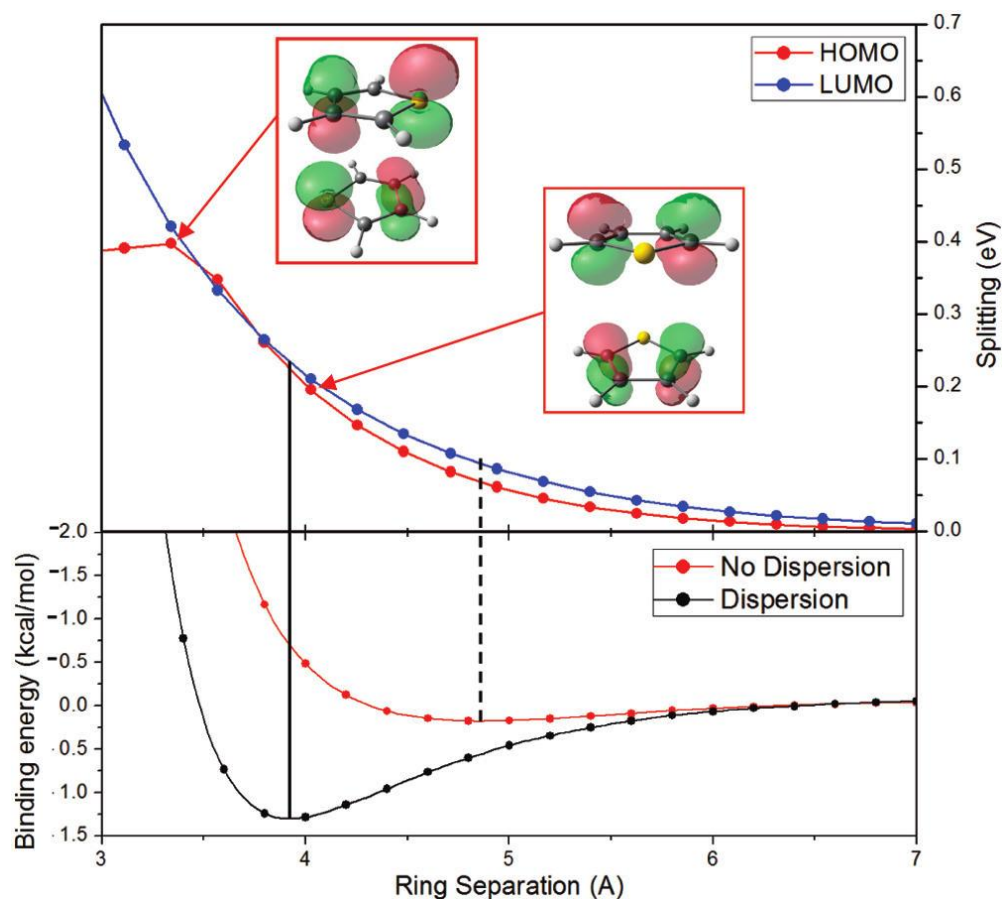


Figure 4.8. (Lower panel) Binding energy with DCPs (black), and without DCPs (red), as a function of the displacement of one thiophene monomer in the T1 dimer along the direction “iv” indicated in Figure 4.4B. **(Upper panel)** Energy splitting between two highest occupied orbitals (S_{HOMO} , red) and the two lowest unoccupied molecular orbitals (S_{LUMO} , blue) as a function of displacement distance. Insets show the molecular orientations for two displacements along with representations of the highest occupied molecular orbitals. Note that there is a change in the dimer HOMO character upon decreasing the intermonomer distance below 4 Å, c.f. left and right orbital insets. The relative phases of the orbitals are indicated as green and red. The vertical black lines show the values that are predicted for S_{HOMO} and S_{LUMO} when dispersion is taken into account (solid) and when dispersion is not taken into account (dashed).

S_{LUMO} decreases in a slow, exponential fashion as a function of displacement. S_{HOMO} shows a similar trend in the 4-7 Å displacement range, but different behaviour is observed at distances less than 4 Å. The nonexponential behaviour in the range of 3.0-3.5 Å arises from the reordering of monomer orbitals. At small displacements, interactions within the dimer cause the HOMO-1 to be composed of the monomer HOMO-1, rather than the monomer HOMO (as is the case for all other examples described in this section). These HOMO-1 orbitals are shown in the left-most inset in Figure 4.8 and can be compared with HOMOs shown in the right-most inset.

An important point to extract from the data shown in Figures 4.5-4.8 in the cases where the calculations were performed with dispersion-corrected DFT is that the largest orbital splittings are not necessarily obtained for dimers that have the largest BEs. This may seem counterintuitive at first thought. However, it should be kept in mind that BE is derived from the interactions associated with all of the orbitals within a dimer, whereas S_{HOMO} and S_{LUMO} involve only the monomer HOMO and LUMO orbitals. Therefore stronger binding in a dimer of any kind does not necessarily result in larger orbital splittings. A second important point can be derived from Figure 4.8 in which it can be seen that smaller monomer separations generally, but not always, result in larger orbital splittings. For example, in the model stacked T1 dimer system, S_{HOMO} values are smaller at intermonomer separations of 3.0 than at 3.4 Å (vide supra). This may indicate that orbital splitting as an indication of the transfer integral in equation 1 breaks down

at short intermonomer separations. These two points should be kept in mind for the rational design of molecules for semiconductor applications.

Incorporating DCPs into the calculations for determining orbital splittings is critical to their accurate description when using DFT methods. Without the use of DCPs, the orbital splittings of the π -stacked dimer is predicted to be approximately 50% smaller than those predicted when dispersion is included in the DFT calculation of the dimer structure. This is a very clear demonstration of the impact of the theoretical method on the predicted electronic structure-function properties of organic materials.

Binding Energies and Orbital Splittings in Mono- and Oligothiophene Dimers.

Having outlined how dimer structure can influence orbital splittings, we now examine the S_{HOMO} and S_{LUMO} values in the minimum energy structures for mono and oligothiophenes as predicted by dispersion-corrected DFT. Geometry optimizations were applied to a variety of dimers at varying starting positions and used to relax the structures to their minimum energy configurations.

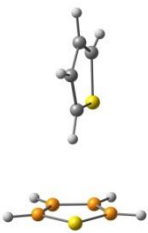
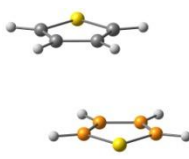
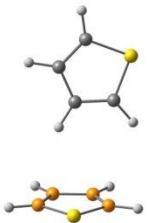
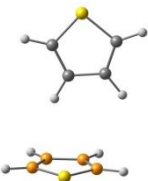
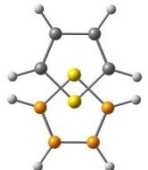
T1 Dimers.

Dimers of simple thiophenes (T1) have been well-studied^{16,22,33} and most dimers are found to have a T-shaped structure, similar to that displayed by T1A, C, and D (see table 4.1). Two of the structures can be described as π -stacked (for

example T1B, T1E). Coplanar structures of thiophenes are generally very weakly bound and will not be considered in the present work. The five structures shown in table 4.1 represent a selection of fully optimized T1 dimers with different structural motifs. Detailed discussion of the structural features of T1 dimers will not be presented here, as this has been provided in other works.^{16,22} This thesis will focus on the binding energies and splittings (S_{HOMO} and S_{LUMO}) that result from the orbital overlaps in some representative structures from table 4.1.

The most strongly bound T1 dimer (T1A) has a T-shaped structure with a BE of 2.9 kcal/mol, while the next most strongly bound dimer is the π -stacked T1B with a BE of 2.6 kcal/mol with monomer dipoles antialigned and some slipping between the thiophene rings. On the basis of previous benchmarking efforts, it is expected that these BEs well-reflect those that would be obtained by high-level theoretical methods.¹⁶

Table 4.1. Conformer Label and Selected Optimized Structures of T1 dimers. Binding Energy (BE, kcal/mol), Inter-Ring Separation (R, Å), Angle between Rings (θ , °) and Orbital Energy Splitting (S, eV) are also shown.

Dimer Conformation	BE	R	Angle	S _{HOMO}	S _{LUMO}
 T1A	2.9	4.73	86.4	0.347	0.325
 T1B	2.6	3.81	0	0.102	0.071
 T1C	2.4	4.80	88.86	0.352	0.324
 T1D	2.4	4.78	89.41	0.345	0.347
 T1E	1.8	4.09	0.79	0.316	0.217

Interestingly, the T-shaped dimers have large S_{HOMO} and S_{LUMO} values (see table 4.1), indicating large orbital overlaps between monomers. This is supported by inspection of the T1A dimer orbital isosurfaces, which show the HOMO orbital of one monomer in a bonding arrangement with the HOMO orbital of the second monomer to form the dimer HOMO-1, and the HOMO of one monomer in an antibonding arrangement with the HOMO of the second monomer form the dimer HOMO (see Figure 4.9). It is not clear that the splitting-in-dimer approach can be applied in a straightforward fashion to the T-shaped dimer. Nevertheless, orbital overlap results in a very large splitting between the dimer HOMO and HOMO-1 orbitals and between the LUMO and LUMO+1 orbitals. S values for the most stable π -stacked dimer, T1B, show much lower orbital splitting compared to the T-shaped dimers, as expected from the analysis in Figure 4.2. The T1B dimer orbitals shown in Figure 4.9 indicate that the slipping between monomers causes the dimer HOMO to stabilize relative to a perfectly π -stacked system while the HOMO-1 has destabilized as a result of the monomer positions and their respective orbital phases. Overall, this leads to a decrease in the S_{HOMO} value.

Similar arguments can be made for the LUMO and LUMO+1 systems of T1B where the relative orbital phases and monomer positions decrease the S_{LUMO} value. This is consistent with S_{HOMO} and S_{LUMO} values for dimers in which the monomers are displaced along the “i” and “ii” directions (see Figures 4.4A, 4.5, and 4.6) and agrees with work done by Hutchison et al. in which it was found that tilted T-shape structures have large values for S .¹⁵

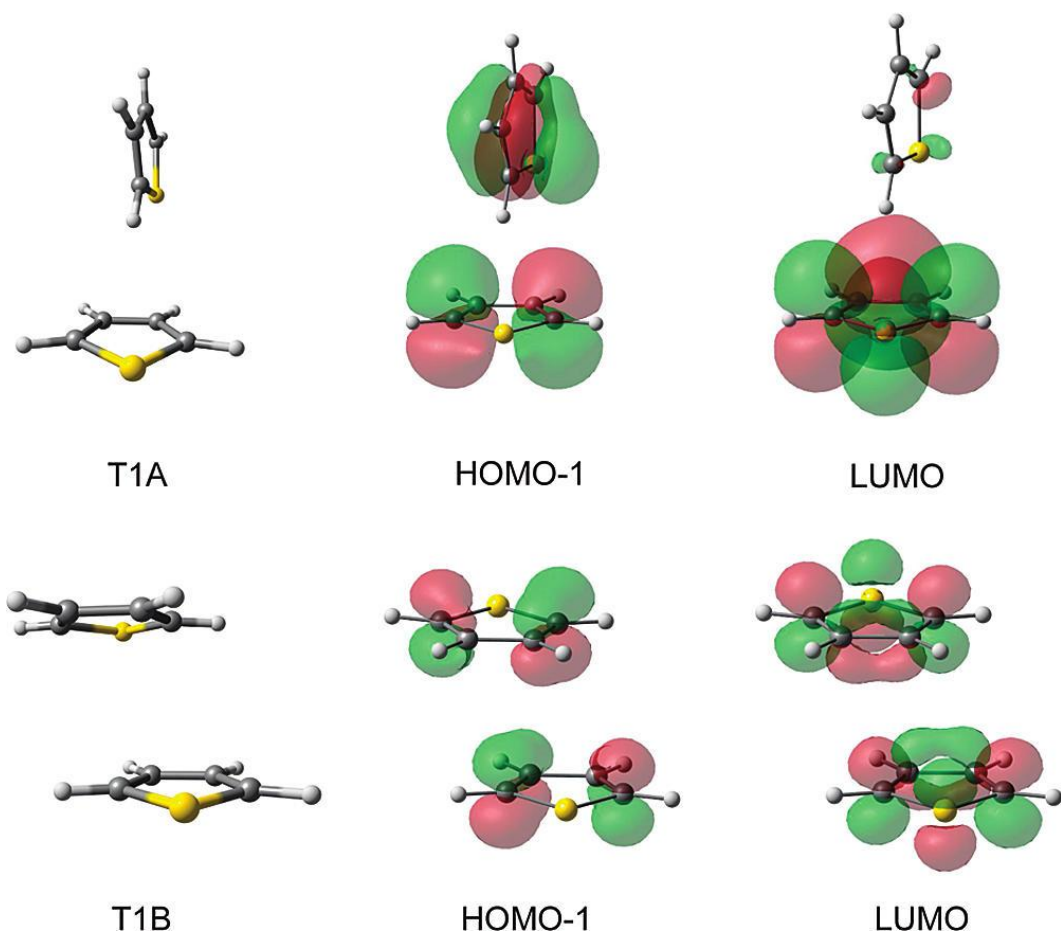


Figure 4.9. Two conformers of T1 dimers with selected associated dimer orbitals.

T-shaped dimers become less energetically favourable in dimers composed for longer-length thiophenes (*vide infra*), relative to π -stacked species. However, herringbone structures are known to be the lowest energy conformations for crystal structures of oligothiophenes.^{32,35} Larger S values are computed for more weakly bound π -stacked dimer structures (see table 4.1)

supporting the conclusion that splitting is not directly proportional to the strength of binding in the dimers.

T2 Dimers.

Some structural information along with BE and *S* data for the optimized T2 dimers are provided in Table 4.2 and 4.3. For dimers of T2, the lowest energy complexes are predominantly π -stacked structures. This is consistent with previous work on benzothiophene dimers,²² which showed that π -stacking (dispersion) interactions quickly dominate over the dipole-induced dipole interactions that are present in the T-shaped structures as the size of the thiophene system increases. BEs range from 7.6 to 4.4 kcal/mol and depend to some extent on the intermonomer ring angles (see tables 4.2 and 4.3). That is, as the angle between two planar monomers increases, point contacts between them decrease and binding energies become smaller. It is interesting to note that the BE of T2A, the most strongly bound π -stacked T2 dimer, is almost three times larger than the BE of T1B, the most strongly bound π -stacked T1 dimer. The “extra” binding in the T2 dimer may simply be the result of more point contacts, viz., a larger number of atom-atom interactions as compared to dimers of T1.

Table 4.2. Conformer Label and Selected Optimized Structures of T2 dimers. Binding Energy (BE, kcal/mol), Inter-Ring Separation (R, Å), Angle between Rings (θ , °) and Orbital Energy Splitting (S, eV) are also shown. Table 4.3 lists the remainder of the T2 dimers.

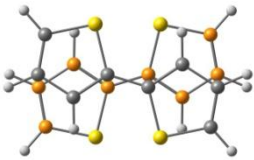
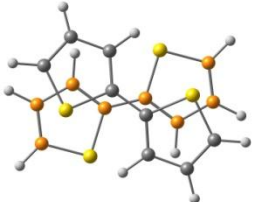
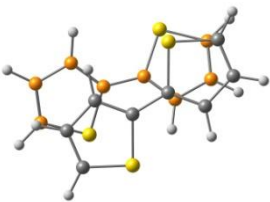
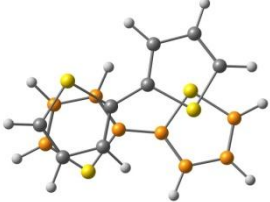
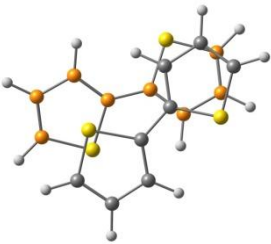
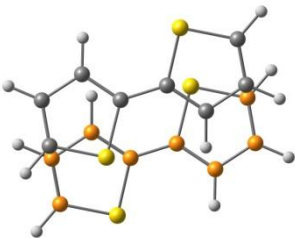
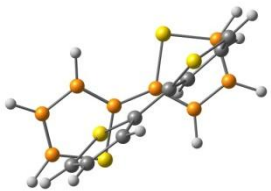
Dimer Conformation	BE	R	Angle	S _{HOMO}	S _{LUMO}
 T2A	7.6	3.64	2.8	0.237	0.155
 T2B	7.2	3.79	6.4	0.150	0.162
 T2C	6.1	3.89	18.3	0.243	0.106
 T2D	6.0	3.84	20.9	0.356	0.082

Table 4.3. Conformer Label and Selected Optimized Structures of T2 dimers. Binding Energy (BE, kcal/mol), Inter-Ring Separation (R, Å), Angle between Rings (θ , °) and Orbital Energy Splitting (S, eV) are also shown.

Dimer Conformation	BE	R	Angle	S _{HOMO}	S _{LUMO}
 T2E	6.0	3.87	21.6	0.286	0.068
 T2F	5.9	3.87	0.0	0.305	0.026
 T2G	4.4	4.88	67.9	0.308	0.336

The monomer dipoles in T2A are approximately perpendicular to each other. One might assume that antialignment of the monomer dipoles would confer more stability on the dimers, but this is not clear, in particular for the case of T2A. In fact, several dimers having monomer dipoles aligned while the antialigned structures have BEs that are within 0.2 kcal/mol of each other. Similar findings

for dimers of benzothiophenes were reported in reference 22. This suggests that dipole-dipole interactions have only a small influence on the relative orientation of monomers in T2 dimers.

Dimers of T2 have a broad range of S values, despite the fact that some of them have significant structural similarities. As was noted above, the most strongly bound dimers do not have the largest splitting values. The largest S_{HOMO} , for example, is obtained for T2D, a structure that has a calculated BE that is 1.6 kcal/mol lower than the most strongly bound dimer, T2A (see table 4.2).

It is interesting to note that of the metastable structures found, dimers T2C, D, E, and F have BEs that are within 0.2 kcal/mol (or 3%) of each other while values of S_{HOMO} and S_{LUMO} for these species span ranges of 0.113 eV ($\sim 40\%$) and 0.080 eV ($>100\%$), respectively. This points to a high degree of sensitivity in carrier transport in these thiophenes which will become even more apparent as the size of the thiophene systems studied here increases (vide infra).

The orbital overlap leading to S_{HOMO} and S_{LUMO} for some of the T2 dimers can be seen in Figure 4.10. T2A has significant rotational displacement between the constituent monomers. Nevertheless, S_{HOMO} and S_{LUMO} values are fairly large, viz. 0.237 and 0.155 eV, respectively. The former can be understood by considering the structure of the dimer in the context of Figures 4.5-4.8. The S_{LUMO} value results because good orbital overlap is achieved from having orbital density along the C-C bonds between adjacent thiophene rings and the monomer C-C bonds overlay each other in the dimer.

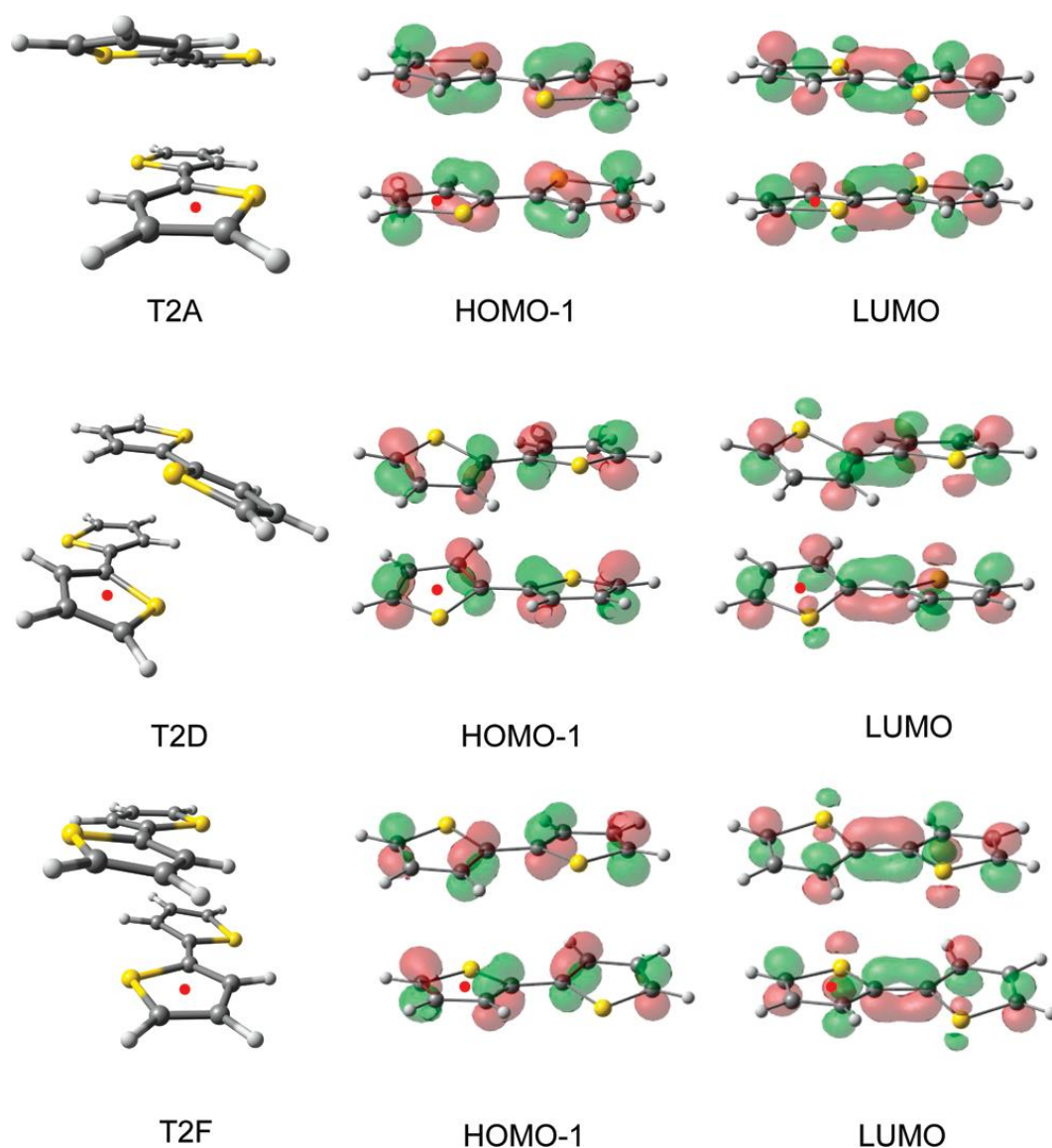


Figure 4.10. Orbital isosurfaces for three representative dimers of the optimized T2 system as found using DCP-DFT. Red dots are used to identify the same rings in each view of a dimer structure.

T2D has a rotated and slipped (along the “i” direction, see Figure 4.4A) structural motif that leads to overlap between the one of one monomer and one

ring of the second monomer. T2F has a dipole aligned slipped structure that maintains some overlap between both of the rings of each monomer. In keeping with the analyses derived from Figures 4.5 and 4.6, respectively, T2D and T2F have structures that lead to relatively large S_{HOMO} (>0.3 eV). For example, Figure 4.5 shows a significant amount of splitting can occur even with slipping displacements of ca. 2 Å. However, S_{LUMO} values are more sensitive to such slipping displacement. The slipping along the “i” direction also reduces the overlap between the LUMO orbital density that is associated with the C-C bonds connecting the monomer thiophene rings. This leads to small S_{LUMO} (<0.09 eV) values for T2D and T2F.

T3 Dimers.

Six minimum energy structures were found for the T3 dimer. Tables 4.4 and 4.5 list the BEs and S values along with the other structural parameters. Three of the more structurally interesting dimers are shown in Figure 4.11. All of the T3 dimers have slipped π -stacked arrangements with average intermonomer ring angles below 7.5° . No T-shaped structures were found and so π -stacking interactions are seen to completely dominate over dipole-induced dipole interactions. Binding energies range from 10.3 to 9.5 kcal/mol. All of the dimers have average separations ranging from 3.80 to 3.86 Å and display, to varying extents, relative displacements along the short axes (viz. the “i” direction) of the dimers. As is the case for the T2 dimers, it is not clear that the alignment of the dipoles add much to the stability of the dimers.

Table 4.4. Conformer Label and Selected Optimized Structures of T3 dimers. Binding Energy (BE, kcal/mol), Inter-Ring Separation (R, Å), Angle between Rings (θ , °) and Orbital Energy Splitting (S, eV) are also shown. Table 4.5 lists the remainder of the T3 dimers.

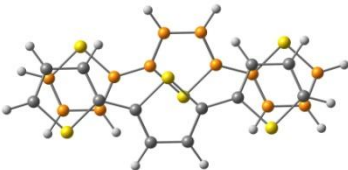
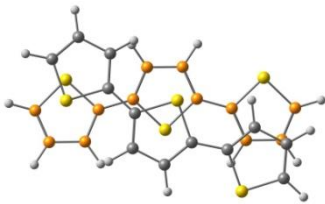
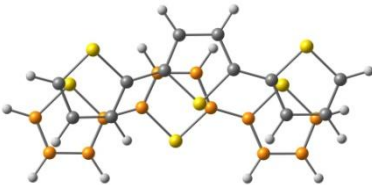
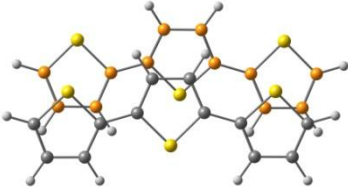
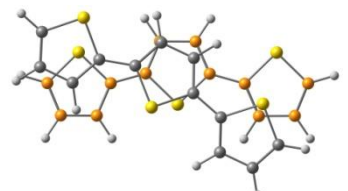
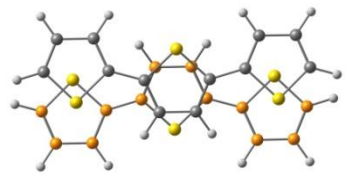
Dimer Conformation	BE	R	Angle	S _{HOMO}	S _{LUMO}
 T3A	10.29	3.80	0.20	0.183	0.013
 T3B	10.21	3.83	0.22	0.152	0.176
 T3C	10.05	3.84	3.10	0.334	0.054

Table 4.5. Conformer Label and Selected Optimized Structures of T3 dimers.
Binding Energy (BE, kcal/mol), Inter-Ring Separation (R, Å), Angle between Rings (θ , °)
and Orbital Energy Splitting (S, eV) are also shown.

Dimer Conformation	BE	R	Angle	S _{HOMO}	S _{LUMO}
 T3D	9.99	3.86	2.66	0.161	0.041
 T3E	9.87	3.81	7.40	0.263	0.150
 T3F	9.54	3.85	0.10	0.376	0.157

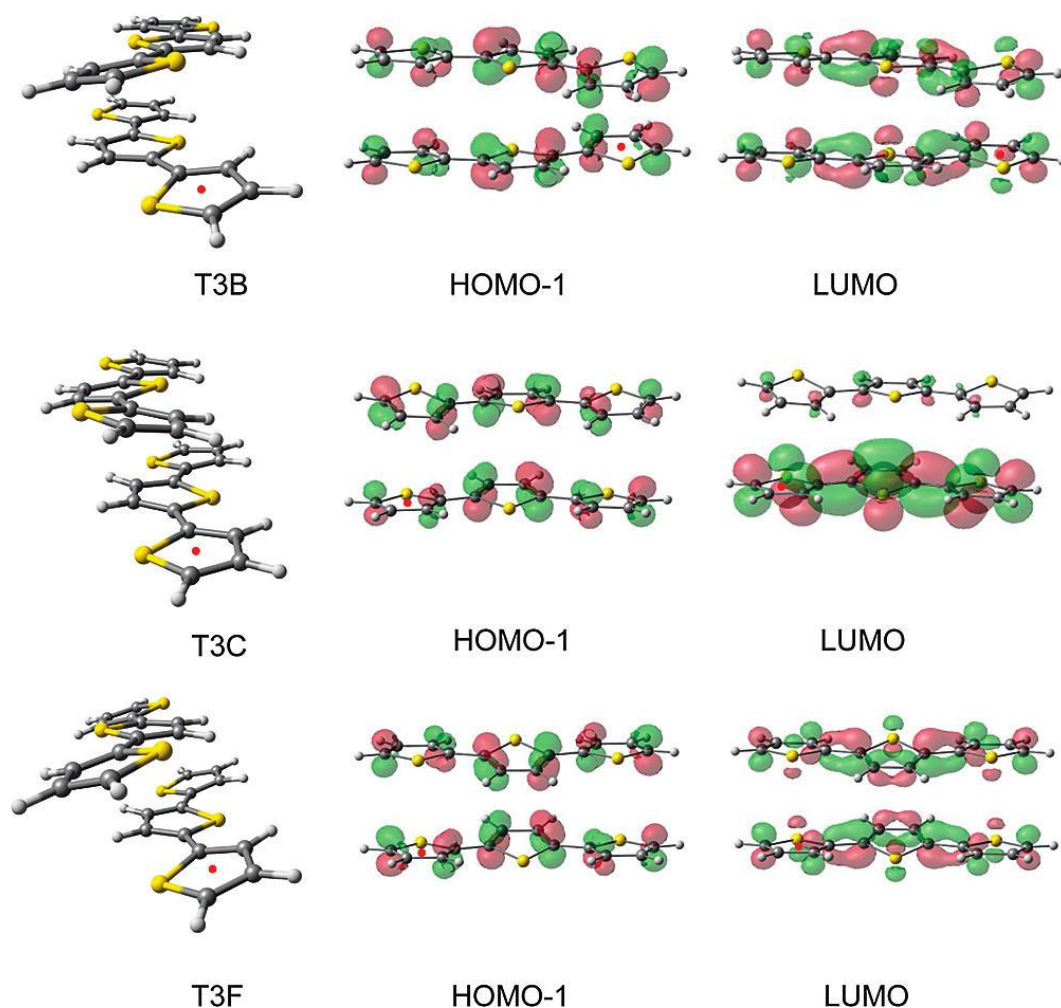


Figure 4.11. Orbital isosurfaces for two representative dimers of the optimized T3 system as found using DCP-DFT. Red dots are used to identify the same rings in each view of a dimer structure.

Dimers of T3 display a fairly broad range of S values, despite the small differences in BEs between structures. That is, all the structures have BEs that are within a 0.8 kcal/mol (ca. 7%) of each other, whereas the S_{HOMO} values range from 0.376 to 0.152 eV and the S_{LUMO} values from 0.176 to 0.013 eV). The most strongly bound dimer, T3A and the most weakly bound dimer, T3F, are predicted

to have the largest S_{HOMO} value. This once again illustrates the absence of correlation between stability of the structures and their splitting parameters.

T3B has a BE of 10.2 kcal/mol, making it one of the more strongly bound dimers found during the calculations. It has a rotated, slipped (along “i”) structure with reasonable S_{HOMO} and S_{LUMO} values (see table 4.4). Despite the relative displacement of monomers within the dimer, some limited HOMO/LUMO overlap is achieved (see Figure 4.11). The overlap of the orbital density associated with C-C bonds between thiophene rings contributes to S_{LUMO} for T3B.

T3C also has a relatively large BE with a value of 10.1 kcal/mol. In this case, the dimer has monomer relative displacements along the “i” and “ii” directions. Consistent with the analyses in Figures 4.5 and 4.6, and with the example of T2D, this dimer is found to have a large value for S_{HOMO} and a small value for S_{LUMO} .

T3F is an example of a more weakly bound dimer, with a BE of 9.5 kcal/mol and with a large S_{HOMO} and a small S_{LUMO} . The structure has one of the monomers displaced along the “i” direction to the extent that there is overlap only between the central rings of the monomers. The central rings are themselves displaced relative to each other by ca. 2 Å and it can be seen from this region of Figure 4.5 that this leads to the large predicted splittings. The orbital pictures in Figure 4.11 support this analysis.

Dimers of T4, T5 and T6.

The calculations predict limited structural diversity in oligothiophene dimers with increasing monomer size. All dimer structures are dominated by π - π interactions with variances that are similar to those that were observed in the T3 (and smaller) dimers. That is, the different dimer structural motifs are those associated with small relative displacements of the monomers along the axes labelled “i ” and “ii ” (see Figure 4.4A) and/or by a relative rotation of the monomers.

Table 4.6 summarizes the calculated results for dimers composed of T4, T5, and T6. Included in the table are labels indicating the structural motifs of the dimers, BEs, and S_{HOMO} and S_{LUMO} values. The former are labelled according to the nature of the relative monomer displacements/rotations, as indicated in Figure 4.4.

As can be seen from Table 4.6, the range of BE values are quite low despite the structural variation of the dimers. BEs differ by only 0.6, 0.8, and 0.7 kcal/mol for the T4, T5, and T6 dimers, respectively. These models, which neglect polymer matrix and crystal packing effects, suggest that thin films composed of these oligothiophenes will have a significant number of conformations that are energetically accessible at room temperature [RT(298 K) = 0.59 kcal/mol]. Despite the small differences in conformer BEs, the splitting parameters are predicted to vary considerably. Values of S_{HOMO} (S_{LUMO}) have ranges of 0.217 (0.199), 0.273 (0.125), and 0.188 (0.092) eV for T4, T5, and T6 dimers, respectively. Most plastic electronic devices are composed of hole

transporting thin films and this may speak to some of the sensitivity seen in these devices.

The main findings of this subsection support the earlier conclusion that larger binding energies do not necessarily confer larger orbital splittings upon a dimer. This fact should be considered when designing organic materials for electronic transport.

These calculations also predict that a significant number of energetically closely spaced conformations of dimers exist and that the conformations can have very different orbital splittings. At room temperature, these conformations will have a significant Boltzmann population, suggesting that it may be difficult to engineer crystals that do not contain regions of low S values.

TABLE 4.6. Binding Energy (BE, kcal/mol), HOMO (S_{HOMO} , eV), and LUMO Splitting (S_{LUMO} , eV) Ranges for Various Structures of T4, T5, and T6 Dimers^a

Dimer	Displacement (structure label)	BE	S_{HOMO}	S_{LUMO}
T4	i, iii (T4A) i, ii (T4B) i, ii (T4C) ii (T4D) i (T4E)	14.1 -13.5	0.379 -0.162	0.213 -0.014
T5	i, ii (T5A) i, ii (T5B) i (T5C) i (T5D)	17.9 -17.1	0.379 -0.106	0.136 -0.011
T6	i, ii (T6A) ii (T6B) i, ii (T6C) i, iii (T6D)	21.9 -21.2	0.287 -0.099	0.122 -0.030

^a Structural motifs are indicated by the nature of the relative displacements of the monomers within the dimers. Bold indicates the lowest energy structure of the dimer group.

Changes in Splittings as a Consequence of Molecular Vibration

In the previous section, it was demonstrated that minor differences in structure can lead to large changes in orbital splitting. It is therefore possible that small changes in structure due to motions associated with zero-point vibration may also result in large changes in S . The Marcus equation takes into account electron-phonon coupling in a semiclassical fashion. Nevertheless, it is interesting to explore how vibrations and orbital overlap are coupled in some of these thiophenes. To do this, normal-mode analyses were performed on two T4 dimers as well as a T5 and T6 dimer. The T4 system has 174 vibration modes, many of which involve motions that introduce substantial changes in the relative position

of the two monomer units relative to each other. Three modes can be described as rotation, slipping, and breathing modes, as shown in Figure 4.12. Changes in S values for a particular dimer were determined by computing S for the structures representing the vibration turning points of each mode. These values are compiled in Table 4.7. Note that higher energy vibration modes, which usually involve bond stretching or bending, tend not to change the relative positions of the monomers in a dimer and therefore do not have a large impact on splitting.

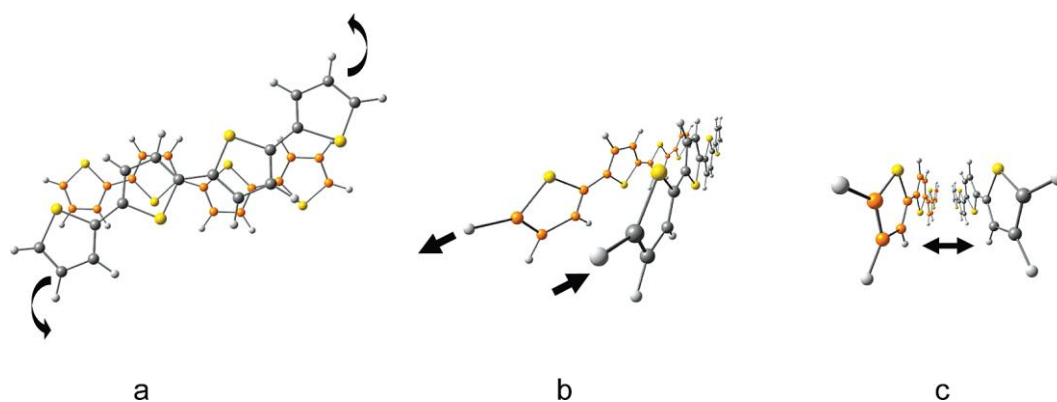


Figure 4.12. Perspective images showing (a) rotation, (b) slipping, and (c) breathing vibration modes in a T4 dimer. The carbon atoms in one monomer are coloured orange to help with differentiation.

TABLE 4.7. Vibration Mode, Frequency (cm^{-1}), and Changes in S_{HOMO} and S_{LUMO} (eV) at the Inner/Outer Vibration Turning Points for the T4A, T4D, T5B, and T6A Dimers.

Vibration Mode	frequency	ΔS_{HOMO}	ΔS_{LUMO}
T4D^a			
rotation	13.2	0.000/0.000	-0.029/-0.029
slipping	28.5	+0.024/-0.038	-0.014/+0.020
breathing	80.2	+0.020/-0.019	+0.007/-0.006
T4A^b			
rotation	16.4	-0.003/+0.002	-0.002/+0.001
slipping	15.8	0.000/0.000	-0.001/-0.001
breathing	90.8	+0.002/-0.003	+0.003/-0.007
T5B^c			
rotation	7.1	0.000/-0.003	0.000/+0.002
slipping	18.3	-0.012/+0.010	+0.002/0.000
breathing	109.4	-0.001/-0.001	0.000/+0.001
T6A^d			
rotation	7.3	0.000/0.000	0.000/0.000
slipping	18.2	-0.012/+0.011	-0.006/+0.005
breathing	85.8	-0.008/+0.008	+0.013/-0.015

^a For the minimum energy structure of T4D, $S_{\text{HOMO}} = 0.242$ and $S_{\text{LUMO}} = 0.213$. ^b For the minimum energy structure of T4A, $S_{\text{HOMO}} = 0.162$ and $S_{\text{LUMO}} = 0.180$. ^c For the minimum energy structure of T5B, $S_{\text{HOMO}} = 0.107$ and $S_{\text{LUMO}} = 0.011$. ^d For the minimum energy structure of T6A, $S_{\text{HOMO}} = 0.284$ and $S_{\text{LUMO}} = 0.030$.

For T4D, the vibration mode described as rotation leads to no significant change in S values. However, the slipping and breathing modes change S_{HOMO} by as much as ca. 16% for the slipping mode and ca. 8% for the breathing mode relative to the minimum energy structure. Smaller changes were found for S_{LUMO}

with the slipping mode changing the LUMO splitting by as much as ca. 9% and the breathing mode by as much as ca. 3%. Much smaller changes are seen in dimer T4A with the largest change seen in S_{LUMO} via the breathing mode leading to a change in splitting that is ca. 4% of that in the minimum energy structure.

Dimer T5B has a significant change in the ΔS_{HOMO} as seen in table 4.7 for the slipping mode with a value of ca. 11%. Table 5 also shows the splitting changes in dimer T6A. The slipping mode leads to a change of ca. 4% in the HOMO while the breathing mode leads to a change of ca. 3%. Larger percent changes in S_{LUMO} are predicted for the breathing mode in T6A but this is the result of having a very small S_{LUMO} for the minimum energy structure.

These data show that zero-point vibration may have a measurable impact on orbital splittings and, therefore, to mobility. In a crystal environment, such motions are expected to lead to band broadening.

4.4 Conclusion

This chapter showed the implications of orbital overlap on the carrier transport properties of oligothiophenes containing up to six rings within the “splitting-in-dimer” approximation, using density-functional theory with dispersion-correcting potentials. The results show that the proper accounting of dispersion interactions between thiophene monomers is critical for predicting correct intermonomer separations and, therefore, accurate orbital splittings. Using the thiophene dimer as a model system, we demonstrated that orbital splittings increase as intermonomer distances are reduced, but decrease when the monomers approach each other too closely. This implies that there may be an ideal intermolecule separation that provides the best transport properties. We also found that oligothiophene dimers have several low energy conformations within room-temperature thermal energy of the minimum energy structures. Despite small differences in the energies and geometries of dimers within an oligothiophene family, large differences in orbital splitting were found. This allows us to conclude that dimer binding energies and orbital splittings are not correlated. This chapter also revealed that orbital splittings can vary by as much as 10% as a result of low-energy vibration modes that change the relative positions of monomers within dimers.

These results reveal a number of important points to consider when engineering thin film devices requiring good carrier mobility. The transport properties depend on a number of molecular properties in a complicated fashion and this relationship is becoming increasingly well understood. This molecular

level understanding may lead to a more rational approach to fabricating hybrid solar cell devices that will provide better device performance.

4.5 References

1. Liu, W.; Liu, R.; Wang, W.; Li, W.; Liu, W.; Zheng, K.; Ma, L.; Tian, Y.; Bo, Z.; Huang, Y. J. *Phys. Chem. C* **2009**, *113*, 11385–11389.
2. Oikawa, K.; Monobe, H.; Nakayama, K.; Kimoto, T.; Tsuchiya, K.; Heinrich, B.; Guillon, D.; Shimizu, Y.; Yokoyama, M. *Adv. Mater.* **2007**, *19*, 1864–1868.
3. Mazzeo, M.; Vitale, V.; Della Sala, F.; Pisignano, D.; Anni, M.; Barbarella, G.; Favaretto, L.; Zanelli, A.; Cingolani, R.; Gigli, G. *Adv. Mater.* **2003**, *15*, 2060–2063.
4. Kim, Y.; Cook, S.; Tuladhar, S. M.; Choulis, S. A.; Nelson, J.; Durrant, J. R.; Bradley, D. D. C.; Giles, M.; McCulloch, I.; Ha, C.; Ree, M. *Nat. Mater.* **2006**, *5*, 197–203.
5. Wu, M. W.; Conwell, E. M. *Chem. Phys. Lett.* **1997**, *266*, 363–367.
6. Kjelstrup-Hansen, J.; Norton, J. E.; da Silva Filho, D. A.; Bredas, J. L.; Rubahn, H. *Org. Electronics* **2009**, *10*, 1228–1234.
7. Bredas, J. L.; Calbert, J. P.; da Silva Filho, D. A.; Cornil, J. *Proc. Nat. Acad. Sci. U.S.A.* **2002**, *99*, 5804–5809.
8. Marcus, R. A. *Rev. Mod. Phys.* **1993**, *65*, 599–610.

9. Bredas, J. L.; Beljonne, D.; Coropceanu, V.; Cornil, J. *Chem. Rev.* **2004**, *104*, 4971–5003.
10. Hutchison, G. R.; Ratner, M. A.; Marks, T. J. *J. Am. Chem. Soc.* **2005**, *127*, 2339–2350.
11. Irfan, A.; Zhang, J.; Chang, Y. *Chem. Phys. Lett.* **2009**, *483*, 143–146.
12. Coropceanu, V.; Cornil, J.; da Silva Filho, D. A.; Olivier, Y.; Silbey, R.; Bredas, J. L. *Chem. Rev.* **2007**, *107*, 926–952.
13. Kwon, O.; Coropceanu, V.; Gruhn, N. E.; Durivage, J. C.; Laquindanum, J. G.; Katz, H. E.; Cornil, J.; Bredas, J. L. *J. Chem. Phys.* **2004**, *120*, 8186–8194.
14. Deng, W.; Goddard III, W. A. *J. Phys. Chem. B.* **2004**, *108*, 8614–8621.
15. Hutchison, G. R.; Ratner, M. A.; Marks, T. J. *J. Am. Chem. Soc.* **2005**, *127*, 16866–16881.
16. Tsuzuki, S.; Honda, K.; Azumi, R. *J. Am. Chem. Soc.* **2002**, *124*, 12200–12209.
17. Graf, D. D.; Campbell, J. P.; Miller, L. L.; Mann, K. R. *J. Am. Chem. Soc.* **1996**, *118*, 5480–5481.
18. Graf, D. D.; Duan, R. G.; Campbell, J. P.; Miller, L. L.; Mann, K. R. *J. Am. Chem. Soc.* **1997**, *119*, 5888–5899.

19. Johnson, E. R.; Becke, A. D.; Sherrill, C. D.; DiLabio, G. A. *J. Chem. Phys.* **2009**, *131*, 034111-1-034111-7.
20. Johnson, E. R.; DiLabio, G. A. *Chem. Phys. Lett.* **2006**, *419*, 333–339.
21. Mackie, I. D.; DiLabio, G. A. *J. Phys. Chem. A* **2008**, *112*, 10968–10976.
22. Mackie, I. D.; McClure, S. A.; DiLabio, G. A. *J. Phys. Chem. A* **2009**, *113*, 5476–5484.
23. Hamprecht, F. A.; Cohen, A. J.; Tozer, D. J.; Handy, N. C. *J. Chem. Phys.* **1998**, *109*, 6264–6271.
24. Perdew, J. P.; Burke, K.; Ernzerhof, M. *Phys. Rev. Lett.* **1996**, *77*, 3865–3868.
25. (a) Becke, A. D. *J. Chem. Phys.* **1993**, *98*, 5648–5652. (b) Lee, C.; Yang, W.; Parr, R. G. *Phys. Rev. B* **1988**, *37*, 785–789.
26. Perdew, J. P.; Chevary, J. A.; Vosko, S. H.; Jackson, K. A.; Pederson, M. R.; Singh, D. J.; Fiolhais, C. *Phys. Rev. B* **1992**, *46*, 6671–6687.
27. DiLabio, G. A. *Chem. Phys. Lett.* **2008**, *455*, 348–353.
28. Johnson, E. R.; Mackie, I. D.; DiLabio, G. A. *J. Phys. Org. Chem.*, in press.

29. Frisch, M. J.; Trucks, G. W.; Schlegel, H. B.; Scuseria, G. E.; Robb, M. A.; Cheeseman, J. R.; Montgomery, J. A. Jr.; Vreven, T.; Kudin, K. N.; Burant, J. C.; Millam, J. M.; Iyengar, S. S.; Tomasi, J.; Barone, V.; Mennucci, B.; Cossi, M.; Scalmani, G.; Rega, N.; Petersson, G. A.; Nakatsuji, H.; Hada, M.; Ehara, M.; Toyota, K.; Fukuda, R.; Hasegawa, J.; Ishida, M.; Nakajima, T.; Honda, Y.; Kitao, O.; Nakai, H.; Klene, M.; Li, X.; Knox, J. E.; Hratchian, H. P.; Cross, J. B.; Adamo, C.; Jaramillo, J.; Gomperts, R.; Stratmann, R. E.; Yazyev, O.; Austin, A. J.; Cammi, R.; Pomelli, C.; Ochterski, J. W.; Ayala, P. Y.; Morokuma, K.; Voth, G. A.; Salvador, P.; Dannenberg, J. J.; Zakrzewski, V. G.; Dapprich, S.; Daniels, A. D.; Strain, M. C.; Farkas, O.; Malick, D. K.; Rabuck, A. D.; Raghavachari, K.; Foresman, J. B.; Ortiz, J. V.; Cui, Q.; Baboul, A. G.; Clifford, S.; Cioslowski, J.; Stefanov, B. B.; Liu, G.; Liashenko, A.; Piskorz, P.; Komaromi, I.; Martin, R. L.; Fox, D. J.; Keith, T.; Al-Laham, M. A.; Peng, C. Y.; Nanayakkara, A.; Challacombe, M.; Gill, P. M. W.; Johnson, B.; Chen, W.; Wong, M. W.; Gonzalez, C.; Pople, J. A. Gaussian 03, Revision D.01; Gaussian, Inc.: Pittsburgh, PA, **2004**.
30. Zhurko, G. A.; Zhurko, D. A. Chemcraft, version 1.6.
www.chemcraftprogram.com.
31. <http://www.wavefun.com>.
32. Zhang, G.; Pei, Y.; Ma, J. J. Phys. Chem. B **2004**, *108*, 6988–6995.

33. Rodriguez-Ropero, F.; Casanovas, J.; Aleman, C. J. *Comput. Chem.* **2007**, *29*, 69–78.
34. Antolini, L.; Horowitz, G.; Kouki, F.; Garnier, F. *AdV. Mater.* **1998**, *10*, 382–385.
35. Siegrist, T.; Kloc, C.; Laudise, R. A.; Katz, H. E.; Haddon, R. C. *Adv. Mater.* **1998**, *10*, 379–382.
36. MP2 is sometimes used for calculations of these types. However, with large basis sets, MP2 generally overbinds dispersion-bound systems. More computationally intensive approaches, such as CCSD(T) can be used but only for small systems (ca. less than 15 heavy atoms).

Chapter 5

Conclusion

This thesis has described the synthesis of stable water-soluble CdSe nanorods and their successful incorporation into nanocomposite thin films via electrostatic layer-by-layer assembly. An ELBL bulk heterojunction architecture in the nanocomposite films was achieved and the electrical characteristics of the multilayers were analyzed by integrating the ELBL thin films into solar cell devices. Current-voltage analysis was discussed in the context of film morphology and nanoparticle surface chemistry. Poor charge mobility and low shunt resistances were found to lead to low conversion efficiencies in the assembled thin films. The carrier transport properties of the polymeric component of the multilayers were studied using density functional theory with dispersion correcting potential to account for the long range interactions inherent to thin films. The structure-function relationship between thiophene dimers and their charge transport characteristics were studied with large variations in transport predicted between conformers. Transport was found to be sensitive to molecular motion at room temperature.

This chapter will highlight the main results of the preceding chapters and look into potential research directions of ELBL assembly of thin films and the investigation into their device performance.

5.1 Chapter Summaries

Chapter 1

Chapter 1 discussed the background to this thesis and provided the motivation for the investigation in succeeding chapters. Optoelectronic processes between conducting polymers and semiconductor nanoparticles were highlighted along with the methods for characterizing the photoelectrical properties of photoactive thin films. The molecular origins behind device parameters were also discussed and an overview of semiconductor nanoparticles was given using CdSe and CdTe as case studies. A background on the synthesis and physical chemistry of semiconductor nanoparticles was presented, and the integration of these particles into functional devices was highlighted by looking at the design principles behind polymer-based third-generation photovoltaics. The effect of particle size and shape, film morphology and nanoparticle surface chemistry were all discussed in the context of device performance. Future applications were also highlighted to bring attention to some of the new avenues of research in the field of polymer-based third-generation optoelectronics.

Computational studies of charge transport in organic semiconductors were also highlighted. A short introduction to density functional theory (DFT) was provided, followed by a discussion on charge transport in organic semiconductors using thiophenes as a case study. Finally, the energy splitting in dimer approach to modeling charge transport was presented.

Chapter 2

Chapter 2 presented the procedures behind the synthesis of stable water-soluble semiconductor nanoparticles and their incorporation into functional thin films using electrostatic layer-by-layer (ELBL) assembly. In order to fabricate photoactive films, highly stable solutions of water-soluble CdSe nanorods were synthesized. Characterization of the material provided insight into their optical and electrical properties and showed them to be excellent candidates for optoelectronics applications. Fabrication of nanocomposite thin films was successfully achieved via the partnering of CdSe nanorods with two photoactive polymers using ELBL assembly. Nanoscale control over film thickness and the realization of a bulk heterojunction architecture was shown through thorough characterization of the multilayer thin films.

Chapter 3

Chapter 3 discussed the electrical characterization of photoactive thin films and the proof-of-concept to developing functional devices. The ELBL films synthesized in Chapter 2 were integrated into device architectures for electrical characterization and solar cell fabrication. Fitting the IV curves to a one-diode model allowed for the interpretation of the electrical characterization in terms of film chemistry. Nanorod aspect ratio and orientation were found to play significant roles in overall performance. The quality of the multilayers was

assessed in the context of thin film uniformity with low shunt resistance values attributed to film roughness. Nanorod orientation and film quality were further characterized via cross-sectional scanning electron microscopy (SEM). Charge transfer (CT) in the materials was confirmed through photoluminescence (PL) quenching experiments.

Chapter 4

Chapter 4 used computational chemistry as a tool to go beyond the limitations of experiment to investigate the fundamentals behind charge transport in the polymeric component of the nanocomposite films. Density functional theory (DFT) was used along with optimized dispersion correcting potentials to account for the long-range non-covalent interactions inherent to organic thin films. A variety of dimer conformers were calculated using the DCP-DFT approach which allowed for structure-function relationships to be established regarding carrier transport in these materials. Using the energy splitting in dimer approach, the splittings of simple T1 systems were first calculated to gain an understanding of which structural transformations led to specific changes in splitting. Dimers up to T6 were calculated using an orbital analysis to rationalize the structure-function results. It was discovered that thiophene conformers close in energy display a large variation in transport properties. In addition, frequency calculations showed that very small changes in the positions of atoms that make up the dimers can lead to significant changes in carrier transport.

5.2 Proposed Research Directions

Layer-by-Layer Film Deposition onto High Surface Area Electrodes

The technology developed in this thesis involves the layer-by-layer deposition of optoelectronic photoactive material onto electrode surfaces. The technique allows for the deposition to occur on a variety of surface topographies that opens the door towards a number of potential applications. In LEDs and third-generation photovoltaics, the electrode most commonly used is a transparent conducting oxide (TCO) such as ITO. ITO acts as either the hole collector in the case of solar cells or the hole injector in LEDs. A large effort to increasing the performance of these devices involves the fabrication of high surface area electrodes.^{1 - 4} Electrodes with high surface area can increase the number of critical CT events at the electrode/PAL interface as well as improve the overall architecture of the PAL within the device. In one example, Singer et al. deposited a PAL of P3HT/PCBM onto high surface area ZnO electrodes and showed a 20-fold increase in short-circuit current.⁵ Hoertz et al. showed that current densities in high surface area nanoelectrodes (see Figure 5.1) exceed those on planar ITO electrodes in addition to having comparable optical transparency.¹

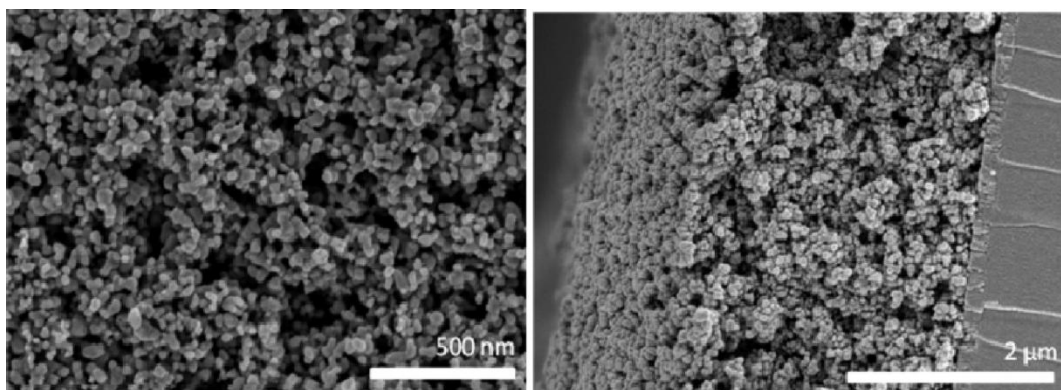


Figure 5.1. Cross-sectional SEM images of high surface area nanoITO electrode. Reprinted with permission from ref. 1. Copyright © 2010 American Chemical Society.

To date, devices using high surface area electrodes do not compete with conventional flat electrodes despite the improvement that should be gained by the increase in surface area and improved electrical properties. A better overall PAL architecture would also be expected assuming full infiltration of the PAL material onto the electrode surface. Conventional spin-casting techniques may not allow for good infiltration of the PAL leading to overburdens of material on the electrode (see Figure 5.2). In order for high surface area electrodes to make an impact in photovoltaics, excellent deposition of the PAL is needed.



Figure 5.2. A) Incomplete infiltration of PAL onto high surface area electrode. B) Complete infiltration of PAL

The ability of electrostatic layer-by-layer assembly to add bilayers to high surface area material was shown by Xiao et al. by using ELBL to assemble bilayers of poly(diallyldimethylammonium chloride) (PDADMAC) and polyacrylic acid (PAA) onto negatively charged cellulose acetate (CA) nanofibers.⁶ Figure 5.3 shows successful deposition of multiple layers of PDADMAC and PAA onto the nanofibers through ELBL assembly.

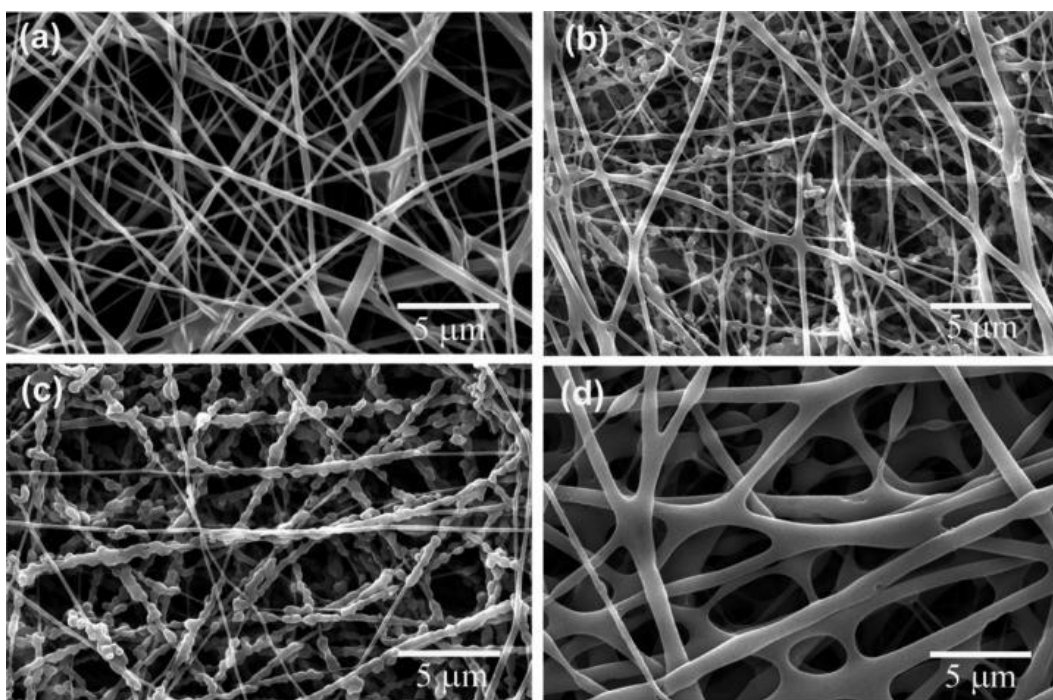


Figure 5.3. SEM images of CA nanofibers assembled with (a) three, (b) four, (c) five, and (d) six bilayers of PAA/PDADMAC. Reprinted with permission from ref. 6. Copyright © 2009 American Chemical Society.

These types of studies show that ELBL onto complex shapes is possible. Infiltration of the PAL into high surface area electrodes may also allow for

improved contact to the electrode and a resultant improvement in device performance.

Electric Field Alignment of Nanorods

In the Introduction as well as in Chapter 3 of this thesis, the importance of nanorod alignment to device performance was discussed. Particles that lie perpendicular to the electrode are in the direction of charge transport, requiring less hopping events for the charges to reach the electrical contacts. Chapter 3 showed evidence that the thin films in this thesis were predominantly parallel to the electrode surface. This is an area of research which needs to be addressed in order to achieve devices with good performance.

Nanorods have a polarization along their c-axis and are therefore able to be manipulated by electric fields. This approach may allow for the introduction of a desired anisotropy into photoactive thin films that contain semiconductor nanorods. In one study, Hu et al. showed how localized electric fields could be used to align nanorods of both CdSe and CdTe.⁷ Figure 5.4 shows the results of their experiments with the HR-TEM images displaying the alignment of CdSe nanorods at the surface of the electrode. The electric field applied was 4.1×10^6 V/m supplied by 9 volts of applied potential. Ryan et al. used electric fields to align nanorods of CdS in toluene between two gold electrodes.⁸ In this study, nanorods were aligned with domain sizes larger than $0.5 \mu\text{m}^2$ as shown in Figure 5.5. Such large scale alignment is important for the potential device applications.

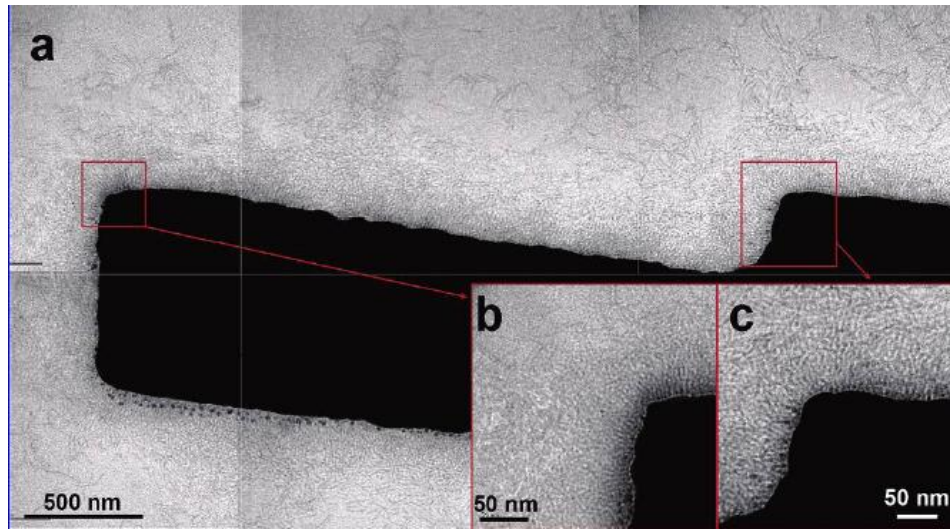


Figure 5.4. TEM images showing alignment of CdSe nanorods using electric fields around a single electrode (a) along with magnifications (b and c) showing the nanorods perpendicular to the electrode surface. Reprinted with permission from ref. 7. Copyright © 2006 American Chemical Society.

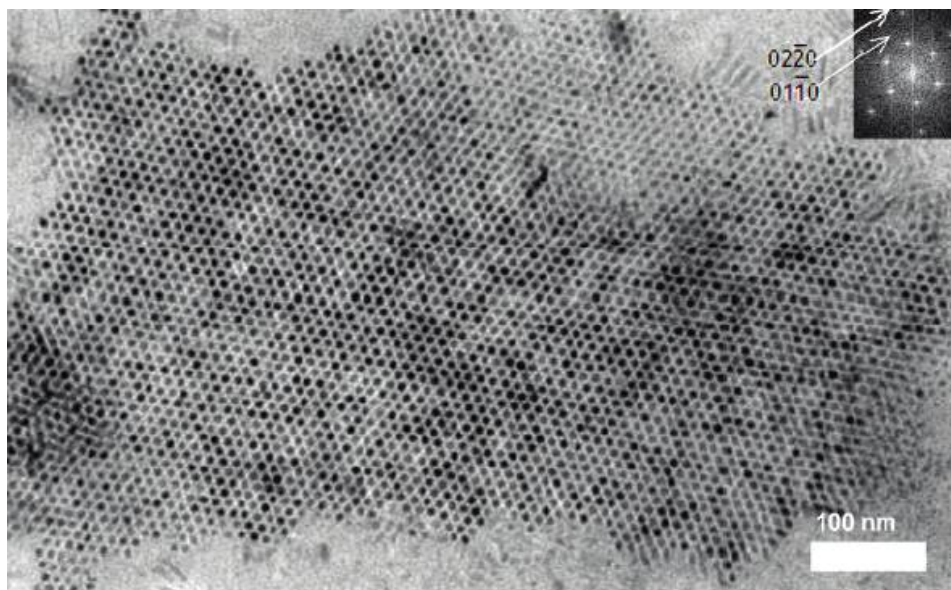


Figure 5.5. Alignment of CdS nanorods using electric fields. Domain sizes exceeding $0.5 \mu\text{m}^2$ are important for device applications. Reprinted with permission from ref. 8. Copyright © 2006 American Chemical Society.

Similar methods may be used for nanorod/polymer nanocomposites to align the particles along a desired direction. The design of a hybrid solar cell device contains two electrodes sandwiching a nanocomposite PAL. Annealing the thin film to a point that the polymer matrix is close to its glass transition temperature (T_g), and the application of a strong electric field across the device may induce a degree of ordering (see Figure 5.6).

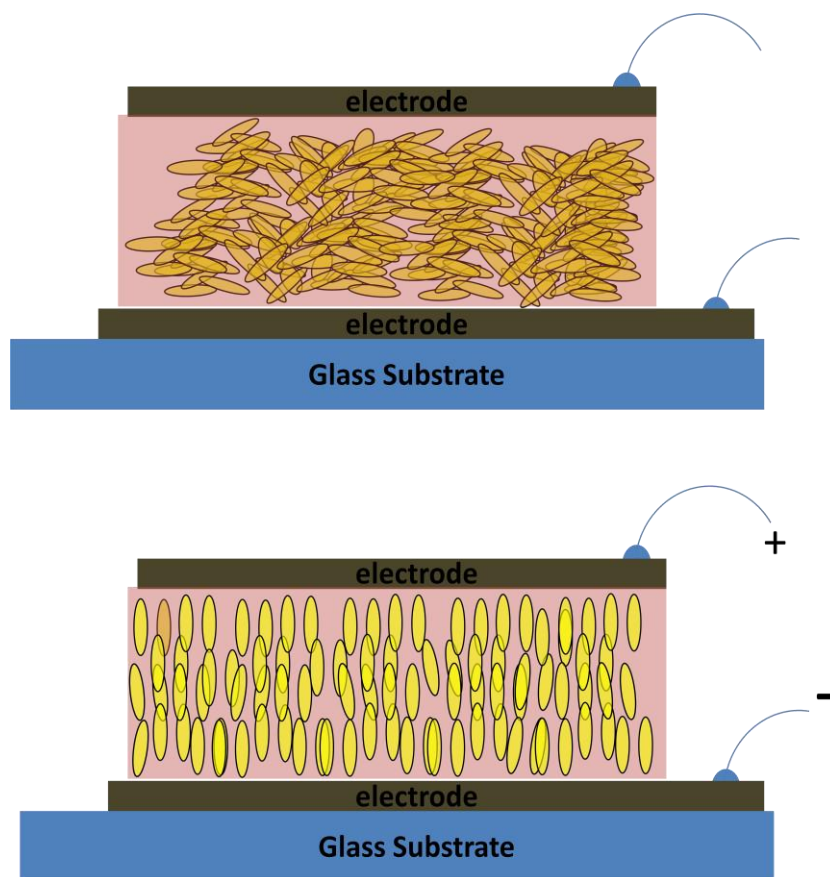


Figure 5.6. Ordering induced in nanorods within the PAL of a hybrid device. The polymer matrix would need to be brought to its T_g in order to allow the nanorods to have mobility.

Modeling Charge Transfer between CdSe and Thiophenes

In order to fully describe hybrid solar cell performance, a computational study of CT between conducting polymer and semiconductor nanocrystals is essential. Bredas et al. has used computational chemistry to explore exciton dissociation and recombination processes in cofacial complexes of perylenebismide (PTCDI) and phthalocyanine (Pc).⁹ This quantum chemical treatment of the optoelectronic mechanisms offers insight into device performance that cannot be obtained from experiment alone.

The methodology used by Bredas begins with modeling the charge transfer process as an electron transfer reaction governed by the Marcus theory of electron transfer much as was the case for carrier transport in Chapter 4. Equation 5.1 shows the rate of electron transfer with the Gibbs free energy term included on the right hand side. The Gibbs free energy can be considered the driving force for electron transfer.

$$5.1 \quad k_{ET} = \frac{4\pi^2}{h} \frac{1}{\sqrt{4\pi\lambda k_B T}} V^2 \exp\left(-\frac{(G^o + \lambda)^2}{4\lambda k_B T}\right)$$

To determine the Gibbs free energy term in the above expression, the differences in energy between donor and acceptor systems before and after charge transfer are calculated (see equation 5.2). The equation includes the term for the Coulombic attraction between the electron and the hole in the exciton. This

Coulombic term can be calculated using a pairwise summation of the charges and distances between atoms in the donor-acceptor pair.

$$5.2 \quad \Delta G_{dis}^o = E^{D^+} + E^{A^-} - E^{D^*} - E^A + \Delta E_{coul}$$

$$5.3 \quad \Delta E_{coul} = \sum_{D^+} \sum_{A^-} \frac{q_{D^+} q_{A^-}}{4\pi\epsilon_o \epsilon_s r_{D^+ A^-}} - \sum_{D^*} \sum_A \frac{q_{D^*} q_A}{4\pi\epsilon_o \epsilon_s r_{D^* A}}$$

Adapting this methodology to the thiophene-CdSe system may provide insight into the charge transfer mechanisms in hybrid solar cell devices. The differences between transfer and recombination rates could be calculated along with the changes that arise when nanorod dimensions are modified. Various binding motifs between the thiophenes and nanoparticles could be calculated and the resulting Coulombic terms included in the above expressions. In order to calculate the energies in equation 5.1, geometry optimizations of both thiophenes and nanoparticles must give accurate energies in a variety of electronic states.

Geometry optimization has shown interesting surface reconstruction on the surface of CdSe nanoparticles.^{10,11} The effect these reconstructions have on

the band gap of material has been shown by Galli et al.¹² The changes modify the values of the conduction band (CB) and valence band (VB) edges and thus effect the offset to in the type-II heterojunction. The symmetry of the molecular orbitals are also known to affect the ability of donor / acceptor pairs to undergo CT. Figure 5.7 shows the orbital analysis used by Bredas to predict which energy levels are involved in the CT process. Isosurfaces can also be generated on the nanocrystals using standard quantum chemistry methods. Analysis of the interaction between thiophene and nanocrystal orbitals may prove insightful to understanding CT between the components.

Reorganization energies (changes in bond lengths and geometry) can also be calculated although the reorganization energies in semiconductor nanoparticles are expected to be quite small and may not lead to large contributions to the overall expression in 5.1. Thus far, the reorganization energy for quantum dots have not been reported however it is expected to be quite small due to the delocalization of the 1s electron.¹³ Solvent reorganization can also play a role in electron transfer and these contributions may also be included in the above methodology.

The above methodology may allow for a strong connection between the synthetic chemistry used in the design of photoactive material and the underlying theories that help explain the optoelectronic processes.

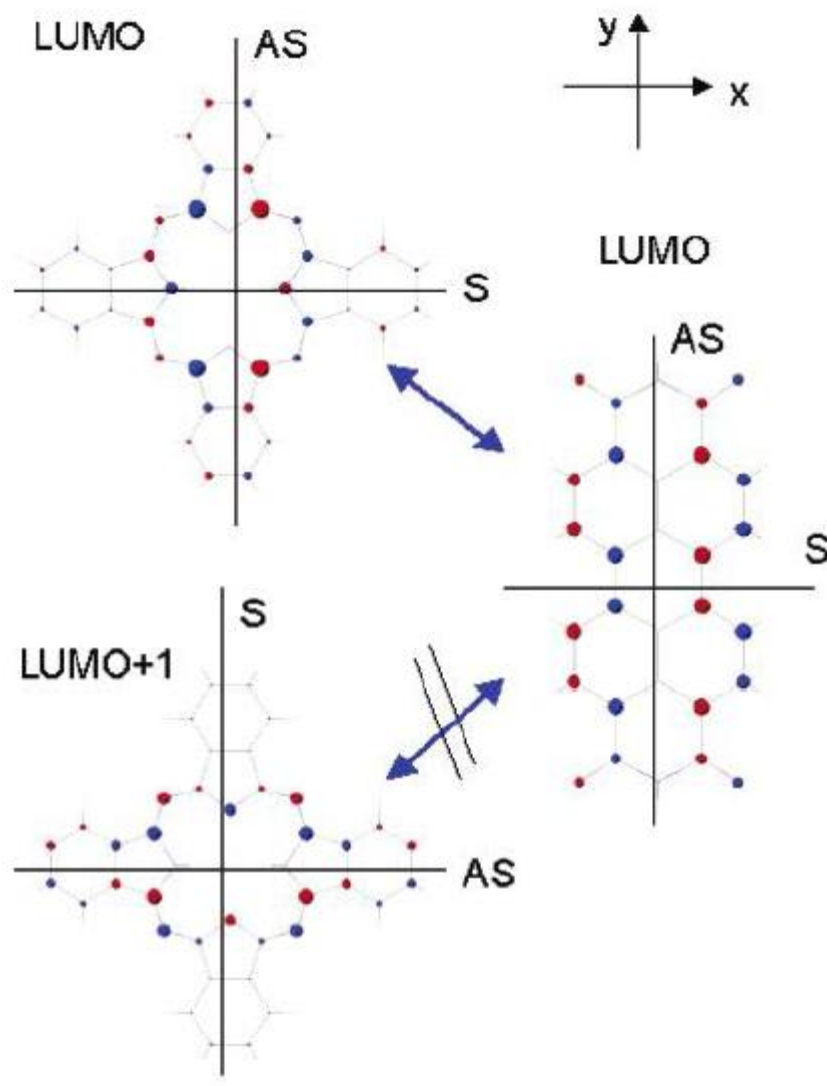


Figure 5.7. Orbital analysis of HOMO and LUMOs between PTCI and PC. Symmetry allows certain molecular arrangements to undergo CT while others forbid it. Reprinted with permission from ref. 9. Copyright © 2005 American Chemical Society.

Another aspect of solar cell design that may benefit greatly from computational studies is film morphology. Most quantum chemistry methods are much too demanding on computational resources to handle the large number of atoms required to give an accurate description of thin film morphology. Other

methods, such as course-grained approaches, can handle a large number of atoms while giving fairly accurate results. Huang et al. used this approach to model the morphology of thiophene/PCBM thin films.¹⁴ The authors found that the method accurately described the structure of the materials over a wide range of thermodynamic conditions. The scale of their study was able to predict phase separation in films for OPV devices. Figure 5.8 shows an example of the bulk heterojunction morphology predicted in Huang's study.

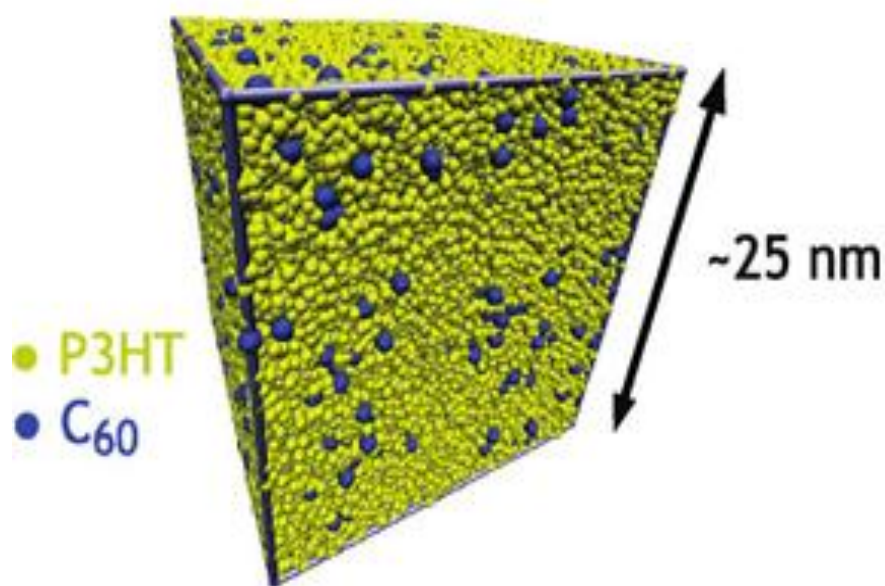


Figure 5.8. Bulk heterojunction of the thiophene/PCBM system as predicted by a course grained approach used by Huang. Reprinted with permission from ref. 14. Copyright © 2010 American Chemical Society.

This approach may prove useful for nanoparticle/polymer systems in order to understand the environment around each nanoparticle which the polymer matrix provides. Taking a portion of this environment may allow for a full quantum chemical treatment of the nanoparticle-polymer interaction in order to elucidate some of the CT parameters for this system. Simulated annealing experiments could also be conducted to predict the changes that occur with temperature increases in the film.

5.3 References

1. Hoertz, P.G.; Chen, Z.; Kent, C.A.; Meyer, T.J. *Inorg. Chem.* **2010**, *49*, 8179.
2. Krause, K.M.; Taschuk, M.T.; Harris, K.D.; Rider, D.A.; Wakefield, N.G.; Sit, J.C.; Buriak, J.M.; Thommes, M.; Brett, M.J. *Langmuir* **2010**, *26*, 4368 - 4376.
3. Jiang, Q.W.; Wang, G.R.L.F.; Gao, X.P. *Electrochem. Comm.* **2010**, *12*, 924 - 927.
4. Wallace, G.G.; Chen, J.; Mozer, A.J.; Forsyth, M.; MacFarlane, D.R.; Wang, C. *Mat. Today* **2009**, *12*, 20 - 27.
5. Jr, R.S.A.; Gunther, D.; Ueda, A.; Pan, Z.; Collins, W.E.; Mu, R.; Singer, K.D. *Nanotechnology* **2009**, *20*, 465204.
6. Xiao, S.; Wu, S.; Shen, M.; Guo, R.; Huang, Q.; Wang, S.; Shi, X. *ACS Appl. Mater. Interfac.* **2009**, *1*, 2848 - 2855.
7. Hu, Z.; Fischbein, M.D.; Querner, C.; Drndic, M. *Nano Lett.* **2006**, *6*, 2585 - 2591.
8. Ryan, K.M.; Mastroianni, A.; Stancil, K.A.; Liu, H.; Alivisatos, A.P. *Nano Lett.* **2006**, *6*, 1479 - 1482.

9. Lemaure, V.; Steel, M.; Beljonne, D.; Bredas, J.L.; Cornil, J. J. Am. Chem Soc. **2005**, *127*, 6077 - 6086.
10. Yu, M.; Fernando, G.W.; Li, R.; Papadimitrakopoulos, F.; Shi, N.; Ramprasad, R. J. Comp. Mater. Des. **2007**, *14*, 167 - 174.
11. Yu, M.; Fernando, G.W.; Li, R.; Papadimitrakopoulos, F.; Shi, N.; Ramprasad R. Appl. Phys. Lett. **2006**, *88*, 231910.
12. Puzder, A.; Williamson, A.J.; Gygi, F.; Galli, G. Phys. Rev. Lett. **2004**, *92*, 217401.
13. Boulesbaa, A.; Huang, Z.; Wu, D.; Lian, T. J. Phys. Chem. C **2010**, *114*, 962 - 969.
14. Huang, D.M.; Faller, R.; Do, K.; Moule, A.J. J. Chem. Theory Comput. **2010**, *6*, 526 - 537.